SEISMIC MODELING OF COMPLEX STRATIFIED RESERVOIRS

A Dissertation

by

HUNG-LIANG LAI

Submitted to the Office of Graduate Studies of
Texas A&M University
in partial fulfillment of the requirements for the degree of

DOCTOR OF PHILOSOPHY

May 2007

Major Subject: Geophysics

SEISMIC MODELING OF COMPLEX STRATIFIED RESERVOIRS

A Dissertation

by

HUNG-LIANG LAI

Submitted to the Office of Graduate Studies of
Texas A&M University
in partial fulfillment of the requirements for the degree of

DOCTOR OF PHILOSOPHY

Approved by:

Chair of Committee,	Richard L. Gibson
Committee Members,	Akhil Datta-Gupta
	David W. Sparks
	Joel S. Watkins
	Mark E. Everett
Head of Department,	John H. Spang

May 2007

Major Subject: Geophysics

ABSTRACT

Seismic Modeling of Complex Stratified Reservoirs. (May 2007)
Hung-Liang Lai, B.S., National Cheng-Kung University, Taiwan;
M.S., National Chung-Cheng University, Taiwan
Chair of Advisory Committee: Dr. Richard L. Gibson

Turbidite reservoirs in deep-water depositional systems, such as the oil fields in the offshore Gulf of Mexico and North Sea, are becoming an important exploration target in the petroleum industry. Accurate seismic reservoir characterization, however, is complicated by the heterogeneous of the sand and shale distribution and also by the lack of resolution when imaging thin channel deposits. Amplitude variation with offset (AVO) is a very important technique that is widely applied to locate hydrocarbons. Inaccurate estimates of seismic reflection amplitudes may result in misleading interpretations because of these problems in application to turbidite reservoirs. Therefore, an efficient, accurate, and robust method of modeling seismic responses for such complex reservoirs is crucial and necessary to reduce exploration risk.

A fast and accurate approach generating synthetic seismograms for such reservoir models combines wavefront construction ray tracing with composite reflection coefficients in a hybrid modeling algorithm. The wavefront construction approach is a modern, fast implementation of ray tracing that I have extended to model quasi-shear wave propagation in anisotropic media. Composite reflection coefficients, which are computed using propagator matrix methods, provide the exact seismic reflection amplitude for a stratified reservoir model. This is a distinct improvement over conventional AVO analysis based on a model with only two homogeneous half spaces. I combine the two methods to compute synthetic seismograms for test models of turbidite reservoirs in the Ursa field, Gulf of Mexico, validating the new results against exact calculations using the discrete wavenumber method. The new method, however, can also be used to generate synthetic seismograms for the laterally heterogeneous, complex stratified reservoir models. The results show important frequency dependence that may be useful for exploration.

Because turbidite channel systems often display complex vertical and lateral heterogeneity that is difficult to measure directly, stochastic modeling is often used to

predict the range of possible seismic responses. Though binary models containing mixtures of sands and shales have been proposed in previous work, log measurements show that these are not good representations of real seismic properties. Therefore, I develop a new approach for generating stochastic turbidite models (STM) from a combination of geological interpretation and well log measurements that are more realistic. Calculations of the composite reflection coefficient and synthetic seismograms predict direct hydrocarbon indicators associated with such turbidite sequences. The STMs provide important insights to predict the seismic responses for the complexity of turbidite reservoirs. Results of AVO responses predict the presence of gas saturation in the sand beds. For example, as the source frequency increases, the uncertainty in AVO responses for brine and gas sands predict the possibility of false interpretation in AVO analysis.

ACKNOWLEDGMENTS

Special thanks to Dr. Gibson for his guidance, encouragement and support during my study at A&M. Whenever I run into problems with research or lose direction, he is always there to help me out. Also, I would like to thank my committee Dr. Datta-Gupta, Dr. Sparks, Dr. Watkins, and Dr. Everett.

I gratefully acknowledge support for this work from the National Science Foundation Information Technology Research program under grant number ACI-0081510 and the Department of Energy National Petroleum Technology Office under project DE-FC26-02NT15342. I would also like to acknowledge contributions from Nancy Amato, Jyh-Ming Lien, Roger Pearce, and Samuel Rodriguez (Dept. of Computer Science, Texas A&M University)

I want to thank colleagues in the Seismic Lab at A&M. Koung-Jin helped me a lot in research and generously left his Linux box for my work. Ravi and Hoa shared valuable research suggestions with me. Also, I would like to thank Sung Yuh, Costas Tzimeas, Pablo, Seung, and John. I always remember you guys being nice to me.

Finally, I appreciate the support from my family. They are the strongest backup and encouraged me to accomplish my Ph.D.

TABLE OF CONTENTS

Page

CHAPTER Page

CHAPTER Page

LIST OF TABLES

LIST OF FIGURES

FIGURE Page

FIGURE Page

FIGURE Page

FIGURE Page

FIGURE Page

FIGURE Page

FIGURE Page

FIGURE Page

FIGURE Page

FIGURE Page

FIGURE Page

FIGURE Page

FIGURE Page

CHAPTER I

INTRODUCTION

1.1 Motivation and Overview

Turbidite reservoirs in deep-water depositional systems such as the oil fields in offshore Gulf of Mexico and the North Sea are becoming an important exploration target in the petroleum industry. However, accurate seismic reservoir characterization is complicated not only by the heterogeneity of the sand and shale distribution, but also by the lack of resolution when imaging thin channel deposits. Amplitude variation with offset (AVO) is a very important technique that is widely applied to locate hydrocarbons, but inaccurate estimate of seismic reflection amplitudes because of these problems in application to turbidite reservoirs may lead to misleading interpretations. Therefore, an efficient, accurate, and robust method of modeling seismic responses for such complex reservoirs is crucial and necessary to reduce exploration risk.

Wavefront construction (WFC) methods not only provide fast and robust tools for computing ray theoretical traveltimes and amplitudes for multivalued wavefields (Vinje et al., 1993; Lambaré et al., 1996; Lucio et al., 1996; Vinje et al., 1999; Gibson, Jr., 1999; Mispel and Williamson, 2001; Mispel, 2001; Kaschwich and Gajewski, 2003; Rüger, 2004; Lai et al., 2004; Gibson, Jr. et al., 2005), but also have strong potential to model propagation in complex, multiple layered, 3-D earth models, such as salt dome structures. They simulate a wavefront propagating through a model using a mesh that is refined adaptively to ensure accuracy as rays diverge during propagation. However, an implementation for quasi-shear (qS) waves in anisotropic media can be very difficult, since the two qS slowness surfaces and wavefronts often intersect at shear-wave singularities. The shear wave singularities cause difficulties on both wavefront mesh initiation and interpolation as the wavefront propagates. Though Mispel (2001) presents WFC modeling for vertically transverse isotropic media, a full implementation in the general anisotropic media is still not available.

This dissertation follows the style and format of Geophysics.

AVO is a powerful technique to locate hydrocarbons in the reservoir because seismic reflection responses change dramatically with offset as fluid saturation changes in in the pore space (Domenico, 1976; Ostrander, 1984; Murphy, 1984; Rutherford and Williams, 1989; Castagna et al., 1998; Ross, 2000; Smith and Sondergeld, 2001; Zillmer, 2006; Wandler et al., 2007). However, conventional AVO analysis considering P-wave reflection from a simple interface between two welded half spaces is limited when applying AVO analysis to thin reservoir models. The thin layer tuning effect, the superposition of reflections from the top and bottom of a relative thin reservoir, can be included in the AVO modeling (Widess, 1973; Almoghrabi and Lange, 1986; Juhlin and Young, 1993; Bakke and Ursin, 1998; Liu and Schmitt, 2003), but it is more difficult to predict the seismic responses when there is strong internal fluctuation of rock properties in the thin layer, such as in turbidite reservoirs. Therefore, accurate estimate of amplitude of AVO responses is important and necessary to avoid false interpretations.

Turbidite reservoirs with strongly heterogeneous rock properties for sand and shale beds can make accurate and fast seismic modeling for the AVO responses difficult. Turbidity currents developing channel, levee and sheet-like deposits results in complex vertical and lateral heterogeneity in turbidite reservoirs. Though binary models (Takahashi et al., 1999; Stovas et al., 2004; Stovas et al., 2006) containing the mixtures of sands and shales have been proposed to modeling turbidite reservoirs in previous work, the models do not produce realistic seismic properties. Hence, an improved stochastic turbidite model (STM) generated from a combination of geological interpretation and well logs is proposed to simulate direct hydrocarbon indicators associated with turbidite sequences (Lai and Gibson, Jr., 2005). The STMs provide important insights to predict the seismic responses for the complexity of turbidite reservoirs.

Wave propagation through multi-layered media including reflection, transmission and conversion complicates seismic modeling. The propagator matrix method has been introduced to solve for reflection and transmission coefficients in media with horizontally stratified isotropic layers (Thomson, 1950; Haskell, 1953; Gilbert and Backus, 1966). Instead of the direct computation of the plane layer responses, the reflectivity method (Kennett and Kerry, 1979; Booth and Crampin, 1983; Müller, 1985) is also applied to model wave propagation for such layer stacked models. Furthermore, Gibson, Jr. (2004, 2005) suggested the propagator matrix method to quickly

compute the composite P-wave reflection coefficient for stratified reservoir models.

However, generating the complete synthetic seismograms in complex stratified reservoir is computationally expensive, especially for the large number of seismograms required for a complete seismic survey model including lateral heterogeneity. Červený (1989) suggested a hybrid approach which combines ray tracing modeling in overburden layers with the reflectivity method in a laterally varying thin transition layer. Here, I would propose a hybrid algorithm combining fast and accurate WFC ray tracing with the complete solution of composite reflection coefficients in a stack of complex stratified layers. It can be a powerful tool for seismic modeling in such complex stratified turbidite reservoir models.

1.2 Objectives

In Chapter II, the objective is to solve the S-wave singularity problem and ensure that qS wave WFC modeling can correctly separate the two qS waves in both wave propagation and mapping the ray data. These ray solutions can be verified with the analytic solutions and used to generate synthetic seismograms. The results for both qS waves are validated with other independent methods. A full demonstration of qS wave WFC modeling in general anisotropic media is also one of the objectives.

In Chapter III, the primary goal is to develop a hybrid algorithm combining the fast WFC ray tracing with composite reflection coefficients to generate full waveform synthetic seismograms for the complex, stratified reservoir models. This will be accomplished using composite reflection coefficients that include all of the influence of layering in a reservoir on the reflected signal, not simply a single boundary as is done in conventional analysis. The main task in the WFC part is to implement WFC reflection modeling. Some modification of WFC in the interface are performed to achieve this. The ray data of reflection are correctly combined with composite reflection coefficients obtained by the propagator matrix method to generate full wavefront synthetic seismograms. The complete seismograms will help us to understand the influence for the internal fluctuation of rock properties while hydrocarbons charge in the pore space.

In Chapter IV, STMs are proposed to simulate seismic responses and predict the uncertainty in AVO analysis for such complex stratified reservoirs. The complex of vertical and lateral heterogeneity are predicted in a range of possible seismic responses

by stochastic modeling. Comparison of binary and stochastic turbidite models is discussed. Full waveform synthetic seismograms and AVO analysis in STMs for different frequencies are performed to predict AVO responses.

1.3 Dissertation Structure

This will briefly describe the content and provide previews of each chapter. Chapter I gives a general introduction to the scientific problems related to this dissertation and a clear review of previous work. I also address the problems that I want to solve in each chapter. Chapter II includes quasi-shear wave ray tracing by wavefront construction in 3-D, anisotropic media. A full demonstration of S wave WFC in the general anisotropic media is shown. A set of verification results for traveltimes and amplitudes and validation for the synthetic seismograms demonstrate the accuracy and robustness of S wave WFC. In Chapter III, I extend WFC algorithms for reflection modeling in multi-region models. Fast ray tracing results are combined with the composite reflection coefficient in the target reservoir to generate complete synthetic seismogram for P wave reflection in complex, stratified models. Chapter IV includes the building of STMs and the usage of the method developed in Chapter III to generate P wave reflection synthetic seismograms for both STMs and binary models. The predicted AVO responses are discussed, too. Chapter V concludes the content of each chapter to form the conclusion of this dissertation.

CHAPTER II

QUASI-SHEAR WAVE RAY TRACING BY WAVEFRONT CONSTRUCTION IN 3-D, ANISOTROPIC MEDIA

2.1 Introduction

An accurate knowledge of velocity anisotropy can be very important for interpreting and processing seismic data. For example, Levin (1979), Alkhalifah and Tsvankin (1995), Grechka and Tsvankin (1998), and Grechka et al. (2001) described methods for estimating the moveout velocities in transversely isotropic (TI) media, which can be difficult to estimate from surface seismic data. Banik (1984) and Winterstein (1986) showed that neglecting anisotropy can easily lead to substantial misfits of layer thicknesses when analyzing seismic data. Leslie and Lawton (1999), Grech et al. (2002), and Hornby et al. (2003) showed that corrections for shale anisotropy are necessary to obtain accurate subsurface seismic images.

Shear wave anisotropy can be even more difficult to treat in data processing and interpretation than P-wave anisotropy. Levin (1978, 1979, 1980) pointed out quasi-SV (qSV) waves usually do not have hyperbolic traveltime curves and that moveout velocity varies with distance. Winterstein (1986) concluded that layer thickness obtained from SH-wave data can be significantly thicker than P-wave data in the presence of anisotropy and the percentage of clay in layers dominates the magnitude of anisotropy. Measurement of shear wave splitting also provides further information on earth properties that cannot be obtained from quasi-P (qP) data. For example, shear wave splitting measured from vertical seismic profiles can be interpreted in terms of crack-induced anisotropy (Crampin, 1985; Shearer and Chapman, 1989; Douma and Crampin, 1990; Horne et al., 1997; Crampin and Chastin, 2003; Nistala and McMechan, 2005). Such information regarding crack properties from quasi-S (qS) wave splitting can provide important insights for understanding reservoir performance (Ramos-Martinez et al., 2000).

Efficient and accurate numerical modeling to support processing of these wave propagation phenomena can be more difficult than for qP-wave data. In particular, S-wave propagation in anisotropic media is complicated by the S-wave singularities,

where the two qS-wave slowness surfaces cross or touch (Crampin, 1985; Shearer and Chapman, 1989; Chapman and Shearer, 1989; Coates and Chapman, 1990; Červený, 2001; Vavryčuk, 2001). There are three main types of S-wave singularity: point, kiss and line, and they can appear in weakly or strongly anisotropic media (Crampin and Yedlin, 1981; Červený, 2001; Vavryčuk, 2001).

In strongly anisotropic media, triplications can also complicate propagation of qS-waves, and they have been directly observed in vertical seismic profile field data (Slater et al., 1993). The magnitude of the Thomsen anisotropy parameter δ controls the occurrence of off-axis qSV-wave triplications in TI media (Thomsen and Dellinger, 2003), and Vavryčuk (2004) derived other formulas that can identify the conditions under which triplications develop.

Ray tracing, based on a high frequency approximation to the wave equation, is an efficient and accurate method to study qS or qP-wave propagation in 3D, anisotropic media (Červený, 1972; Hanyga, 1982; Shearer and Chapman, 1989; Gajewski and Pšenčik, 1987; Červený, 2001). Recently developed wavefront construction (WFC) methods in particular have the potential to be robust and accurate for applications to isotropic and anisotropic media (Vinje et al., 1993; Lambaré et al., 1996; Lucio et al., 1996; Vinje et al., 1999; Gibson, Jr., 1999; Mispel and Williamson, 2001; Mispel, 2001; Kaschwich and Gajewski, 2003; Rüger, 2004; Gibson, Jr. et al., 2005). Though not the fastest possible approach, WFC approaches can still be more efficient and reliable than implementations based on shooting methods. The solutions provide results for computation of synthetic seismograms as well as traveltime fields, which is very important for many modeling applications. The results allow for fast, approximate modeling of propagation in 3-D, prior to, for example, more exact modeling using finite differences. Furthermore, these methods are able to compute multiple arrivals at the point of the model (Lambaré et al., 1996; Lucio et al., 1996; Vinje et al., 1996), a result that will be important for many inversion and modeling applications, such as Kirchhoff migration.

The implementation of WFC for quasi-compressional waves is relatively straightforward, and is a fairly natural extension of isotropic algorithms (Gibson, Jr., 1999; Mispel, 2001; Gibson, Jr. et al., 2005). A WFC approach also has strong potential to be very useful for qS-wave modeling (Mispel, 2001; Lai et al., 2004), since it can simplify the modeling of the triplications that are often present even in homogeneous models for the same reasons that tracking of multiple arrivals is facilitated

for qP-wave modeling. However, accurate simulations of qS-wave propagation are complicated significantly by S-wave singularities (Figure 2.1). The difficulties arise because the intersections of qS-wavefronts, and slowness surfaces, complicate the automatic construction of meshes to represent the waves and because the conventional ray tracing equations are degenerate at singularities. Kiss singularities are particularly difficult, since the waves have identical velocities and non-unique displacement vectors.

In this chapter, we show how the mesh construction problem can be addressed using particle motion as the primary criterion for correctly creating meshes that represent qS wavefronts in anisotropic media with singularities. We also suggest some simple steps to help reduce problems associated with the stability of the ray equations and describe how a mesh refinement procedure provides accurate initial meshes even in the presence of kiss singularities. After summarizing these methods, we present results from WFC simulations for several models of varying degrees of complexity to show the correctness of the implementation. Though Mispel (2001) presents results for vertically transverse isotropic (VTI) media, our new implementation allows for more general symmetries including those presented here. After a sequence of verification/validation tests, we demonstrate the ray data can be accurately estimated by the mapping algorithm. A validation of multivalued traveltimes for a qSV-wave wavefront with a triplication caused by intrinsic anisotropy demonstrates accurate modeling of multivalued arrivals. Finally, a comparison of WFC synthetic seismograms with discrete wavenumber full waveform solutions provides further confirmation of accuracy.

2.2 Wavefront Construction Method

The ray solutions developed from asymptotic ray theory provide the equations for travel times and amplitudes in general anisotropic media. The calculation of ray paths and travel times are based on the following set of ordinary differential equations (Červený, 1972; Gajewski and Pšenčik, 1987; Červený, 2001):

$$\begin{aligned} \frac{dx_i}{d\tau} &= a_{ijkl}\, p_l\, D_{jk}\, /D \\ \frac{dp_i}{d\tau} &= -\frac{1}{2}\frac{da_{njkl}}{dx_i} p_n\, p_l\, D_{jk}\, /D, \end{aligned} \tag{2.1}$$

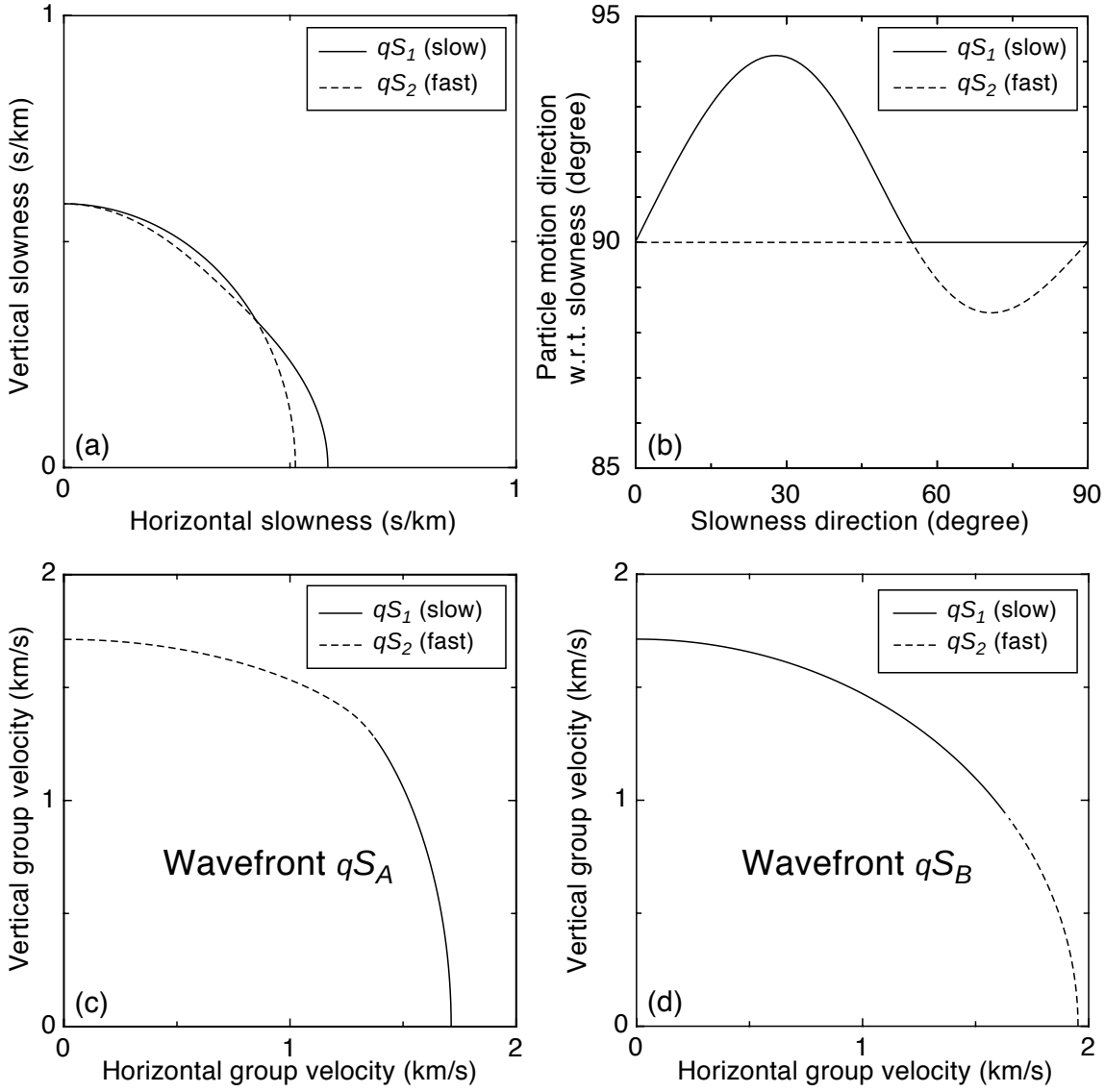

Fig. 2.1. Illustration of the two quasi-shear wavefronts (arbitrarily named qS_A and qS_B) in the presence of shear wave singularities. (a) Cross-section of two qS-wave slowness surfaces for a VTI model (see Table 2.1) in a vertical plane. One is slower (qS_1); the other is faster (qS_2). (b) Particle motion directions are calculated with respect to slowness directions. It suggests the reason to choose the correct wave type (qS_1 and qS_2) for qS_A and qS_B wavefronts. (c) By using particle motion as a criterion to separate two qS-waves, qS_A wavefront is determined. (d) Then, the other wavefront is for qS_B-wave.

where x_i are spatial coordinates of the ray path, τ is travel time, and the p_i are components of the slowness vector. The quantities a_{ijkl} are the elastic moduli normalized by the density. D is the trace of the matrix D_{jk} and D_{jk} is denoted as

$$\begin{aligned}
D_{11} &= (\Gamma_{22}-1)(\Gamma_{33}-1)-\Gamma_{23}^2,\\
D_{22} &= (\Gamma_{11}-1)(\Gamma_{33}-1)-\Gamma_{13}^2,\\
D_{33} &= (\Gamma_{11}-1)(\Gamma_{22}-1)-\Gamma_{12}^2,\\
D_{12} &= D_{21} = \Gamma_{13}\Gamma_{23}-\Gamma_{12}(\Gamma_{33}-1),\\
D_{13} &= D_{31} = \Gamma_{12}\Gamma_{23}-\Gamma_{13}(\Gamma_{22}-1),\\
D_{23} &= D_{32} = \Gamma_{12}\Gamma_{13}-\Gamma_{23}(\Gamma_{11}-1),\\
D &= trD_{jk} = D_{11}+D_{22}+D_{33}.
\end{aligned} \tag{2.2}$$

Since the term D_{jk}/D can be expressed by $g_j\, g_k$ (Gajewski and Pšenčik, 1987), the equations (2.1) can be written as

$$\begin{aligned}
\frac{dx_i}{d\tau} &= a_{ijkl}\, p_l\, g_j\, g_k\\
\frac{dp_i}{d\tau} &= -\frac{1}{2}\frac{da_{njkl}}{dx_i} p_n\, p_l\, g_j\, g_k,
\end{aligned} \tag{2.3}$$

where g_j is polarization vector, or displacement vector, and the eigenvector of Christoffel matrix Γ_{jk}:

$$\Gamma_{jk} = a_{ijkl}\, p_i\, p_l. \tag{2.4}$$

We use the fifth order Runge-Kutta methods to solve the ray ordinary differential equations.

Given initial values for x_i and p_i, the results from these sets of equations provide a straightforward method for computing an individual ray path, including traveltime. Amplitude can be computed using finite-difference methods to evaluate the Jacobian that is related to geometrical spreading. The WFC approach extends this by explicitly tracking the propagation of a wavefront mesh through the model. This enhances the calculations in two ways. First, the knowledge of the wavefront geometry allows a much more effective mapping of multivalued results, since it is easy to identify unique wavefront elements arriving from a triplication, for example. Second, by adaptively

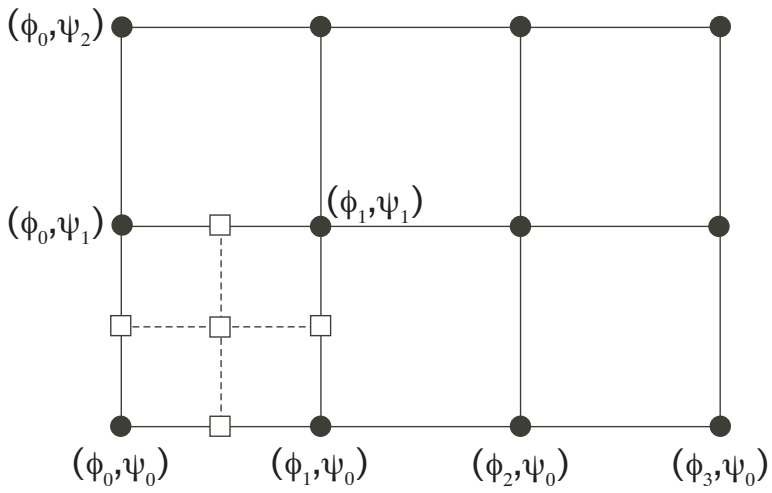

Fig. 2.2. Schematic illustration of the logical geometry of a wavefront mesh constructed by quadrilateral cells. Each cell is bounded by four rays' takeoff angles. Dot and square represent exiting and interpolated rays, respectively. Dashed lines is the new boundaries of the new quadrilateral cells. (Adapted from Gibson, Jr. et al., 2005).

interpolating the wavefront mesh, the method can accelerate computations by using high ray density only where needed for accuracy. There are two primary steps in the algorithm, defining the initial mesh and then propagating it forward through the model, interpolating cells as needed to maintain accuracy.

The initial set of rays can be chosen based on some limited set of takeoff angles, or it can occupy all directions around the source point. Our implementation defines the wavefront mesh in terms of quadrilateral cells (Gibson, Jr. et al., 2005). Figure 2.2 demonstrates the logical geometry of a wavefront mesh constructed by quadrilateral cells. Each cell is bounded by the takeoff angles of the four rays, both azimuth ϕ and declination ψ. This kind of geometric setting will facilitate the coding task. For example, it is straightforward to subdivide a quadrilateral cell for 5 new rays and easy to define the neighboring indices of rays.

After selecting a range of angles and increments in both azimuth and declination takeoff angles, the initial mesh is easily set up using the Cartesian coordinates of points on the rays at an initial time $d\tau$. The mesh is then propagated forward an increment in time $d\tau$ by again using points on the rays, but the key step in the WFC algorithm is the interpolation test that is then applied. Specifically, the paraxial traveltime error is computed by finite-difference methods using data from three points

in the mesh cell defining one point as the reference location. By applying a Taylor series expansion of traveltime on a reference point $\mathbf{x}'$, the traveltime on a nearby location $\mathbf{x}$ can be written:

$$\tau(\mathbf{x}) \approx \tau(\mathbf{x}') + p_i(x_i - x_i') + \frac{1}{2}\frac{\partial^2\tau}{\partial x_i \partial x_j}(x_i - x_i')(x_j - x_j'), \tag{2.5}$$

where the first derivatives term, p_i (slowness vector) are given by $p_i = \partial\tau/\partial x_i$, and the second derivatives can be computed by

$$\frac{\partial^2\tau}{\partial x_i \partial x_j} = \frac{p_i}{\gamma_k}\left(\frac{\partial x_j}{\partial \gamma_k}\right)^{-1}, \tag{2.6}$$

where the γ_k are the ray coordinates, which can be taken as the two takeoff angles (azimuth ϕ and declination ψ) and the traveltime τ (Červený, 2001). The paraxial correction, the summation of the first and second order terms of the equation (2.5), is then computed for the mesh point opposite the reference location. Here, the second derivatives at a reference point in equation (2.6) are computed by using two nearby points (one is along azimuth, the other is along declination) to calculate the paraxial time correction at the diagonal point in a quadrilateral cell. Since all points are on the same wavefront, this correction should be zero, but if the actual value exceeds a predefined threshold, the mesh cell is interpolated on the previous wavefront to improve accuracy (Figure 2.3). Additional details on the general algorithm are provided by Gibson, Jr. et al. (2005).

Amplitude, determined by the geometric spreading and source characteristics, is also available in the ray method by calculating the transport equation (Červený, 1972; Gajewski and Pšenčik, 1987; Červený, 2001). Amplitude along a ray caused by a point source in an isotropic medium can be written as follows

$$A(\tau) = \left[\frac{\rho(\tau_0)v(\tau_0)J(\tau_0)}{\rho(\tau)v(\tau)J(\tau)}\right]^{1/2} G(\phi_0, \psi_0) \tag{2.7}$$

where $\rho(\tau_0)$, $v(\tau_0)$ and $J(\tau_0)$ are calculated at the source, and $\rho(\tau)$, $v(\tau)$ and $J(\tau)$ are calculated at time τ along a ray. The term $[\frac{J(\tau_0)}{J(\tau)}]^{1/2}$ describes the geometric spreading. G is the source radiation pattern. $G(\phi_0, \psi_0)$ is the amplitude at the source, measured in the direction specified by takeoff angles (the azimuthal ϕ_0 and declinational ψ_0

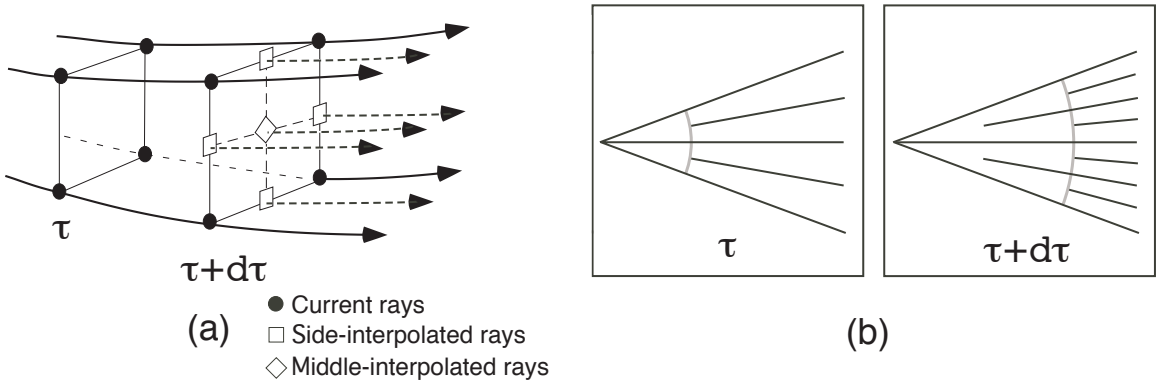

Fig. 2.3. Schematic illustration of the wavefront propagation and its ray interpolation. (a) An wavefront element is constructed by four rays (solid lines with arrows) and interpolated rays (dashed lines with arrows) are inserted if the wavefront curvature exceeds a criterion. (b) Examples of side views show new rays inserted whenever needed for accuracy.

angles). The function

$$J(\tau) = \left| \frac{\partial x_i}{\partial \gamma_j} \right| \tag{2.8}$$

is the *jacobian* of the transformation from the Cartesian coordinates x_i to the ray coordinates γ_j. The physical meaning of J is that it measures the expansion or contraction of a ray tube along a ray (Červený, 1972; Červený, 2001). It is important for implementations that the partial derivatives in $J(\tau)$ are the same quantities in equation (2.6).

2.2.1 Adaptations for a qS-wave Implementation

The algorithm described above is essentially the same for isotropic models or for qP-wave simulation in anisotropic media, but there are three unique and crucial problems caused by S-wave singularities for qS-wave calculations. The first issue is simply complications associated with qS-wave ray tracing in singular directions and in the vicinity of qS-wave singularities, and it is relevant for conventional ray methods or for WFC. The other problems are unique to WFC solutions and are both related to correct mesh definitions. During the initial mesh construction, care must be taken to correctly associate a unique wave type with the two initial qS-wave meshes, since wavefronts normally intersect. This is also a challenge during

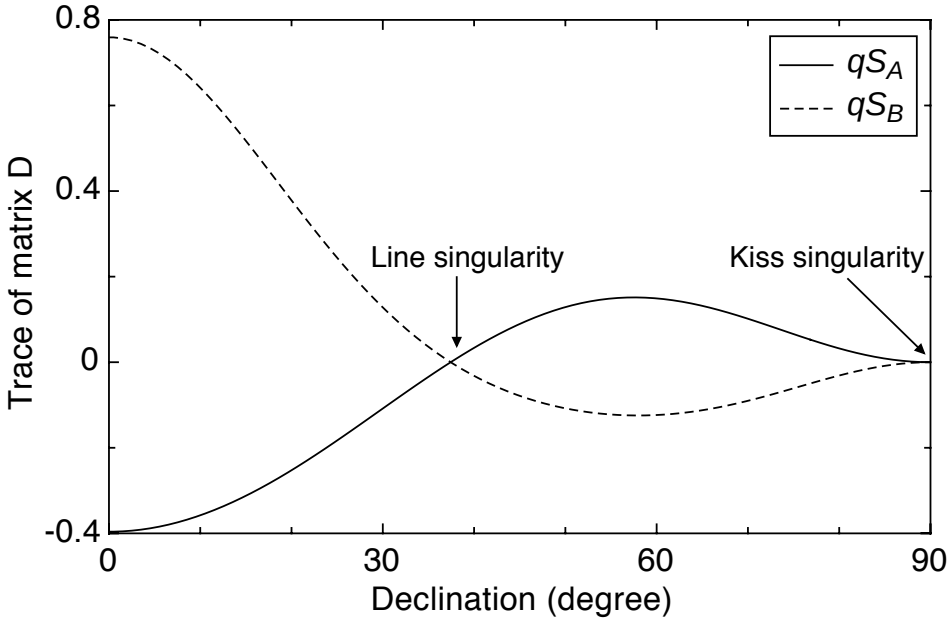

Fig. 2.4. The trace element of the matrix D_{ij} is plotted against the declination angle of slowness vectors for two qS-waves in a VTI model (Table 2.1). D values of two qS-waves are zero in both line and kiss singularities.

wavefront mesh interpolation at later traveltimes, whenever a portion of wavefront crosses a singularity. Appendix A presents the flowchart of the algorithms of qS wave ray tracing by WFC. Below we outline solutions for each of these problems.

qS-wave Ray Tracing

qS-wave ray tracing has difficulties when the singularities are present (Shearer and Chapman, 1989; Coates and Chapman, 1990; Červený, 2001; Vavryčuk, 2001). Because of the equality of the two qS-wave slownesses, the Christoffel matrix is degenerate and the denominator D in the equations (2.1) becomes zero. The right-hand-side of the equations then yield infinite values. Figure 2.4 demonstrates the trace element of the matrix D_{ij} is plotted against the declination angle of slowness vectors for two qS-waves in a VTI model (Table 2.1). D values of two qS-waves are zero in both line and kiss singularities. 90° suggests the axis of symmetry.

Though singularities are found at points or on a line, the numerical instabilities can arise in the vicinity of singularities (Shearer and Chapman, 1989; Červený, 2001; Vavryčuk, 2001). In homogenous models, we have errors in qS-wave ray tracing when

Table 2.1. Density-normalized constants for the model 2 in units of GPa, obtained from a realistic earth model.

$$\begin{pmatrix} 10.36 & 2.73 & 2.83 & 0 & 0 & 0 \\ 2.73 & 10.36 & 2.83 & 0 & 0 & 0 \\ 2.83 & 2.83 & 9.51 & 0 & 0 & 0 \\ 0 & 0 & 0 & 2.93 & 0 & 0 \\ 0 & 0 & 0 & 0 & 2.93 & 0 \\ 0 & 0 & 0 & 0 & 0 & 3.81 \end{pmatrix}$$

the takeoff angles are very close to the singularity. In heterogeneous models, such as those with a gradient in velocity, we find that this problem can generate in erroneous, sharp bends in ray trajectories when the slowness goes through the singular directions. We apply a small perturbation of elastic constants in the presence of singularities to minimize these problems; however, it is still possible to have some inaccurate ray tracing since the Christoffel matrix is very sensitive to a minor change of anisotropy. Also, the perturbation of elastic constants introduce an artificial error. In this case, it is possible to apply the incorrect qS-wave.

However, the problem can be overcome by also computing the polarization vector of the traced ray whenever the slowness approaches the singular directions. Near a singularity, we can then compare the predicted particle motion on the point of the ray to ensure that is similar to the preceding point. The incorrect qS-wave will normally have a particle motion that is nearly perpendicular, which can be easily detected. Since the ray tracing algorithm itself is independent of the polarization vector and the polarization vector of a ray changes gradually along the raypath, we expect that the two qS rays can be distinguished in the presence of singularities. Because the value of the denominator D causes the algorithm instability in the vicinity of singularity and the non-uniqueness of eigenvectors of the Christoffel matrix at the singular directions (Equation 2.1), it can be used as an indicator to apply the additional check of particle motion.

2.2.2 Mesh Initialization

The second problem is the correct initialization of the two qS wavefront meshes in the presence of shear wave singularities. This arises because the simplest way to distinguish qS-waves when moving from one slowness vector direction to the next is to sort them in order of increasing velocity, so that qS_1 and qS_2, for example, would be the slower and faster waves. However, because the physical wavefronts intersect and change order of velocities, the construction of wavefront meshes must instead assign initial ray velocities and geometries using a criterion other than magnitude of phase or group velocity (Figure 2.1). Because particle motion vectors will generally change direction relatively slowly on the wavefront, we can instead use this as the means of distinguishing the wave type (qS_1 and qS_2), and in the following text, we will label the resulting wavefronts qS_A and qS_B to avoid confusion with the numerical subscripts that imply velocity sorting. Though the two wavefronts can be recognized as qSV and SH in the VTI media, in this context, we will still retain the notation of qS_A and qS_B waves to help clarify the WFC implementation.

When initializing the qS-wave wavefront meshes, we arbitrarily choose one particle motion vector as the reference polarization direction for the first slowness vector direction for qS_A and use the other for qS_B. Appendix B displays a flow chart illustrating the detailed steps for choosing the correct wave type (qS_1 or qS_2) for the qS_A or qS_B waves. We iterate through all directions of interest to select the wave types that make the polarization directions at all nodes consistent. Our current implementation of this algorithm uses the conventional ray coordinate system, where the ray parameters are the azimuth and declination takeoff angles. Once the two qS-wavefronts are initialized, they can be propagated through the earth model separately. Note that special care has to be taken with polarization tests near kiss singularities, where the particle motion vector can change orientation quickly. Temporarily subdividing the mesh to ensure that the vector changes slowly from point to point allows these singularities to be treated correctly.

2.2.3 Mesh Interpolation

The last problem is correctly assigning initial velocities and directions for new rays when interpolating the wavefront mesh cells that cross singularities, and the solution is the same as for the mesh initialization. After creating the first wavefront at time

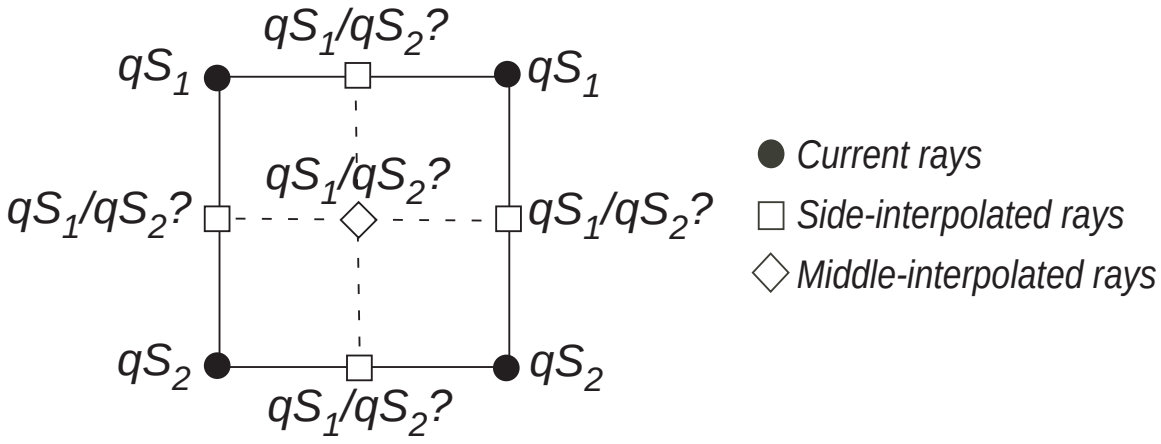

Fig. 2.5. A schematic illustrates the wave types of interpolated rays are tested to ensure that the correct qS-wave ray is selected to maintain a physically meaningful wavefront mesh while a portion of the wavefront crosses a singularity.

$\tau_\circ$, we propagate it through the earth model at equal increments of time $d\tau$ (normally $\tau_\circ = d\tau$, though this is not required). Each time a new ray is inserted to maintain accuracy, the particle motion is tested to ensure that the correct qS-wave ray is selected to maintain a physically meaningful wavefront mesh (Figure 2.5). This test can be skipped when the existing rays in a mesh cell are all either qS_1 or qS_2. Because field quantities are assumed to vary slowly with direction in the ray approximation, we can safely assume that the interpolated ray can be chosen on the basis of the velocities of the existing rays in this case.

2.3 Examples of Wavefront Meshes

A sequence of tests applied to increasingly complex models shows the accuracy and robustness of the qS-wave WFC implementation. We begin with a homogeneous, VTI model with a line singularity, then demonstrate that the results are still accurate for a tilted symmetry axis and for a model with a velocity gradient.

2.3.1 Homogeneous, VTI Model

Figure 2.6 (Table 2.2) shows cross-sections of slowness surfaces and wavefronts for two qS-waves in the vertical plane of the homogeneous, VTI test model. Two important and potentially complex aspects of anisotropic wave propagation occur in this model.

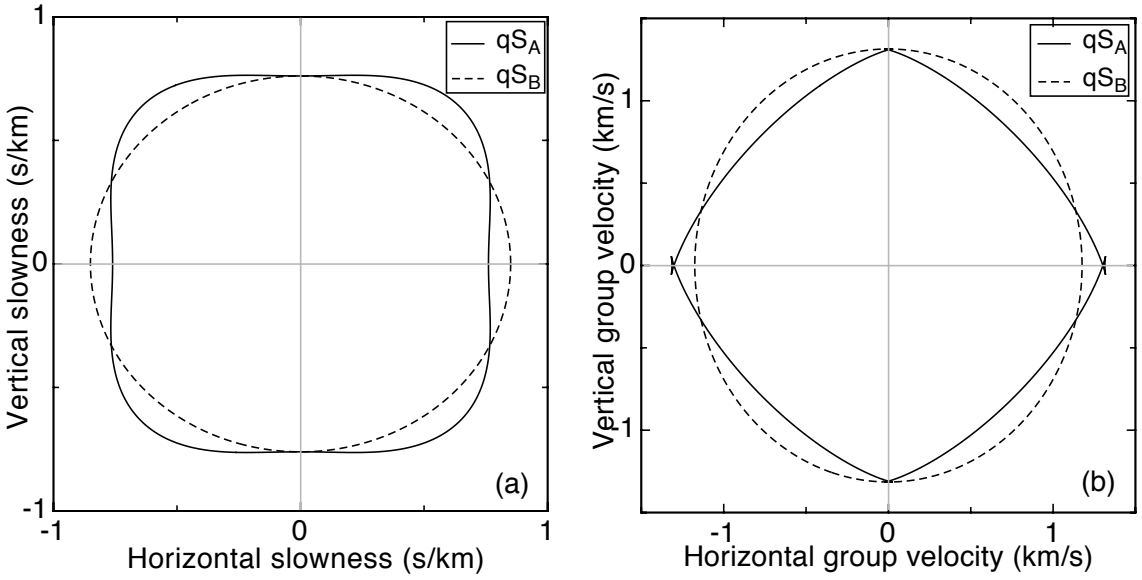

Fig. 2.6. By using particle motion as a criterion to separate two qS-waves, qS_A and qS_B waves are distinguished in a VTI model with line singularities (see Table 2.2). (a) Cross-section of two qS-wave slowness surfaces for the model in the vertical plane. (b) Cross-section of two qS-wave wavefronts for the model in the vertical plane. Note the order of the outer and inner lines in (a) are exchanged in (b) because the values in (b) is about the reciprocal in (a).

One is a line singularity in the direction about 67° from the axis of symmetry. The other is a qSV-wavefront (qS_A) with two small on-axis triplications in the horizontal and vertical direction. The concave outward shape of the slowness surface results in cusps in the wavefront.

This model tests whether the algorithm can correctly separate the two qS-wavefronts prior to propagating them and whether it correctly interpolates wavefront meshes with a triplication as the travel through the earth model. As noted above, this separation is rather difficult when line singularities are present, though propagating the wavefronts after initialization is not challenging in the homogeneous case. Figure 2.7 shows the results in side views for the two qS-wavefront meshes at 0.1 s and after propagating the wavefronts to a total time of 1.4 s in an increment of 0.1 s. The size of the earth model is 4x4x4 km^3. Since the model is homogenous, the final mesh is the same shape as the initial wavefront, but the non-uniform mesh spacing is a consequence of the automatic mesh refinement during propagation. As expected for a VTI medium, the variation in interpolation is independent of azimuth.

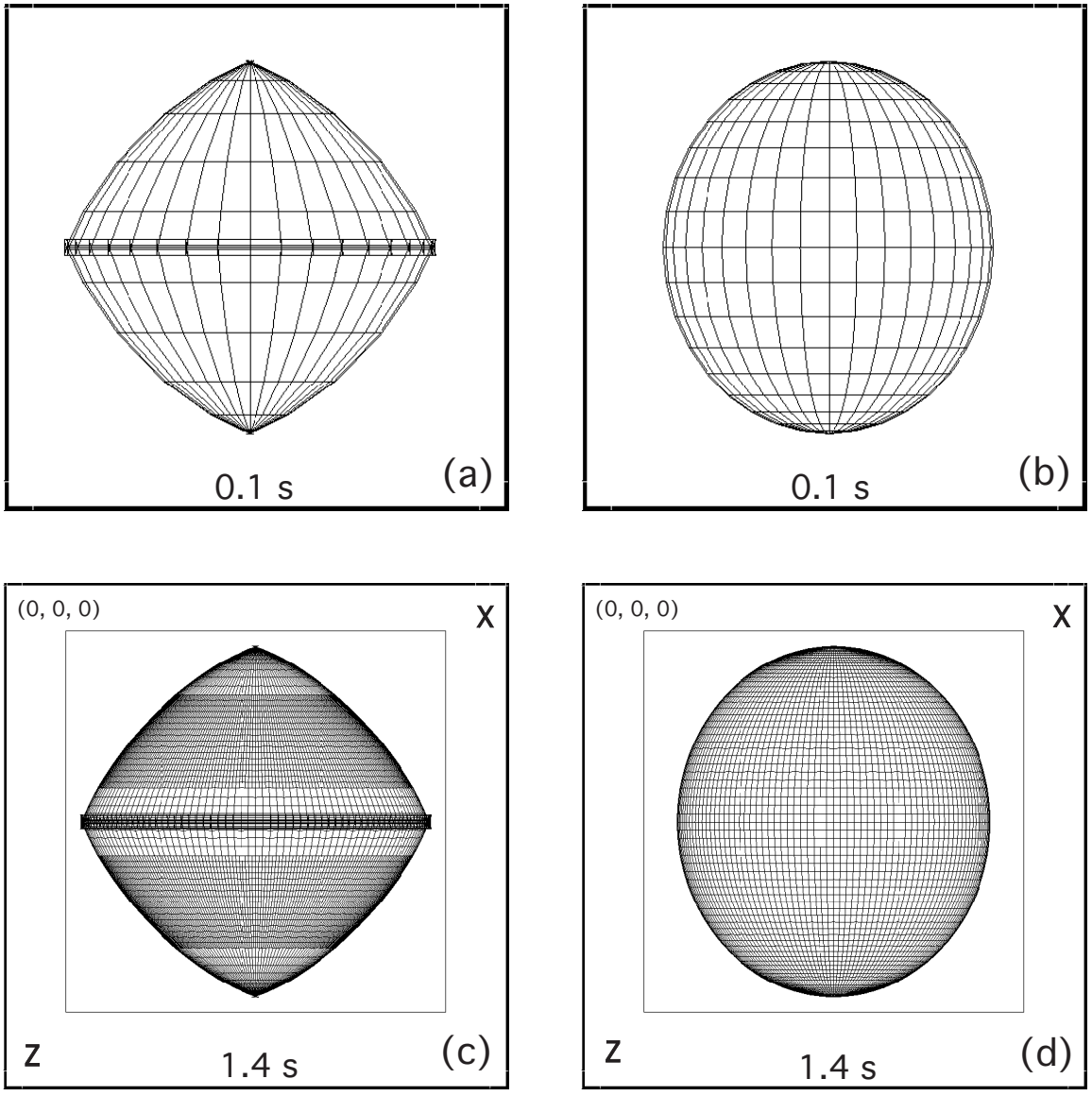

Fig. 2.7. Side views of two initial qS-wave wavefront meshes at time 0.1 s, generated in the ray coordinate system are shown in (a) and (b) (the same as the analytic solution, see Figure 2.6 (b)). Side views of two final meshes showing the results after propagating the wavefronts to a total time of 1.4 s in an increment of 0.1 s in the model 1 (see Table 2.2) are shown in (c) and (d).

.

Table 2.2. Density-normalized elastic constants for the model 1 in units of GPa (Adapted from Thomsen, 1986).

$$\begin{pmatrix} 7.80 & 5.04 & 5.78 & 0 & 0 & 0 \\ 5.04 & 7.80 & 5.78 & 0 & 0 & 0 \\ 5.78 & 5.78 & 8.67 & 0 & 0 & 0 \\ 0 & 0 & 0 & 1.73 & 0 & 0 \\ 0 & 0 & 0 & 0 & 1.73 & 0 \\ 0 & 0 & 0 & 0 & 0 & 1.38 \end{pmatrix}$$

2.3.2 Homogeneous, Tilted TI Model

We use a TI model with a tilted axis of symmetry for the second example. This type of medium has been recognized as a feature of overthrust areas and causes problems in conventional imaging methods. (Isaac and Lawton, 1999; Vestrum et al., 1999; Grechka et al., 2001; Kumar et al., 2004). Thus, in the example we consider the same elastic moduli as in the previous example, but rotate the coordinates 45° about the $y-$ and $z-$axes. All components of the tensor elastic moduli are non-zero and it will help show that our algorithm can handle general anisotropic cases. Specifically, though the basic material properties are the same, the test will show that we can automatically take into account singularities located in an arbitrary direction. Figure 2.8a and 2.8b show the ray paths through the model for a portion of the wavefront at time 1.5 s, which have takeoff angles between 0° to 3° in azimuth and −90° to 90° in declination. The size of the earth model is still 4x4x4 km^3. Because the rays are no longer propagating in a symmetry plane, they display dramatic lateral changes in propagation directions. Figure 2.8c, 2.8d, 2.8e, and 2.8f show the results in 3D views for the two qS-wavefronts after propagating to a total time of 0.8 and 1.5 s, again with an increment of 0.1 s. The wavefronts are correctly modeled and are rotated versions of the previous results (Figure 2.7c and 2.7d).

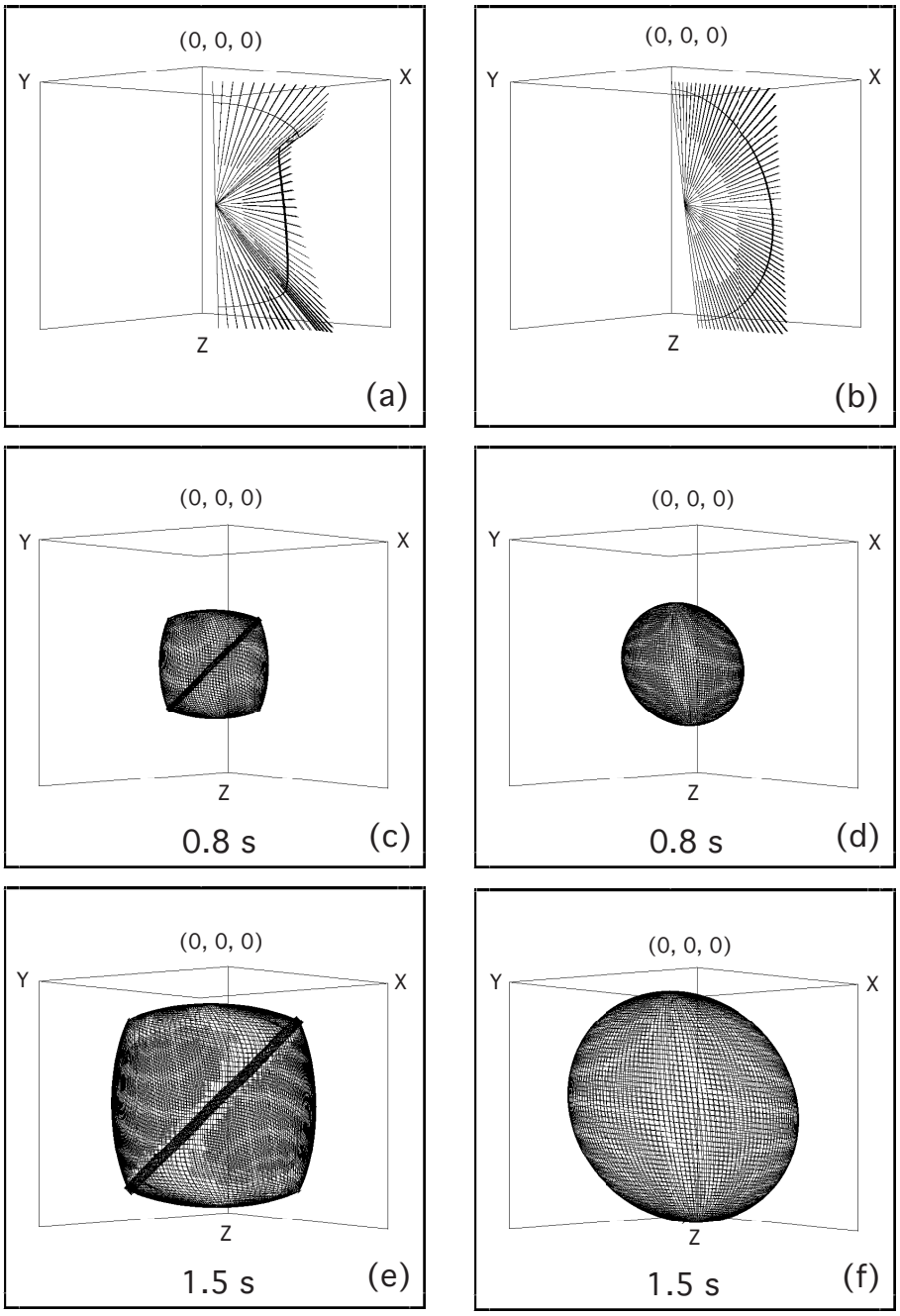

Fig. 2.8. 3D views of the qS-wave raypaths (straight lines) for a portion of the wavefront at time 1.5 s in a tilted TI model are shown in (a) and (b), which have takeoff angles between 0° to 3° in azimuth and −90° to 90° in declination. The tilted TI model is generated by rotating the coordinates 45° about the Y- and Z- axes in the model 1 (see Table 2.2). 3D views of the final wavefront meshes for two qS-waves after propagating the wavefront to a total time of 0.8 s in an increment of 0.1 sec through the tilted TI earth model are shown in (c) and (d). 3D views of the final wavefront meshes to a total time of 1.5 s are shown in (e) and (f).

2.3.3 Heterogeneous, VTI Model

Singularities complicate qS-wave ray tracing through an anisotropic model with gradients because wavefronts can cross singularities during propagation, and care must be taken even after the initial mesh construction step. Our third example shows that the algorithm correctly handles this case as well. The moduli are the same as the previous VTI model (see Table 2.2), but a strong gradient of 0.7 km/s per kilometer is applied to the earth model.

Figure 2.9a and 2.9b show that a set of rays, having takeoff angles between 0° to 3° in azimuth and −90° to 90° in declination, bends dramatically because of the strong gradient in velocity. Note the high ray density in the horizontal direction, which shows the small local triplication on the qSV wavefront. One qS-wave ray can consist of both qS_1 and qS_2 wave types while slowness vector directions cross a line singularity (see Figure 2.1). This test therefore demonstrates the effectiveness of the particle motion tracking procedure and the modification of qS-wave ray tracing described in the Method section. Figure 2.9c, 2.9d, 2.9e and 2.9f show the results in side views for the two qS-wavefronts after propagating to a total time of 0.5 and 1.3 s. The size of the model is 10x10x10 km^3. The wavefronts show some distortion in shape because of the velocity gradient.

2.4 Verification and Validation

By a sequence of verification and validation tests, we demonstrate the accuracy and robustness of the mapping algorithm for qS-wave implementation. We began with a verification test of mapping two qS-wave traveltimes in a homogeneous, VTI model. Then we show the mapping algorithm can deal with multivalued traveltimes. Also, the mapped ray data are used to generate synthetic seismograms and compared against the full waveform solutions.

2.4.1 Traveltimes

First of all, we used a 2-D array of 6400 receivers uniformly distributed on the surface (see Figure 2.10a) to test the accuracy of mapping two qS-wave traveltimes in the homogeneous, VTI model (see Table 2.1). The earth model size is 10x10x10 km^3. Source is located at (5, 5, 2.5) (km). Figure 2.10b demonstrates that two qS wave

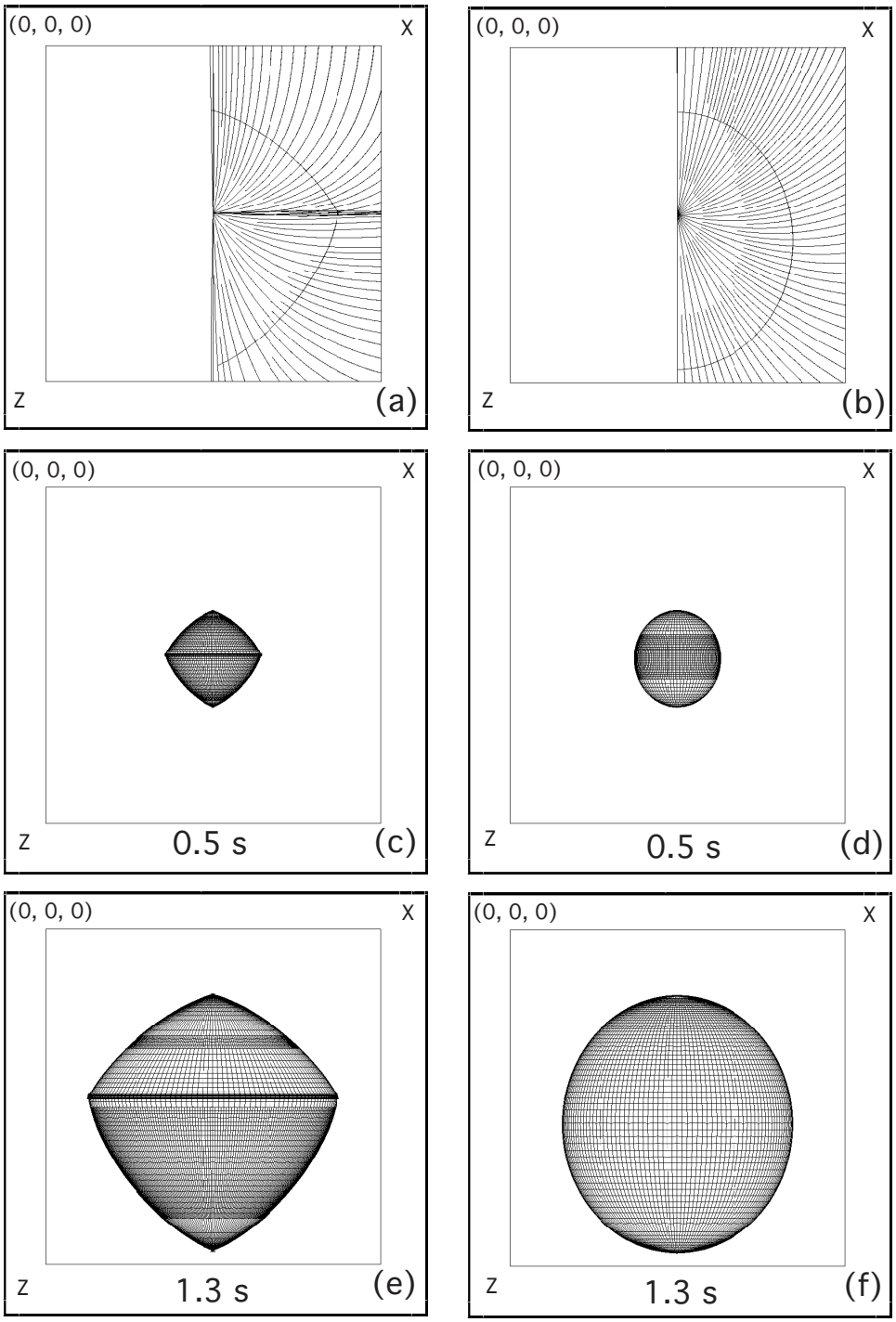

Fig. 2.9. Side views of the qS-wave raypaths (curve lines) in a heterogeneous VTI earth model with a linear gradient 0.7 km/s per kilometer are shown in (a) and (b). Due to a strong gradient in velocity, the raypaths bend dramatically. See the text for more description. Side views of the final wavefront meshes for two qS-waves after propagating for a total time of 0.5 s in an increment of 0.1 s in this heterogeneous VTI earth model are shown in (c) and (d). Side views of the final wavefront meshes after propagating the wavefront for 1.3 s are shown in (e) and (f).

slowness surfaces have a line singularity at around 53° away from the axis of symmetry. This receiver array will include the line singularity to ensure the mapping algorithm can correctly separate two qS traveltime fields. Figure 2.10c and 2.10d are the ray spreading diagrams of qSV- and SH-waves, respectively, which display rays integrated to one second traveltime from the source point, with the initial slowness vector having a constant angular increment of 5° (Ben-Menahem et al., 1991). The wavefront, which is the locus of points on the rays at 1 s, is also displayed. The qSV-wave slowness surface is slightly concave inward and causes the ray density higher around this direction than others.

Figure 2.11a and 2.11b show the side views of two qS waves for a vertical slice of wavefronts at 1.2 s and raypaths showing new rays are adaptively inserted to ensure accuracy as rays diverge during propagation. Figure 2.12a and 2.12b demonstrate the accuracy of traveltimes with a predefined threshold 1 ms during the mesh interpolation. The means of traveltime errors for both two qS-waves are less than three order of magnitude below the predefined threshold. Also, we have better accuracy and less scattered distribution of traveltimes in the SH wave mapping than the qSV wave (Figure 2.12a and 2.12b) because the SH wave has a smoother wavefront surface than the qSV wave. The traveltime errors are the residuals of mapped traveltimes with respect to the analytic solutions. Two major steps of the WFC algorithms dominate these errors. While inserting the new rays in the mesh interpolation and mapping ray data from the mesh, simply averaging the Cartesian Coordinates of the existing rays for the new ray start points and extrapolation of traveltimes from a nearby ray result in the errors. Therefore, mapping the traveltimes of a smoother wavefront surface will be more accurate because of less error is introduced in averaging the Cartesian Coordinates for the new ray start points. In addition, Figure 2.12c and 2.12d show the traveltime errors in the 2-D plots for SH and qSV waves, respectively. Generally speaking, the traveltime errors are azimuthally symmetric and this demonstrates the mapping algorithm does a systematic job.

2.4.2 Multivalued Traveltime Fields

The preceding tests show that the method correctly identifies wave types during mesh construction and interpolation, even when singularities and triplications are present in arbitrary directions. Here we demonstrate the accuracy of computed multivalued

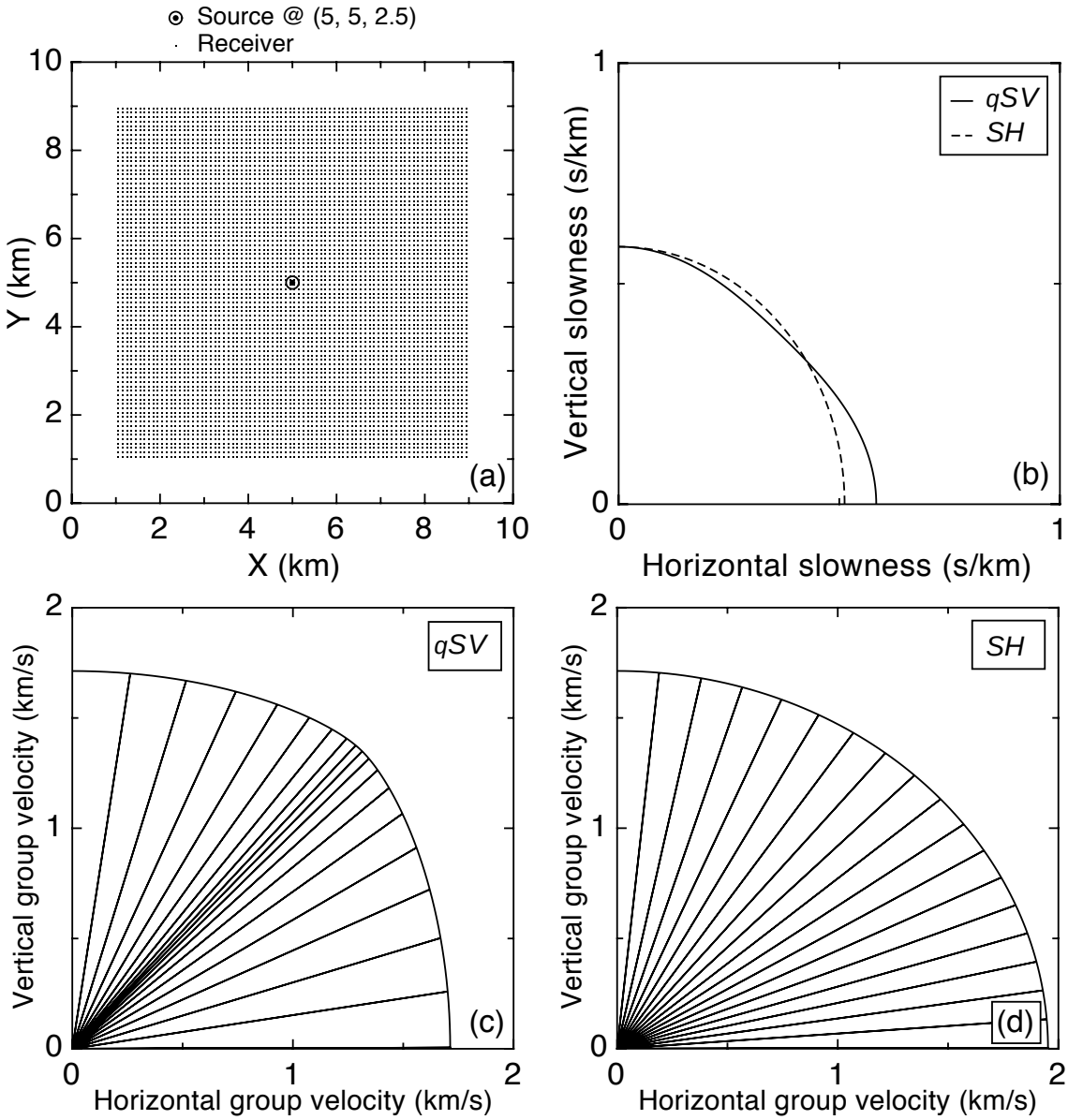

Fig. 2.10. (a) Top view of the source-receiver geometry for verifying two qS-wave traveltime wavefields, which including the line singularity. The earth model size is 10x10x10 km^3. Source is at (5, 5, 2.5). 6400 receivers are uniformly distributed on the surface. (b) Cross-section of two qS-wave slowness surfaces for the model 2 (see Table 2.1) in the vertical plane. Ray spreading diagrams and their wavefronts at 1 sec in the vertical plane for qSV- and SH- waves are shown in (c) and (d), respectively. See the text for the computation.

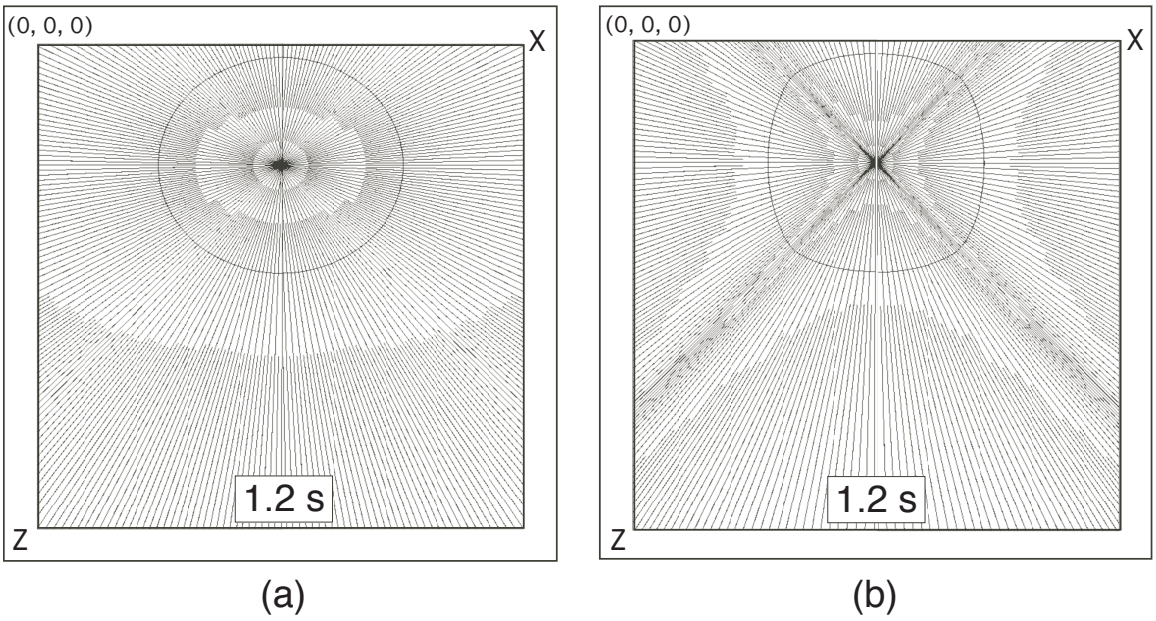

Fig. 2.11. Side views of two qS waves for a vertical slice of wavefronts at 1.2 s and raypaths are shown in (a) and (b), where (a) is identified as SH wave and (b) is qSV wave.

traveltimes by propagating a qSV-wave wavefront through a VTI model that has a triplication caused by its intrinsic anisotropy. The model 3 (Table 2.3) has strong anisotropy. For example, the horizontal SH velocities is about 30% larger in the vertical direction (see Figure 2.13d).

The source-receiver geometry for the validation is shown in Figure 2.13a, and the cross sections of the two qS-wave slowness surfaces show the complexity of propagation (Figure 2.13b). The qSV-wave slowness surface is concave outward at angles between 30° to 60° from the axis of symmetry, causing a distinct off-axis qSV-wave triplication in the wavefront (Figure 2.13b). Figure 2.13c shows the ray spreading diagram. The wavefront, which is the locus of points on the rays at 1 s, is also displayed. Because the qSV-wave slowness surface is concave outward from P to Q, the rays, or normals to the slowness surface, form a triplication. The ray amplitudes in the triplication are expected to much higher than elsewhere in the synthetic seismograms. However, according to previous studies (Thomsen and Dellinger, 2003; Vavryčuk, 2004), the SH-wave doesn't have the same behavior and its ray spreading diagram shows a more even distribution of rays (Figure 2.13d).

The traveltimes computed by the WFC compare very closely to those computed

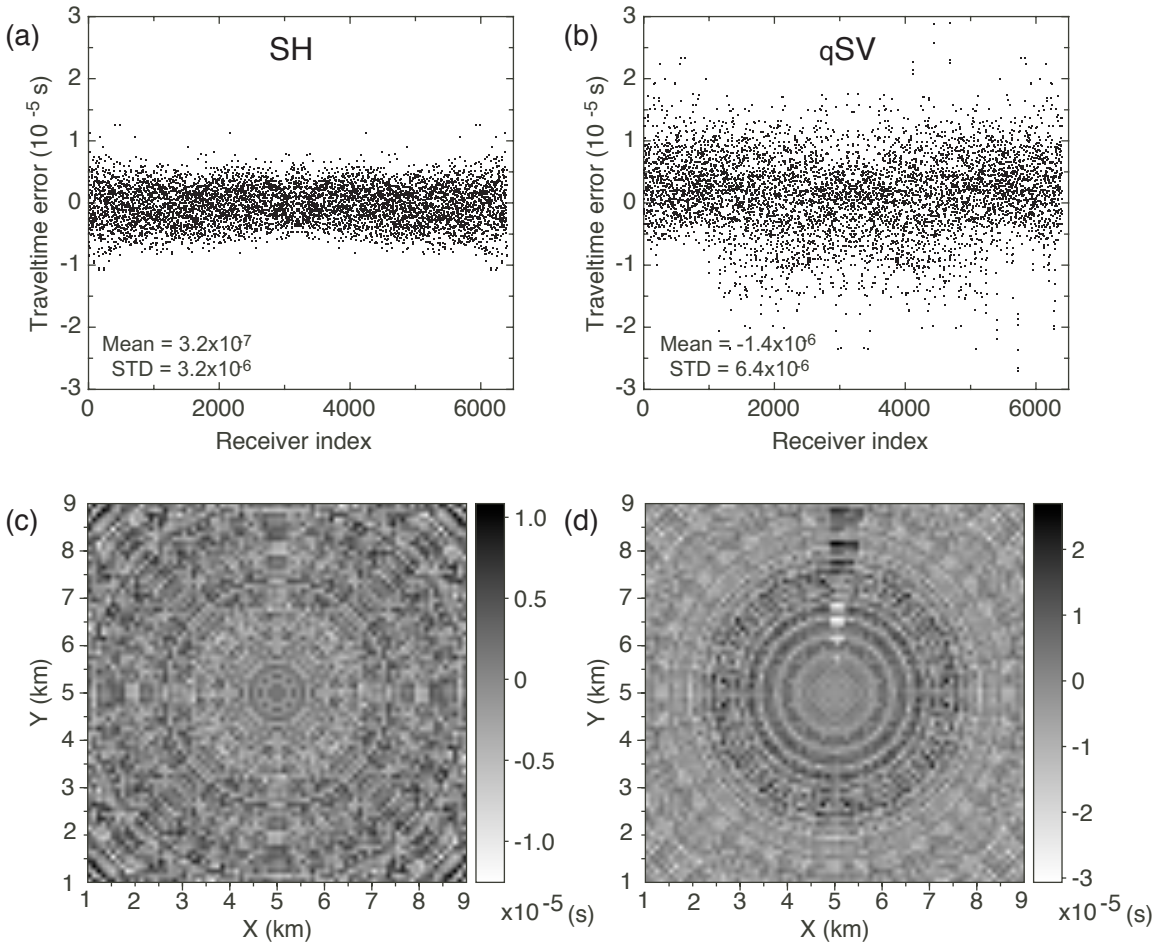

Fig. 2.12. Verification of accuracy for two qS-wave traveltimes. Traveltime errors with respect to the analytic solutions for SH and qSV waves are shown in (a) and (b), respectively. 6400 receivers are uniformly distributed on the surface. The earth model size is 10x10x10 km^3. Source is at (5, 5, 2.5). Statistical results of mean and standard deviation are presented, too. The 2-D plot of traveltime errors for SH and qSV waves are shown in (c) and (d), respectively.

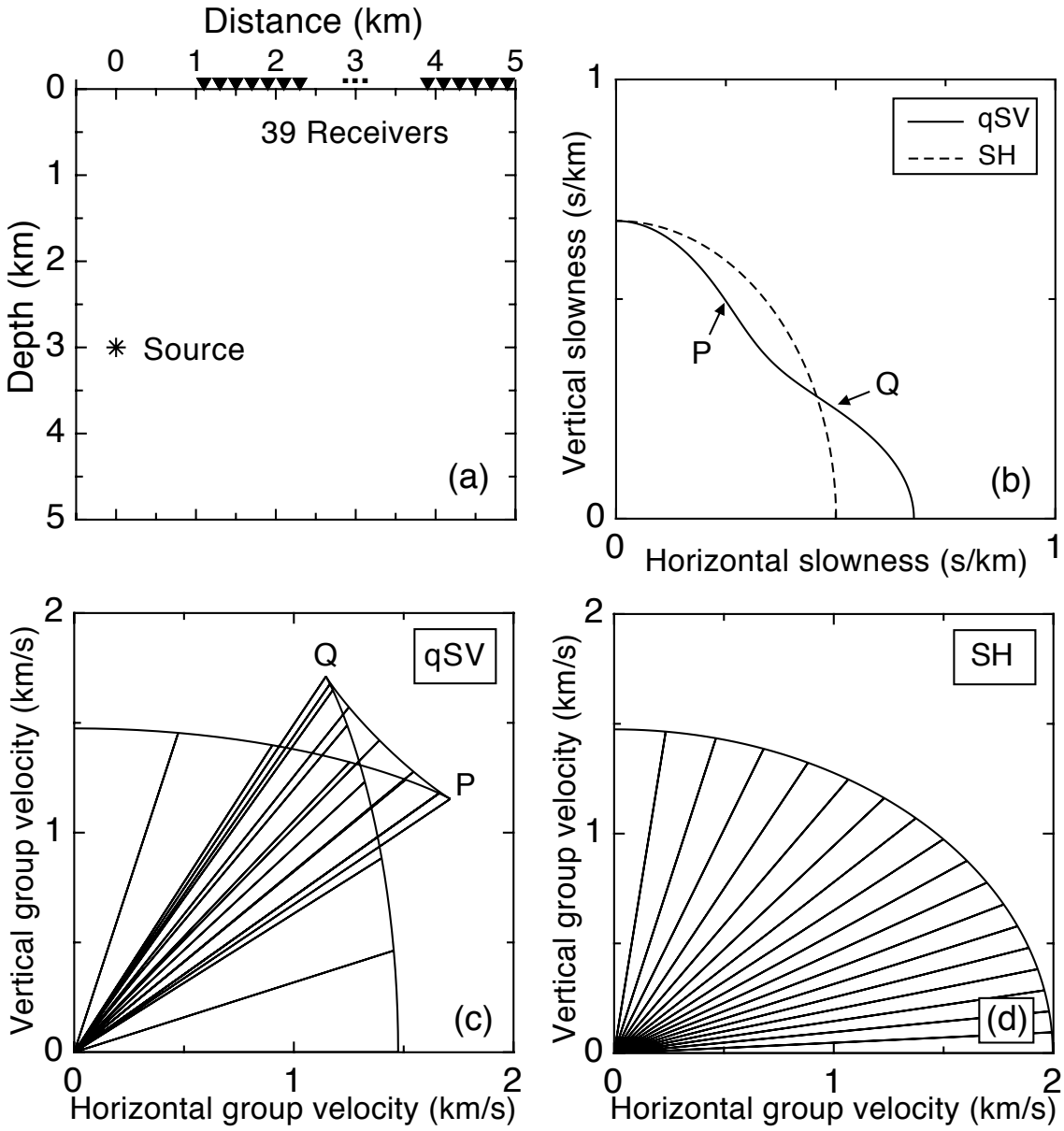

Fig. 2.13. (a) Source-receiver geometry for mapping a qSV-wave wavefront with a triplication. (b) Cross-section of two qS-wave slowness surfaces for the model (see Table 2.3) in the vertical plane. Ray spreading diagrams and their wavefronts at 1 sec in the vertical plane for qSV- and SH- waves are shown in (c) and (d), respectively. See the text for the computation.

Table 2.3. Density-normalized constants for the model 3 in units of GPa (Adapted from Shearer and Chapman, 1989).

$$\begin{pmatrix} 12.60 & 4.66 & 4.54 & 0 & 0 & 0 \\ 4.66 & 12.60 & 4.54 & 0 & 0 & 0 \\ 4.54 & 4.54 & 12.27 & 0 & 0 & 0 \\ 0 & 0 & 0 & 2.18 & 0 & 0 \\ 0 & 0 & 0 & 0 & 2.18 & 0 \\ 0 & 0 & 0 & 0 & 0 & 3.99 \end{pmatrix}$$

analytically (Figure 2.14). Though we have some slightly larger traveltime errors in the portion PQ of the wavefront, the maximum error is less than 1 ms, which was the value we use for the predefined error threshold in the accuracy test of the mesh interpolation. Except for the caustic cusp, the maximum error is less than one tenth of the predefined threshold. This shows our WFC algorithm can deal with the mesh interpolation in a wavefront with cusps and evaluate the multivalued traveltimes correctly.

2.4.3 Amplitudes

We also generate amplitudes to demonstrate our WFC algorithm can separate two qS-wave amplitude fields and map them correctly. Again, we used the same source-receiver geometry and model in Figure 2.10. Because the analytic solutions for amplitudes are not available in anisotropic media, we showed the plots of amplitudes instead of their errors. However, in the later section we will use discrete wavenumber method to generate full waveform synthetic seismograms for verification of amplitudes. Figure 2.15a and 2.15b show amplitudes are plotted against the receiver index for SH and qSV waves, respectively. Comparing to qSV wave, SH wave has gradual variation in amplitude because of the smoother wavefront surface and uniformly distributed rays (see Figure 2.10c and 2.10d). Figure 2.15c and 2.15d demonstrate the 2-D plot of amplitudes for SH and qSV waves, respectively. Due to the concave inward slowness surface (Figure 2.10b), qSV wave has relative high amplitudes in a

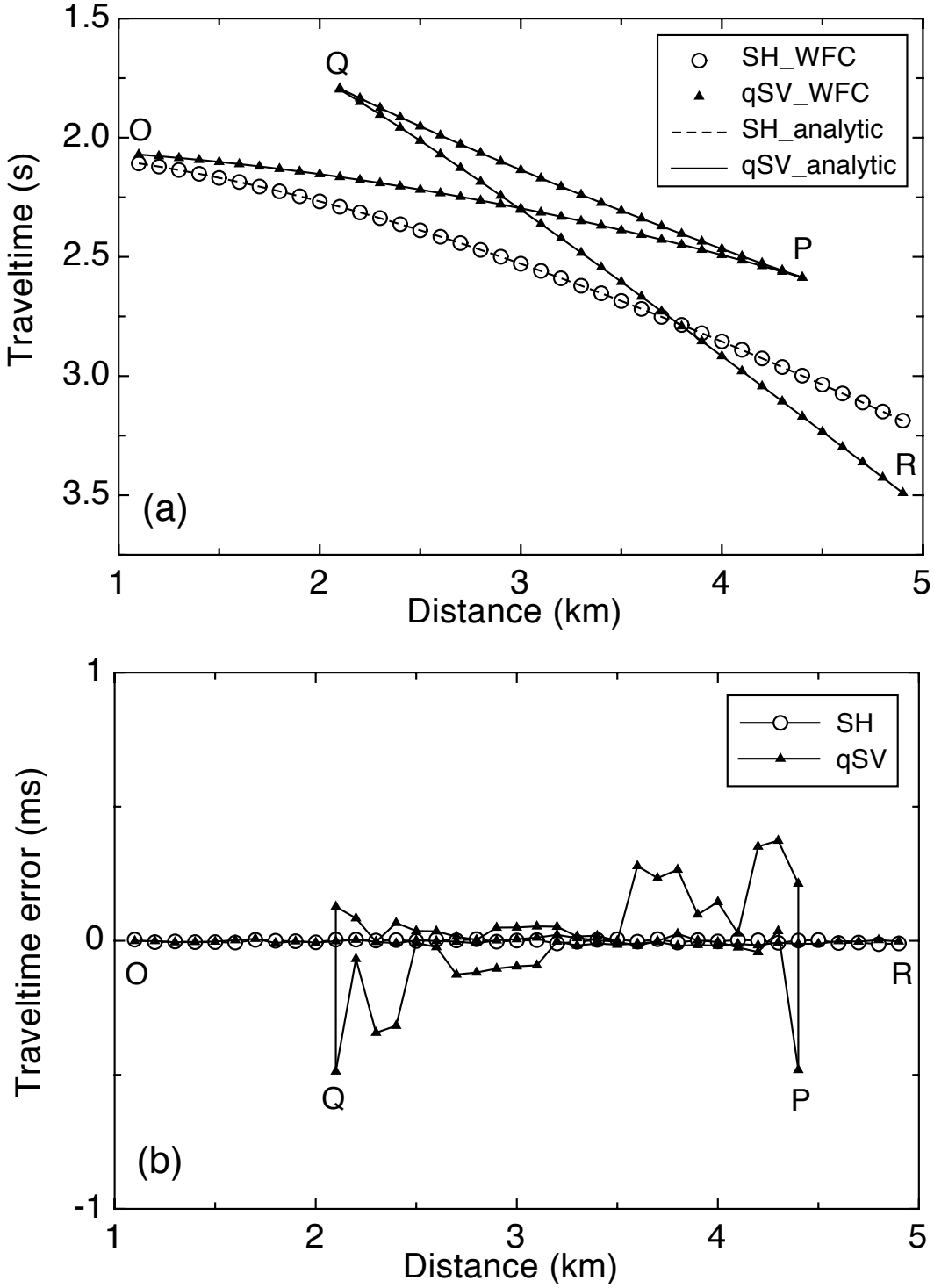

Fig. 2.14. Validation of multivalued traveltimes for a qSV-wave wavefront with a triplication. (a) Comparison of traveltimes between WFC mapping results and analytic solutions. (b) The maximum error is less than 1 ms, which was the value we use for the predefined threshold in the mesh interpolation.

Table 2.4. Density-normalized constants for the model 4 in units of GPa (Adapted from Ben-Menahem et al., 1991).

$$\begin{pmatrix} 28.16 & 21.44 & 16.24 & 0 & 0 & 0 \\ 21.44 & 28.16 & 16.24 & 0 & 0 & 0 \\ 16.24 & 16.24 & 16.16 & 0 & 0 & 0 \\ 0 & 0 & 0 & 2.48 & 0 & 0 \\ 0 & 0 & 0 & 0 & 2.48 & 0 \\ 0 & 0 & 0 & 0 & 0 & 3.36 \end{pmatrix}$$

ring shape.

2.4.4 Synthetic Seismograms

The full waveform solutions obtained by the discrete wavenumber method provide an independent solution to verify the accuracy of ray theoretical seismograms from the WFC. This will help confirm the accuracy of amplitude and particle motion results as well as traveltimes. The following results apply a Ricker wavelet with 10 Hz central frequency.

The first set of results use an ellipsoidal anisotropic model to generate the synthetic seismograms (Table 2.4). Figure 2.16 compares the source-receiver geometry and the cross-section of two qS-wave wavefronts, while Figure 2.17 shows the qS-wave synthetic seismograms generated by vertical and horizontal point forces for qSV and SH waves, respectively. The solid traces are the full waveform solutions from the discrete wavenumber method, and the dashed traces indicate the WFC results. The root mean squares of errors in maximum amplitude between these two sets of seismograms are 1.10%, 0.52% and 0.31% for horizontal, vertical and radial components, respectively. These small errors show accurate calculations by the WFC.

The second model for generating synthetic seismograms is a VTI model with a line singularity (Table 2.1). The source-receiver geometry is the same as in Figure 2.16a. Figure 2.10c and 2.10d shows two qS-wave ray spreading diagrams and wavefronts for this VTI model. The receiver array will include the line singularity in the

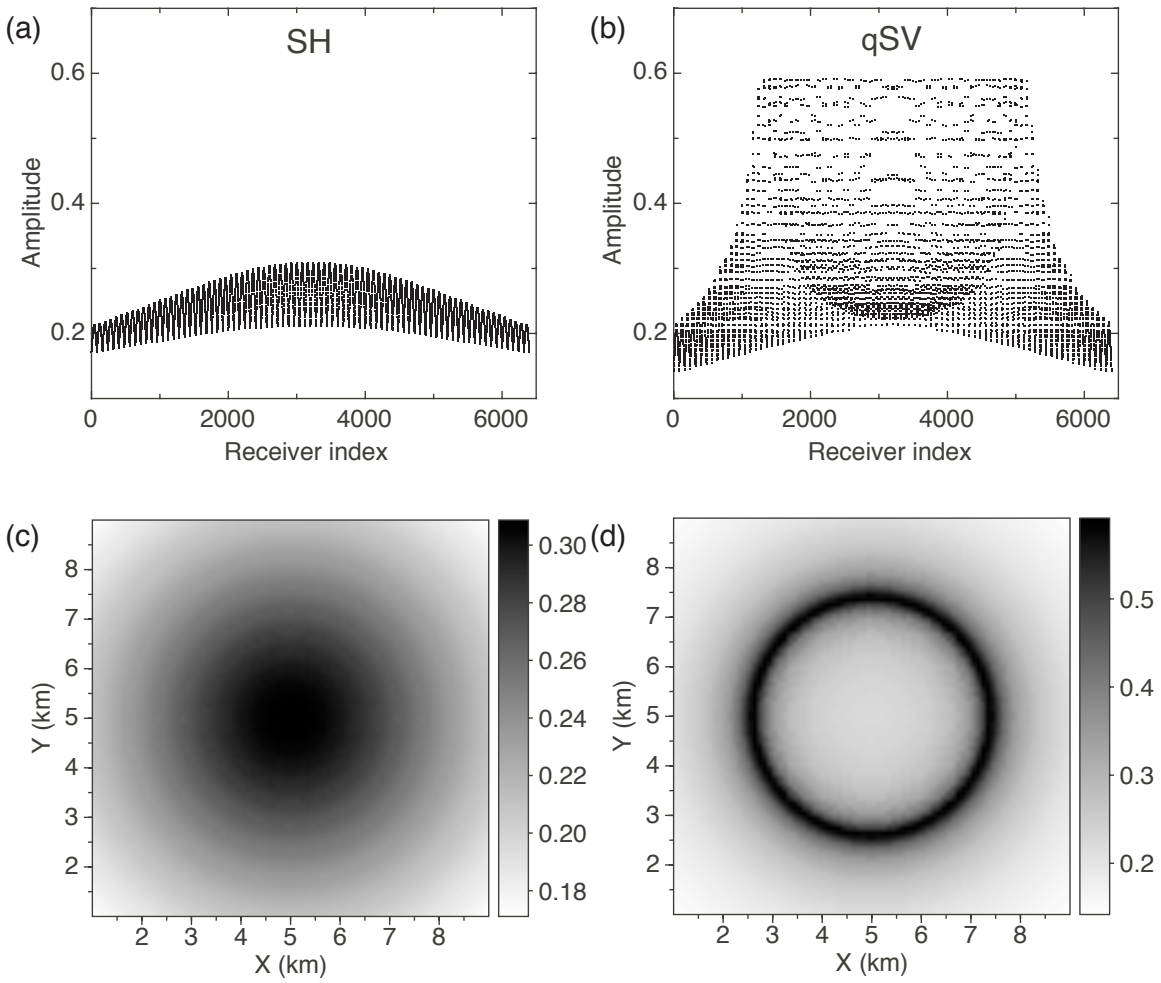

Fig. 2.15. Amplitudes are plotted against the receiver index for SH and qSV waves are shown in (a) and (b), respectively. Comparing to qSV wave, SH wave has gradual variation in amplitude because of the smoother wavefront surface and uniformly distributed rays (see Figure 2.10c and 2.10d). The 2-D plot of amplitudes for SH and qSV waves are shown in (c) and (d), respectively. Due to the concave inward slowness surface (see Figure 2.10b), qSV wave has relative high amplitudes in a ring shape.

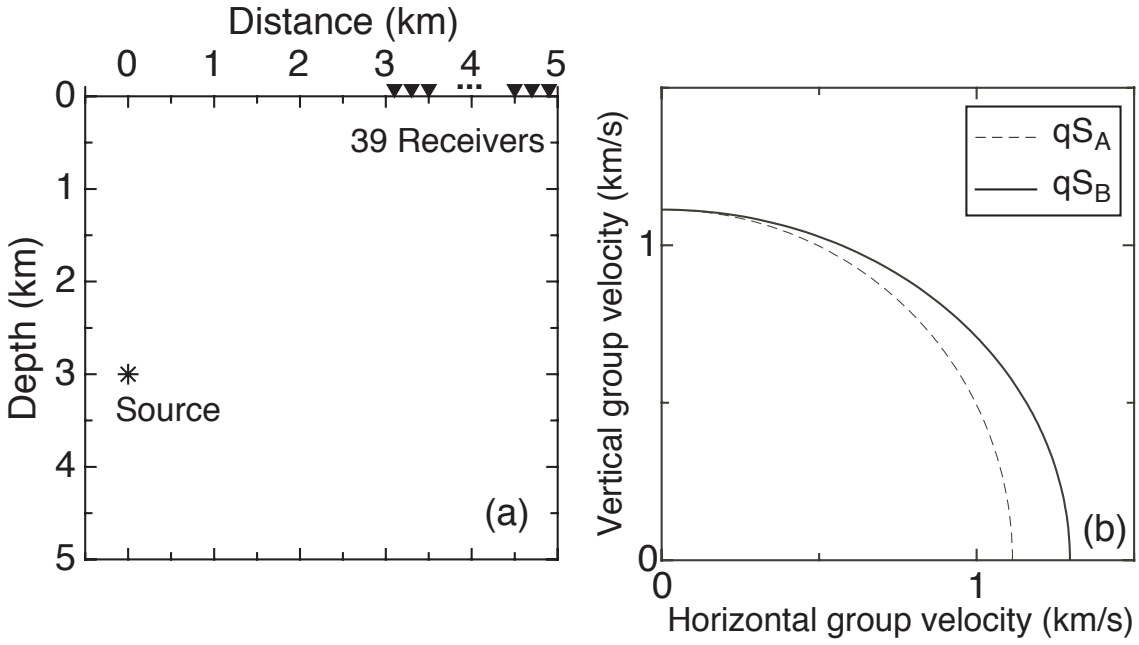

Fig. 2.16. (a) Source-receiver geometry for generating synthetics seismograms in the validation with full waveform solutions. (b) Cross-section of two qS-wave group velocities for an ellipsoidal anisotropic model (see Table 2.4) in the vertical plane.

synthetic seismograms. Figure 2.18 shows qS-wave synthetic seismograms generated by point forces for the model. The root mean square of residuals with respect to the maximum amplitude between these two results are 2.50%, 2.14% and 1.64% for horizontal, vertical and radial components, respectively. Again, they suggest a good agreement between these two methods.

The final synthetic seismogram test uses the model with strong anisotropy and a significant triplication (Figure 2.13c and 2.13d). Velocity in the cusp can be about 43% larger than in the horizontal direction. The source-receiver geometry is also the same as in Figure 2.13a. Again applying vertical and horizontal point forces for qSV and SH waves, respectively, the WFC and discrete wavenumber results still compare well (Figure 2.19). The root mean square of residual maximum amplitude errors, however, increase to 1.40%, 8.52% and 9.69% for tangential, vertical and radial components, respectively. The SH wave results do still show a good agreement in amplitude and waveform (Figure 2.19a). In the vertical component (Figure 2.19b), the arrivals in OP are too weak to be clearly visible, but a close examination shows that both methods predicted relative weak amplitudes here. Also, there are some

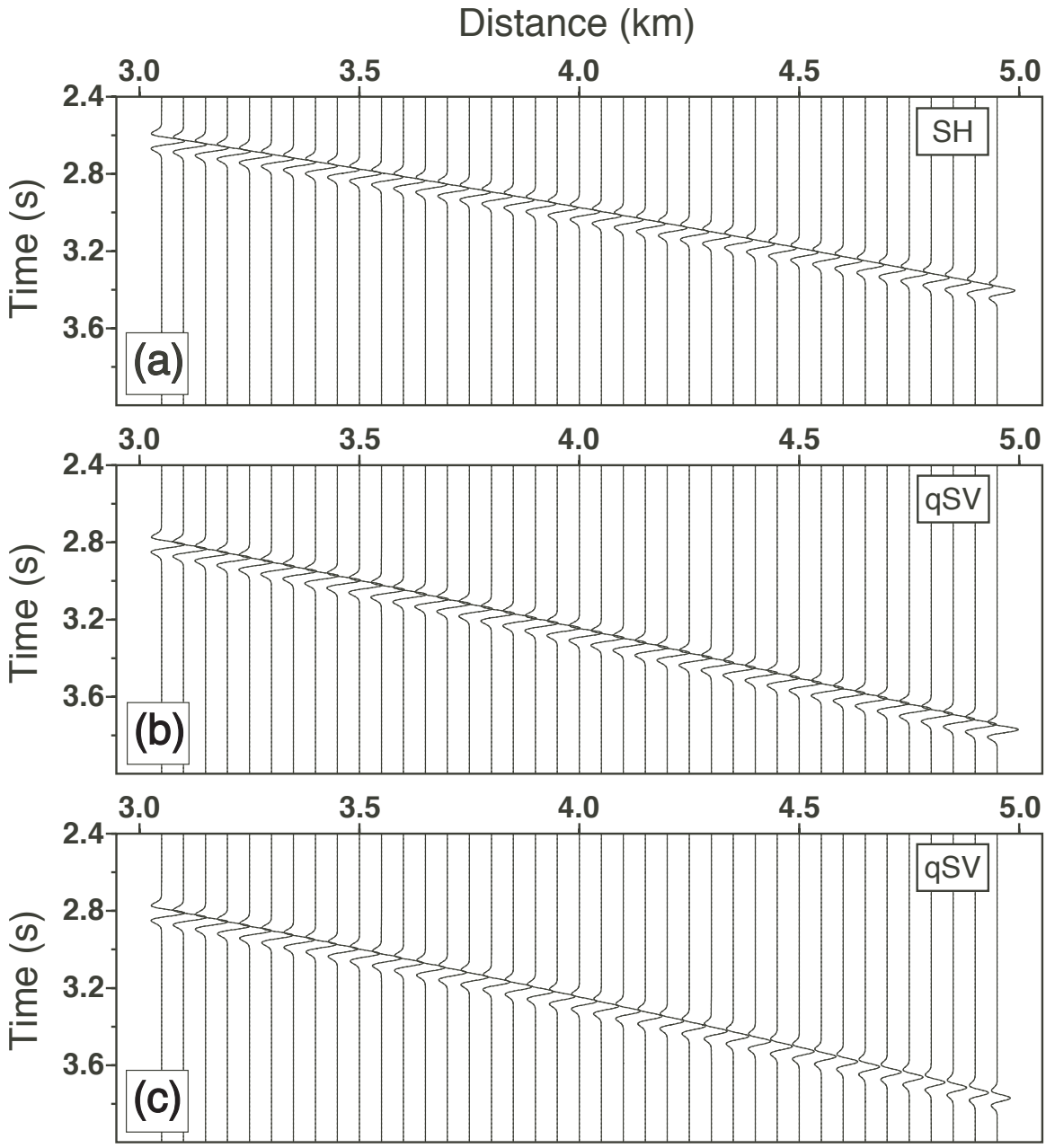

Fig. 2.17. qS-wave synthetic seismograms generated by point forces for an ellipsoidal anisotropic model (see Table 2.4). Solid traces are the full waveform solutions obtained by the discrete wavenumber method. Dashed traces are generated by the WFC method. (a) is the horizontal component of SH wave. (b) is the vertical component of qSV wave. (c) is the radial component of qSV wave. The root mean square of residuals with respect to the maximum amplitude between these two results are 1.1%, 0.52% and 0.31% for horizontal, vertical and radial components, respectively.

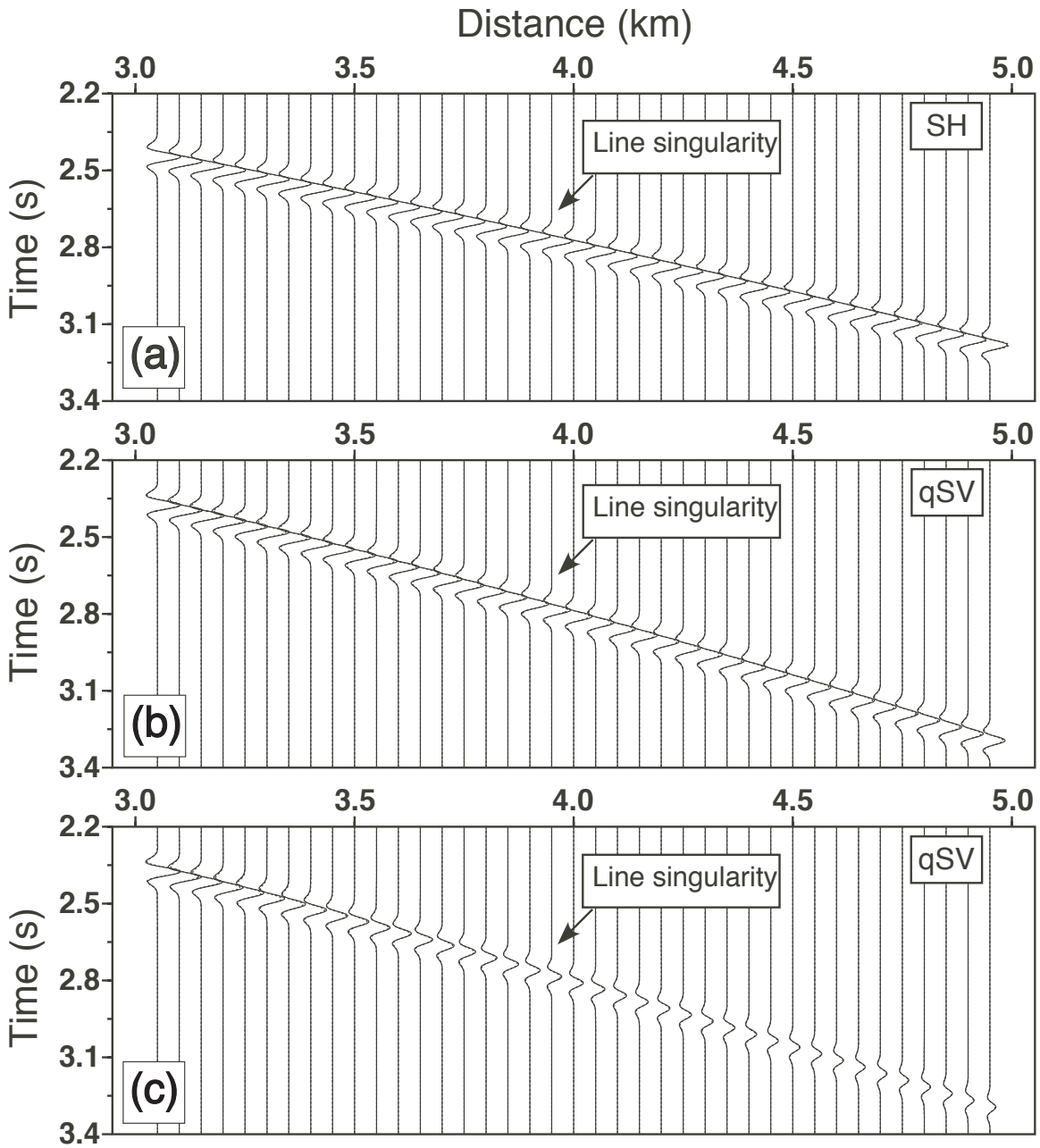

Fig. 2.18. qS-wave synthetic seismograms generated by point forces for the model (see Table 2.1) with a line singularity. See Figure 2.17 for the same description. (a), (b), and (c) are for the horizontal, vertical, and radial components, respectively. The root mean square of residuals with respect to the maximum amplitude between these two results are 2.5%, 2.14% and 1.64% for horizontal, vertical and radial components, respectively.

strong amplitude arrivals beyond caustic cusps, which are not predicted by the WFC method (see near point P).

However, the errors for the qSV wave are in waveform, not just amplitude, and this is in part because our current implementation does not apply the KMAH index that is required for fully correct modeling of waveforms around triplications (Červený, 2001). White (1982) also compared traveltimes and amplitudes of the off-axis qSV-wave triplication between numerical Fourier inversion method and asymptotic ray theory. The ray method based on the first-order ordinary differential equation cannot predict the arrivals beyond the caustic cusps. Geometrical spreading is also complicated in off-axis qSV-wave propagation, and erroneously large amplitudes are predicted near cusps. Similar results were found in both vertical and radial components of synthetic seismograms (Figure 2.19b and 2.19c). Future modifications of the code will incorporate the KMAH index factor into the phase of qS-wave arrivals, but even here the predicted synthetic seismograms are accurate enough to gain important insights in body wave propagation, and traveltimes are accurate.

2.5 Conclusions

WFC is a powerful simulation method that can provide multivalued ray theoretical solutions for 3-D models. It has strong potential to model propagation in complex, multiple layered earth models, such as salt dome structures. Previous work has included implementations for isotropic media, and for quasi-compressional wave modeling in anisotropic media. Though quasi-shear wave propagation is more complicated, the WFC still is an attractive modeling approach, and we have shown that particle motion vectors are an effective criterion for creating initial wavefront meshes and for guiding wavefront interpolation while propagating wavefronts through an earth model.

We have demonstrated results for two homogeneous, transversely isotropic models show that line singularities are correctly handled. Modeling wavefronts through a heterogeneous, VTI model is also correct. A verification of two qS-wave traveltimes for a VTI model with a line singularity demonstrates the accuracy and robustness of propagating wavefronts and mapping algorithms. Ray amplitudes are also shown. Then, a verification of multivalued traveltimes for a wavefront with a triplication shows the WFC method is capable to map multivalued arrivals correctly. In addi-

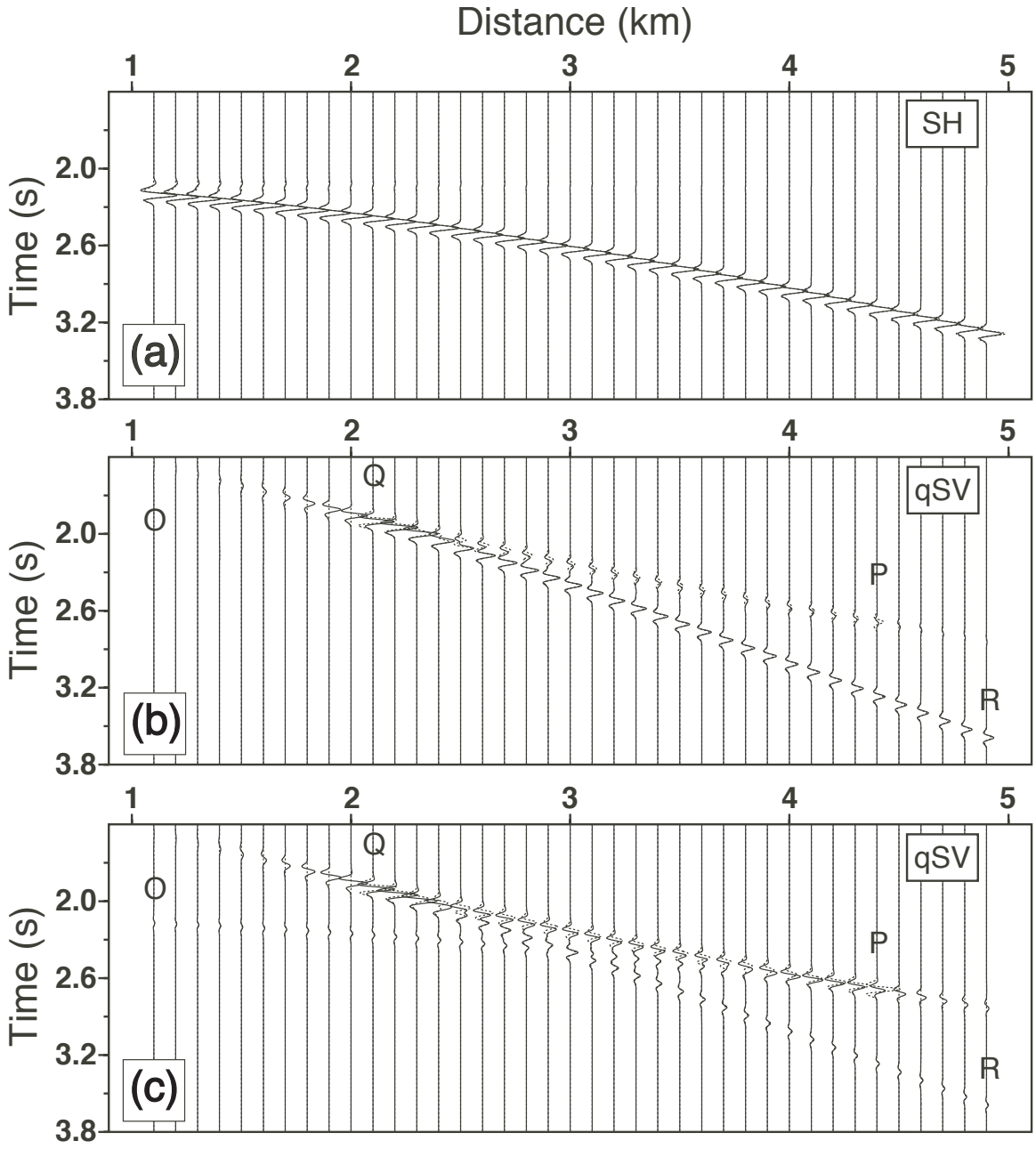

Fig. 2.19. qS-wave synthetic seismograms generated by point forces for the model (see Table 2.3). See Figure 2.13 for the source-receiver geometry, and cross-sections of two qS wavefronts. See Figure 2.17 for the same description. (a), (b), and (c) are for the tangential, vertical, and radial components, respectively. The root mean square of residuals with respect to the maximum amplitude between these two results are 1.4%, 8.52% and 9.69% for tangential, vertical and radial components, respectively. See the text for the discussion.

tion, the ray data obtained by WFC are used to generate synthetic seismograms for these models and compared to the full waveform solutions generated by the discrete wavenumber method. Except the qSV-wave modeling around triplications, all the comparisons of synthetic seismograms demonstrate a excellent agreement between these two methods.

In future extensions of this work, we will use these qS-wave synthetic seismograms to compare with recorded field data and focus the implementation in multilayered models.

CHAPTER III

RAY TRACING INCLUDING COMPOSITE REFLECTION COEFFICIENTS IN STRATIFIED MEDIA

3.1 Introduction

Amplitude variation with offset (AVO) is a very important technique to locate hydrocarbons because the reflection amplitude at different angles of incidence changes significantly when fluids in a formation change from brine to gas, for example (Domenico, 1976; Ostrander, 1984; Murphy, 1984; Rutherford and Williams, 1989; Castagna et al., 1998; Ross, 2000; Smith and Sondergeld, 2001; Zillmer, 2006; Wandler et al., 2007). However, some limitations often lead to false conclusions. Classic AVO analysis based on the approximation of the Zoeppritz equation is valid only for P-wave reflection from the interface between two solid half-spaces. Though the thin layer tuning effect can be included in the AVO modeling (Almoghrabi and Lange, 1986; Juhlin and Young, 1993; Bakke and Ursin, 1998; Liu and Schmitt, 2003), it is more difficult to understand the composite reflection by the conventional AVO analysis when there are many layers in a turbidite reservoir model. Also, the classic AVO analysis assumes that the reflections of each interface are independent from the others generated by other interfaces. Only reflections are considered, and transmissions, conversions, and multiple waves are all neglected. However, these wavefields may include useful information to detect hydrocarbon in the rock.

AVO analysis in complex stratified reservoir models, such as turbidite reservoirs in the Gulf of Mexico, is thus very crucial in petroleum exploration. The turbidite reservoirs are often composed of a couple of thin sand/shale layers and complex distributions of velocity and density. Therefore, seismic modeling for a complete synthetic seismograms in these complex stratified, thin reservoir models is necessary to accurately predict reflection amplitudes and location of hydrocarbons.

Wave propagation through multi-layered media including reflection, transmission and conversion complicates seismic modeling. The Thomson-Haskell propagator matrix (Thomson, 1950; Haskell, 1953) was developed to obtain reflection and transmission coefficients and solve the propagated stress and displacement vector fields

through horizontally stratified isotropic layers. Gilbert and Backus (1966) implement the application of the propagator matrix to seismology.

Comparing to direct computation of the plane layer responses in the propagation matrix method, the reflectivity method (Kennett and Kerry, 1979) obtains reflection and transmission matrices iteratively by starting at the first layer and increment one layer for each iteration until we have reach the total stack. Booth and Crampin (1983) extended the reflectivity methods from horizontal stratified isotropic structures to stratified anisotropic structures. Also, Müller (1985) demonstrate a tutorial of using the reflectivity method to generate the complete synthetic seismograms for a point force in a layer stack model.

Gibson, Jr. (2004, 2005) suggested the use of the propagator matrix method to quickly compute the composite P-wave reflection coefficient for stratified reservoir models. Though the internal velocity fluctuations complicate the model and lead to strong scatterings in amplitude, example calculations show that the fluids still produce measurable AVO anomalies in the the reflection amplitudes.

However, generating synthetic seismograms for a complex stratified reservoir is computational expensive, especially for the large volume of seismograms required to simulate a complete seismic survey. The problem can be solve by a fast hybrid approach. Červený(1989) introduce a hybrid approach which combines ray tracing modeling in the thick overburden layer or layers with the reflectivity method in a laterally varying thin transition layer. Here, I apply the same idea to generate the complete synthetic seismograms in complex stratified reservoir. This task can be done by integrating the propagator matrix results with fast seismic modeling using ray methods known as wavefront construction to implement fast solutions for synthetic seismograms that model the complications in seismic reflection amplitudes that are caused by complex, stratified reservoir structures. This will be accomplished using composite reflection coefficients that include all of the influence of layering in a reservoir on the reflected signal, not simply a single boundary as is done in conventional analysis. The ray tracing will simulate propagation in the geologic layer over a target layer, while the composite reflection coefficient will model the amplitude of the signal reflected by the stratified reservoir model. In this chapter, I will integrate the propagation matrix results (Gibson, Jr., 2004, 2005) with fast seismic modeling accomplished by ray tracing including composite reflection coefficients in stratified reservoir models.

Below I briefly describe the content of this chapter. First I demonstrate the ray tracing by wavefront construction (WFC) method for reflections in a two-region model with a horizontal or titled interface. A set of verifications of reflection traveltimes and amplitudes in a two-region model with a horizontal or titled interface shows that the WFC method is robust and accurate. Then, I compare the P- wave reflection coefficients between using the propagator matrix method and full waveform synthetic seismograms for a couple of different source frequencies in the simple interface, thin layer embedded and complex stratified models. Finally, I apply the ray tracing including composite reflection coefficients method to a complex stratified reservoir models. The ray data, generated by the WFC method, and composite reflection coefficients, obtained by the propagator matrix method, are combined together to create synthetic seismograms for a turbidite reservoir model in Ursa field, Gulf of Mexico. And they are validated with another independent full waveform synthetic seismograms with discrete wavenumber full waveform solutions for the central frequency at 10, 20, 40 and 60 Hz. Furthermore, the synthetic seismograms for the model embedded with a thin, tilted reservoir are presented.

3.2 Methods

3.2.1 Ray Tracing by Wavefront Construction in Multi-region Models

Though the WFC method is efficient and robust, the ray interpolation step can be very difficult when the ray tube is reflecting or transmitting an interface (Figure 3.1). The folded wavefront patch makes it impossible to accurately estimate the paraxial traveltime errors using the normal implementation (see equation 2.5). An additional check to test whether the ray tube is reflecting and transmitting is applied to ensure the implementation of the WFC method in the multi-region models.

Considering the WFC implementation in multi-region models, Lee and Gibson, Jr. (2005) developed a model-based interpolation ray-tracing method in which the ray interpolation is only performed at the layer interfaces, to simulate the wavefront propagation in the layered models efficiently and easily. However, this modification will encounter difficulties when the ray tube transmits through same surface more than one time. For example, the ray tube may propagate through a salt dome surface twice.

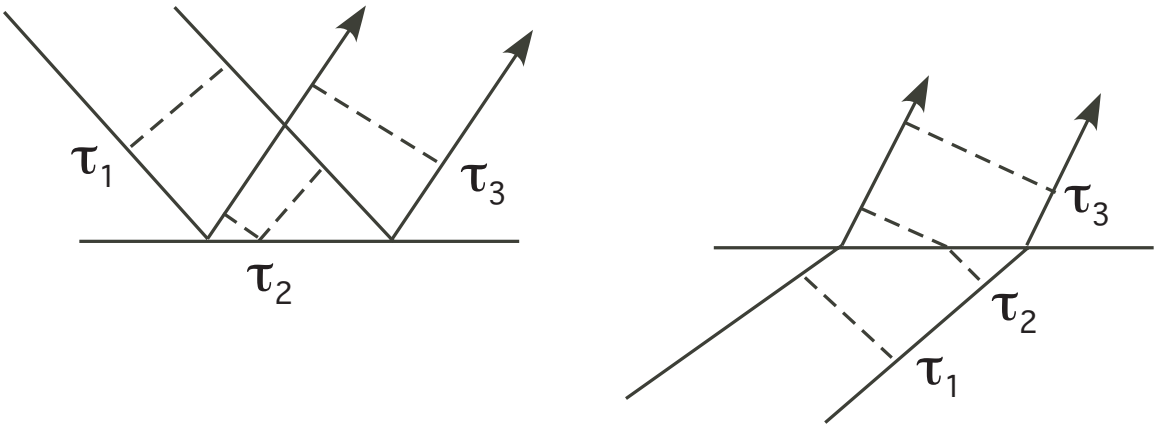

Fig. 3.1. Schematic illustration of the difficulty in the ray interpolation while the ray tube is reflecting and transmitting in an interface.

Therefore, we will not directly apply the model-based interpolation method. Instead, we will utilize the same interpolation procedure as was developed for smooth media (see Chapter II). However, we will never apply interpolation when the ray tube is reflecting from or transmitting across an interface (Figure 3.1). For reflection, the reflected points (or time) of the nearby rays of the ray tube are used to checking whether the patch between the current and next step is reflecting. However, for transmission, we can simply check the region indices of eight points of the piece of the ray tube to detect this transmission condition. A couple of examples will be shown in the Examples section.

Furthermore, in order to correctly use composite reflection coefficients that include the total influence of layering in a reservoir on the reflected signal, the incident angle information of the rays must be stored properly. However, because the new rays may be inserted after the time that the nearby rays are reflected, the new rays have no incident angle information (see the figure on page 47) to exact the magnitude and phase of composite reflection coefficients. Additional care of interpolating the incident angle from the nearby rays is necessary to correctly use the composite reflection coefficients. The verification of incident angles is shown in the figure on page 75. Since the composite reflection coefficients change gradually with the incident angle, the small incident angle errors, mostly less than 2°, suggest the usage of reflection coefficient is precise enough.

The ray data, which includes traveltime, amplitude, geometric spreading, takeoff angle, and incident angle at receivers and the Green's tensor can be used to generate

synthetic seismograms. The Green's tensor G_{ij} which is determined by the medium properties, can be used to calculate the displacement fields at receivers (Ben-Menahem et al., 1991). The medium's response u_i to an arbitrary point force F_j can be written as

$$u_i = G_{ij} F_j, \tag{3.1}$$

where G_{ij} is proportional to $g_i g_j$. And g_i is the eigenvalue of the Christoffel matrix. For the explosive source, the derivative of G_{ij} makes Equation 3.1 to be re-written as

$$u_i = -iw G_{ij} M_{jk} p_k, \tag{3.2}$$

where M_{jk} is the moment tensor and p_k is the slowness vector. We should be careful to explain the synthetic seismogram generated by a explosive source because the term $-iw$ makes the polarity, frequency, and phase changes in the seismograms.

In addition, the Green's tensor obtained by WFC are all real numbers because the computation of displacement field (or transmission and reflection coefficient) in the interface are not included in the WFC modeling. The composite reflection coefficients computed by the propagator matrix method should be correctly included to form a complex Green's tensor for generating synthetic seismograms.

3.2.2 Propagator Matrix Method

The propagator matrix method has been introduced to solve reflection and transmission coefficients in the horizontally stratified isotropic layers (Thomson, 1950; Haskell, 1953; Gilbert and Backus, 1966). Figure 3.2 shows a stack of stratified layers embedded in a half space model (Gibson, Jr., 2004). A P-wave reflection from the stack can be computed by the propagator matrix method and produces the exact solution of a composite reflection coefficient.

Aki and Richard (2002) demonstrate the detail of derivation for the method in chapters 5 and 7. Also, Gibson (2004) shows the derivation for computing the reflection from a stack of layers. The differential equations for the motion-stress vector of the plane waves in homogeneous media can be generalized to a matrix form:

$$\frac{d\mathbf{b}(z)}{dz} = \mathbf{A}(z)\mathbf{b}(z), \tag{3.3}$$

where $\mathbf{b}(z)$ is given by

$$\mathbf{b} = \begin{bmatrix} u_1 \\ u_3 \\ \sigma_{13} \\ \sigma_{33} \end{bmatrix}. \tag{3.4}$$

Equation 3.3 can be solved by

$$\mathbf{b} = \mathbf{F}\mathbf{w}, \tag{3.5}$$

where

$$\mathbf{w} = \begin{bmatrix} P_{down} \\ SV_{down} \\ P_{up} \\ SV_{up} \end{bmatrix}, \tag{3.6}$$

which denotes the amplitudes of P- and S-waves for down- and up-going plane waves. The motion-stress vector $\mathbf{b}$ and amplitude vector $\mathbf{w}$ are related to produces a four by four matrix $\mathbf{F}$. Each of $\mathbf{w}$ and $\mathbf{b}$ is layer dependent. In the upper half space, layer 0, Equation 3.5 is written as $\mathbf{b}^0 = \mathbf{F}^0\mathbf{w}^0$, where the amplitude vector field

$$\mathbf{w}^0 = \begin{bmatrix} 1 \\ 0 \\ P_{up} \\ SV_{up} \end{bmatrix}. \tag{3.7}$$

We assume a unit amplitude of incident P-wave. Similarly, the amplitude vector field in the lower half space is written as

$$\mathbf{w}^{n+1} = \begin{bmatrix} P_{down} \\ SV_{down} \\ 0 \\ 0 \end{bmatrix}. \tag{3.8}$$

Fig. 3.2. A stack of stratified layers embedded in a half space model for propagator matrix computation. The incident plane wave hits the top of the stack (Gibson, Jr., 2004).

Finally, the composite reflection of P-wave in the upper half space is written as

$$\mathbf{F}^0\mathbf{w}^0 = \mathbf{P}^{prod}\mathbf{F}^{n+1}\mathbf{w}^{n+1}, \tag{3.9}$$

where $\mathbf{P}^{prod}$ is the product of n four by four propagator matrices $\mathbf{F}$. Each layer has its own in the model. I only compute P-wave reflection from a stack of stratified layers.

3.2.3 Shuey's Approximation Method

Because I start the comparison of P- wave reflection coefficient in a simple interface half-space model, I introduce the well known Shuey's approximation to understand how it is different from the Zoeppritz equation results.

Shuey (1985) described an approximate solution for the P-wave reflection coefficient from a single interface between two solid half-space, illustrating how the amplitudes at normal incidence, intermediate, and large angles, providing physical insights into the P-wave reflection problem. P-wave reflection coefficient as a function of the incident angle can be written as three term approximation

$$R(\theta) \approx A + Bsin^2(\theta) + C(sin^2(\theta)tan^2(\theta). \tag{3.10}$$

A, the normal incidence P-wave reflection coefficient, is denoted as

$$A = \frac{1}{2}(\frac{\Delta V_p}{\langle V_p \rangle} + \frac{\Delta \rho}{\langle \rho \rangle}). \tag{3.11}$$

B, which describes the P-wave reflection coefficient in the intermediate angles, is given by

$$B = \frac{1}{2}\frac{\Delta V_p}{\langle V_p \rangle} - 2(\frac{\langle V_s \rangle}{\langle V_p \rangle})^2(2\frac{\Delta V_s}{\langle V_s \rangle} + \frac{\Delta \rho}{\langle \rho \rangle}). \tag{3.12}$$

C, which represents the coefficient while approaching the critical angles, is written as

$$C = \frac{1}{2}\frac{\Delta V_p}{\langle V_p \rangle}. \tag{3.13}$$

$\Delta V_p = V_{p2} - V_{p1}$ is the change in compressional velocity and $\langle V_p \rangle = \frac{V_{p2}+V_{p1}}{2}$ is the average in compressional velocity across the interface. $\Delta V_s = V_{s2} - V_{s1}$ is the change in shear velocity and $\langle V_s \rangle = \frac{V_{s2}+V_{s1}}{2}$ is the average in compressional velocity across the interface. $\Delta \rho = \rho_2 - \rho_1$ is the change in density and $\langle \rho \rangle = \frac{\rho_2+\rho_1}{2}$ is the average in density across the interface. Subscription 1 and 2 are for overlying and underlying media, respectively.

3.2.4 Backus Averaging

Since the total thickness of the reservoir in seismic modeling is relatively thin, the well-known Backus averaging (Backus, 1962) will be discussed and its results will be compared. Backus average algorithm estimates an equivalent homogeneous medium with the same effect as the complete horizontally layered stack. For wavelength longer than the total thickness, the medium is can be replaced by a transversely isotropic medium in this method.

3.3 Examples of Ray Tracing of Reflection by Wavefront Construction

Here I present the ray tracing by the WFC method for reflections in a two-region model with a horizontal or titled interface. Figure 3.3a shows a set of sparse initial rays traced through a model with a horizontal surface. Figure 3.3b shows the result after propagating the wavefront through the model, in which new rays are adaptively inserted. And the wavefront at 1.6 s shows the front after it is partially reflected. In order to test the robustness of the algorithms, up-dip (Figure 3.4) and down-dip (Figure 3.5) interface models are also tested and the results suggest the correctness of the ray tracing by WFC method for reflections. In the Verification and Validation

Table 3.1. Velocities and densities of the two-region model.

	Vp (km/s)	Vs (km/s)	$\rho\,(g/cm^3)$
Top layer	3.0	1.5	2.6
Bottom layer	3.2	1.6	2.7

sections, a sequence of source-receiver geometry and models support the accuracy of this method.

3.4 Verification of Traveltimes and Amplitudes

A sequence of verifications is applied to demonstrate the accuracy and robustness of the implementation of reflection in the WFC method. Figure 3.6 shows the top and side views of the source-receiver geometry and model dimension for verifying traveltimes and amplitudes in the two-region models with a horizontal and tilted surfaces. Source is located in the surface and 62 by 62 receivers are uniformly distributed. Table 3.1 gives the velocities and densities of the two-region model.

Figure 3.7 show the wavefront propagates through a two-region model and reflects in a horizontal interface with depth 3 km. The similar model but with a tilted interface is also shown in Figure 3.8. All these wavefronts look reasonable, however, the verification of mapping traveltimes and amplitude will prove the algorithm is correctly implemented.

3.4.1 Traveltimes

Figure 3.9 presents the the traveltime residuals of reflection in a two-region model with a horizontal interface. Traveltimes residuals are plotted against the receiver indices to show the distribution of errors. The statistic results show that the mean is $8.52\text{x}10^{-7}$ s, which is about three order less than the predefined threshold 1 ms for ray interpolation. The standard deviation, $1.02\text{x}10^{-6}$ s, suggests a very good distribution of errors. In the 2-D plot of traveltime errors, generally the errors have very similar values in all azimuthal direction. The peak and trough pattern of errors

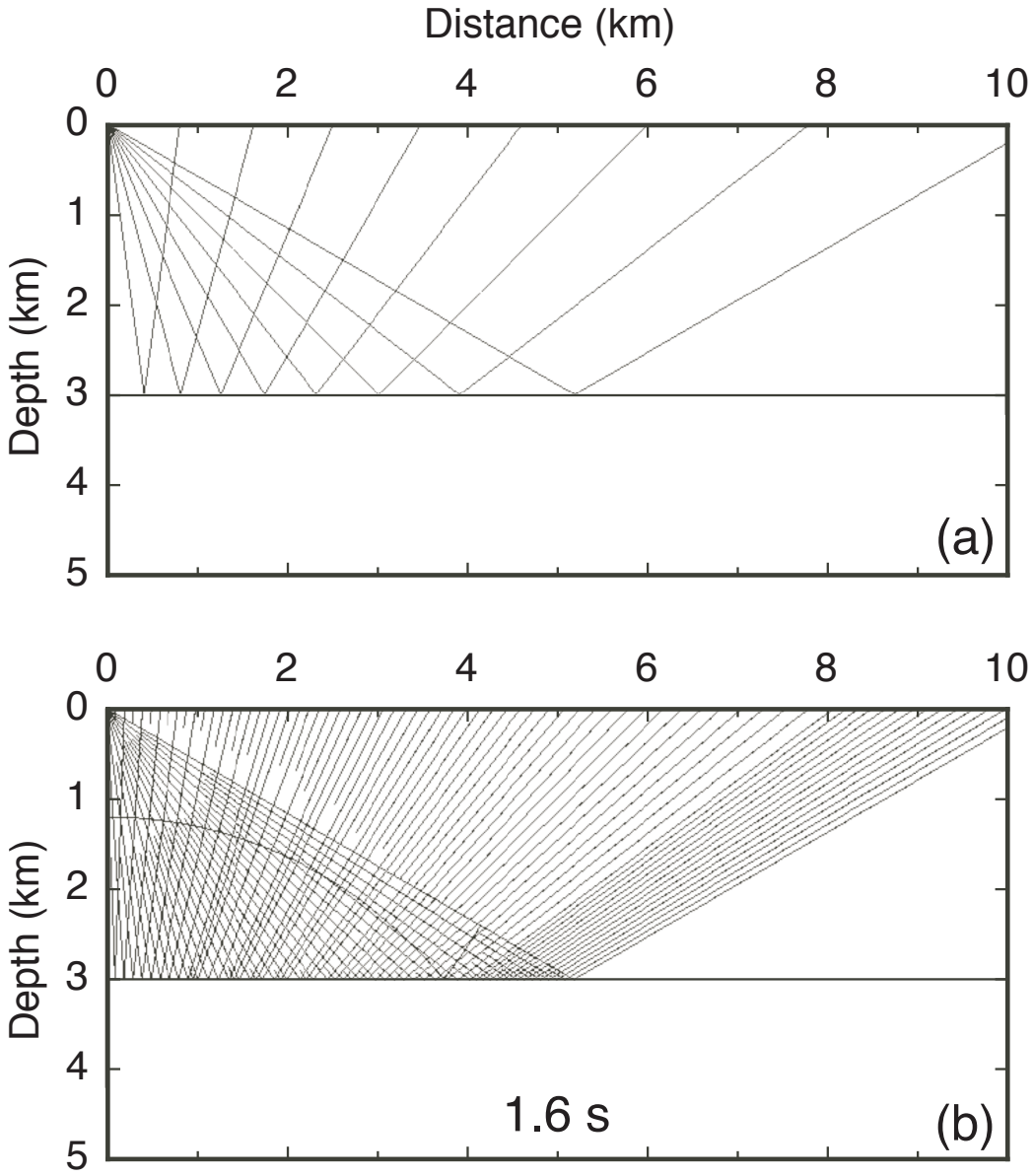

Fig. 3.3. Ray tracing of reflection by wavefront construction in a two-region model with a horizontal surface. (a) A set of initial sparse rays are traced. (b) After propagating the wavefront through the model, new rays are adaptively inserted. And the wavefront at 1.6 s demonstrates the front is partially reflected.

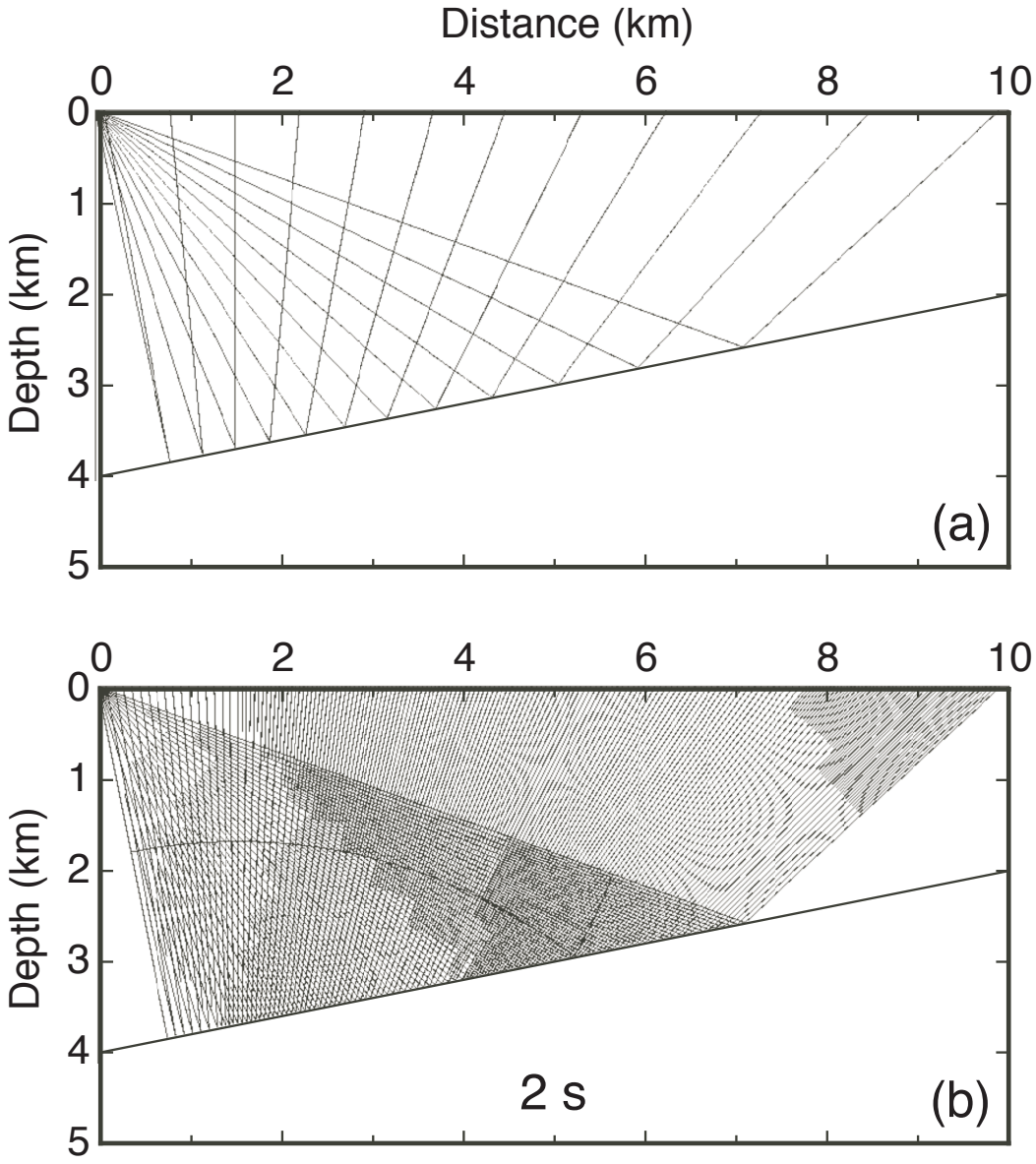

Fig. 3.4. Ray tracing of up-dip reflection by wavefront construction in a two-region model with an up-dip surface. (a) A set of initial sparse rays are traced. (b) After propagating the wavefront through the model, new rays are adaptively inserted. And the wavefront at 2 s demonstrates the front is partially reflected.

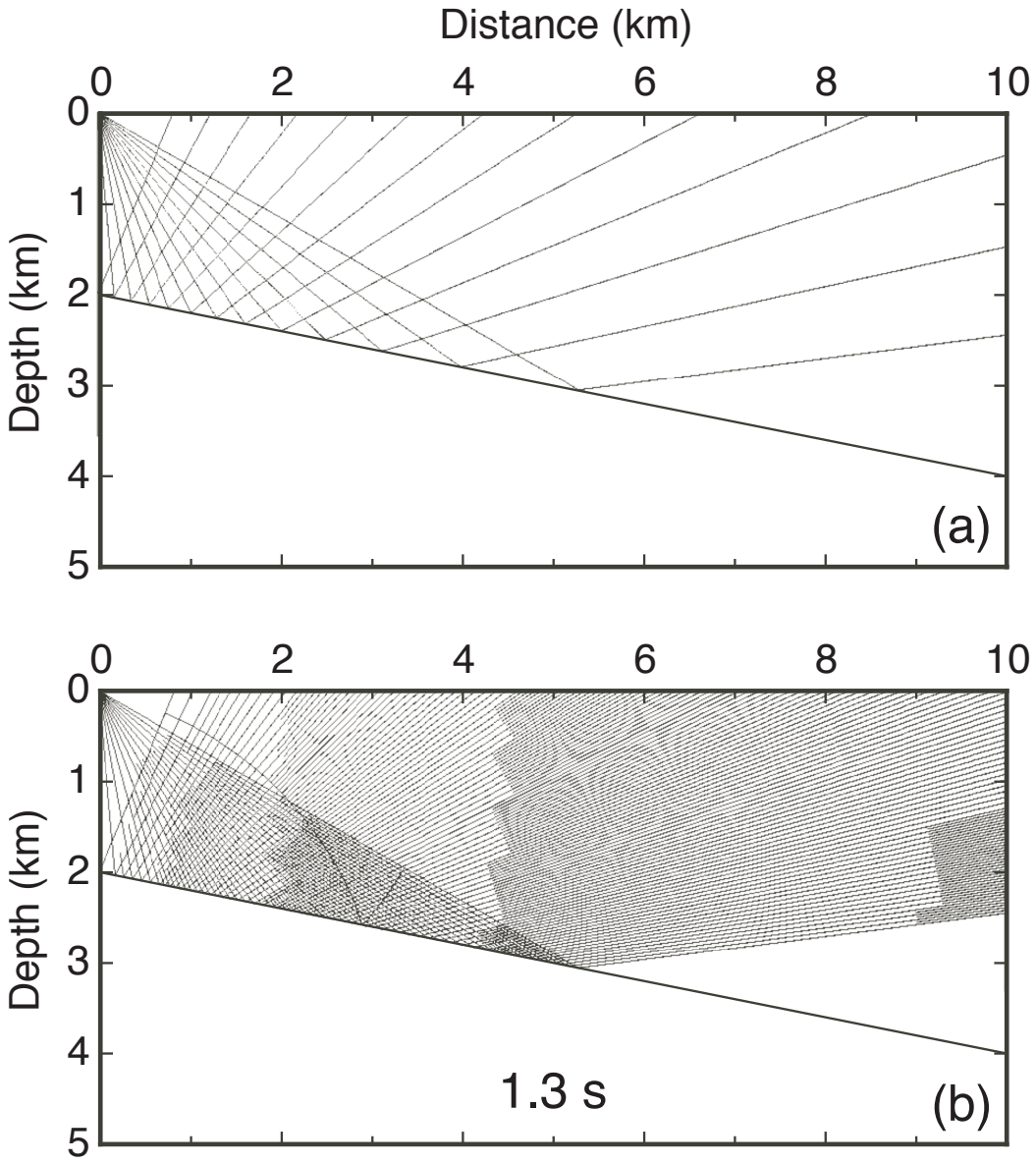

Fig. 3.5. Ray tracing of down-dip reflection by wavefront construction in a two-region model with a down-dip surface. (a) A set of initial sparse rays are traced. (b) After propagating the wavefront through the model, new rays are adaptively inserted. And the wavefront at 1.3 s demonstrates the front is partially reflected.

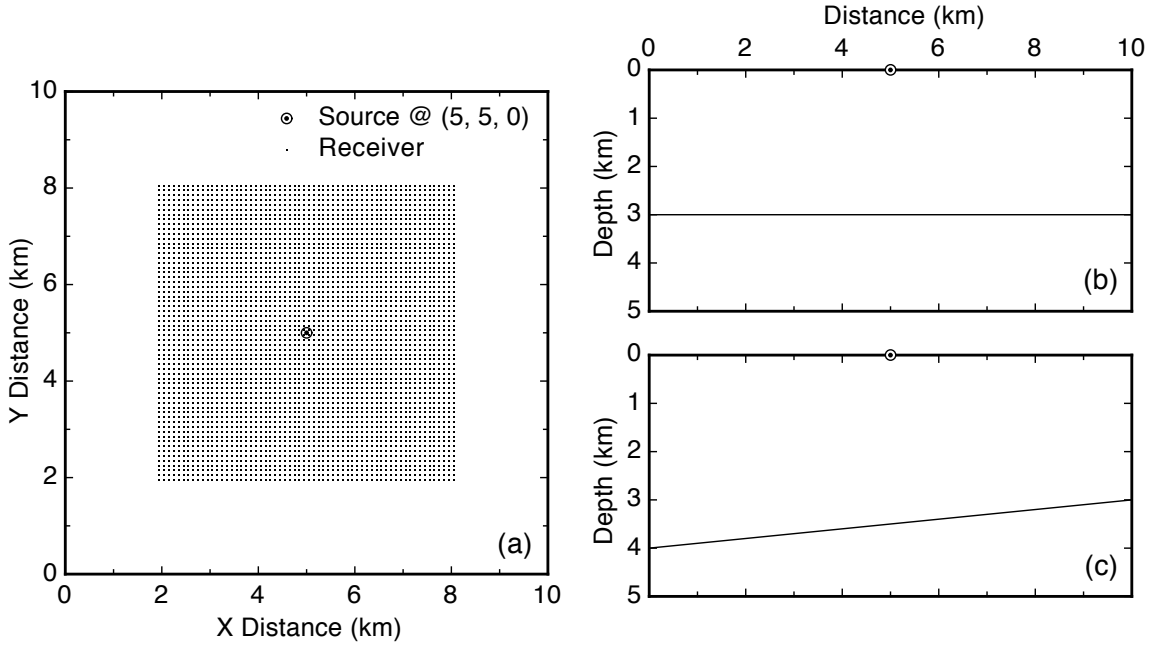

Fig. 3.6. (a) The top view of the source-receiver geometry for verifying of traveltimes and amplitudes in the two-region models with a horizontal and tilted surfaces. The side views of the two-region model with a horizontal and tilted surface are shown in (b) and (c), respectively. This model and source-receiver geometry can verify the mappings of reflection traveltimes and amplitudes in both up- and down-dip surfaces.

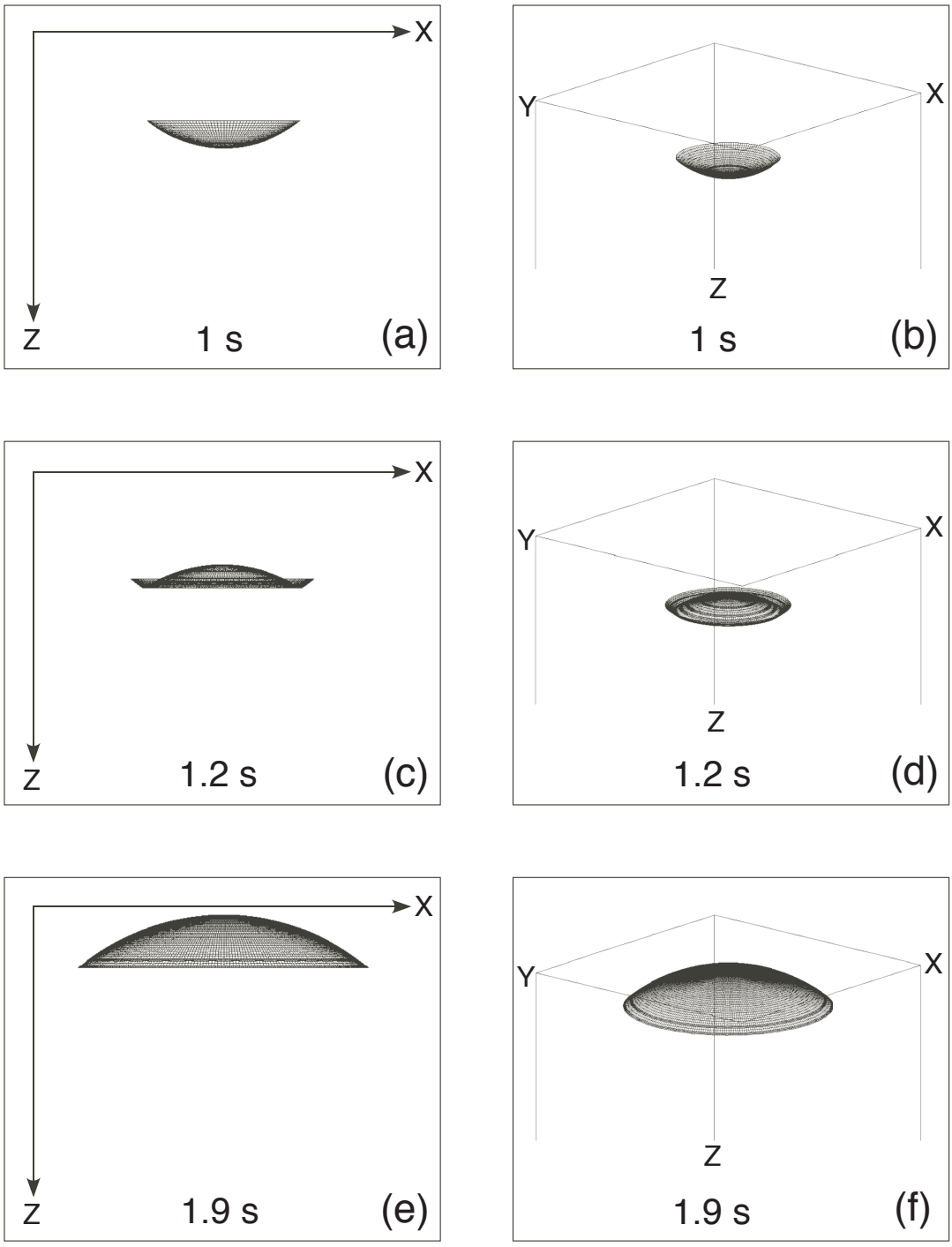

Fig. 3.7. Wavefront propagates through a two-region model and reflects in a horizontal interface with depth 3 km. (a) The side view of the wavefront at time 1 s before it hits the horizontal interface. (b) The 3-D view of (a). (c) The side view of the wavefront at time 1.2 s. Partial wavefront is reflected. (d) The 3-D view of (c). (e) The side view of the wavefront at time 1.9 s after it reflects from the horizontal interface. (f) The 3-D view of (e).

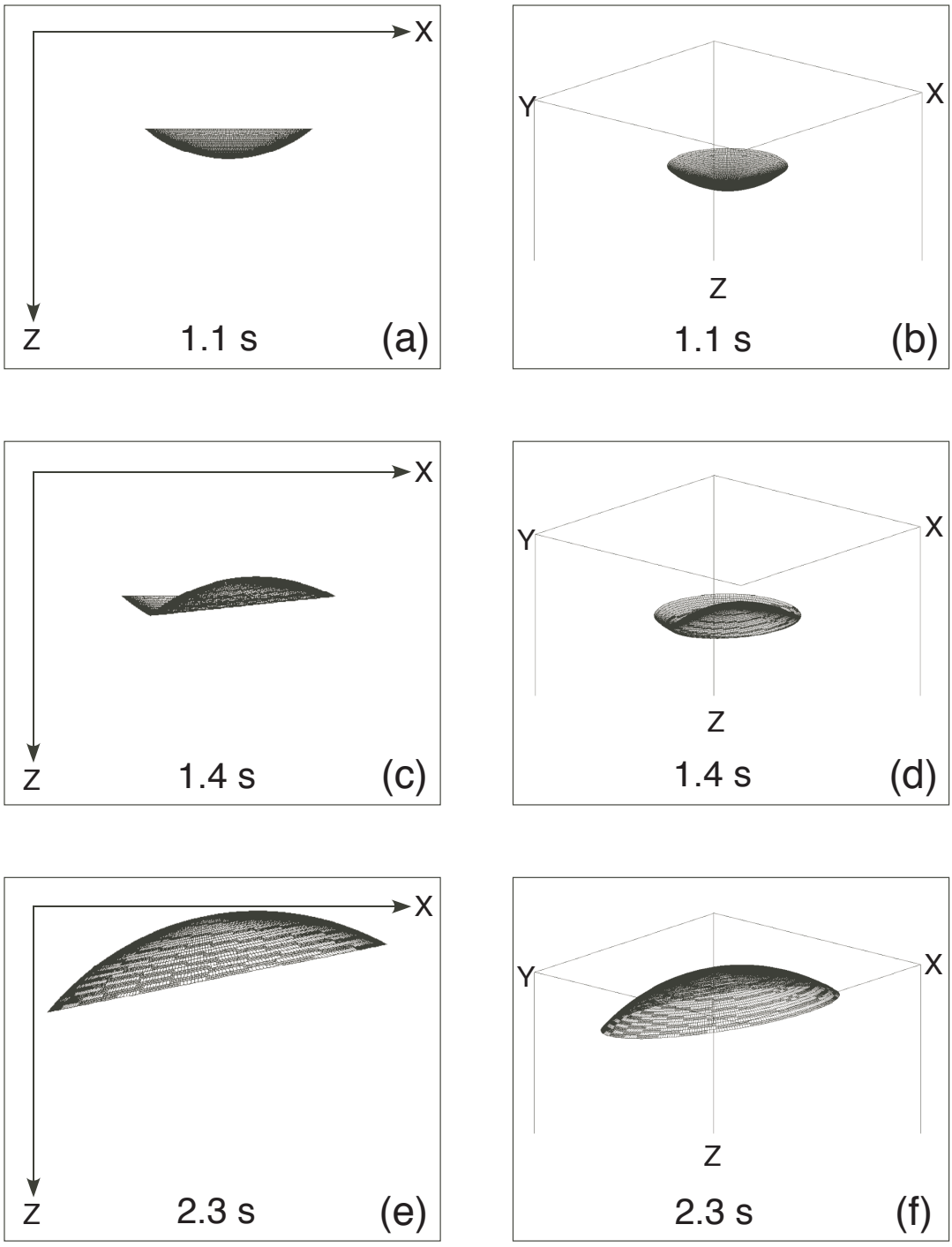

Fig. 3.8. Wavefront propagates through a two-region model and reflects in a tilted interface. (a) The side view of the wavefront at time 1.1 s before it hits the tilted interface. (b) The 3-D view of (a). (c) The side view of the wavefront at time 1.4 s. Partial wavefront is reflected. (d) The 3-D view of (c). (e) The side view of the wavefront at time 2.3 s after it reflects from the tilted interface. (f) The 3-D view of (e).

away from the source suggest some receivers use the same central ray (or patch of the wavefront) for extrapolating the ray data. The closer receivers have smaller errors. The verification for the a two-region model with a tilted interface is also presented in Figure 3.10. Both mean of traveltime errors and standard deviation are slightly larger than the previous model. The 2-D plot of traveltime errors shows a shifted version in the previous model.

3.4.2 Amplitudes

Verifications of amplitude for both two models are also shown since the analytic solutions for amplitude are available. We continue the derivation of Equation 2.8 in the Methods section, Chapter II. Considering an amplitude along a ray in an isotropic, homogeneous medium, it is easy to get $|\frac{\partial x_i}{\partial \gamma_j}| = r^2 sin\theta$ since the wavefront is spherical here. If the focal sphere introduced, the J in Equation 2.8 can be written as a function of distance. Then $J(r_0) = sin\theta$ at τ_0 and $J(r) = r^2 sin\theta$ at τ can be obtained. Amplitude in Equation 2.7 in an isotropic, homogeneous medium is expressed as a function of distance.

$$A(|\mathbf{r}|) = \frac{1}{|\mathbf{r}|} \tag{3.14}$$

where $|\mathbf{r}|$ is the distance from a source point. Though the amplitude is inversely proportional to distance in isotropic media the computation for analytic solutions of amplitude is not trivial. The Cartesian coordinates of the receivers' image with respect to the tilted surface are computed to get the distance from source to receivers.

Figure 3.11 demonstrates the verification of reflection amplitudes in a two-region model with a horizontal interface. The residuals are less than $4.5\text{x}10^{-4}$. The 2-D plot of amplitude residuals are shown. Also, the verification of of reflection amplitudes in a two-region model with a tilted interface is performed (Figure 3.12). Again, the results show a shifted version in the previous model.

3.5 Composite Reflection Coefficient by Propagator Matrix Method

In this section we test and verify the coefficients generated by propagator matrix method for the simple interface, thin layer embedded, and complex stratified models. The results are compared against other independent methods to demonstrate the

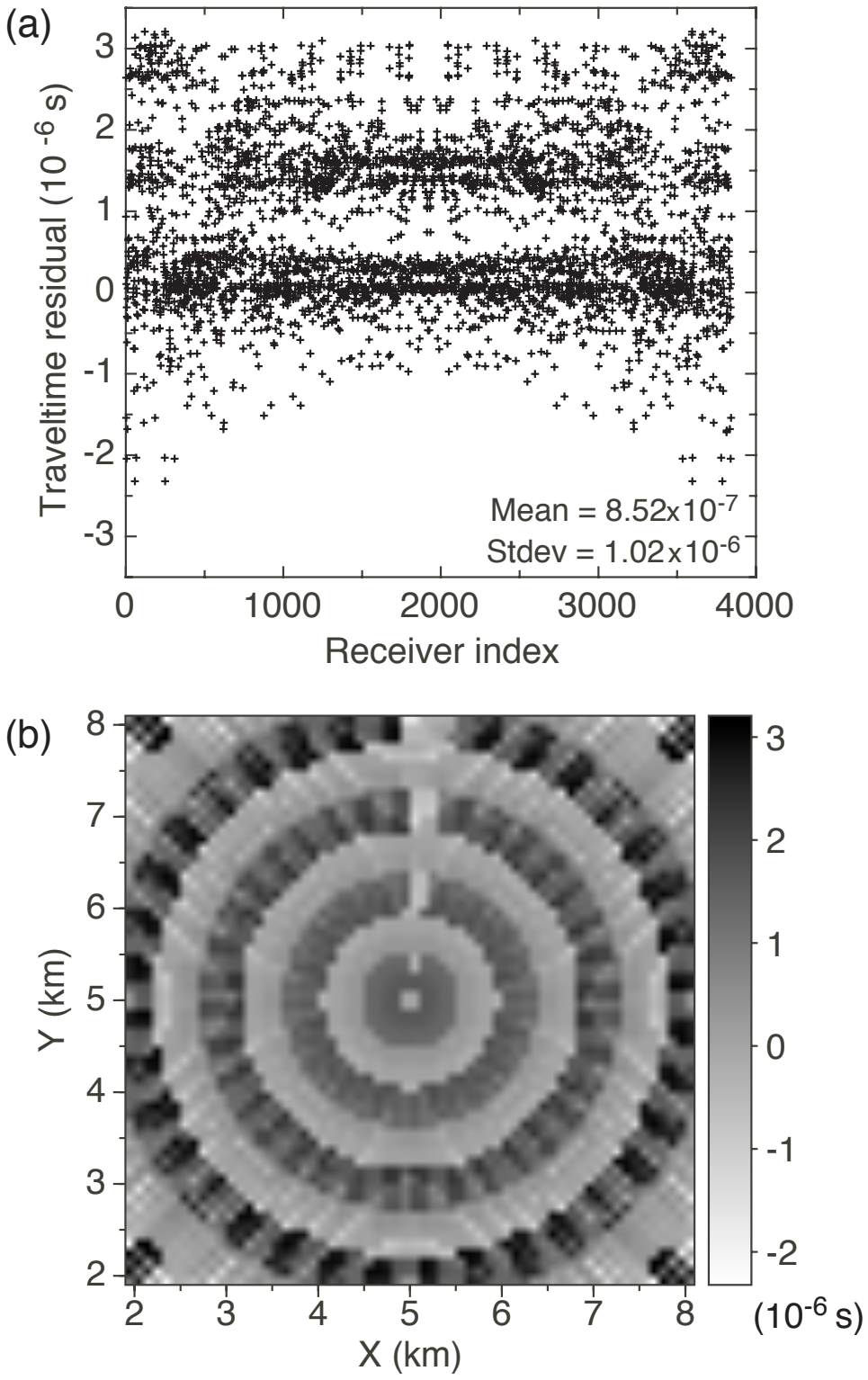

Fig. 3.9. Verification of reflection traveltimes in a two-region model with a horizontal interface. (a) Traveltime residuals are plotted against the receiver indices. The residuals are bounded within $3.5\text{x}10^{-6}$ s. (b) Traveltime residuals are plotted in 2-D.

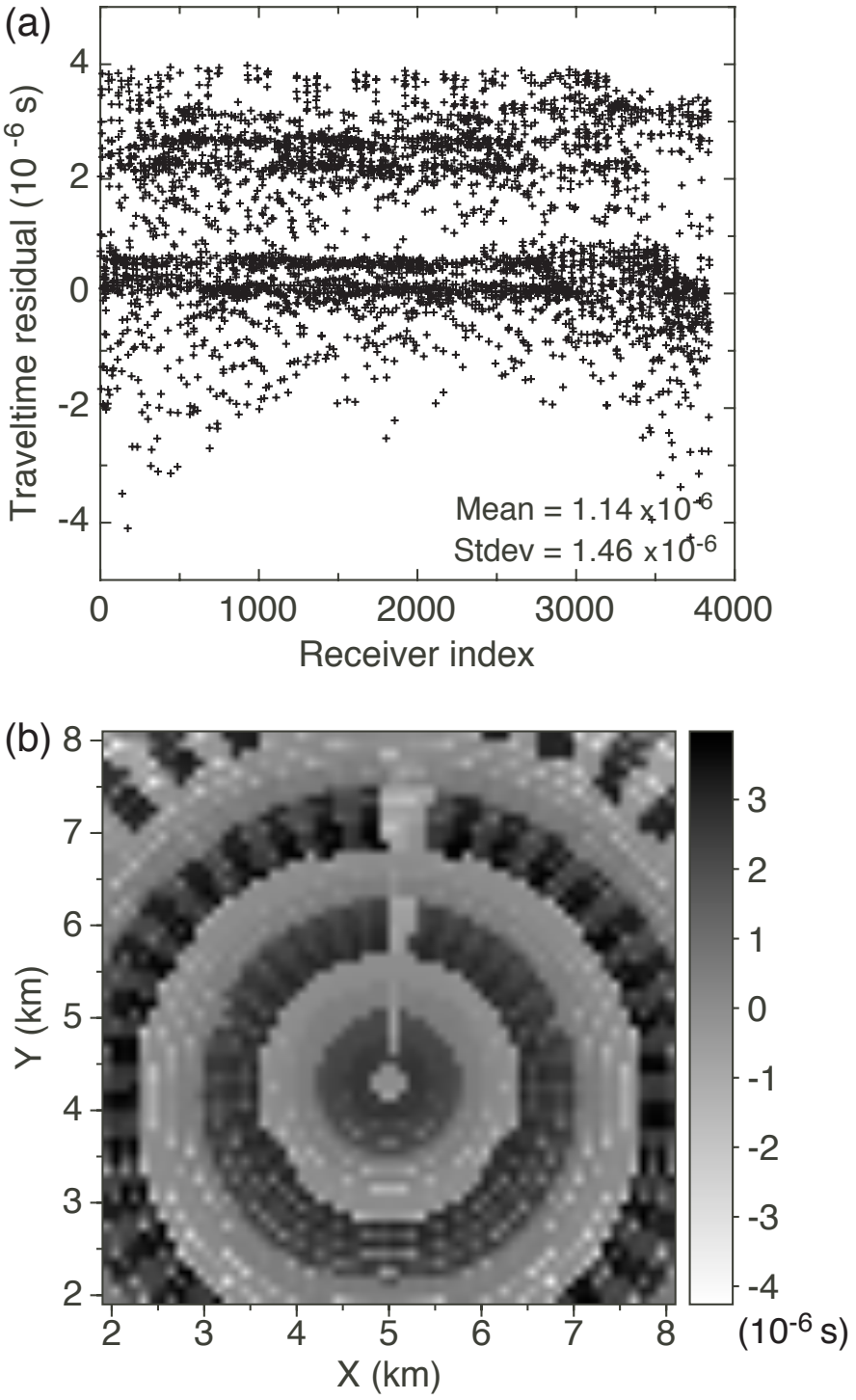

Fig. 3.10. Verification of reflected traveltimes in a two-region model with a tilted interface. (a) Traveltime residuals are plotted against the receiver indices. The residuals are bounded within $4.2\text{x}10^{-6}$ s. (b) Traveltime residuals are plotted in 2-D. The pattern of the residuals is similar to the shifted 2-D plot in the horizontal interface model.

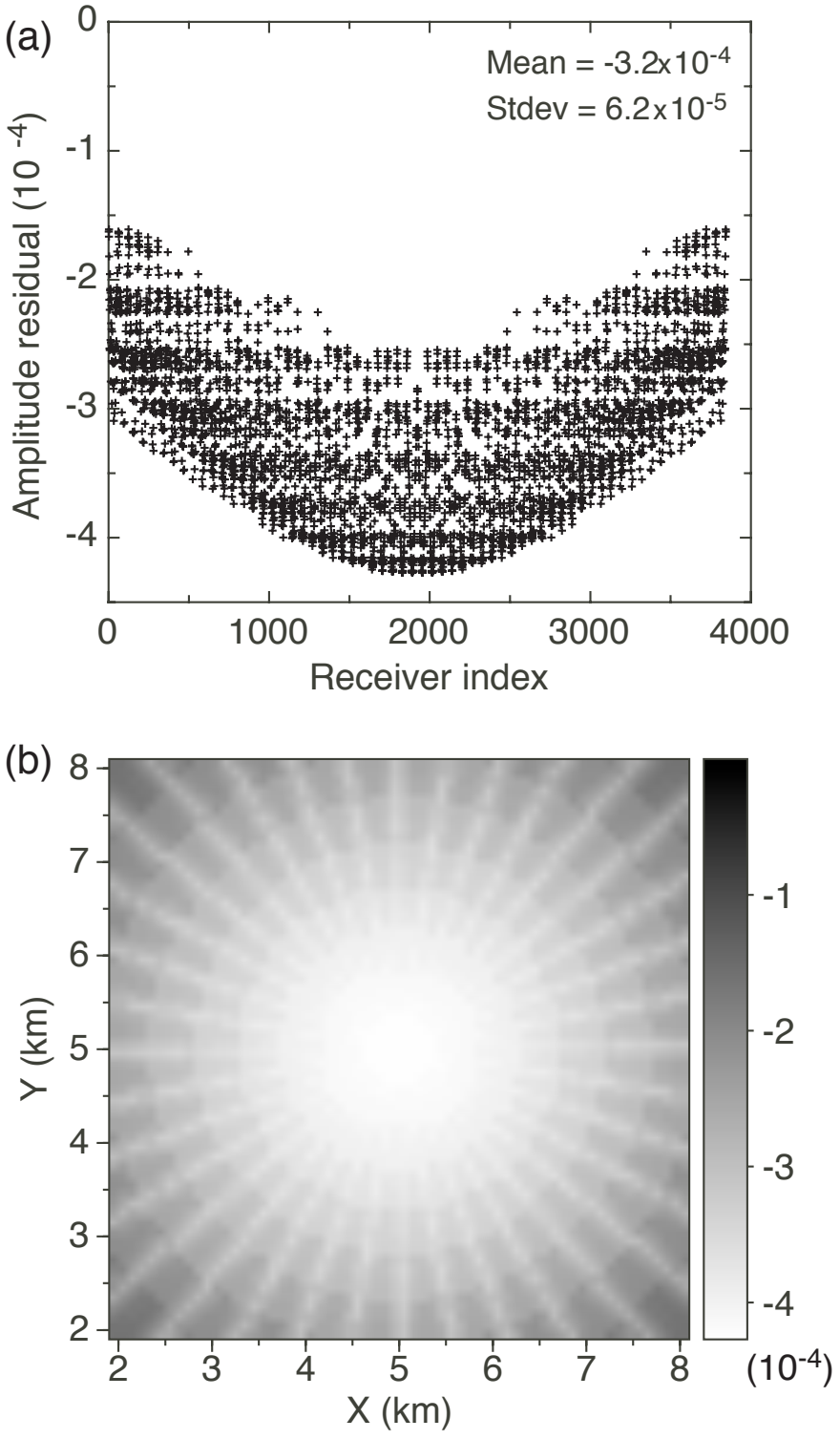

Fig. 3.11. Verification of reflection amplitudes in a two-region model with a horizontal interface. (a) Amplitude residuals are plotted against the receiver indices. The residuals are less than $4.5\text{x}10^{-4}$. (b) Amplitude residuals are plotted in 2-D.

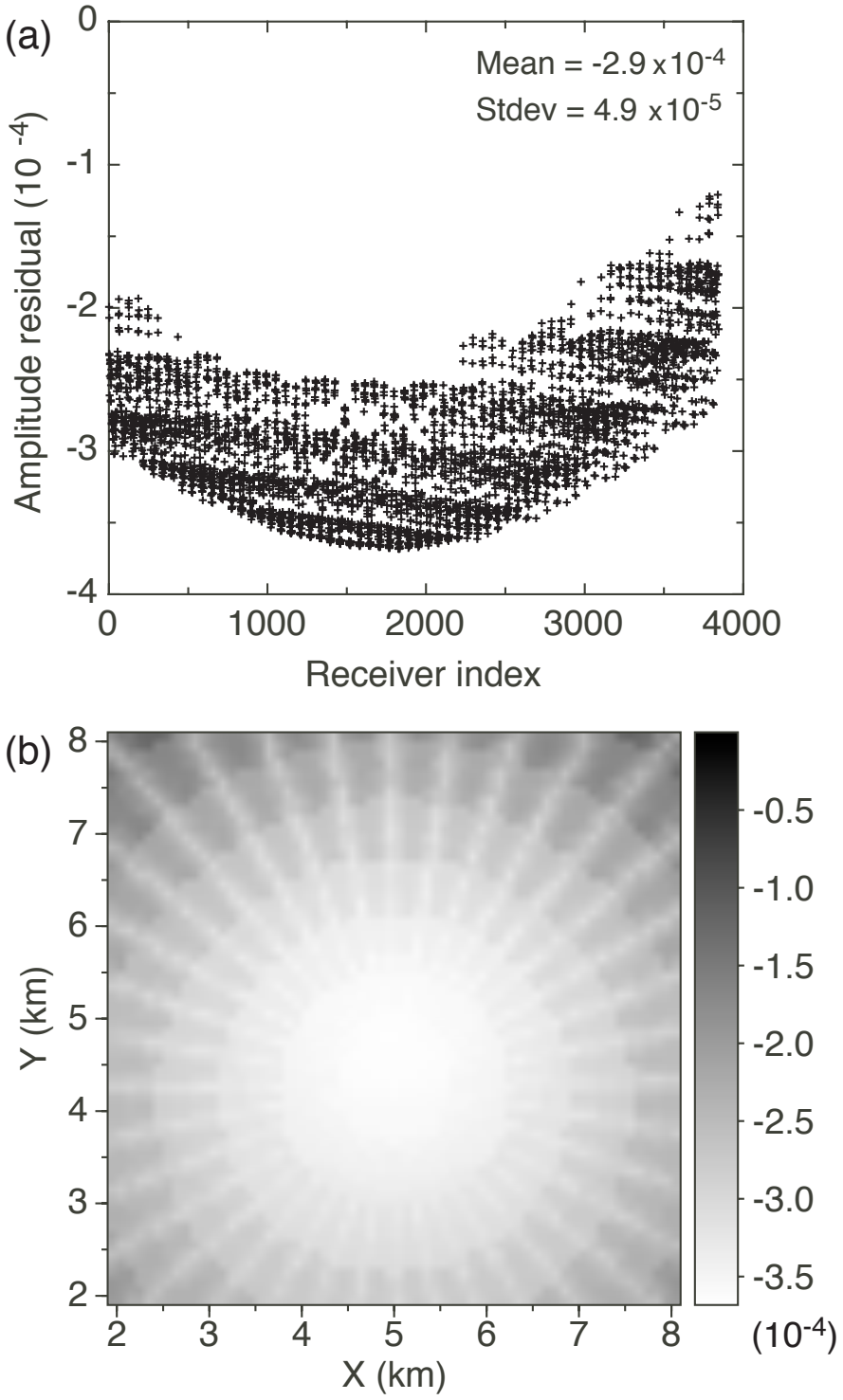

Fig. 3.12. Verification of reflection amplitudes in a two-region model with a tilted interface. (a) Amplitude residuals are plotted against the receiver indices. The residuals are less than $4\text{x}10^{-4}$. (b) Amplitude residuals are plotted in 2-D. The pattern of the residuals is similar to the shifted 2-D plot in the horizontal interface model.

Table 3.2. Velocities and densities of two layers in the simple interface model.

	Vp (km/s)	Vs (km/s)	$\rho\,(g/cm^3)$
Top layer	3.0	1.30	2.38
Bottom layer	2.86	1.27	2.33

accuracy of the propagator matrix method. Because the thin layer, a set of the central frequency at 10, 20, 40, and 60 Hz are applied to discuss the frequency dependence of the reflection coefficients.

3.5.1 Simple Interface Model

A simple interface model constructed by two isotropic layers is set for the comparison of P- wave reflection coefficients obtained by different methods. Table 3.2 gives the velocities and densities of two layers for this model, which have small contrasts of material properties.

We use Shuey's two-term and three-term approximation equations to compute the P- wave reflection coefficients. The Zeoppritz solution can be obtained by the propagator matrix method while setting the layer thickness to zero.

Also, we can use full waveform synthetic seismograms to verify the reflection coefficients. The amplitude attributes can be applied to estimate the reflection coefficients after correcting source and receiver effects and removing the geometric spreading in the seismograms. Because the source and receivers are in a homogeneous, isotropic layer, the correction factor for the radiation pattern of the source type is trivial (see Aki and Richards (2002) Equation 4.29 and Ben-menahem et al. (1991)). Since we use the vertical point force to generate synthetic seismograms, we have to remove the factor $\cos\theta$, where θ is the angle away from the vertical direction. It is also the takeoff angle here. For the receiver effect, because we take the vertical component to estimate the total reflection amplitude, we should recover it by multiplying the receiver correcting factor $\sec\phi$ to the vertical amplitude, where ϕ is the incident angle at the receivers. It is the same as θ because the reflector is horizontal. For the geometric spreading, because the medium is isotropic, amplitude is proportional to the recipro-

cal of distance and can be easily removed. After these three steps of correction, the reflection amplitude at the incident point on the interface can be recovered. Then the normal incident amplitude is normalized to the coefficient obtained by the propagator matrix method.

Figure 3.13 shows comparisons of the reflection coefficient as a function of incident angle for Shuey two-term, three-term approximation, Zeoppritz equation and full waveform synthetic seismograms in the simple interface model. The Zeoppritz results match full waveform synthetic seismograms very well. This suggests the coefficients generated by propagator matrix method are in good agreement with the amplitudes generated by discrete wavenumber method. Also, Figure 3.13a shows that Shuey's two-term approximation provides an accurate estimate, especially when the incident angle within 20°. The errors become noticeable when the incident angle is larger than 30°. The two-term approximation is widely applied in AVO analysis. This comparison suggests why the intercept-gradient plot is limited to the application with small incident angle. However, Shuey's three-term approximation produces reasonable errors even when the incident angle goes up to 50 degrees.

3.5.2 Thin Layer Embedded Model

Here we compute reflection coefficients for a thin layer embedded in a half-space model. In this case, when the layer thickness is close to the characteristic length, the layer thickness, in a thin layer embedded model, reflections from top and bottom interfaces interfere and result in a reflected signal that is not only a function of incident angle but also frequency. Figure 3.14 shows the source-receiver geometry and model parameters. A thin layer with 30 m thickness is inserted at the depth 1 km.

Figure 3.15 shows the P-wave reflection coefficient as a function of frequency and incident angle in a thin layer embedded model, and Figure 3.16 shows the P-wave reflection coefficient and its phase of the normal incident angle as a function of frequency in a thin layer embedded model. At about 47°, the superimposed reflections from top and bottom cancel out. In Figure 3.15, the frequency where this cancellation occures is moving to higher values as the incident angle increases.

In order to compare the reflection coefficient with the full waveform synthetic seismogram, the coefficient has to be convolved with the frequency spectrum of a source wavelet. Ricker wavelets with the central frequency 10, 20, 40, and 60 Hz and

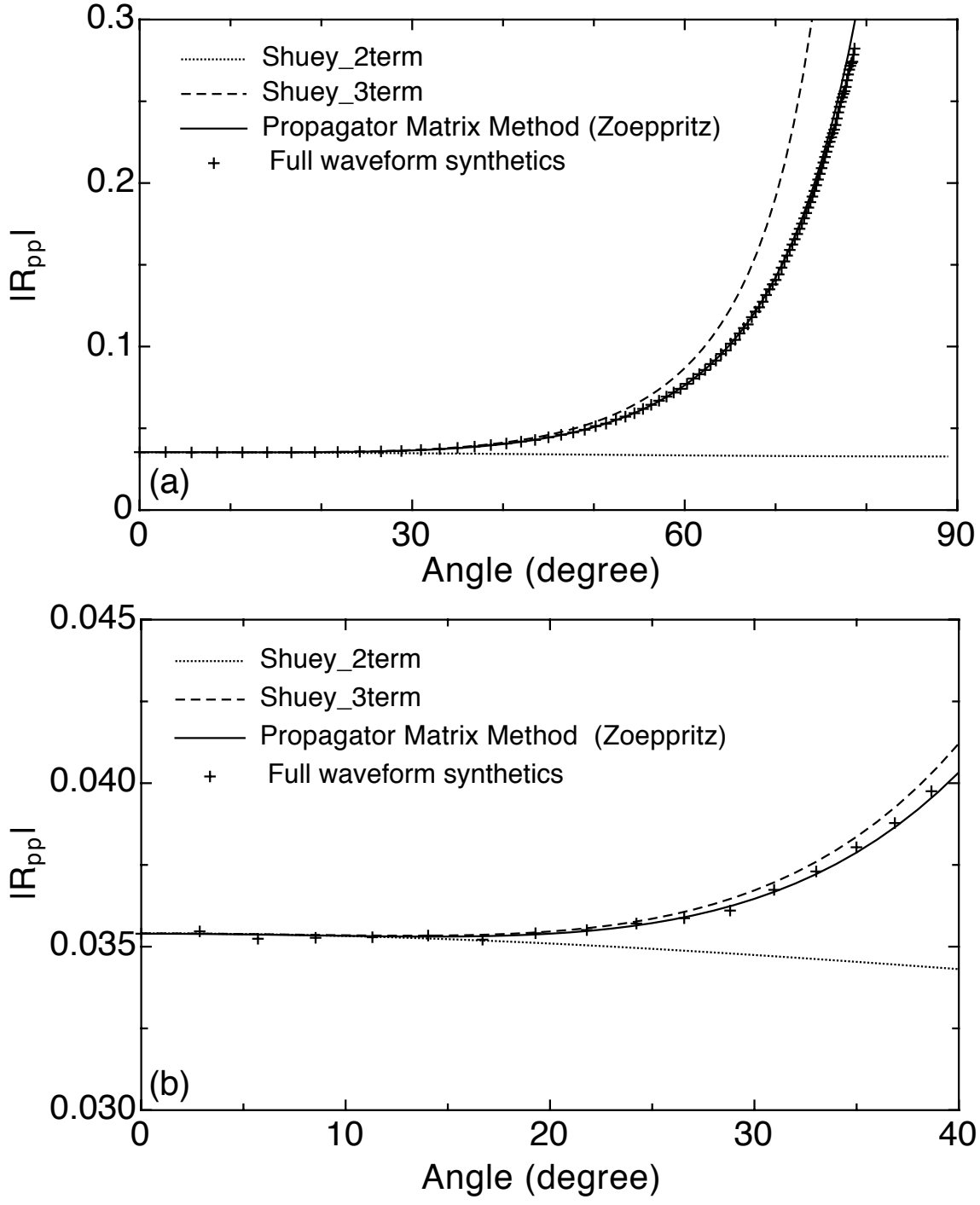

Fig. 3.13. (a) Comparison of P-wave reflection coefficients obtained from Sheuy's two term and three term approximation, Zeoppritz equation and full waveform synthetic seismograms. (b) While the incident angle is less than 20°, all these methods have very close reflection coefficients.

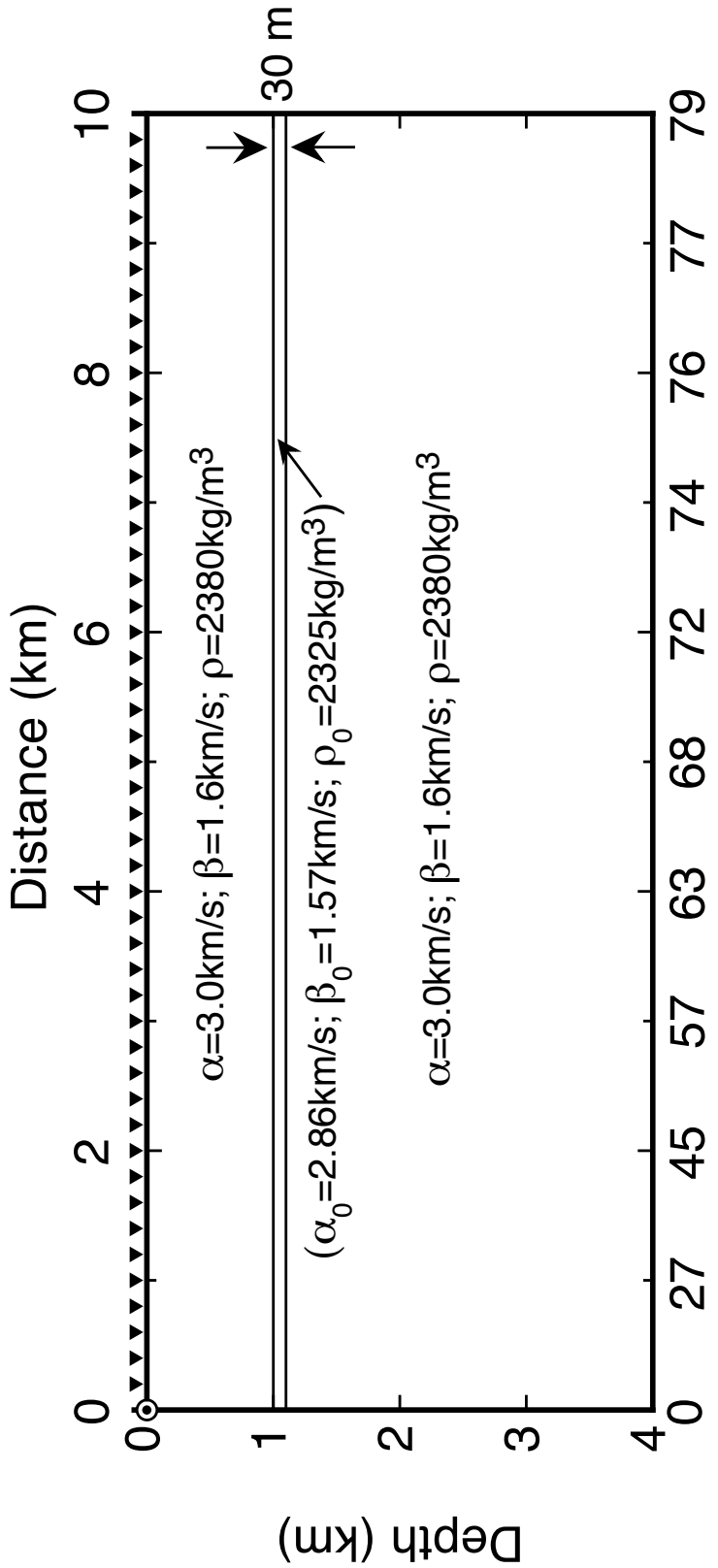

Fig. 3.14. Source-receiver geometry for verifying the reflection coefficients of a thin layer embedded model.

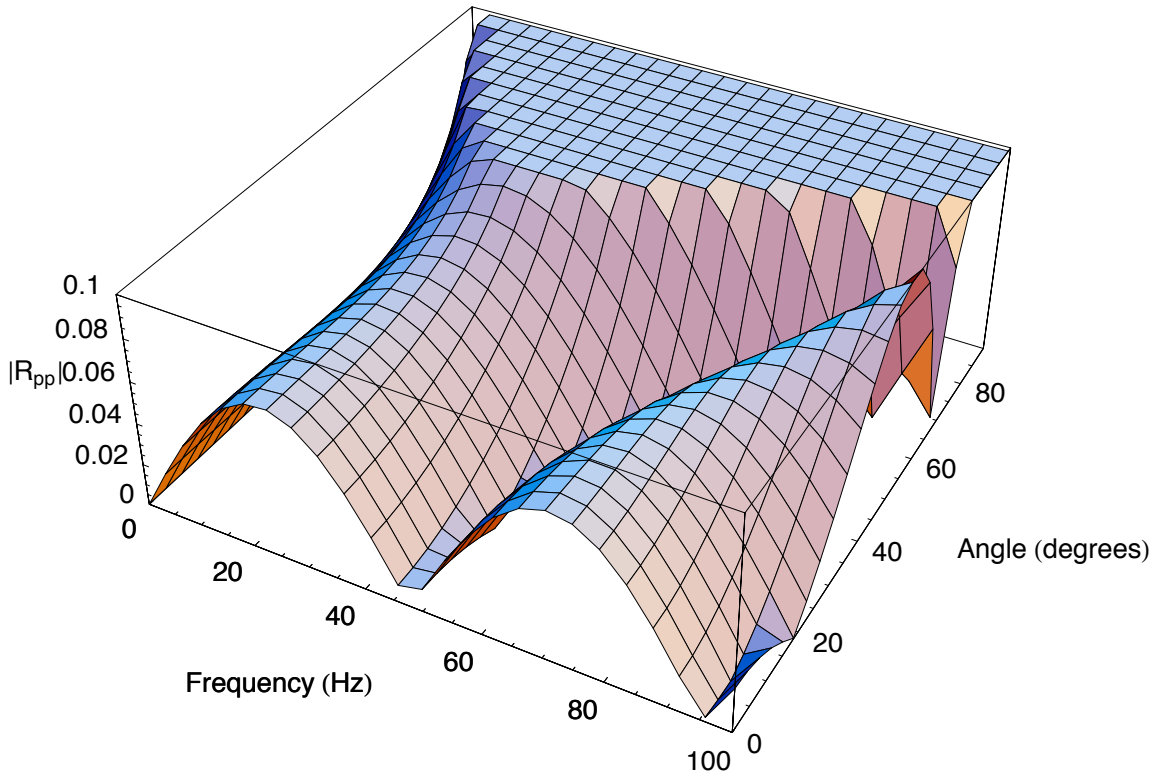

Fig. 3.15. P-wave reflection coefficient as a function of frequency and incident angle in a thin layer embedded model.

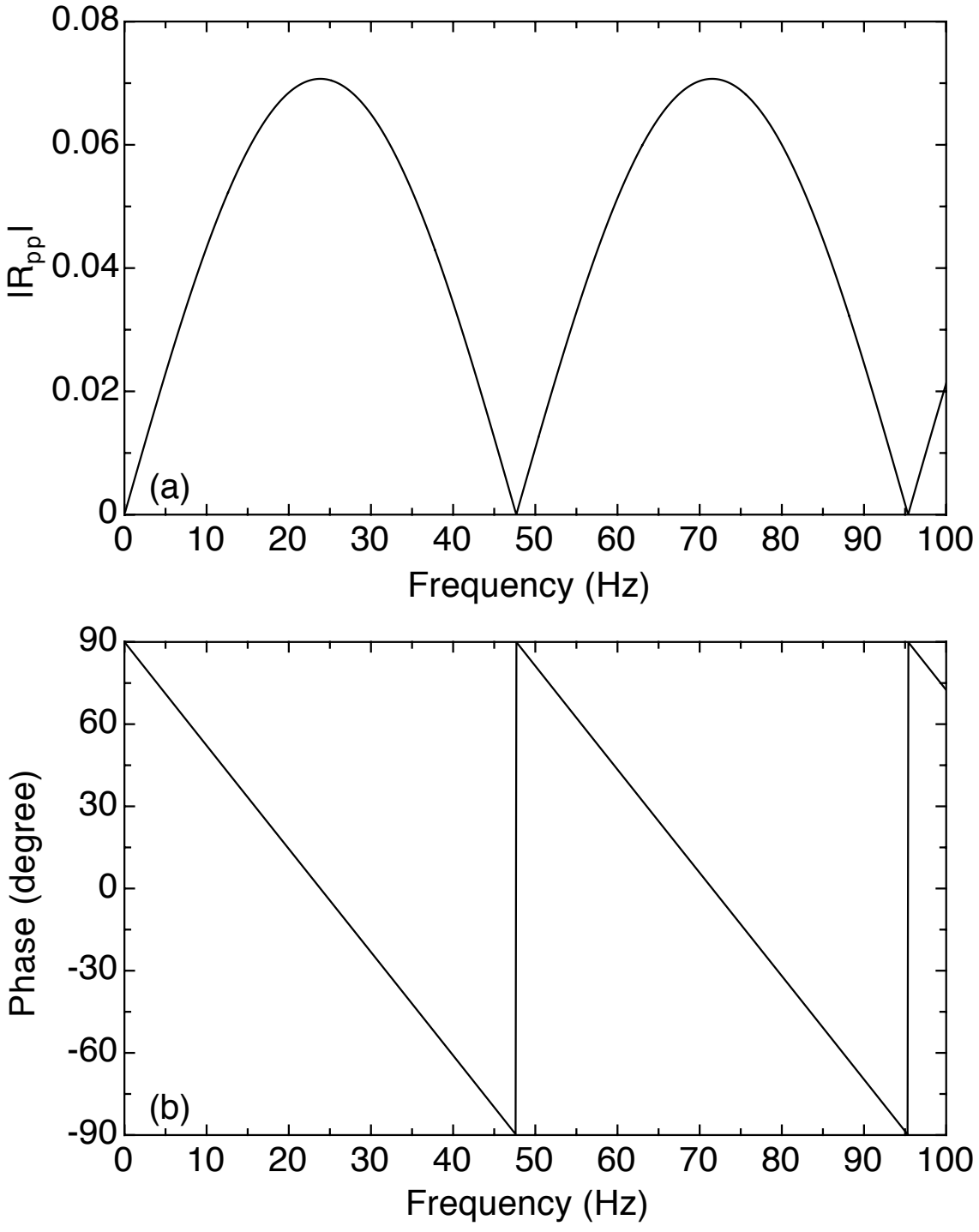

Fig. 3.16. (a) P-wave reflection coefficient of the normal incident angle as a function of frequency in a thin layer embedded model. Superimposed reflection from the top and bottom are totally canceled out around 47°. (b) Phase of reflection coefficient is also plotted.

their frequency spectra are demonstrated in Figure 3.17.

For simplicity, a table with the coefficient computed at 60 frequencies was computed, and values were then interpolated to estimate values at frequencies required to convolve with the corresponding source function, a Ricker wavelet, with an arbitrary frequency. The maximum frequency of the Ricker wavelet is three times the central frequency. The weighted reflection coefficient, which is the sum of all frequency components of the coefficient multiplied by the Ricker wavelet spectrum, can be compared with amplitudes of synthetic seismograms generated by the discrete wavenumber method. The operation of computing weighted reflection coefficient for a Ricker wavelet is given by

$$R_w(\theta) = \frac{\sum_{i=1}^{60} A_i R(f_i, \theta)}{\sum_{i=1}^{60} A_i}, \tag{3.15}$$

where $R_w(\theta)$ is the weighted reflection coefficient, A_i is the magnitude of a corresponding frequency in the amplitude spectrum (Figure 3.17b). $R(f_i, \theta)$ is the reflection coefficient of a corresponding frequency f_i at the incident angle θ in Figure 3.15. For example, in the 10 Hz case, the reflection coefficient at a certain angle θ is computed every 0.5 Hz from 0 to 30 Hz. Also, the weighted factor A_i is computed every 0.5 Hz from 0 to 30 Hz in the amplitude spectrum. Then the sum of weighted reflection coefficients for all frequencies can be used to compare to the amplitude attribute in the synthetic seismograms.

The reflection coefficients from synthetic seismograms are computed by the same method described in the previous simple interface model section. This operation is repeated for the Ricker wavelet with the central frequency at 10, 20, 40, and 60 Hz (Figure 3.18). For the lower frequency at 10 and 20 Hz, the comparison of coefficient demonstrates the propagator matrix results have a good agreement with full waveform synthetic seismograms. However, as the frequency increases, there are some noticeable differences, especially in the 60 Hz case. Figure 3.19 shows the seismic amplitude attribute (thick, red dashed line) is overlapped on synthetic seismogram in a thin layer embedded model for the Ricker wavelet with the central frequency at 60 Hz. Due to the thickness to wavelength ratio is high (6/9), the reflections from the top and bottom start to separated to two wave packs. This results the misfits in the comparison. A single value, the magnitude of the composite reflection coefficient, does not provide a valid measure of a single composed of two arrivals.

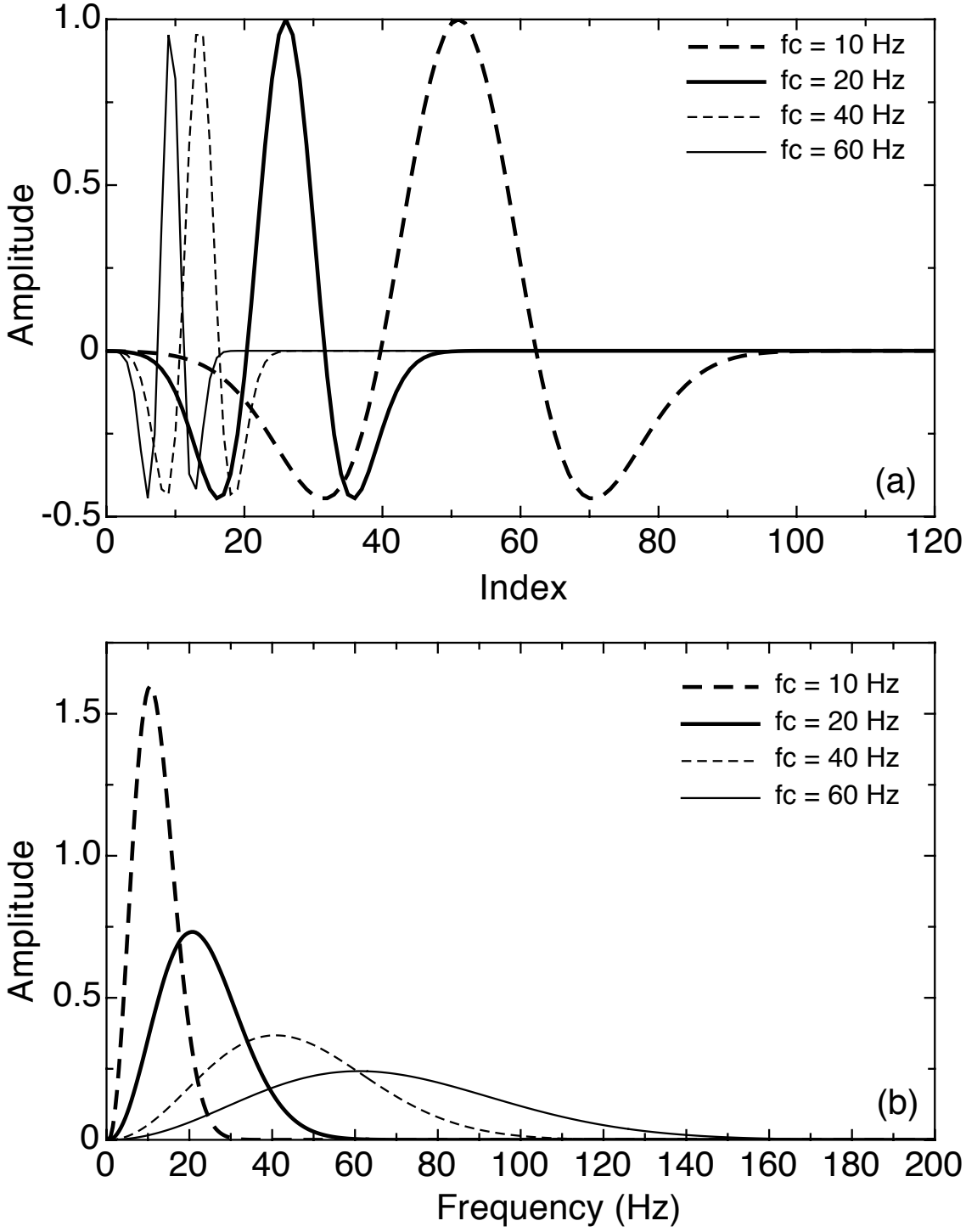

Fig. 3.17. (a) Ricker wavelets with the central frequency 10, 20, 40, and 60 Hz. (b) Frequency spectra of Ricker wavelets with the central frequency 10, 20, 40, and 60 Hz.

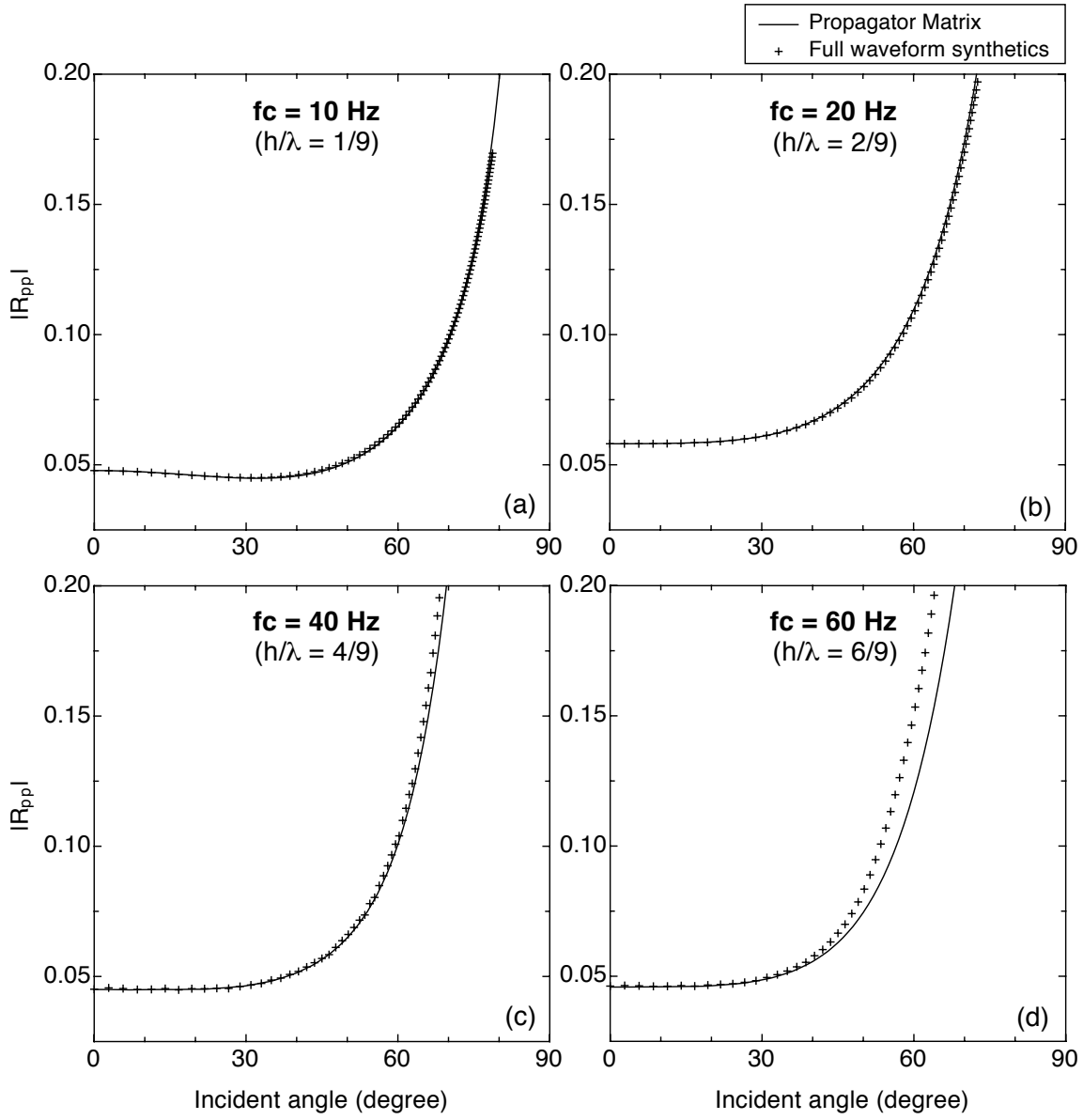

Fig. 3.18. Comparison of P- wave reflection coefficients between the propagator matrix method and full waveform synthetic seismograms in a thin layer embedded model for the Ricker source wavelet with the central frequency at 10, 20, 40, and 60 Hz are shown in (a), (b), (c), and (d), respectively.

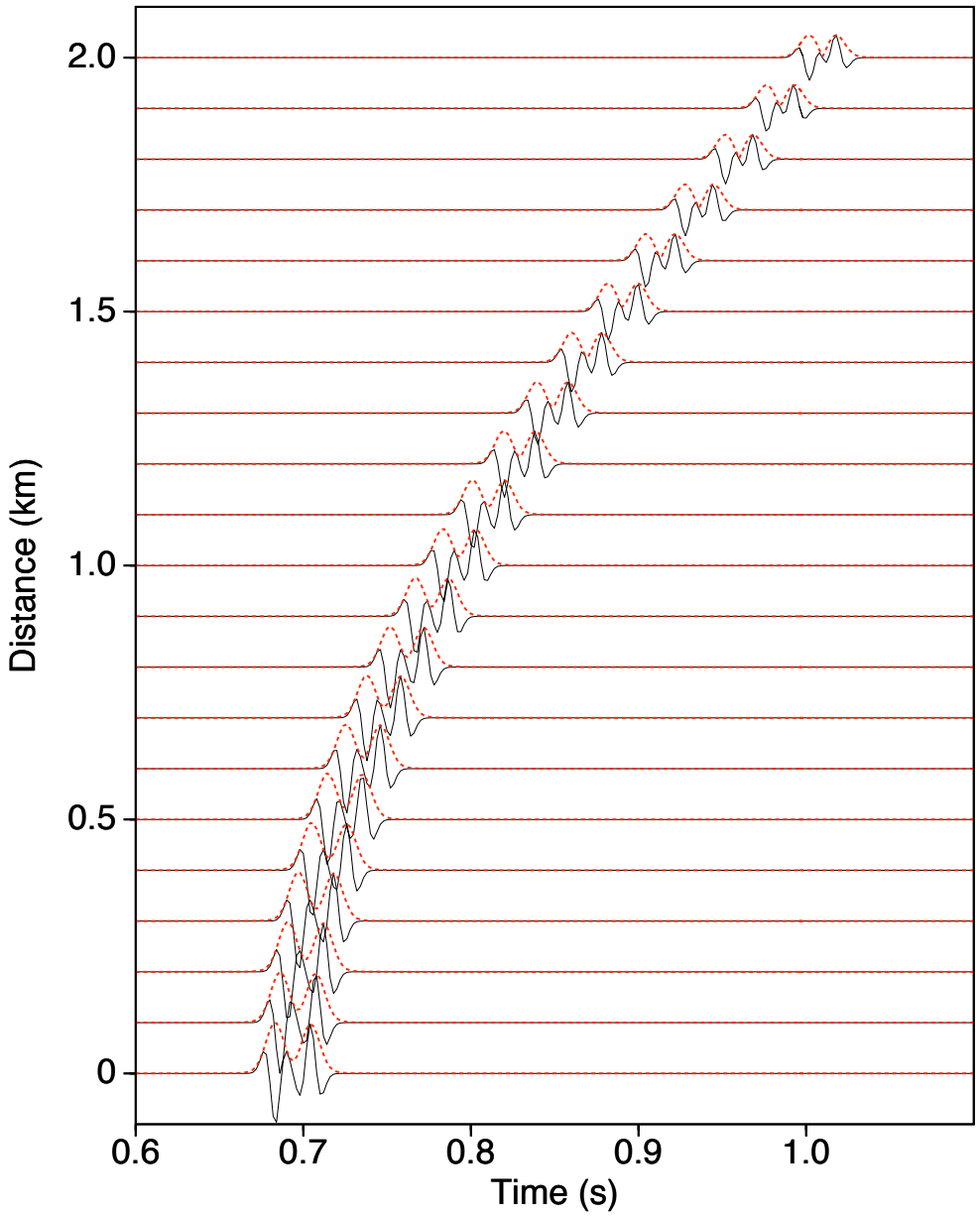

Fig. 3.19. Seismic amplitude attribute (thick, red dashed line) is overlapped on synthetic seismogram in a thin layer embedded model for the Ricker wavelet with the central frequency at 60 Hz.

3.5.3 Complex Stratified Reservoir Model — Application to the Field Data

In this section the well logs of a turbidite reservoir in the Ursa field, Gulf of Mexico will replace the thin layer in the previous model. The application to this complex stratified reservoir demonstrate the accuracy and robustness of the propagator matrix method.

Ursa field, Gulf of Mexico

Well logs in the Ursa field, Gulf of Mexico, are chosen to demonstrate the application to the field data. The Ursa field located in the Mississippi Canyon area of the east-central Gulf of Mexico (Figure 3.20) has abundant hydrocarbons in the reservoirs in the deep water. The field has multiple stacked reservoir horizons and several major reservoir intervals. Here, a 28.6m thick thin reservoir, located depth from 5866m to 5895m, is selected for seismic modeling. Figure 3.21 and 3.22 are the well logs nearby the 28.6 m reservoir. Also, all of the reservoirs in this well are available in Figure 4.6 and 4.7.

In this candidate reservoir, velocity, density and estimated porosity logs have strong internal fluctuation because the mixture of sand and shale beds. Shale beds usually have more condensed grain packing and show relatively lower porosity and higher density in well logs.

In order to generate the synthetic seismograms covering a wide range of the incident angle, a source-receiver geometry and model parameters are set up in Figure 3.23. A 28.6 m thick reservoir with the internal rock properties shown in Figure 3.23b and 3.23c is embedded in the half space model. The rock properties of the half space model are created from the averages of velocities and density from the non-hydrocarbon reservoir measurements near the candidate reservoir. The reservoir consists of 95 layers. Each layer is about 0.3 m in thickness.

Figure 3.24a demonstrates the verification of reflection traveltimes from the top of the complex stratified reservoir in the Figure 3.23a model. Traveltime errors are bounded within 10^{-5} s, where the predefined threshold for the ray interpolation is 1 ms. Also, the verification of reflection amplitudes from the top of the reservoir is presented in Figure 3.24b. Note these amplitudes do not include the reflection coefficients. Only the geometric spreading is considered in the computation. However,

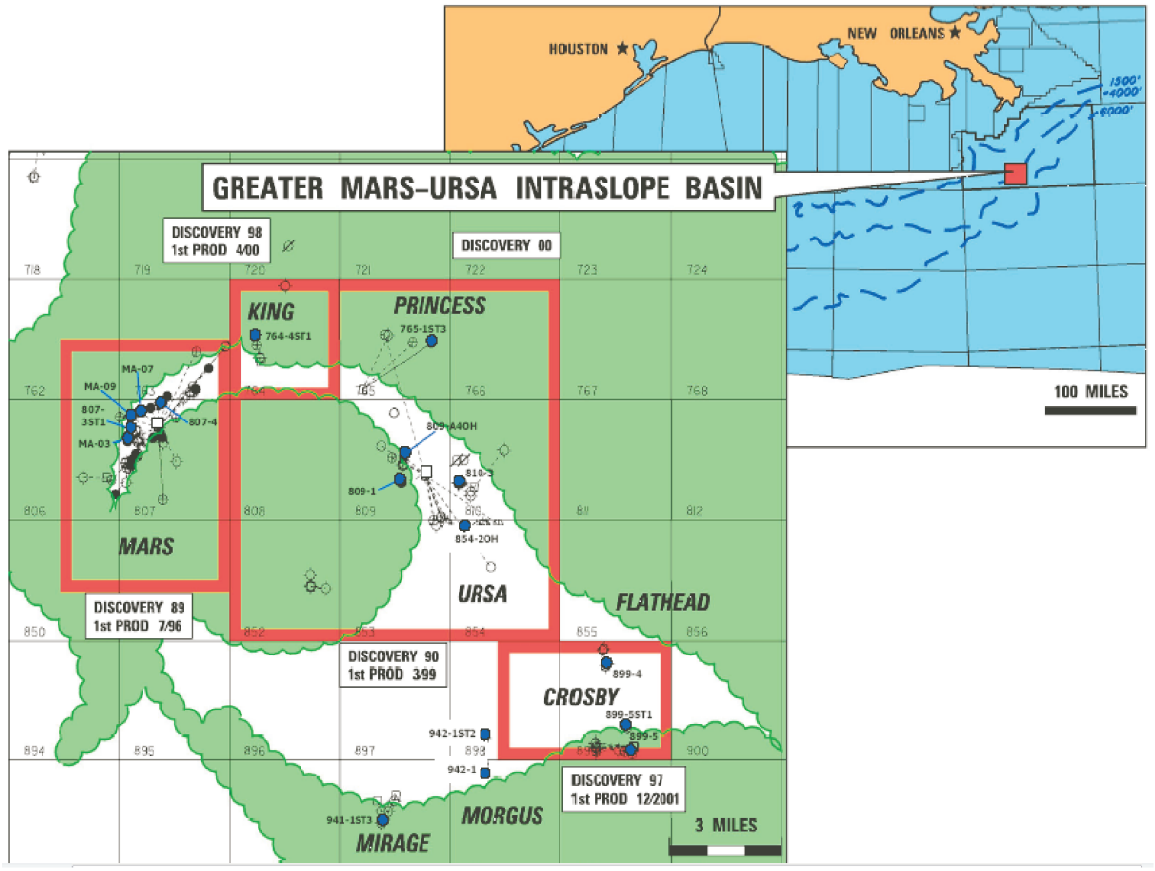

Fig. 3.20. Location map of the Mars-Ursa field. Green represents the areas affected by salt structures. White represents the areas unaffected (Meckel et al., 2002).

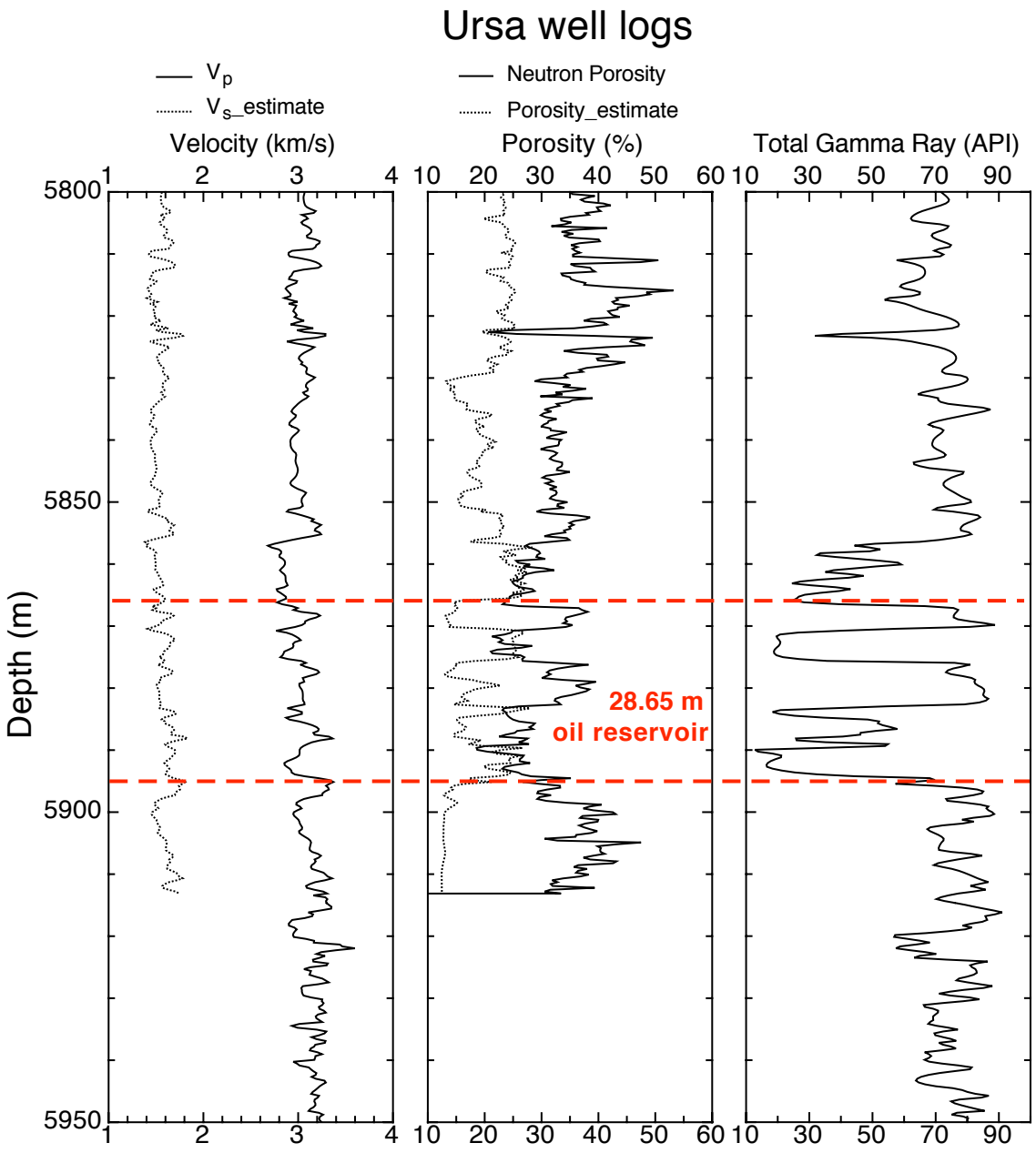

Fig. 3.21. Well logs of 28.6 m thick reservoir in Ursa field, Gulf of Mexico. The reservoir contains the mixture of layers in sand and shale.

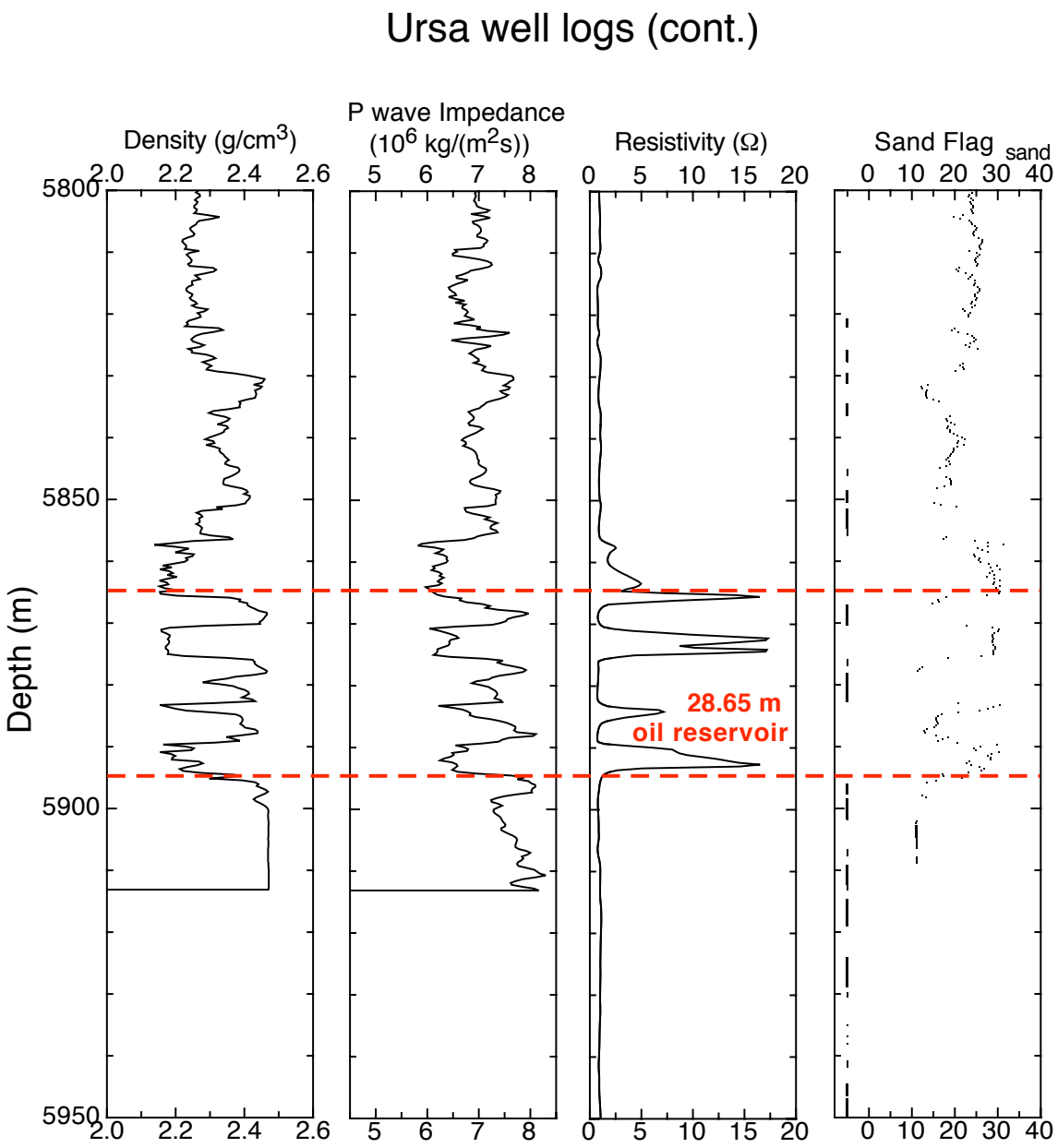

Fig. 3.22. Well logs of 28.6 m thick reservoir in Ursa field, Gulf of Mexico (continue).

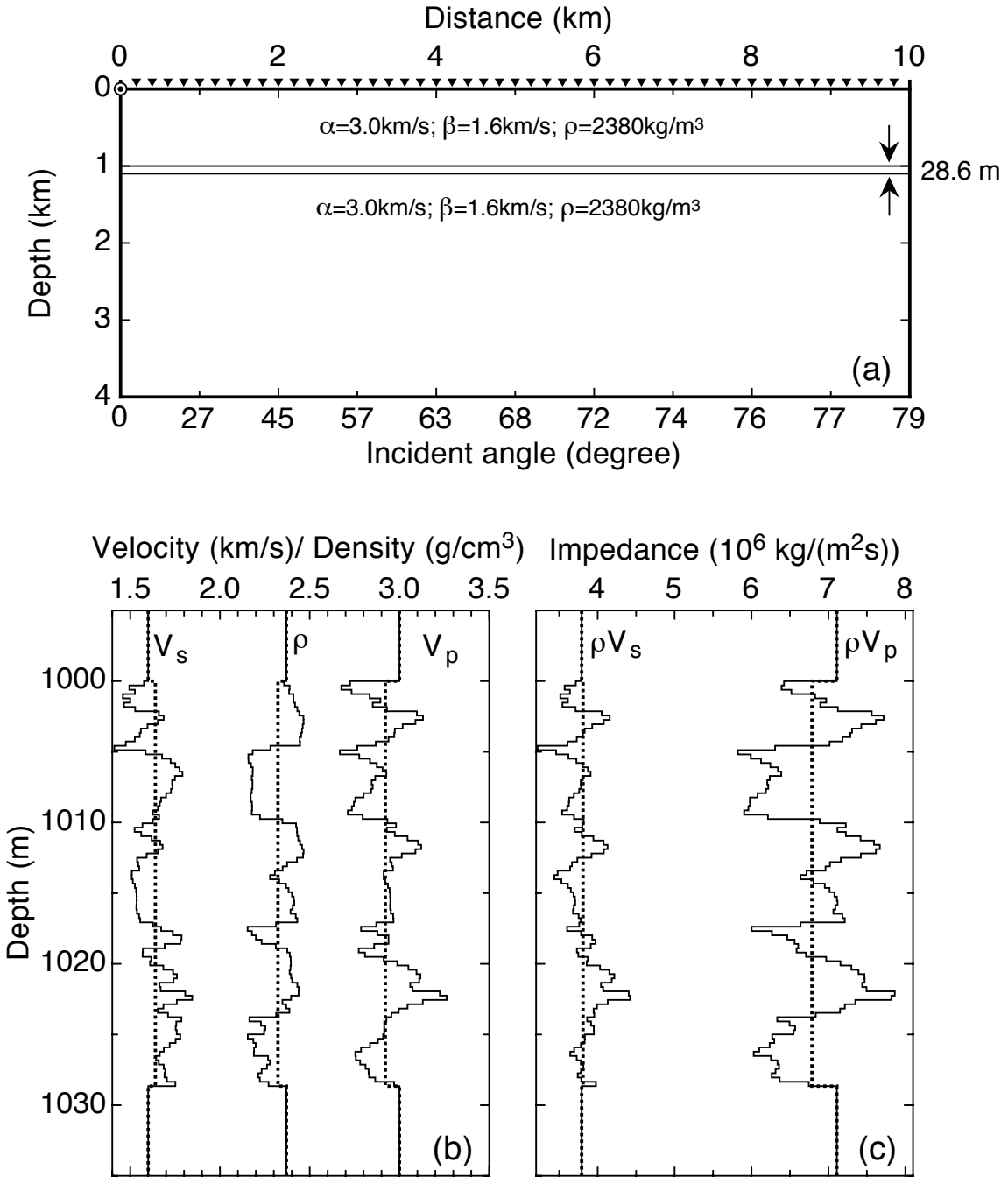

Fig. 3.23. (a) Source-receiver geometry for verifying composite reflection coefficient of a complex stratified reservoir model. (b) Reservoir model parameters extracted from well logs were inserted in a half space model. Dashed lines represent the velocities in the vertical direction in Backus-averaged results. (c) Elastic impedance for P- and S waves.

these amplitudes will be multiplied by complex composite reflection coefficients while generating synthetic seismograms.

Because the ray incident angle information are obtained from the nearest rays, the verification of incident angles shown in Figure 3.25 demonstrates that the errors of incident angles are negligible when applying them to get the corresponding reflection coefficients.

Figure 3.26 shows the composite reflection coefficient as a function of frequency and incident angle in a complex stratified reservoir model (Figure 3.23). Figure 3.27a shows composite reflection coefficient at normal incidence as a function of frequency in a complex stratified reservoir model. The phase is also plotted (Figure 3.27b). Due to the complexity of layering in the reservoir, a totally destructive amplitude is not obtained in this complex model, as was observed in a thin layer embedded model (Figure 3.16). However, a local minimum still suggests the reflections from the top and bottom interfaces and the internal thin layers are partially canceled out around the incident angle 42°. These internal complexity also results in stronger composite reflections while the frequency goes higher. The frequency dependence in such thin, complex reservoir leads to the complexity of reflection coefficients.

Again, we repeat the same procedure of comparing the composite reflections between using the propagator method and full waveform synthetic seismograms in the previous thin layer embedded model. Figure 3.28 demonstrates comparison of P wave reflection coefficients between the propagator matrix method and full waveform synthetic seismograms in a complex stratified reservoir model (Figure 3.23) for the Ricker source wavelet with the central frequency at 10, 20, 40, and 60 Hz, respectively. In the low frequency range, 10 and 20 Hz, two methods have very good agreement and show negligible difference. While the central frequency at 40 Hz, some noticeable errors are obtained for the incident angle after 30°. These misfits become larger when the central frequency goes to 60 Hz.

3.6 Validation – Synthetic Seismograms

Before combining the ray solutions with composite reflection coefficients into a complex Green's tensor, a table of the magnitude and phase for reflection coefficients are computed in a range of frequency and incident angle. The coefficients are computed at 60 frequencies which range from 0 Hz to three times of the source central frequency

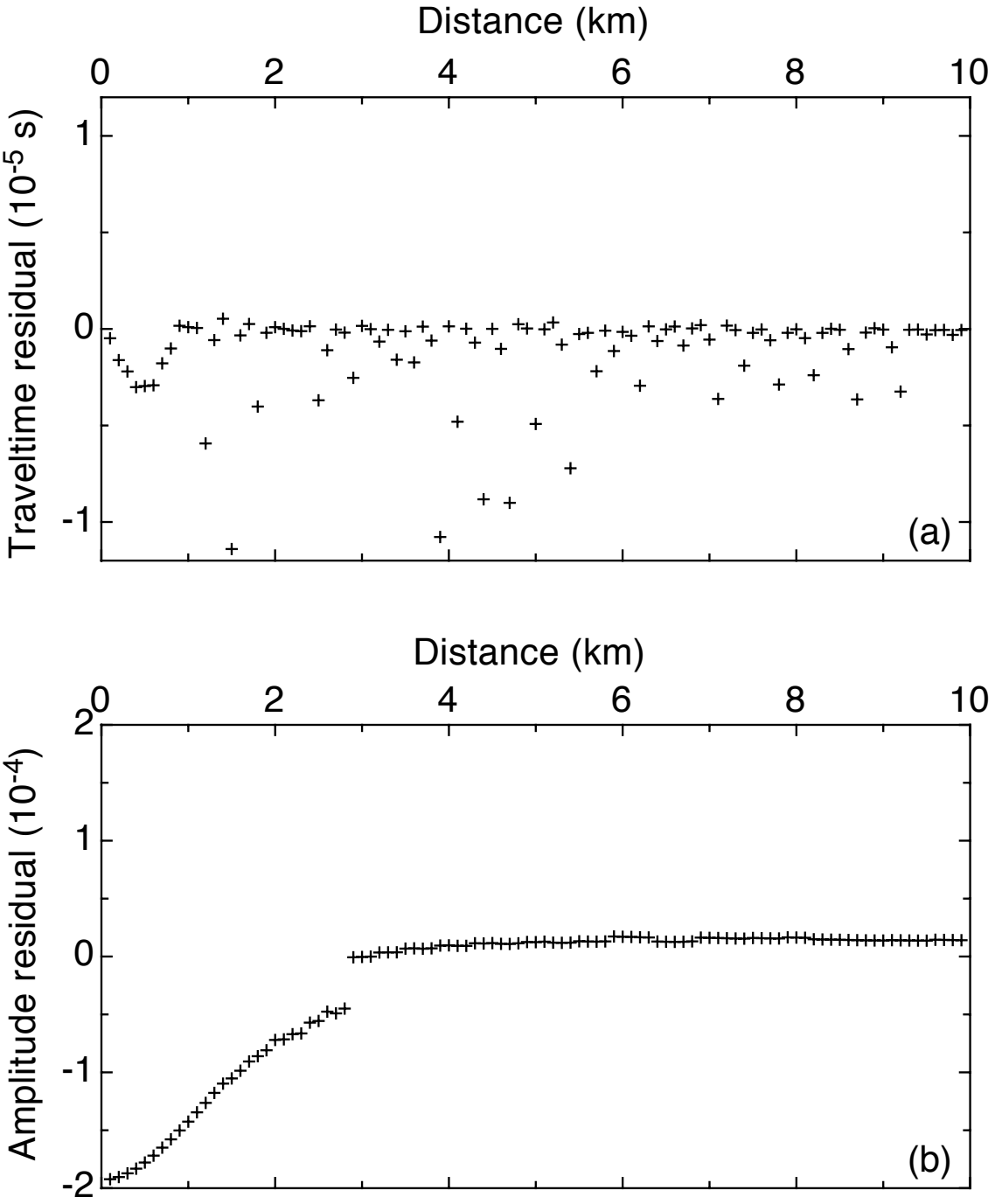

Fig. 3.24. (a) Verification of reflection traveltimes from the top of the complex stratified reservoir in the Figure 3.23a model. Errors are bounded within 10^{-5} s. (b) Verification of reflection amplitudes from the top of the reservoir.

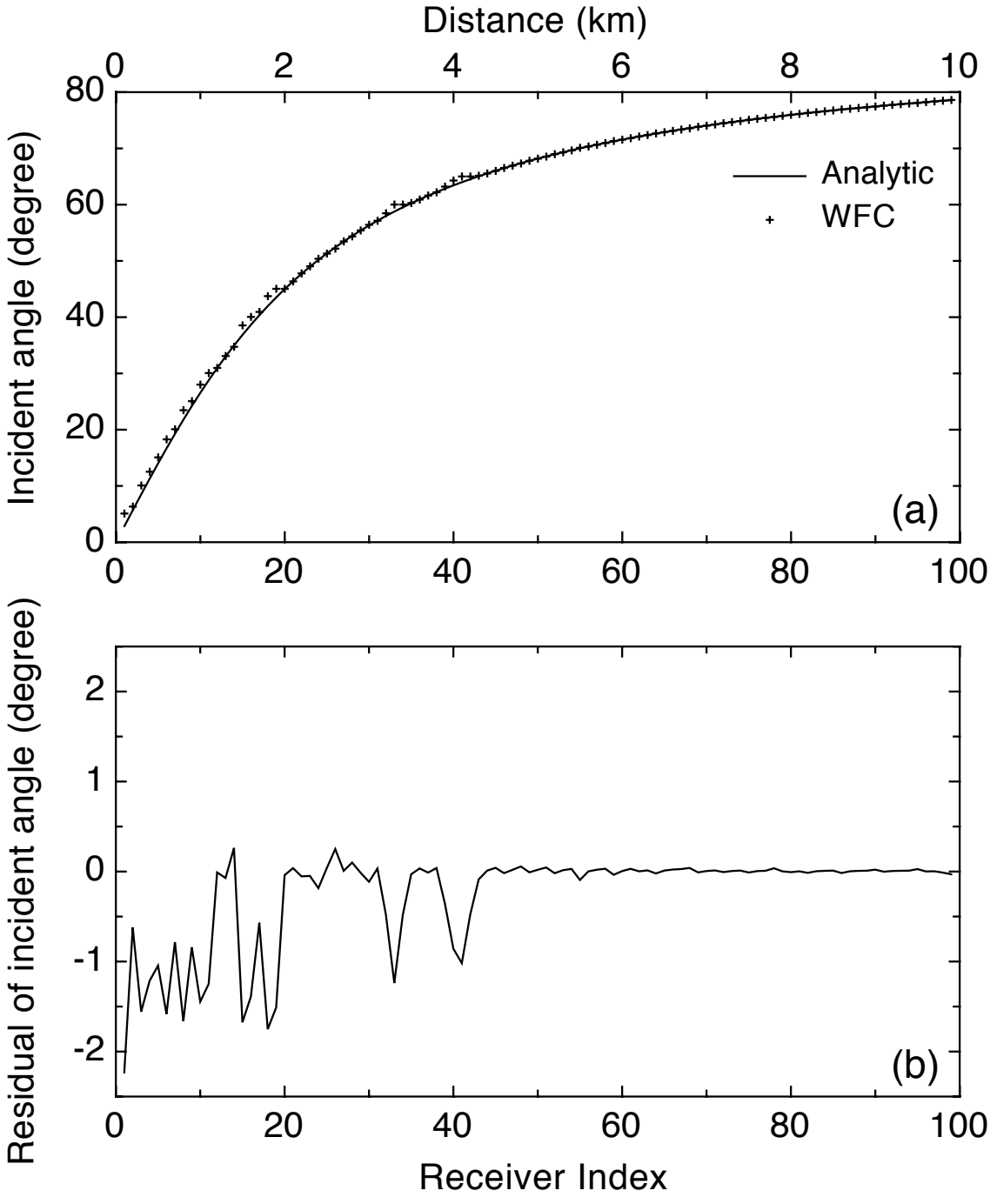

Fig. 3.25. (a) Incident angles obtained by the WFC method are plotted against with the analytic results in the Figure 3.23a model. (b) Verification of incident angles.

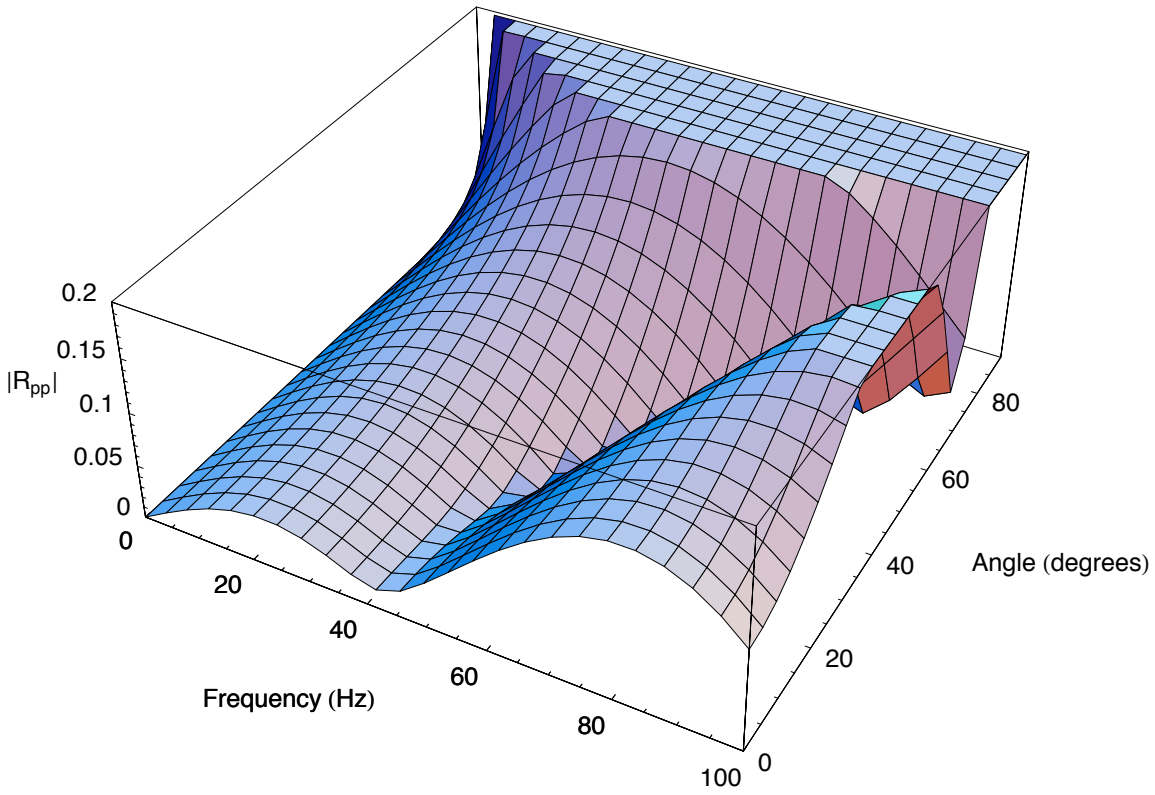

Fig. 3.26. Composite reflection coefficient as a function of frequency and incident angle in a complex stratified reservoir model (Figure 3.23).

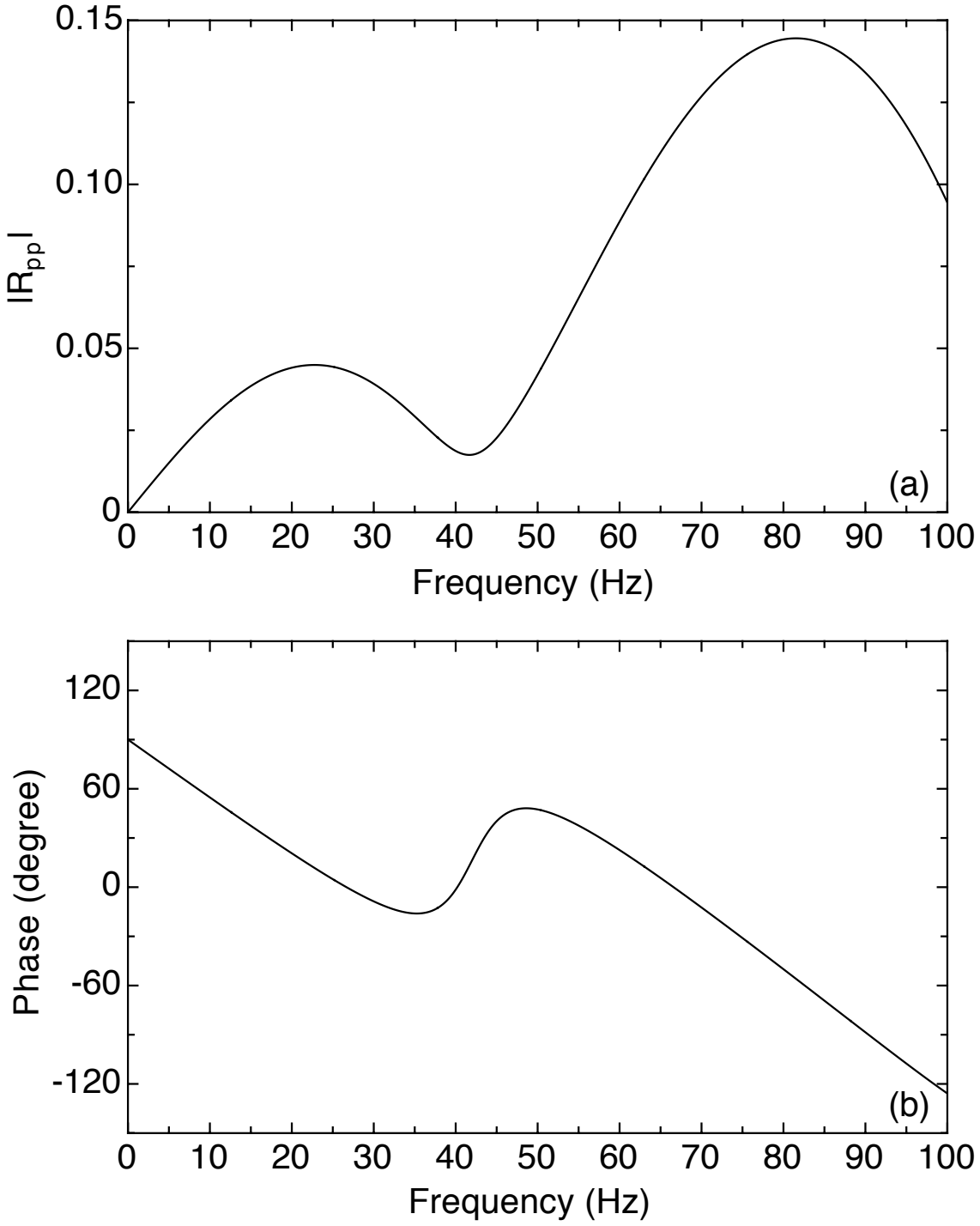

Fig. 3.27. (a) Reflection coefficient of the normal incident angle as a function of frequency in a complex stratified reservoir model. Due to the complex of layers in the reservoir, reflections from the internal thin layers are partially canceled out around the incident angle 42°. (b) Phases of reflection coefficients are also plotted.

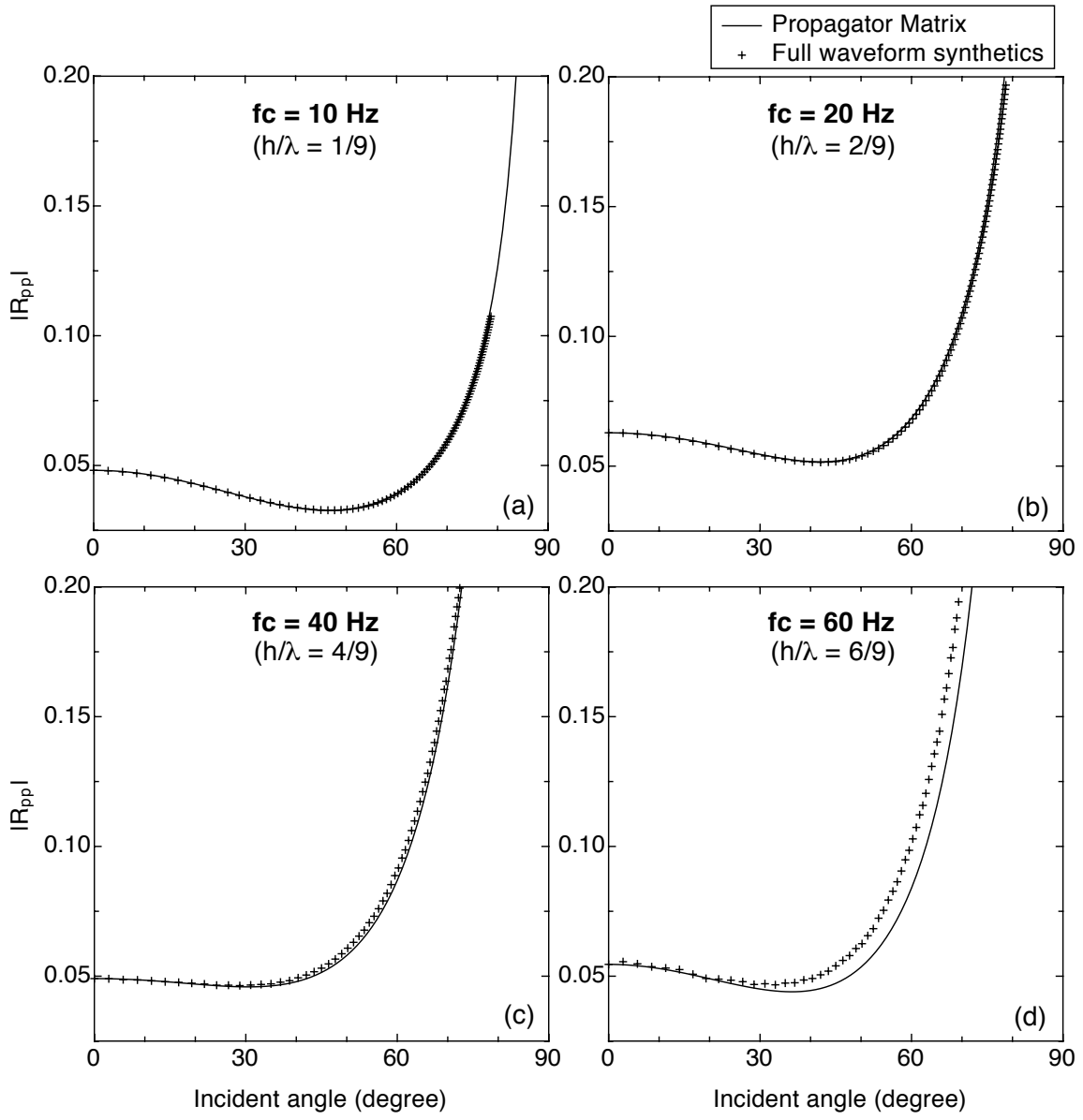

Fig. 3.28. Comparison of P wave reflection coefficients between the propagator matrix method and full waveform synthetic seismograms in a complex stratified reservoir model (Figure 3.23) for the Ricker source wavelet with the central frequency at 10, 20, 40, and 60 Hz are shown in (a), (b), (c), and (d), respectively.

of the Ricker wavelet. The incident angles are considered from 0° to 89° to cover the reflection modeling. Also, while generating synthetic seismograms, we carefully interpolate the reflection coefficients from the table of the coefficients and implement them in the corresponding traces.

3.6.1 Complex Stratified Reservoir Model

After verifying the traveltimes, amplitudes, incident angles and composite reflection coefficients, the ray data and the complex composite reflection coefficients are applied to generate synthetic seismograms. The results are compared with the complete solution synthetics seismogram obtained from the discrete wavenumber method with the central frequency 10, 20, 40, and 60 Hz. Vertical point force and Ricker wavelet are applied to generate vertical and radial component seismograms.

Figure 3.29 shows the comparison of synthetic seismograms for the radial component with the central frequency at 10 Hz between the discrete wavenumber method (black traces) and ray method (dashed red traces). Because only PP wave reflection coefficients are considered, there is no PS wave reflection in the ray results. The overlapped traces show the PP wave reflections from two methods are well-matched, not only in the near offset but also in the far offset. Figure 3.30 demonstrates the comparison result for the vertical component. Still, the comparison of results have a very good agreement. Here, the zoom-in plots for radial and vertical components in the near offset shown in Figure 3.31 demonstrate the detail of matched waveforms.

Figures 3.32, 3.33 and 3.34 are the comparison results for the central frequency at 20 Hz. Figures 3.35, 3.36 and 3.37 are the comparison results for the central frequency at 40 Hz. Figures 3.38, 3.39 and 3.40 are the comparison results for the central frequency at 60 Hz. All of them show excellent agreement of the P- wave reflections, even in the high frequency range. The ray data including composite reflection coefficients can generate the full solution synthetic seismograms of P- wave reflection from a complex stratified reservoir model.

At the low source frequency (10 and 20 Hz), the thickness to wavelength ratio is 1/9. The wavelength is too long to detect the thin layer stack and its internal fluctuation. Therefore, the waveforms in Figures 3.31 and 3.34 still go smoothly and show the results similar to the modeling in a simple interface half-space model. However, while the source frequency goes higher (60 Hz, Figure 3.40), the smaller

seismic wavelength can differentiate the reflections from top and bottom interfaces and show the layering of the internal fluctuation in term of the blocky waveforms .

3.6.2 Tilted, Complex Stratified Reservoir Model

Since the reflection coefficient is a function of frequency and incident angle, the hybrid ray-propagator matrix approach can generate synthetic seismograms for the tilted, complex stratified reservoir models, which is a typical and very important reservoir geometry near a salt structure.

Figure 3.41 shows the source-receiver geometry for generating synthetic seismograms in a half space model with a tilted, complex stratified thin reservoir. The thin layer stack is titled with an angle of 5.7°. With the same table of coefficient, we just need to run WFC modeling for the heterogeneous model then generate its synthetic seismograms quickly. The verification of reflection traveltimes and amplitudes from the top of the reservoir is shown in Figure 3.42, and the verification of incident angles is presented in Figure 3.43. They all show that the ray method produces accurate data for generating synthetic seismograms in the tilted reservoir model. Figure 3.44 demonstrates synthetic seismograms in the radial component, generated from the Figure 3.41 model with the central frequency at 10 Hz. Figure 3.45 is for the vertical component. Because the full waveform synthetic seismogram for this tilted model is not available, only the ray synthetic seismograms are shown.

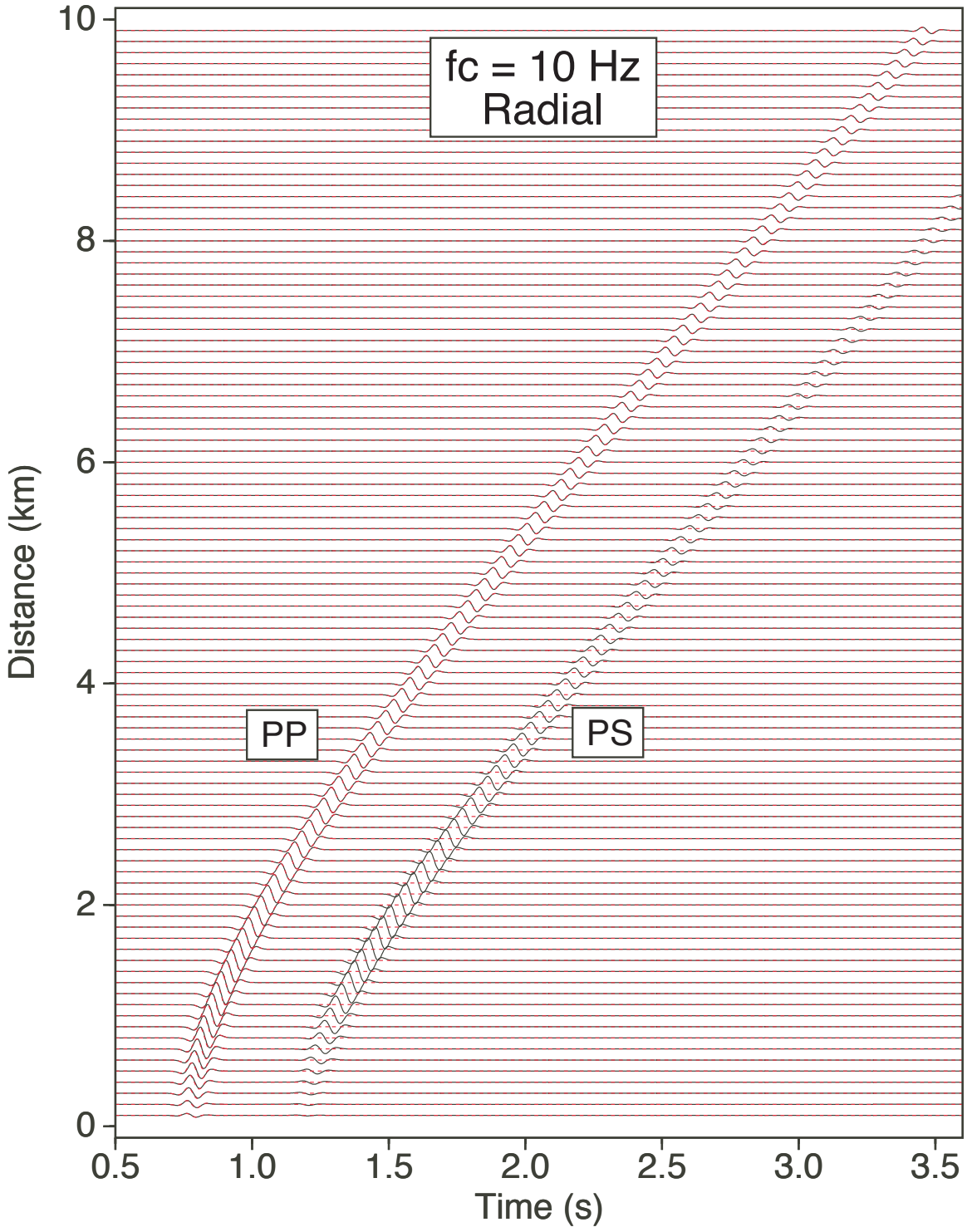

Fig. 3.29. Comparison of synthetic seismograms for the radial component with the central frequency 10 Hz between the discrete wavenumber method (black traces) and ray data including composite reflection coefficient method (dashed red traces).

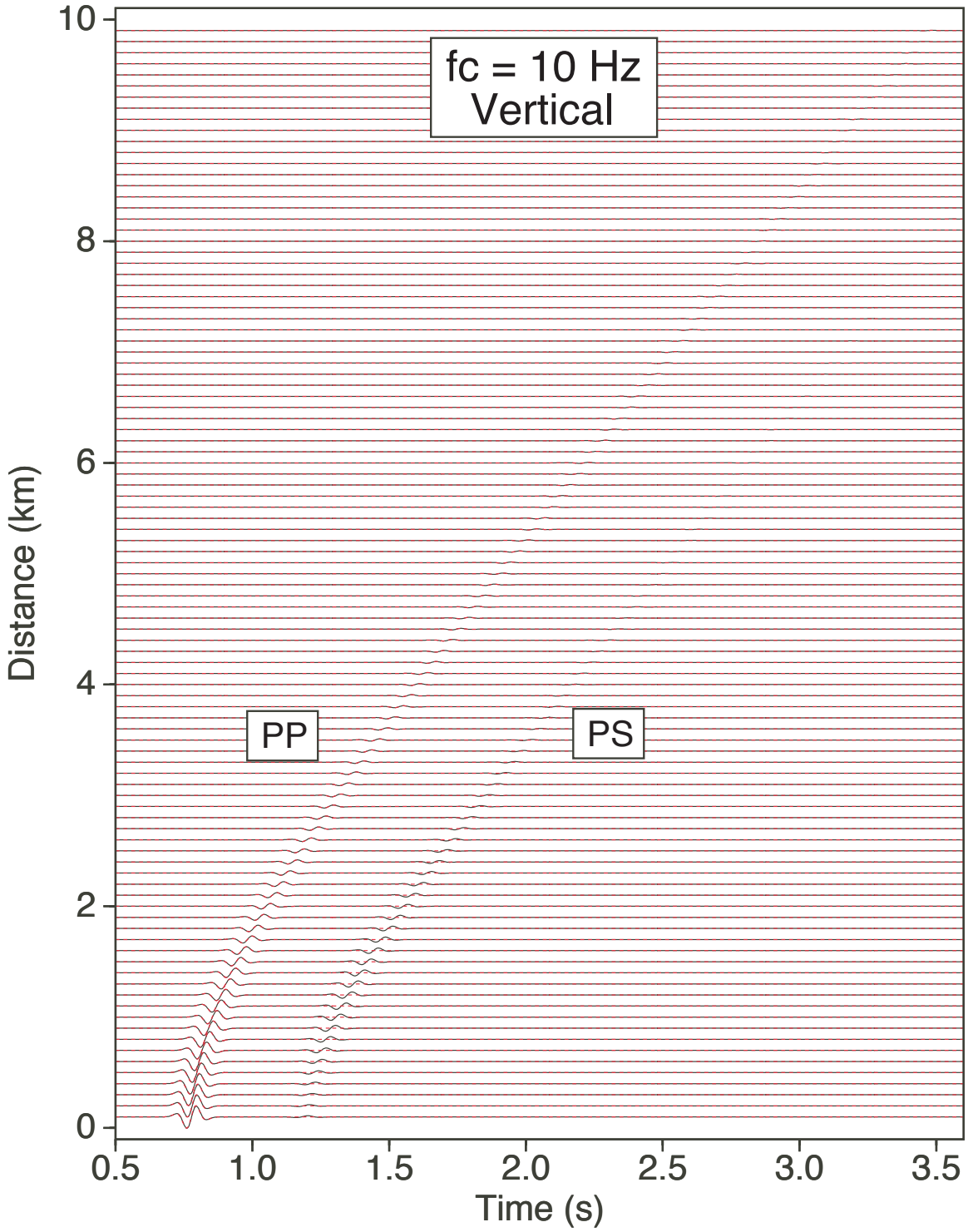

Fig. 3.30. Comparison of synthetic seismograms for the vertical component with the central frequency 10 Hz between the discrete wavenumber method (black traces) and ray data including composite reflection coefficient method (dashed red traces).

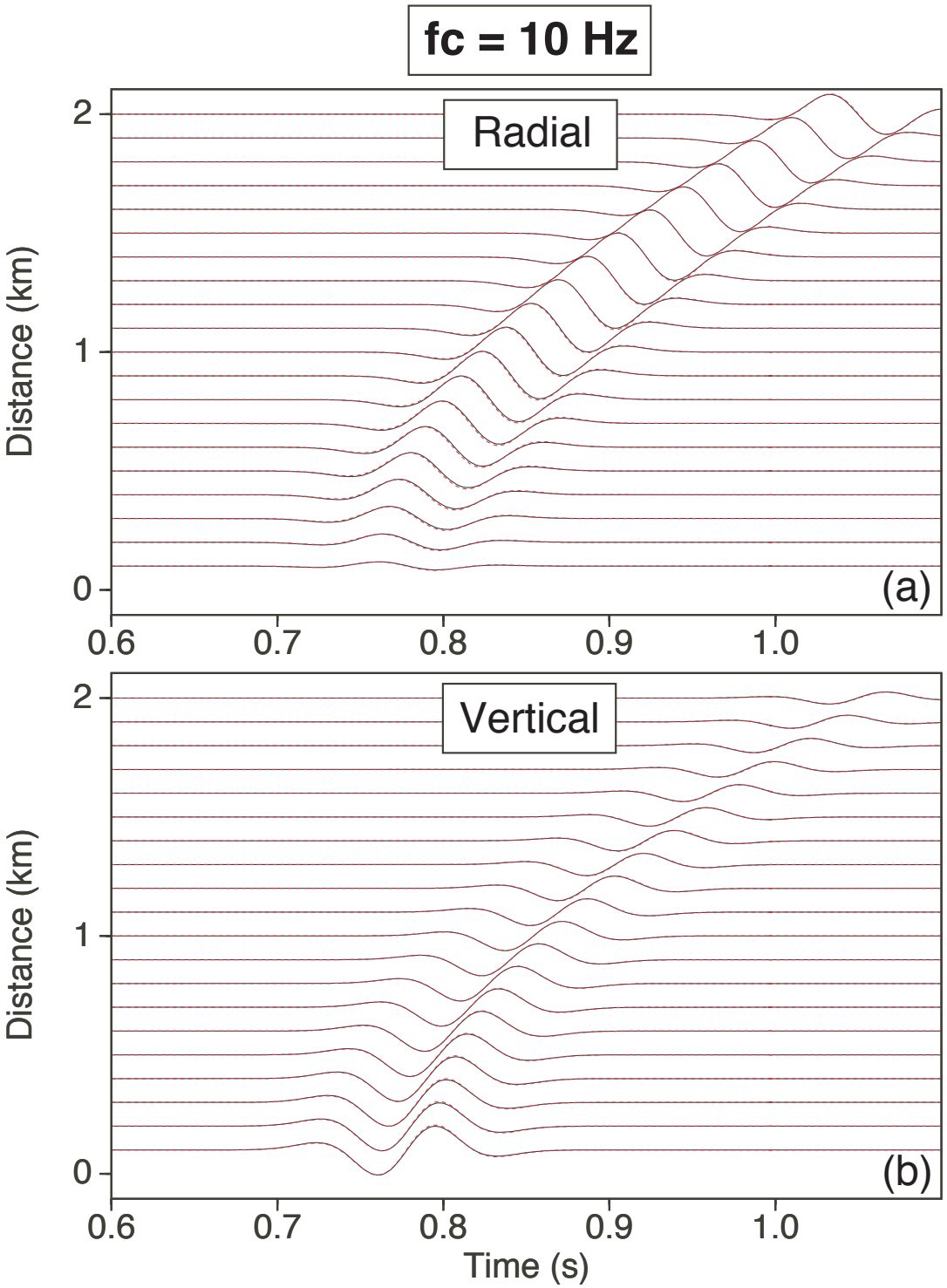

Fig. 3.31. Zoom-in comparison of synthetic seismograms for the central frequency 10 Hz between the discrete wavenumber method (black traces) and ray data including composite reflection coefficient method (dashed red traces). (a) and (b) are for the radial and vertical component, respectively.

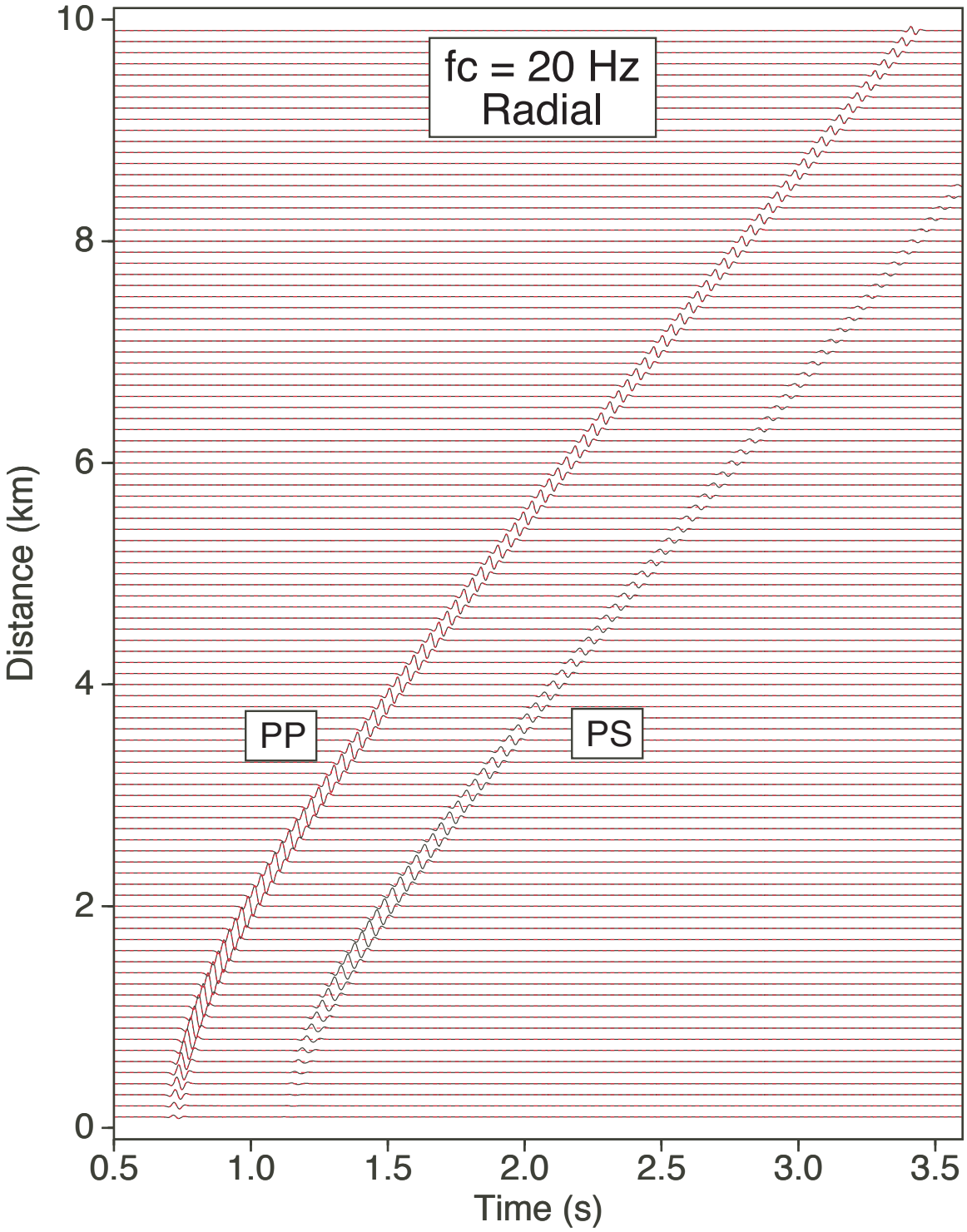

Fig. 3.32. Comparison of synthetic seismograms for the radial component with the central frequency 20 Hz between the discrete wavenumber method (black traces) and ray data including composite reflection coefficient method (dashed red traces).

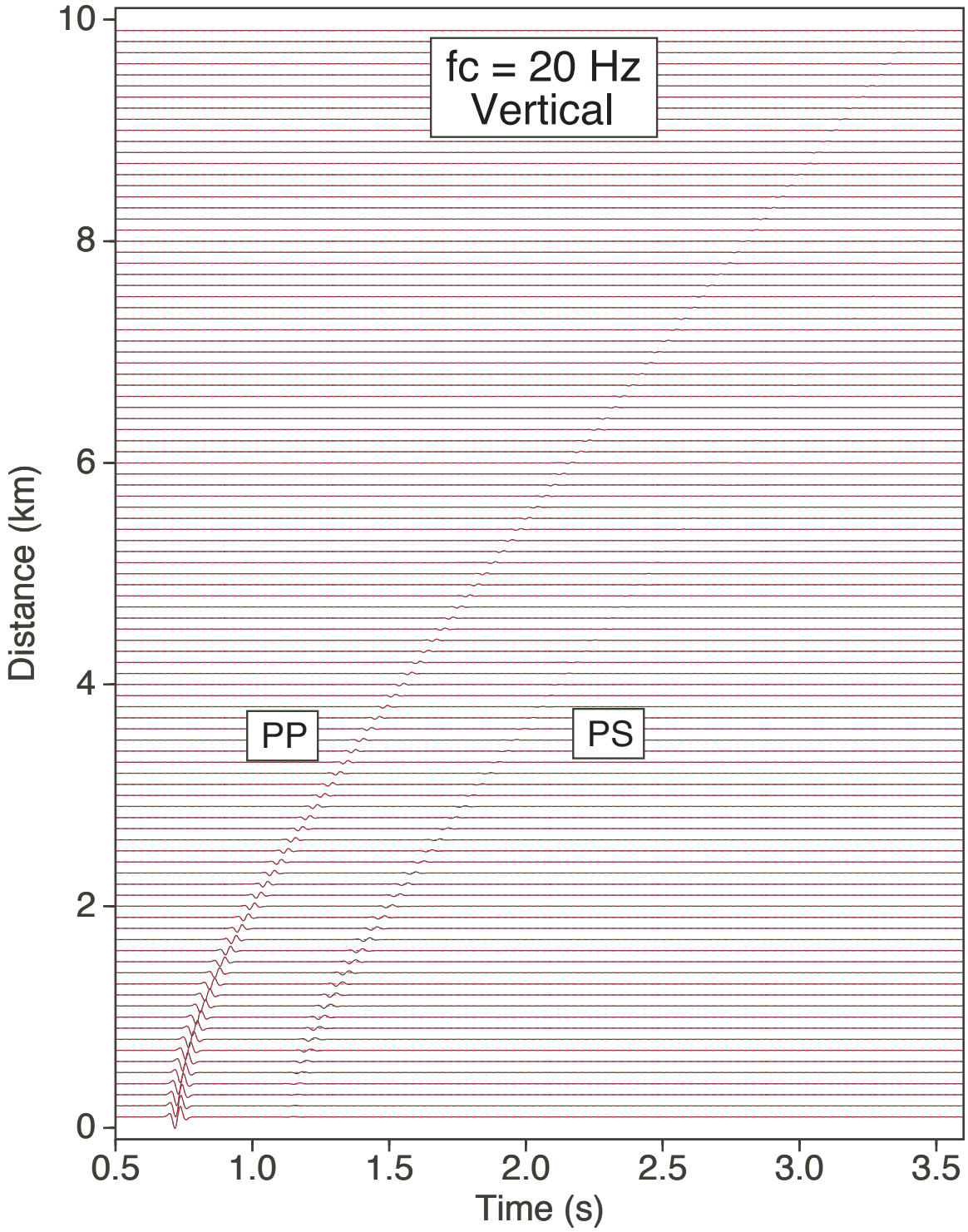

Fig. 3.33. Comparison of synthetic seismograms for the vertical component with the central frequency 20 Hz between the discrete wavenumber method (black traces) and ray data including composite reflection coefficient method (dashed red traces).

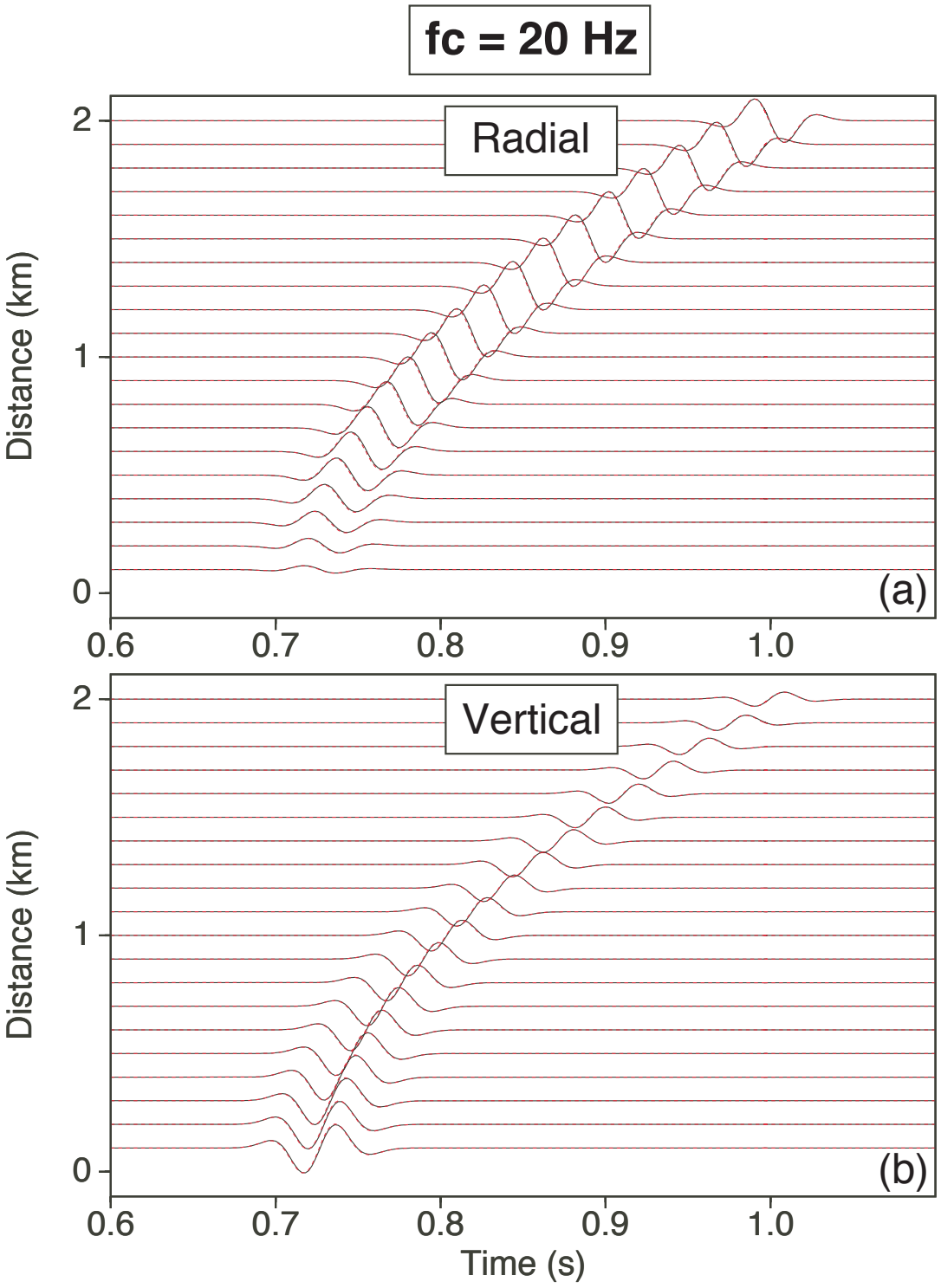

Fig. 3.34. Zoom-in comparison of synthetic seismograms for the central frequency 20 Hz between the discrete wavenumber method (black traces) and ray data including composite reflection coefficient method (dashed red traces). (a) and (b) are for the radial and vertical component, respectively.

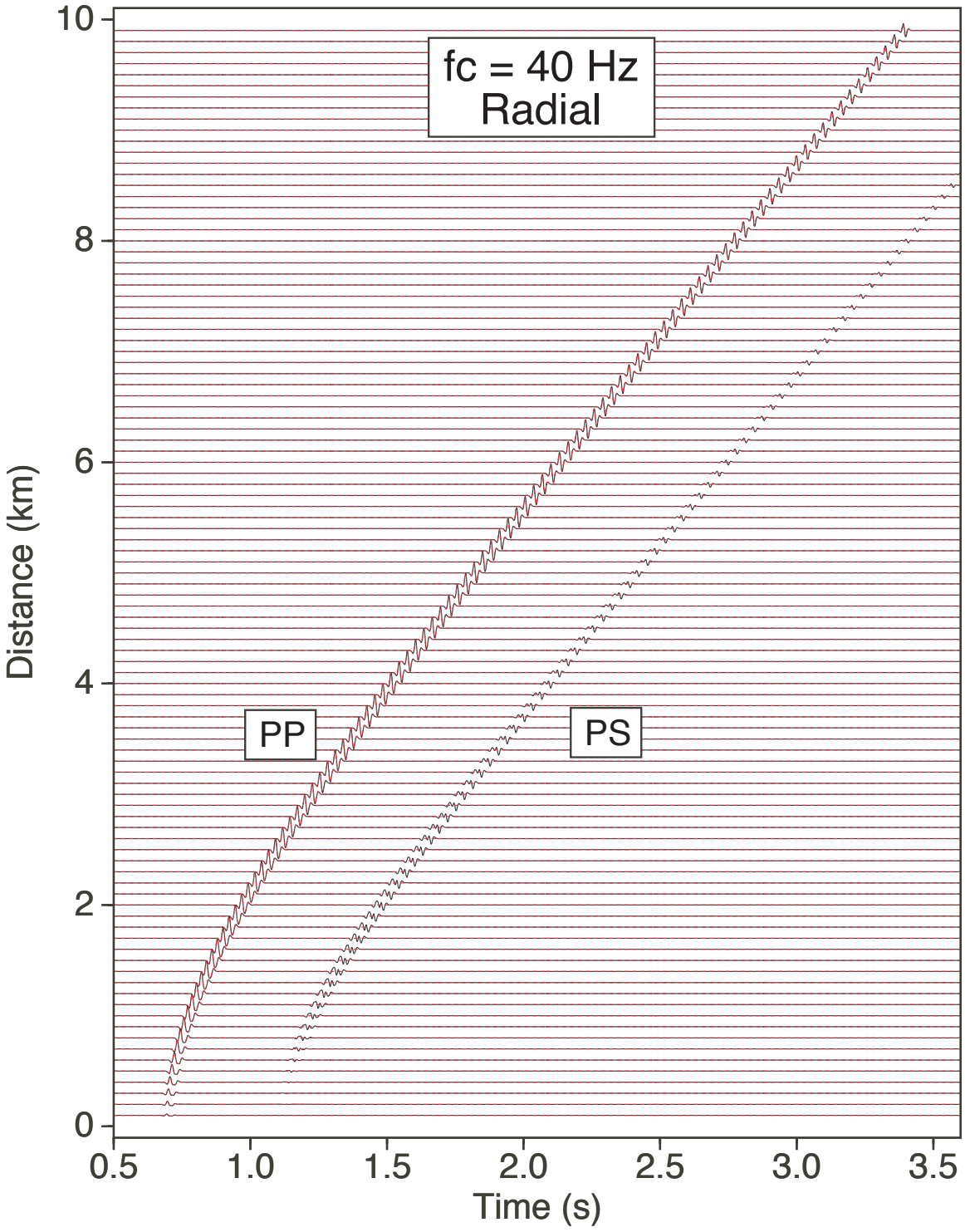

Fig. 3.35. Comparison of synthetic seismograms for the radial component with the central frequency 40 Hz between the discrete wavenumber method (black traces) and ray data including composite reflection coefficient method (dashed red traces).

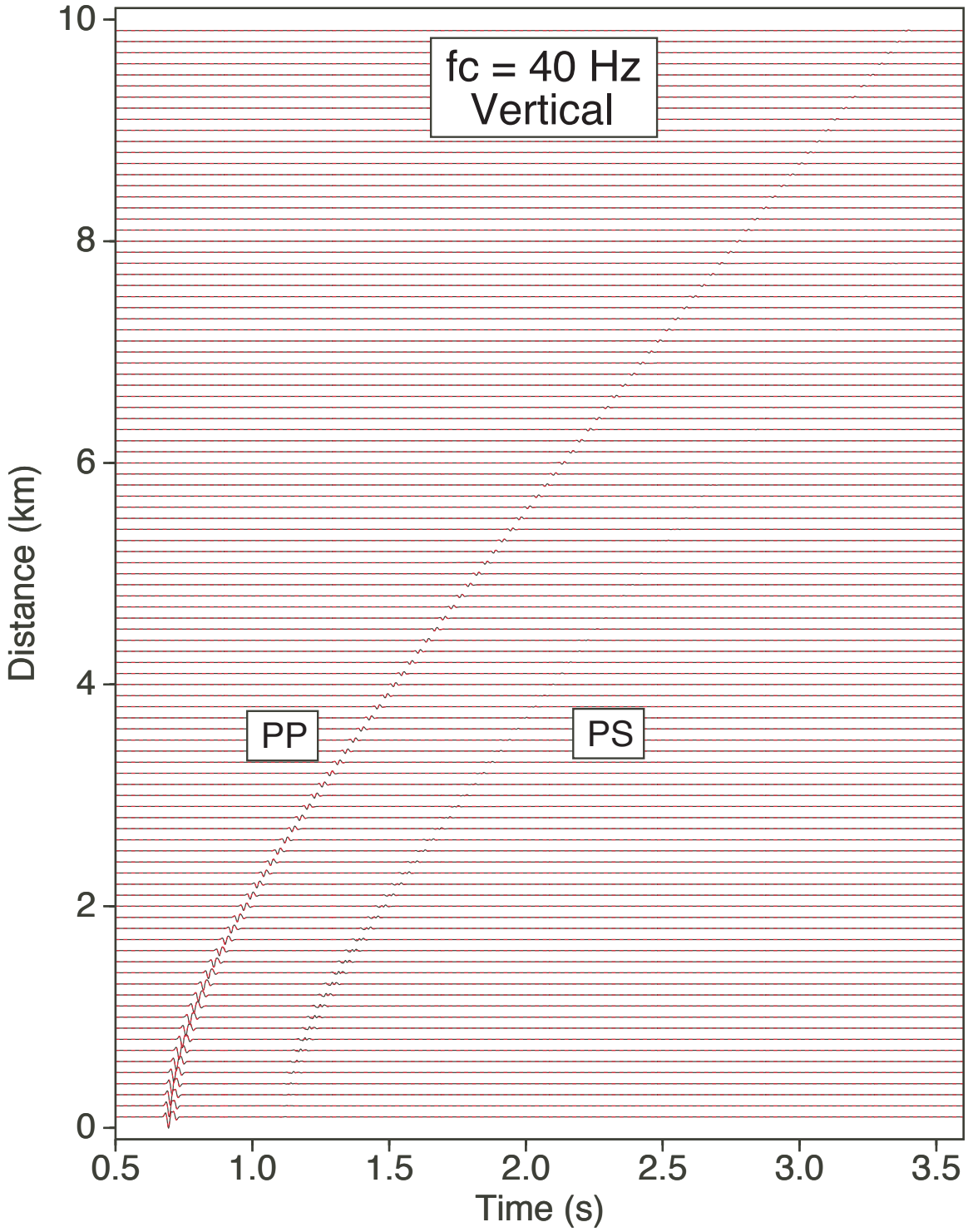

Fig. 3.36. Comparison of synthetic seismograms for the vertical component with the central frequency 40 Hz between the discrete wavenumber method (black traces) and ray data including composite reflection coefficient method (dashed red traces).

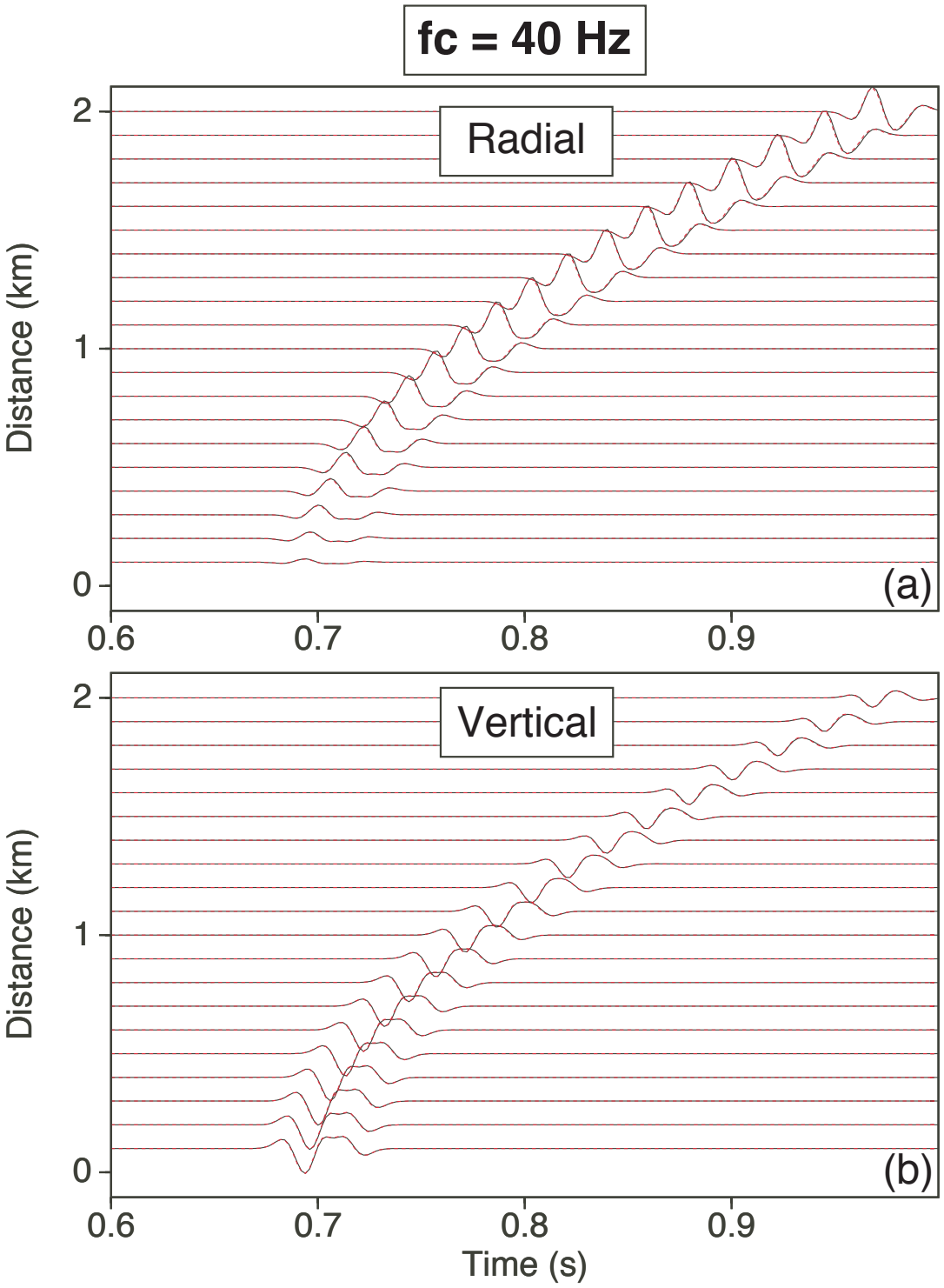

Fig. 3.37. Zoom-in comparison of synthetic seismograms for the central frequency 40 Hz between the discrete wavenumber method (black traces) and ray data including composite reflection coefficient method (dashed red traces). (a) and (b) are for the radial and vertical component, respectively.

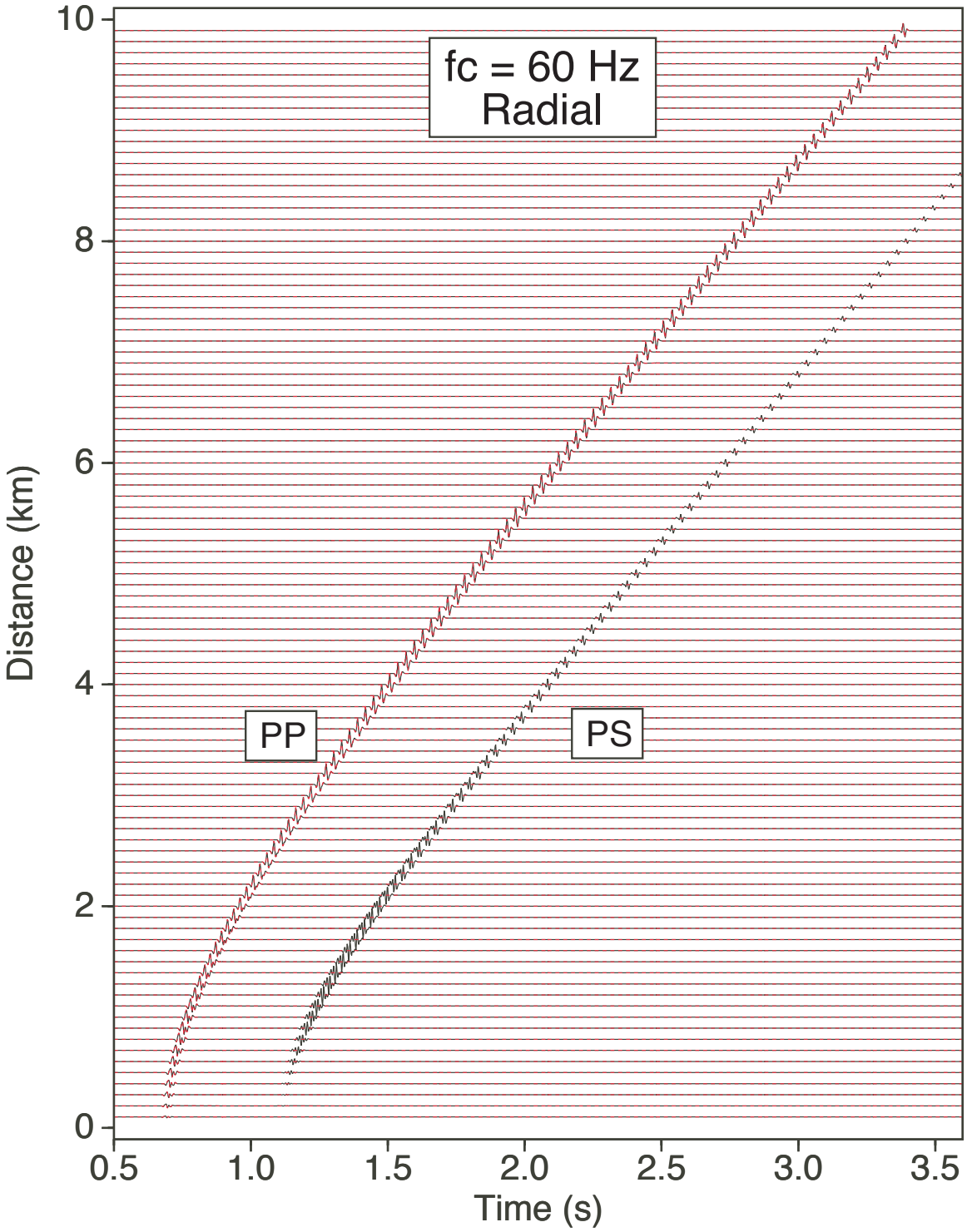

Fig. 3.38. Comparison of synthetic seismograms for the radial component with the central frequency 60 Hz between the discrete wavenumber method (black traces) and ray data including composite reflection coefficient method (dashed red traces).

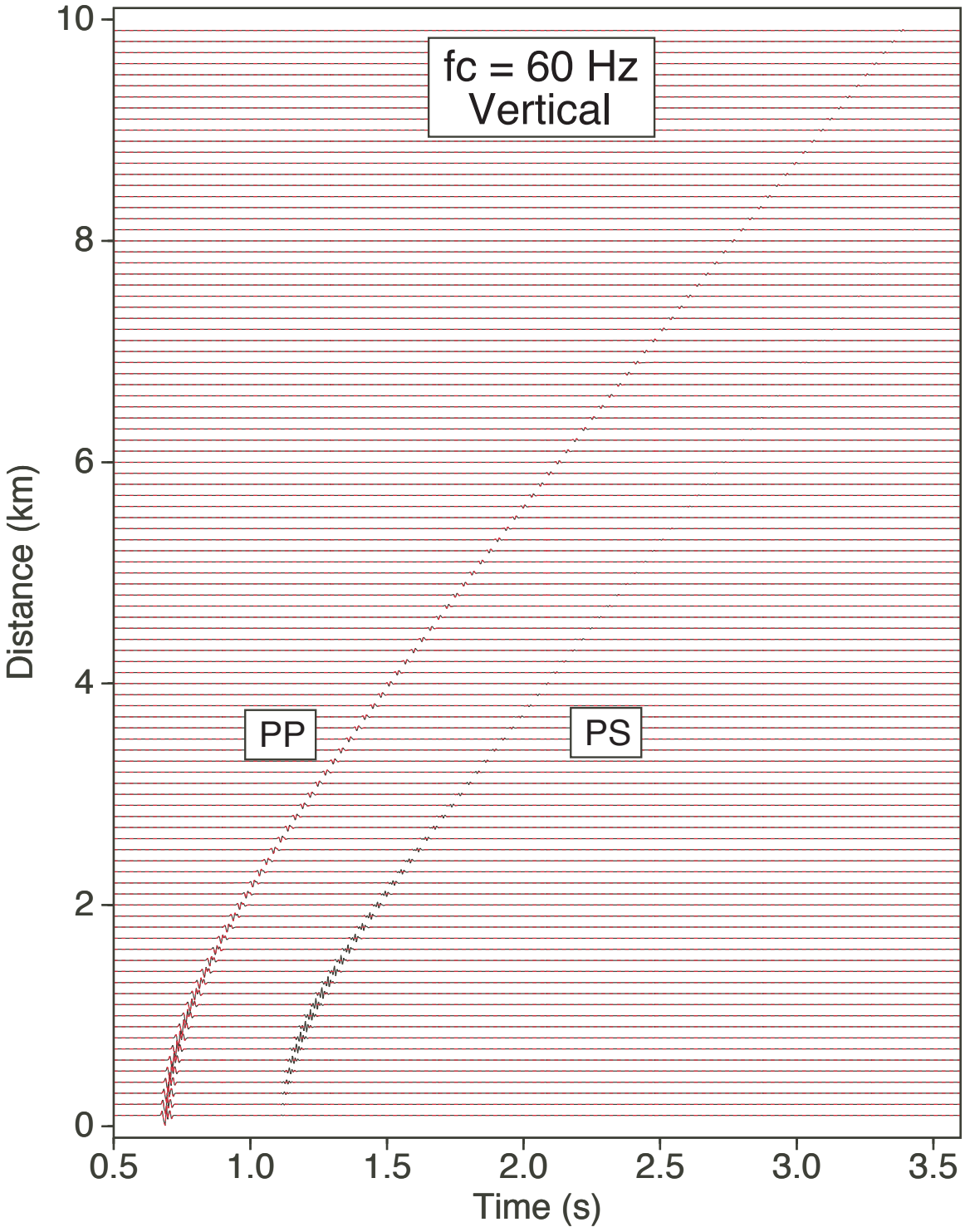

Fig. 3.39. Comparison of synthetic seismograms for the vertical component with the central frequency 60 Hz between the discrete wavenumber method (black traces) and ray data including composite reflection coefficient method (dashed red traces).

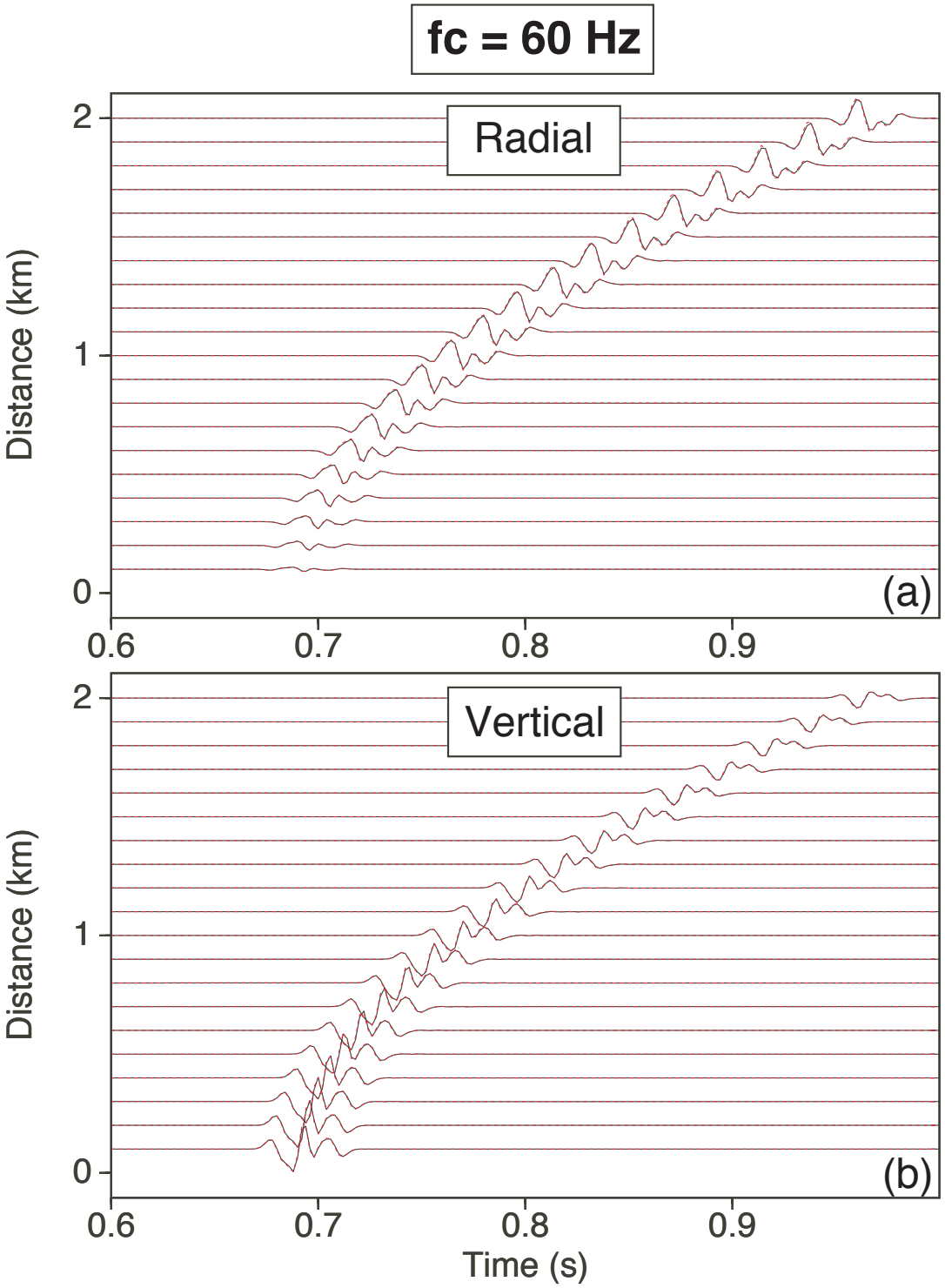

Fig. 3.40. Zoom-in comparison of synthetic seismograms for the central frequency 60 Hz between the discrete wavenumber method (black traces) and ray data including composite reflection coefficient method (dashed red traces). (a) and (b) are for the radial and vertical component, respectively.

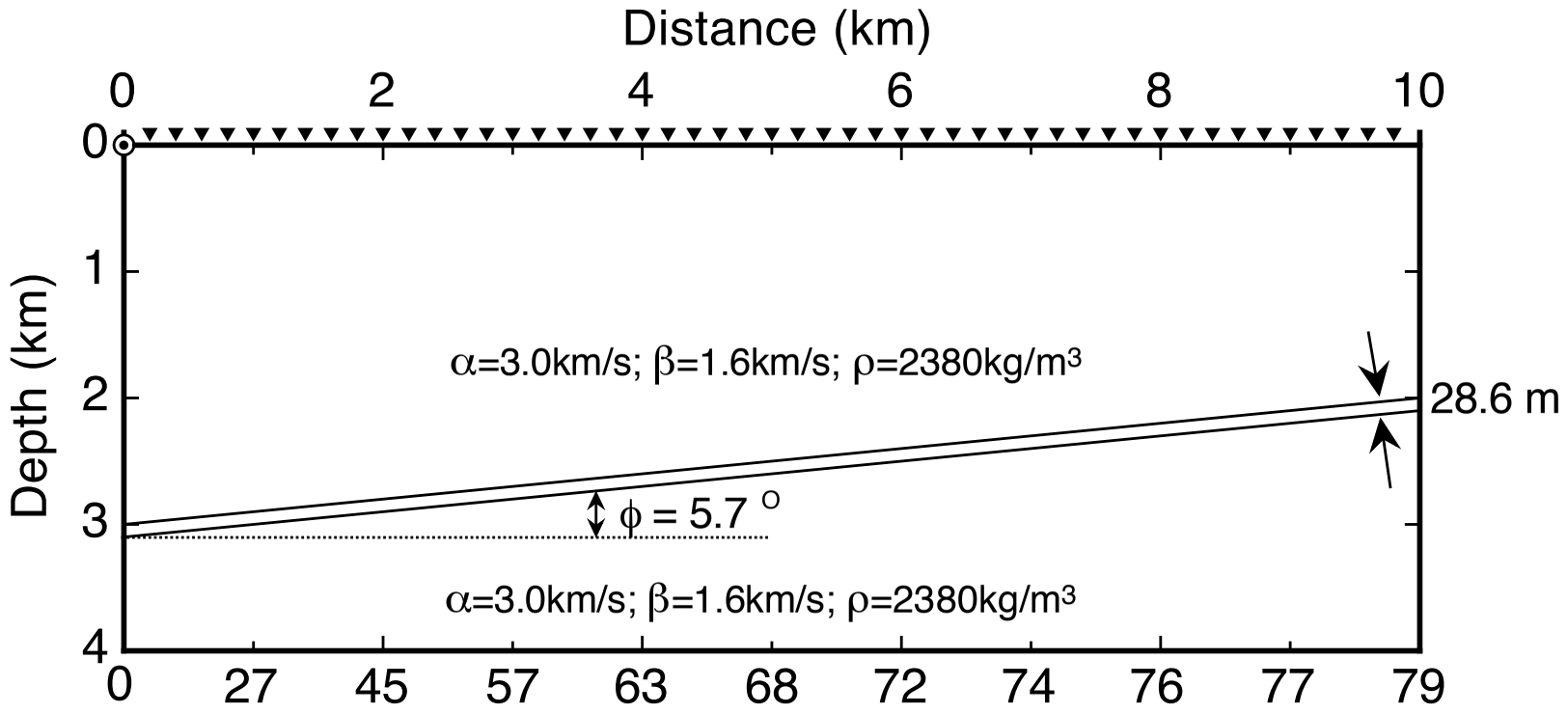

Fig. 3.41. Source-receiver geometry for generating synthetic seismograms in a half space model with a tilted, complex stratified thin reservoir. The complex thin reservoir has the same internal structure and properties as in Figure 3.23b.

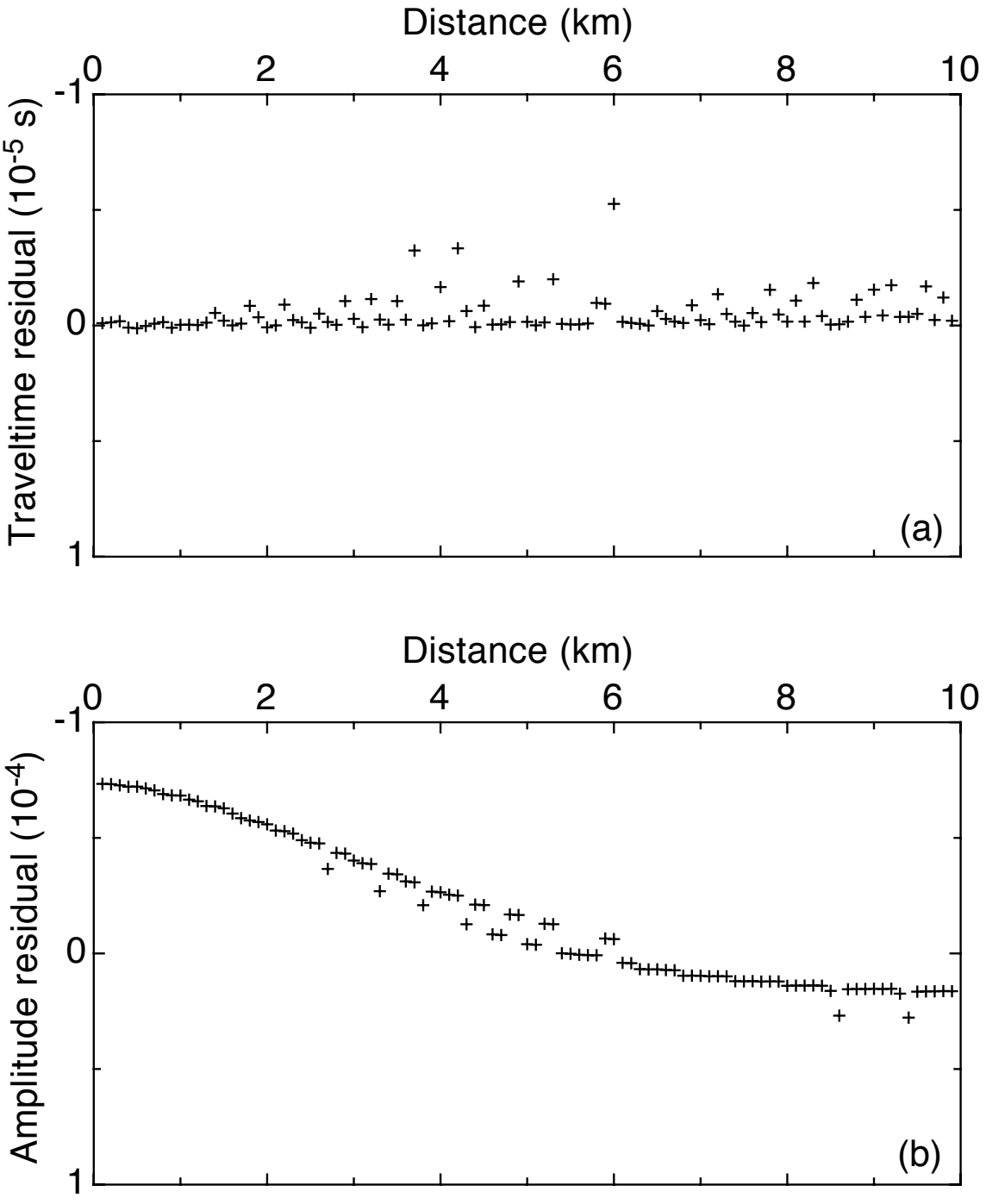

Fig. 3.42. (a) Verification of reflection traveltimes from the top of the reservoir in the Figure 3.41 model. Errors are bounded within 10^{-5} s. (b) Verification of reflection amplitudes from the top of the reservoir.

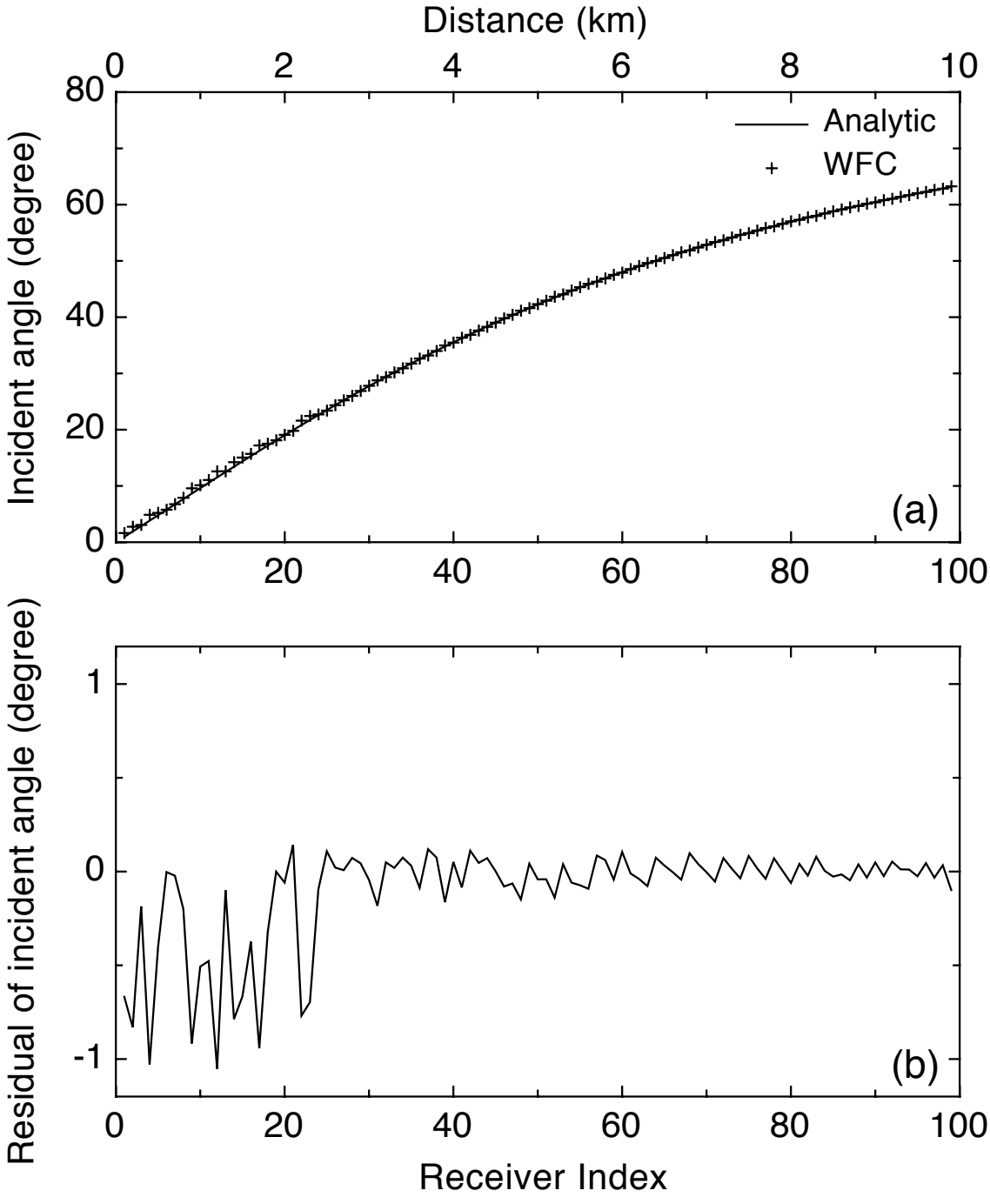

Fig. 3.43. (a) Incident angles obtained by the WFC method are plotted against with the analytic results in the Figure 3.41 model. (b) Verification of incident angles.

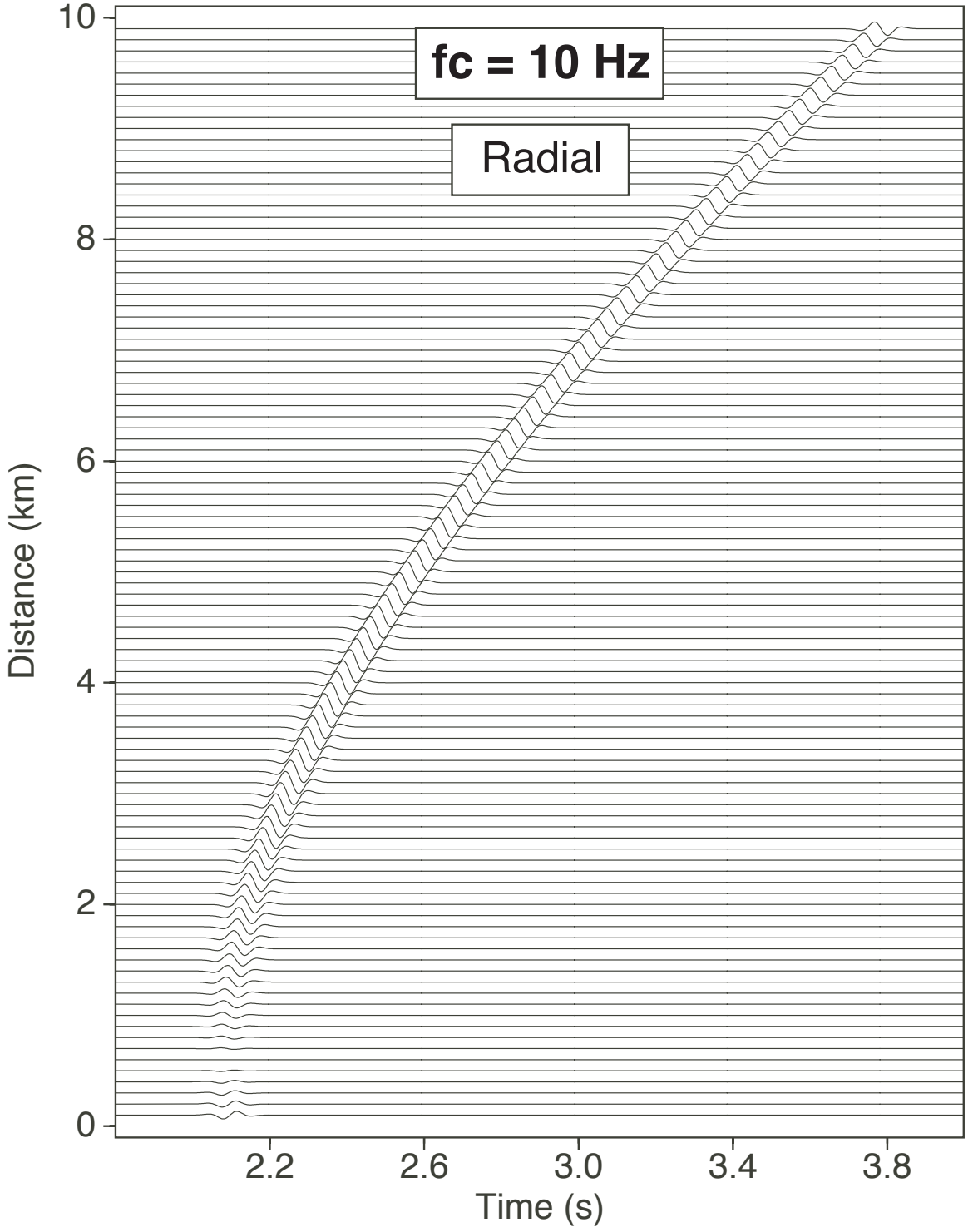

Fig. 3.44. Synthetic seismograms in the radial component, generated from the Figure 3.41 model with the central frequency at 10 Hz.

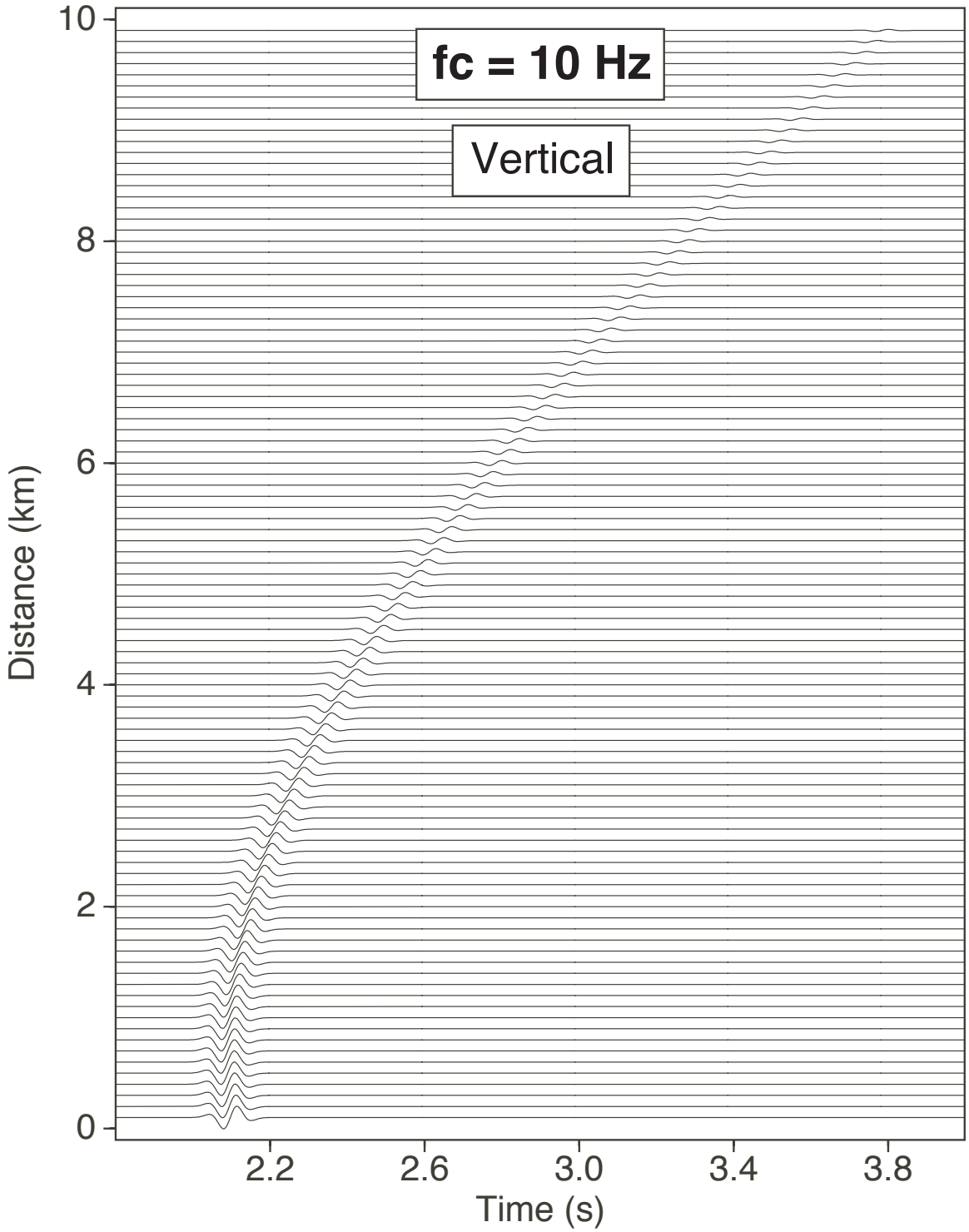

Fig. 3.45. Synthetic seismograms in the vertical component, generated from the Figure 3.41 model with the central frequency 10 Hz.

3.7 Conclusions

The modified WFC method performs a fast modeling to obtain Ray data in multi-region models. Modeling of seismic reflections of traveltimes, amplitudes, and ray incidental angles are shown to be accurate using this approach. On the other hand, the propagator matrix method generates the full solution of P-wave composite reflection for a specific frequency and incident angle in a complex, stratified reservoir, and the reflection coefficients are compared with the results obtained by the discrete wavenumber method.

The hybrid ray-propagator matrix approach can be a fast and accurate method to generate full waveform synthetic seismograms in the complex, stratified reservoir model. The approach implements fast ray tracing in the overburden and the exact solution of P-wave composite reflection coefficients computed by the propagator matrix method to generate the complete synthetic seismograms for the P-wave reflection. A set of the central frequency ranges for the source wavelet is applied to valid the synthetic seismograms with the results generated from discrete wavenumber method. For all frequency ranges, the comparison results demonstrate the full waveform synthetic seismograms for P- wave reflection can be done by the hybrid approach. More importantly, the hybrid method can generate complete synthetic seismograms for the tilted, complex stratified reservoir models.

In future work, extensions of the WFC method can be the converted wave modeling. Then PS wave composite reflection coefficients can be included in the WFC modeling to generate PS wave reflection synthetic seismograms, which is also important information for reservoir characterization.

CHAPTER IV

STOCHASTIC SEISMIC MODELING OF TURBIDITE RESERVOIRS

4.1 Introduction

Turbidite reservoirs in deep-water depositional systems such as the oil fields in the offshore Gulf of Mexico and North Sea are becoming an important exploration target in the petroleum industry. However, they are often not only complicated by the heterogeneity of sand/shale distribution, but also the thin bed resolution problems. Hence, if the reservoir heterogeneity and seismic attributes could be more accurately known, we can reduce exploration risk.

The thickness distribution of sand and shale beds is the most import characteristic for turbidite reservoir models. The corresponding sand/shale ratio is of great interest for in petroleum reservoir models and dominates our turbidite reservoir performance. Many statistical analyses of bed thickness distributions in the turbidite sequences have been done, and the distribution results indicate the bed-thickness distribution are complex and vary with the different locations (Hiscott et al., 1992; Rothman et al., 1994; Pirmez et al., 1997; Talling, 2001).

Hiscott et al. (1992) used formation microscanner (FMS) images obtained in boreholes to estimate the bed thickness distribution in the Izu-Bonin forearc basin. The bed-thickness distribution follows the a power-law rule with an exponent of about one. Rothman et al. (1994) demonstrated the agreement of the bed-thickness distribution between field and borehole (FMS-based) measurements. Both observations are close to a power-law distribution above a small thickness cutoff. However, Pirmez et al. (1997) used a combination of FMS images and geophysical well logs to estimate sandy turbidite successions in the Amazon Fan. The results show bed-thickness distribution is complex, and may not follow a simple power-law behavior. For example, in a log-log plot of bed thickness versus the number of beds with thickness greater than bed thickness, there is a clear change in slope at the thickness of 35 cm.

Because it is difficult to describe the complex heterogeneity of turbidite systems, some simplified reservoir models have been applied to facilitate such analysis. A binary medium constructed from alternating, identical sand and shale layers is the

most common model to represent turbidite reservoirs. Takahashi et al. (1999) demonstrated the estimation of sand/shale ratio using stochastic simulation and Bayes' inversion and discussed the effects in the reflectivity while varying sand thickness and sand/shale ratio (Figure 4.1a). Stovas et al. (2004) used the periodic sand/shale model to estimate the net-to-gross and fluid saturation for turbidite reservoirs (Figure 4.1b). The assumption of the same identical sand units neglects the variation of velocity and density in the sands in real turbidite sequences, which will likely change with grain size and clay content, for example. Further more, Stovas et al. (2006) applied the amplitude variation with offset (AVO) attributes to estimate net-to-gross and oil saturation in such a stack of thin sand-shale layers model. Though the results show the random changes in thickness and rock properties of the sand and shale layers does not have significant variation in AVO attributes, the methods still predict the net-to-gross and oil saturation in a reasonable agreement with the field data. Alternatively, Avseth and Mukerji (2002) classified seismic lithofacies in the deep water clastic systems from well logs, but it is very difficult to correlate the complicate lithofacies with sand/shale bed-thickness distributions, the most important characteristic of turbidite reservoir models. Therefore, an alternating sand/shale turbidite reservoir model is still an attractive choice.

Therefore, an improved stochastic turbidite model (STM) system was proposed to generate inputs for seismic simulations (Lai and Gibson, Jr., 2005). The STMs use observed, continuous bed-thickness distributions and continuous velocity and density distributions to generate more realistic representations of turbidite sequences. Geological interpretations provide essential input to identify lithology and to ensure that statistical measurements are applied to the correct turbidite intervals.

In addition, an important method for identifying hydrocarbons with seismic data is the analysis of the dependence of seismic wave reflections on the angle of incidence of the wave on a target rock formation. Because typical seismic data acquisition locates source and receiver at or near the upper surface of the earth, increasing the distance or offset between them corresponds to an increase in angle of incidence on the target. For this reason, the method is known as the study of AVO.

The AVO technique is very powerful for locating hydrocarbons because the amplitude of seismic reflections at different angles of incidence changes significantly when fluids in a formation change from brine to gas, for example. Ostrander (1984) first proposed this technique to identify amplitude anomalies are caused by gas-saturated

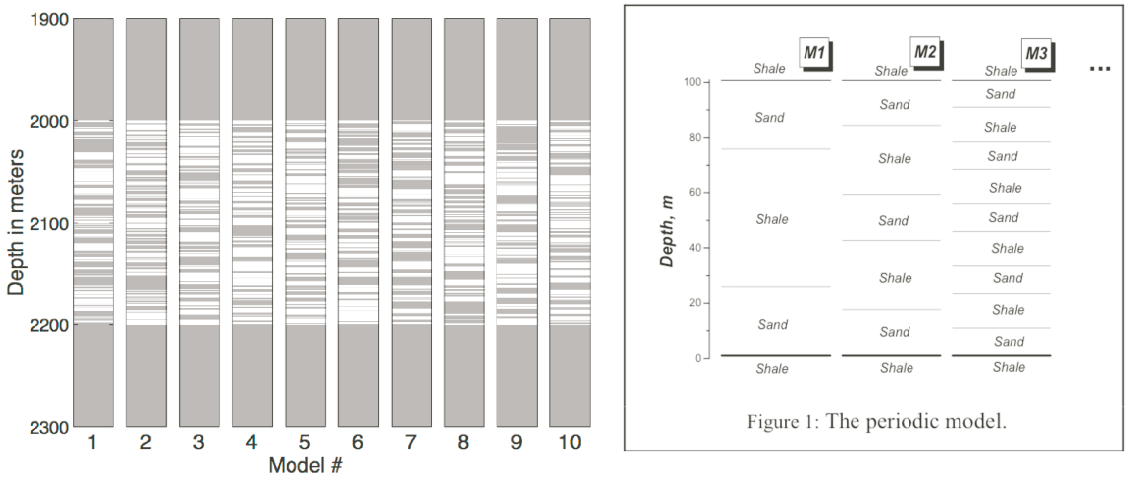

(Takahashi et al. 1999)
(a)

(Stovas et al. 2004)
(b)

Fig. 4.1. Binary models constructed from alternating, identical sand and shale layers is used to represent turbidite reservoir models. (a) Takahashi et al. (1999) implemented stochastic simulation of varying sand/shale ratio to evaluate the turbidite reservoirs. (b) Stovas et al. (2004) used the periodic sand/shale model to present the complexity of lithology in the turbidite reservoirs.

sands embedded in shale, which exhibit the reflection coefficients increase with offset. Rutherford and Williams (1989) demonstrated gas-sand reflections can be grouped into three classes based on AVO characteristics: Class I (high impedance), Class II (small impedance contrast), and Class III (low impedance) sands. Castagna et al. (1998) subdivided Class III sands into Class III and IV based on the sign of the gradient in the AVO crossplot, which is an intercept versus gradient plot for P-wave reflection coefficient (see Background Theory). Class IV gas sands have a negative intercept and positive gradient but exhibit amplitude decrease with offset. Four classes of gas sands can be separated from the fully brine-saturated sands and shales in the AVO crossplots. Further more, the AVO technique is also applied discriminate pore pressure and fluid saturation changes from time-lapse seismic data (Landro, 2001; Kvam and Landro, 2005).

Though AVO analysis is powerful, neglecting the tuning effect may cause AVO responses to be interpreted incorrectly. The tuning effect is the superposition of reflections from the top and bottom of a layer when the layer thickness is thin compared to the seismic wavelength. When such tuning is present, classic AVO analysis, considering the change of the P-wave reflection with offset, may fail to identify fluid

contents or lithology variations. Widess (1973) initially discussed the tuning effect and detectability for a thin bed. Kallweit and Wood (1982) discussed the tuning effect of thin layers for normal incidence waves in terms of resolution by a wedge model. Almoghrabi and Lange (1986) and Juhlin and Young (1993) demonstrated AVO responses including multiple and converted energy of a thin layer embedded in a homogeneous rock may be significantly different from those of a simple interface. Liu and Schmitt (2003) demonstrated the exact solution of the reflection amplitude and AVO responses of a thin layer model for arbitrary incident angles. Therefore, neglecting thin layer effects may make interpretation for AVO responses misleading.

The importance of the converted shear (S) wave reflection from the top and bottom of a layer in AVO responses has been recognized. It may exhibit noticeable amplitude changes in AVO responses; however, its importance is not as well-addressed as the conventional P-wave reflection. Simmons and Backus (1994) demonstrated the significant P-wave reflection changes while the converted S-wave inside a thin reservoir layer is included in AVO analysis. Ramos and Castagna (2001) presented an integrated AVO analysis of P-wave and converted S-wave (from top of the reservoir) reflections may help us better identify the fluid content and decrease the uncertainty associated with velocity and density estimation.

Though these previous contributions address many of the complexities associated with AVO applications, they do not consider the full composite reflection coefficient in the complex stratified turbidite reservoirs, which we will do in this chapter. Gibson, Jr. (2004; 2005) used the propagator matrix method to compute the composite reflection coefficients in a stack of stratified layers model and showed the influence of the internal variation in rock properties for the AVO responses. In Chapter III, the ray tracing including the composite reflection coefficient method has been proved to generate accurate waveform synthetic seismograms for P wave reflection in a complex stratified reservoir model. This fast method is utilized to generate synthetic seismograms for STMs.

Below we first demonstrate how to construct the stochastic seismic models from the cumulative density functions of bed thickness and density for sand and shale layers. Velocities and densities are correlated using a simple deterministic relationship. In order to simulate the turbidite reservoirs in the deep water of Gulf of Mexico, we construct the transform of velocity-density relationship, based on well log measurements. We also introduce methods of AVO technique in the conventional and

tuning models and how to perform fluid substitutions by Gassmann's equation. We show both binary and STMs. Then we present synthetic seismograms and statistical analysis of maximum amplitudes to illustrate the influence on variable heterogeneity in the turbidites on seismic signals. Since the STMs include thin reservoir layers, we conduct the central frequency at 10, 20 and 40 Hz to demonstrate the effect of the frequency dependence modeling of AVO analysis in STMs. Backus averaging is also discussed to demonstrate whether it is possible to replace the complex stratified layers with a homogeneous, transversely isotropic medium. Finally, we apply Gassmanns equation to substitute brine by gas in each sand layer and perform AVO analysis on synthetic seismograms.

4.2 Methods

The following sections summarize the major methods and theoretical concepts that will be applied in the course of this chapter. How to build STMs, AVO analysis, and fluid substitution will be introduced.

4.2.1 Building of Stochastic Turbidite Models

Ray tracing modeling that applies composite reflection coefficients was developed in Chapter III, and it will be used for generating synthetic seismograms for the turbidite models. This approach generates seismic waveform results in plane-layered media for P wave reflection. Therefore, the stochastic turbidite reservoir models must produce a description of the structure in terms of a set of layer thicknesses, along with associated seismic velocity and density. The models will be composed of alternating sand and shale layers, though the thickness and properties of each layer are selected from relevant cumulative distribution functions (CDF). These distribution functions are estimated from field measurements, as are velocity/density relationships.

Statistical Analysis of Sand/Shale Bed Thicknesses

The thickness distributions of sand and shale intervals is the most important characteristic for the turbidite reservoir models. This information helps us to estimate the corresponding sand/shale ratio for assessing the potential of the turbidite unit as a hydrocarbon reservoir.

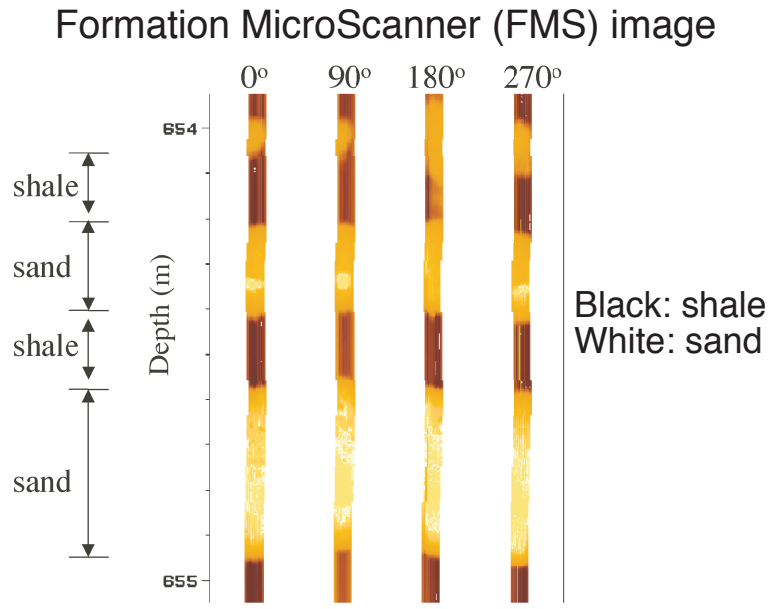

Fig. 4.2. Using FMS images to distinguish sand/shale beds.

In this research, we use the well logs measured in the Amazon Fan by ODP Leg 155, which sampled sand-rich turbidite depositional systems in deep water (Pirmez et al., 1997). Sites 931B, 936A, 944A, and 946A in Leg 155 are selected.

Construction of the models begins with analysis of FMS logs from each of the ODP sites, and these images provide a direct measurement of thicknesses of both sands and shales. In general, each site measures other geologic structures in addition to the turbidites, so we use prior geologic interpretations to ensure that we take measurements only from turbidites (Pirmez et al., 1997). The color of the FMS image indicates the resistivity of the formation, and if the rock has similar mineralogy and is fluid saturated, the darker tone suggests the finer grain rock. Figure 4.2 shows using FMS images to distinguish sand/shale beds. Generally, in the ODP data sets, the sand beds appear in light tones in the FMS images (Hiscott et al., 1992). Based on this rule, we can distinguish sand/shale beds and measure corresponding thicknesses in the turbidite portion of each site. We then used these measurements to create the separate CDFs of bed thickness for sands and shales. Figure 4.3 shows the probability density function (PDF) and CDF of bed thickness distribution measured for the Amazon Fan sites. Both sand and shale bed thickness distributions are complicated, and the data didn't follow simple analytic forms such as exponential or power-law distributions.

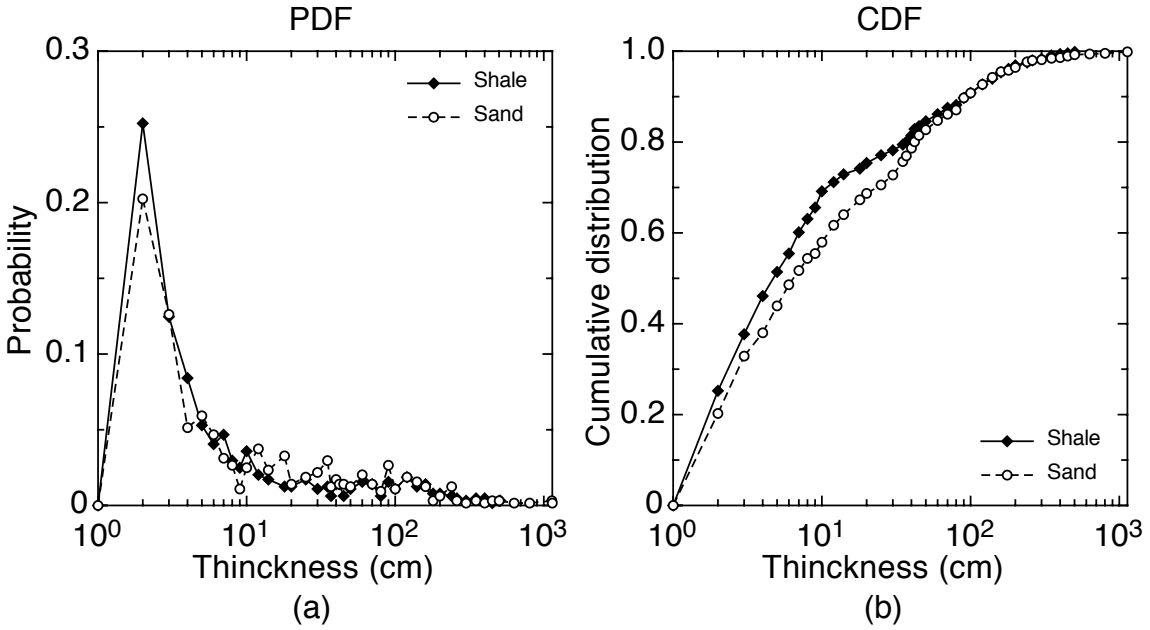

Fig. 4.3. PDFs and CDFs of bed thickness for sand and shale beds in the Amazon Fan sites are shown in (a) and (b), respectively. Both sand and shale bed thickness distributions are complicated and may not follow a simple power-law behavior.

Velocity and Density Transform

Once the sand and shale beds are identified, we can tabulate velocity and density information from the well log for each site as well. The resulting plots of velocity versus density show that the values have high correlation coefficients and that there is a systematic relationship between velocity and density in the turbidite layers, which includes both sand and shale beds. Figure 4.4 shows the linear regression fitting the logarithm of compressional velocity to the logarithm of density in the Amazon fans. Statistical data (m, b, r, n) represent slope, intercept, correlation coefficient, and the number of total well measurements, respectively. The lines through the data are the linear regression results. In each site, then high correlation coefficient shows the clear relationship between parameters. The fitting function in global data will be the velocity and density transform of turbidites in the Amazon Fans. Combining all data together for a single regression (Figure 4.4e), we find that the the two parameters can be related via

$$log(v) \;=\; -0.058 + 1.0058 log(\rho). \tag{4.1}$$

This expression has the same form as the well known Gardner equation (Sheriff and Geldart, 1995) and this transform is for both sand and shale beds in the turbidites.

Statistical Analysis of Sand/Shale Density

Since velocity and density are correlated using a simple deterministic transform, only density information is collected to create the CDF. Tabulated density information from the well logs for each site in the Amazon fans is used to create the PDF and CDF of the density distribution (Figure 4.5). Sand and shale density distributions can be fitted to Gaussian functions. Sand beds have an average density of 1.92. Shale beds have an average density of 2.01 with a broader distribution.

In order to simulate turbidite reservoirs in the deep water in Gulf of Mexico, well logs in the Ursa field are chosen to create the STMs. Figure 4.6 and 4.7 demonstrate well logs in the reservoir intervals distributed from depth 5100m to 5900m. Considering the dominate frequency at 20 Hz, the thickness to wavelength ratio of these reservoirs ranges from 1/15 to 1/3. They are relative thin layers and associated with the strong internal fluctuation in velocity, density and estimated porosity logs because of the mixture of sand and shale beds.

Here we separate sand and shale measurements and will shift the properties of sand and shale from the Amazon Fan (Figure 4.5) to the Mississippi Fan, Gulf of Mexico. Figure 4.8 is the log-log plots of velocity versus density of well logs for both shale and brine sand in the Ursa field, Gulf of Mexico. Considering Figure 4.4 and 4.8, because these two measurements are highly correlated, it would be incorrect to randomly select them independently using two different CDFs. A more physically meaningful approach is to select either density or velocity for the layer at random, and to then choose the other parameter based on the first one.

Density measurements are used to shift the properties of sand and shale from Amazon Fan to the Mississippi Fan. The means of density for sand and shale beds in Figure 4.8 are 2.27 and 2.37 g/cm^3, respectively. Therefore, the mean of density for sand beds in Figure 4.5a are shifted from 1.92 to 2.27. The mean of density in shale beds are shifted from 2.01 to 2.37. Once density measurements are determined, the following two formulas are applied to produce the corresponding velocities for sand and shale beds, respectively.

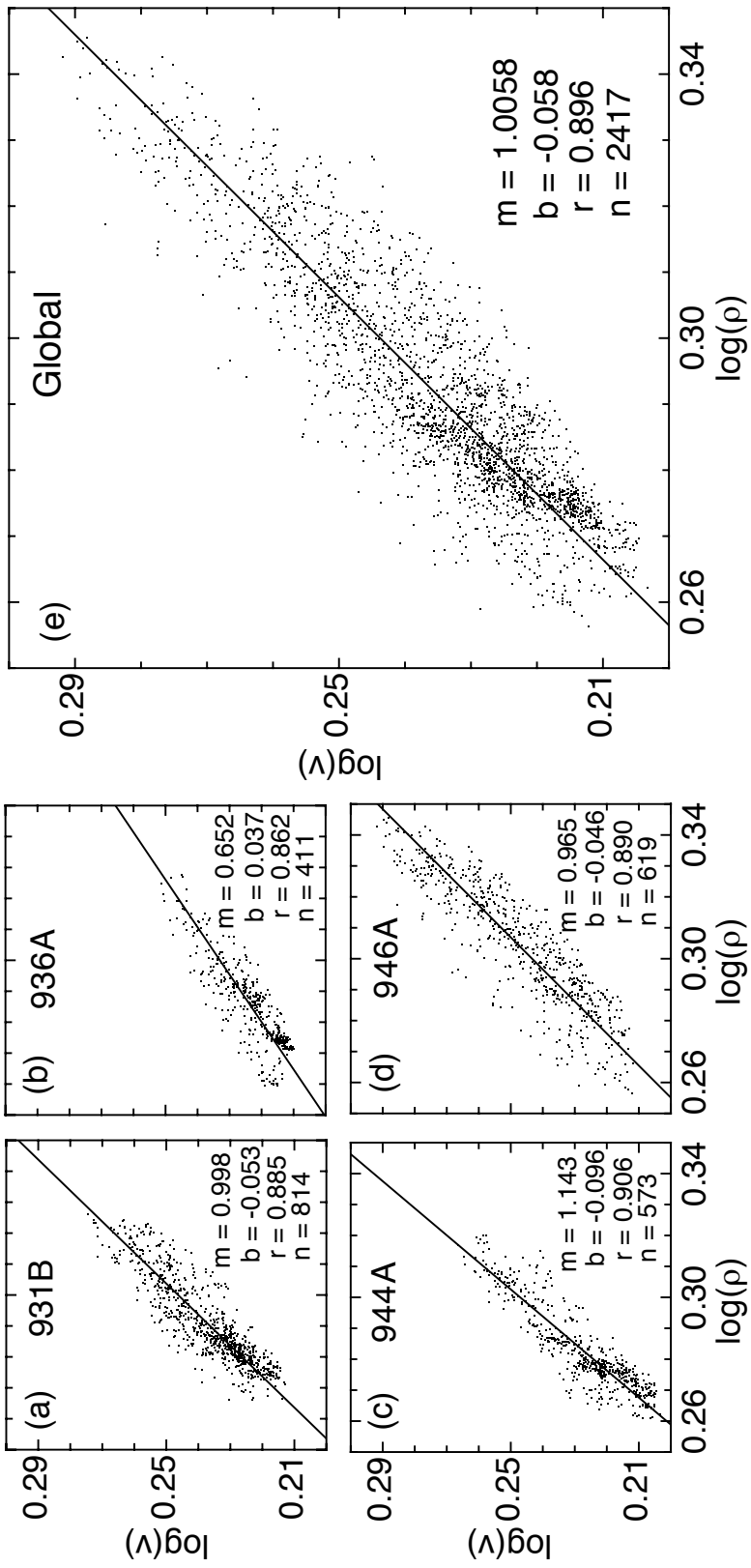

Fig. 4.4. Log-log plots of velocity versus density for each site in the Amazon fans are shown in (a), (b), (c), and (d), respectively. (e) Log-log plots in global. Statistical data (m, b, r, n) represent slope, intercept, correlation coefficient, and the number of total well measurements, respectively. The lines through the data are the linear regression results. The fitting function in global data will be the velocity and density transform of turbidites in the Amazon Fans.

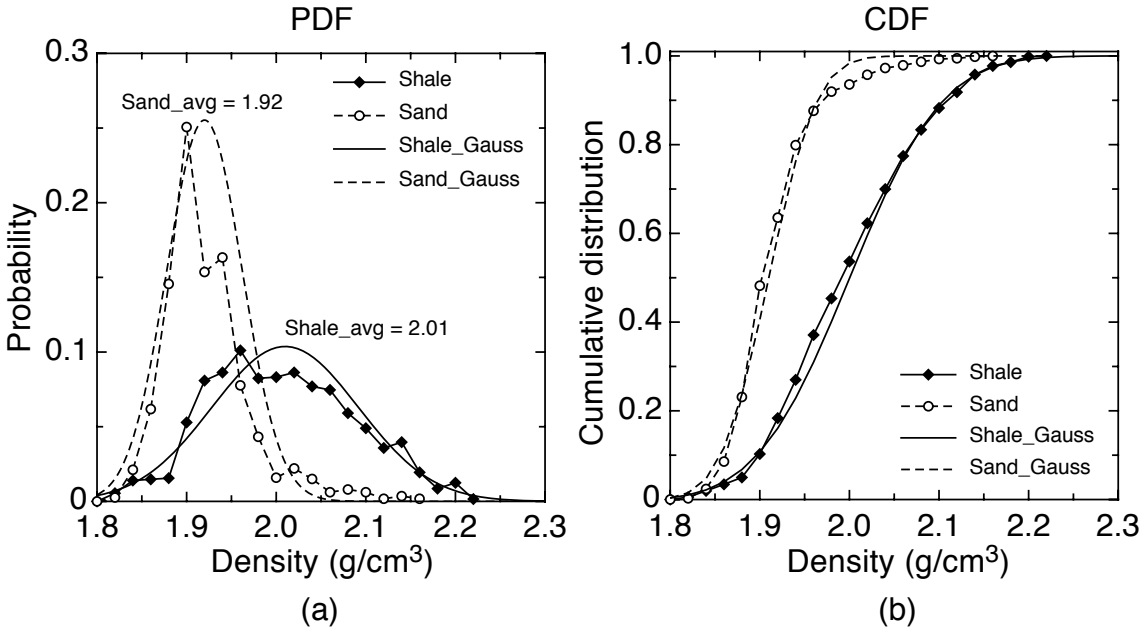

Fig. 4.5. PDFs and CDFs of density distribution measured for the Amazon Fan sites are shown in (a) and (b), respectively. Sand and shale density distributions can be fitted to Gaussian functions. Sand beds have an average density of 1.92. Shale beds have an average density of 2.01 with a broader distribution.

$$Sand: \quad log(v) = -0.47 + 2.56log(\rho) \tag{4.2}$$

$$Shale: \quad log(v) = -0.59 + 2.86log(\rho) \tag{4.3}$$

Building of Stochastic Models - Summary

The model generation begins by specifying a desired total thickness for the turbidite sequence. We then randomly select a bed thickness and a density value from the relevant CDFs, alternating sand and shale until the total thickness is obtained. The velocities are determined by two velocity-density transforms in Equation 4.2 and 4.3. Examples below use a total thickness value of 30 m. If the last layer generated results in a total thickness greater than 30 m, then the thickness of the last bed will be truncated so that the total remains 30 m. Shear wave velocity is not available in the ODP well logs. Therefore, considering the Amazon Fan is a young depositional system

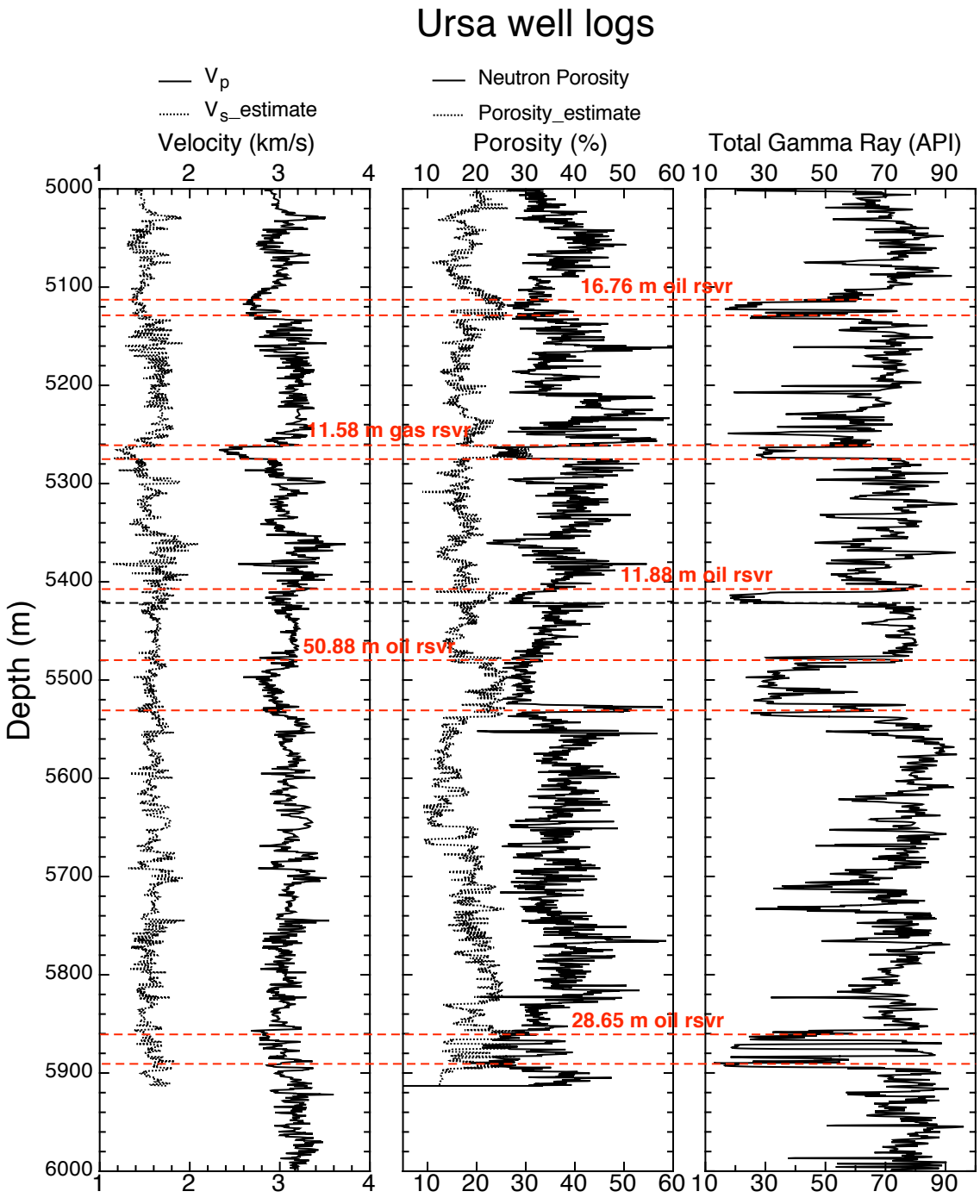

Fig. 4.6. Well logs of reservoirs in Ursa field, Gulf of Mexico.

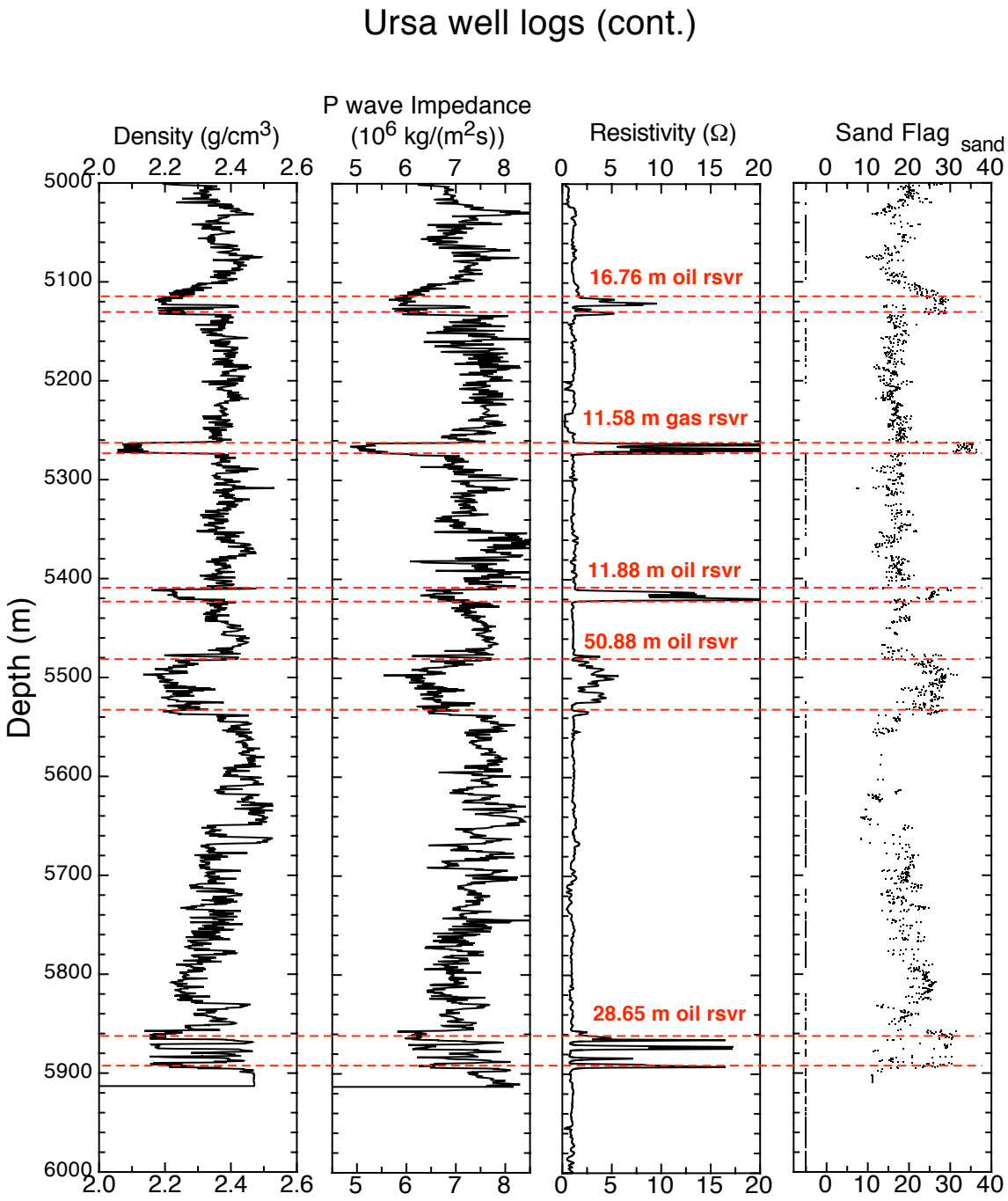

Fig. 4.7. Well logs of reservoirs in Ursa field, Gulf of Mexico (continue).

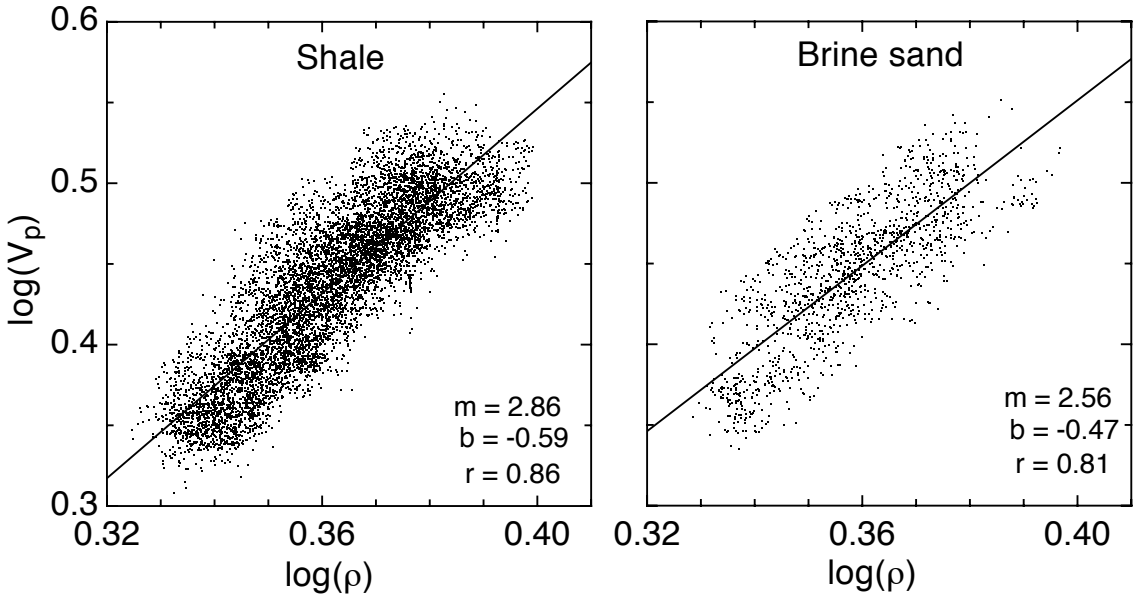

Fig. 4.8. Log-log plots of velocity versus density of well logs for shale and brine sand in the Ursa field, Gulf of Mexico, are shown in (a) and (b), respectively. The density and velocity measurements are highly correlated in shale beds as well as in sand beds. See Fig. 4.4 for the same description of m, b, and r.

with relatively poorly consolidated sediments, we arbitrarily used $Vs = Vp/2.2$ to estimate shear wave velocity in the models. In fact, since no converted shear wave is considered in STMs, the shear wave velocity is not relevant to the results.

4.2.2 Amplitude Variation with Offset

Classic AVO

Shuey (1985) described an approximate solution for the P-wave reflection coefficient from a single interface between two solid half-space, illustrating how the amplitudes at normal incidence, intermediate, and large angles, providing physical insights into the P-wave reflection problem. Considering only the near offset incident angles (about 30°), Castagna and Smith (1994) proposed Shuey's approximation to the Zoeppritz equation can be represented using two parameters, an intercept (A) and gradient (B), given by

$$R(\theta) \approx A + Bsin^2(\theta). \tag{4.4}$$

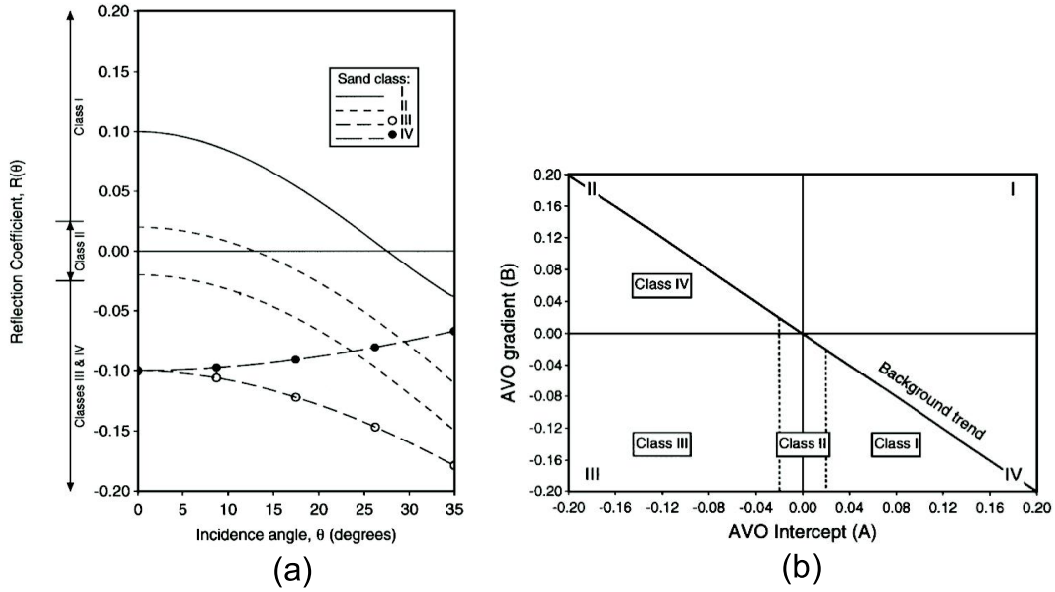

Fig. 4.9. (a) Reflection coefficient variation with incident angle for different gas sands. (b) AVO gradient versus AVO intercept crossplot for four possible gas sands (adapted from Castagna et al., 1998).

A is the normal incidence P-wave reflection coefficient. B represents the P-wave reflection coefficient in the intermediate angles. See Equation 3.11 and 3.12 for the details of terms.

AVO values for typical categories of reservoirs are often classified into four-categories in an A versus B crossplot (Castagna et al., 1998). Figure 4.9 shows the AVO responses four four classes and the possible quadrants for them in A versus B crossplot. The AVO characteristics of gas sands present different behaviors from the brine-saturated sands and shales and can be distinguished.

Tuning AVO

Neglecting the tuning effect caused by the thin layer may result in false interpretation in AVO analysis. Here, we perform a set of variation in reservoir thickness to test the influence of tuning effect in AVO response. Table 4.1 gives model parameters of each layer in the tuning model.

The rock properties of the gas sand is computed by the Gassmann equation.

Table 4.1. Model parameters of each layer in the tuning model.

	$V_p\,(km/s)$	$V_s\,(km/s)$	$\rho\,(g/cm^3)$
Half space	3.0	1.49	2.41
Brine sand	2.85	1.41	2.21
(or gas sand)	2.43	1.46	2.08

Figure 4.10 shows the source-receiver geometry and model parameters. The thickness to wavelength ratio (h/λ) 1/64, 1/32, 1/16, 1/8, 1/4, 1/2, 1 and 2 are considered to generate synthetic seismograms. Vertical point force and Ricker wavelet with the central frequency at 10 Hz are applied.

Figures 4.11 and 4.12 show synthetic seismograms in a thin layer embedded model for h/λ 1/64, 1/32, 1/16, 1/8, 1/4, 1/2, 1 and 2 respectively. The same gain is applied in all seismograms. Brine sand layer model is in solid traces. And gas sand layer model is in thick, dashed traces. After fluid substitution with gas, the larger contrast of elastic impedance causes the stronger amplitudes. The modeling includes the case from tuned to de-tuned and give us a very basic understand of the tuning effect after fluid substitution.

P wave reflections from the top and bottom interfaces are canceled out while the layer is thin. However, while $h/\lambda = 1$ and $h/\lambda = 2$, P wave reflections from the top and bottom of the thin layer are not superimposed and show the opposite polarity in the waveform of the Ricker wavelet. The P wave reflection from the bottom has smaller amplitude than that from the top because of the geometric spreading. The $P - SV$ wave amplitude has very slightly change because of the S wave has small change in velocity after fluid substitution.

A plot of the intercept versus gradient obtained by fitting measured amplitude to the Shuey equation allows AVO analysis for varying h/λ. Figure 4.13 the trajectories of AVO responses for a thin brine or gas sand layer embedded in a half space model while changing h/λ from 1/64 to 2. In the intercept-gradient plot, the distance between brine and gas sand cases suggest the relative thin layer is harder to detect and distinguish when hydrocarbons are present in the pore space. This also explains

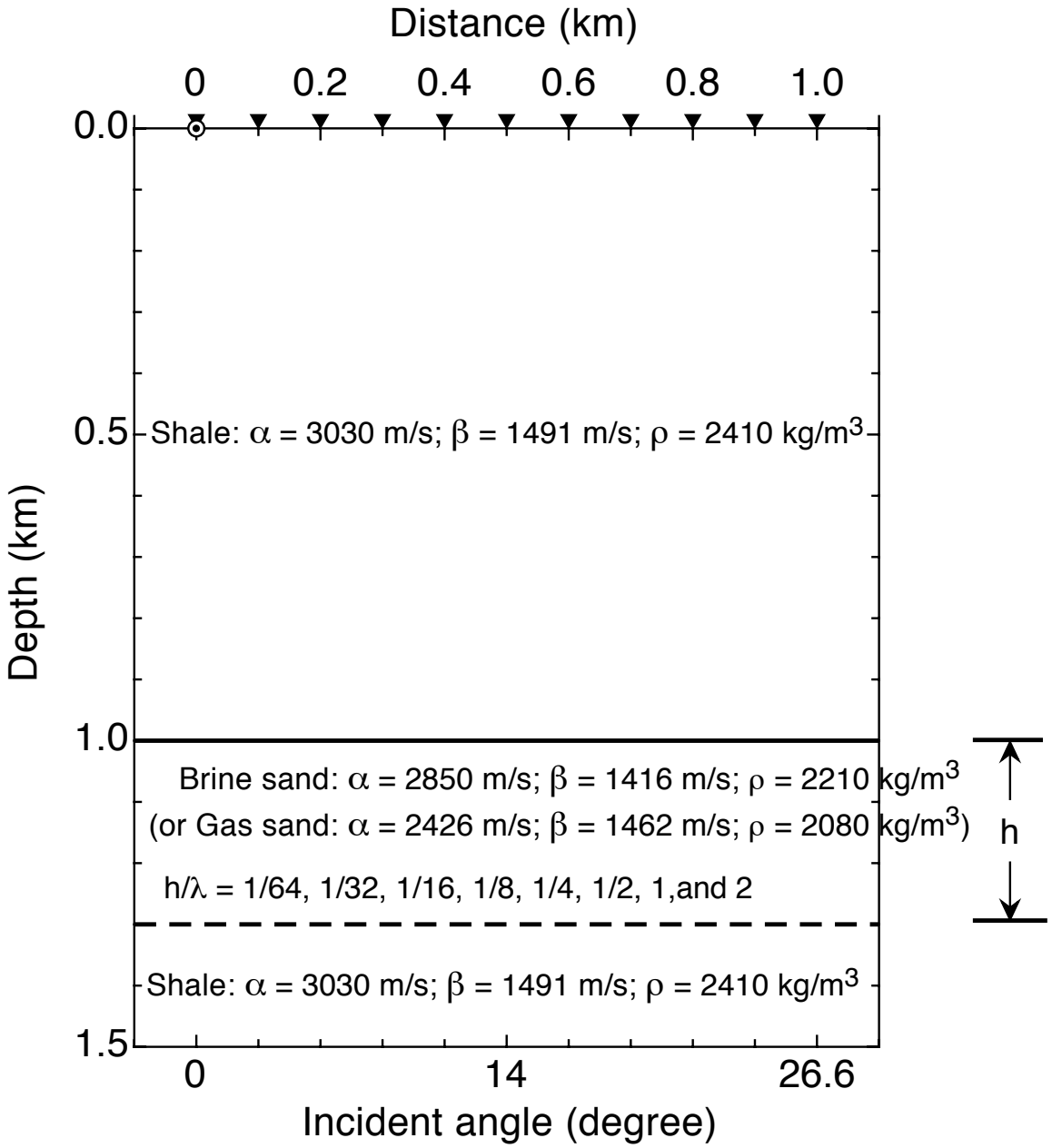

Fig. 4.10. A thin layer embedded model to simulate AVO responses while the gas is charged in the sand reservoir. The thickness to wavelength ratio (h/λ) 1/64, 1/32, 1/16, 1/8, 1/4, 1/2, 1 and 2 are considered to perform seismic modeling.

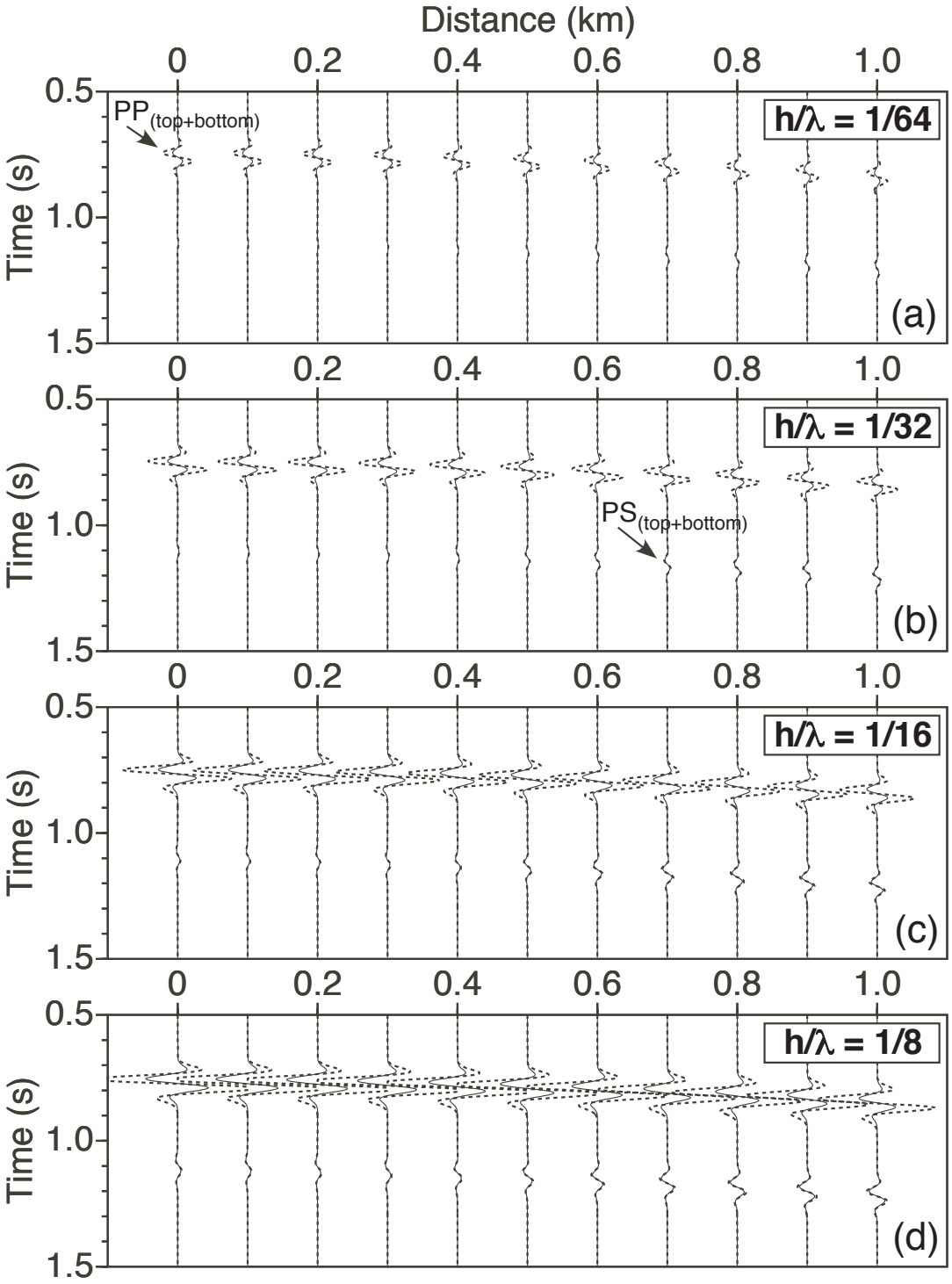

Fig. 4.11. Synthetic seismograms in a thin layer embedded model for thickness to wavelength ratio (h/λ) 1/64, 1/32, 1/16, and 1/8 are shown in (a), (b), (c), and (d), respectively. Synthetic seismograms for brine sand layer model is in solid traces. For gas sand layer model is in thick, dashed traces.

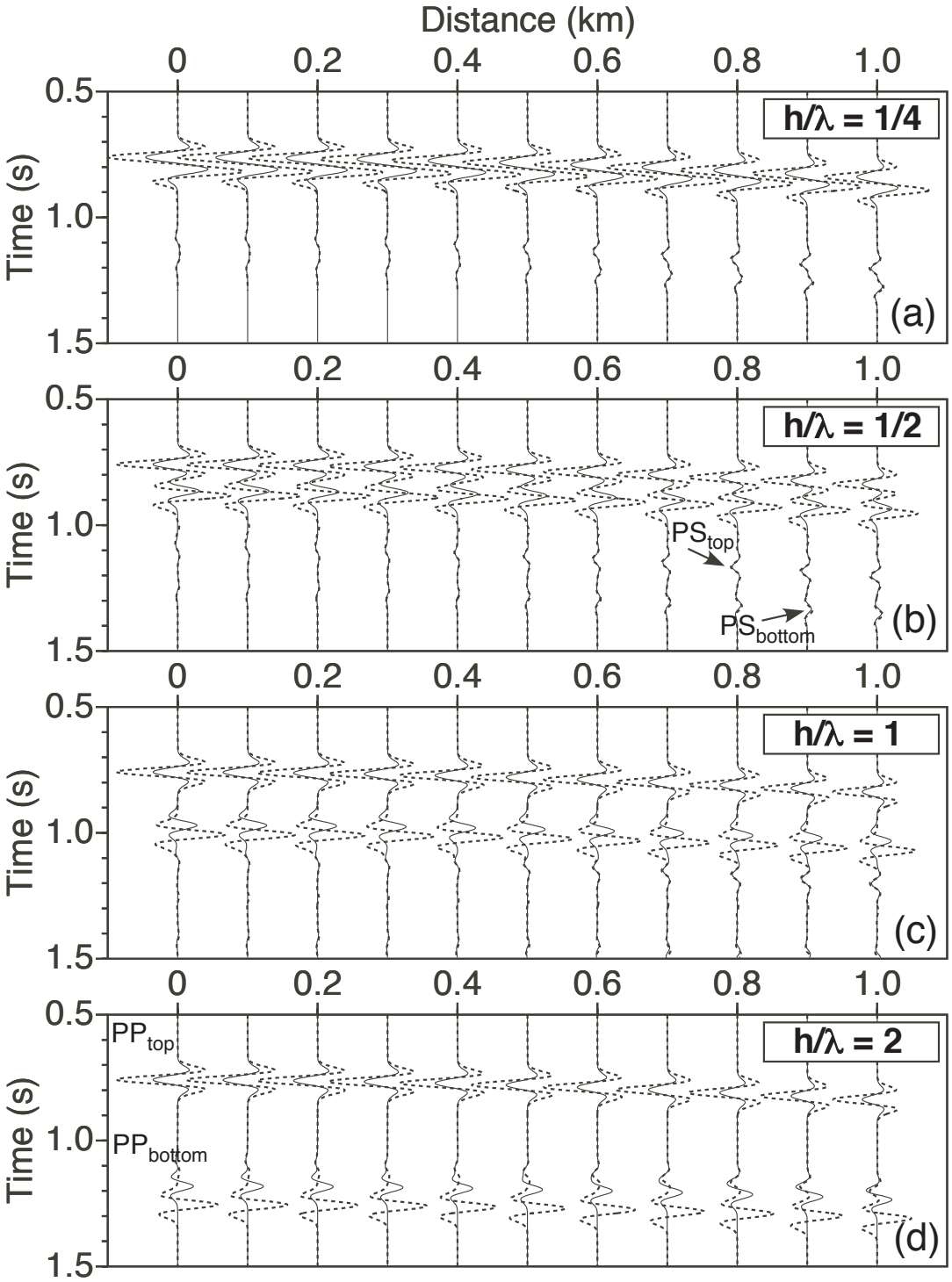

Fig. 4.12. Synthetic seismograms in a thin layer embedded model for thickness to wavelength ratio (h/λ) 1/4, 1/2, 1 and 2 are shown in (a), (b), (c), and (d), respectively. Synthetic seismograms for brine sand layer model is in solid traces. For gas sand layer model is in thick, dashed traces.

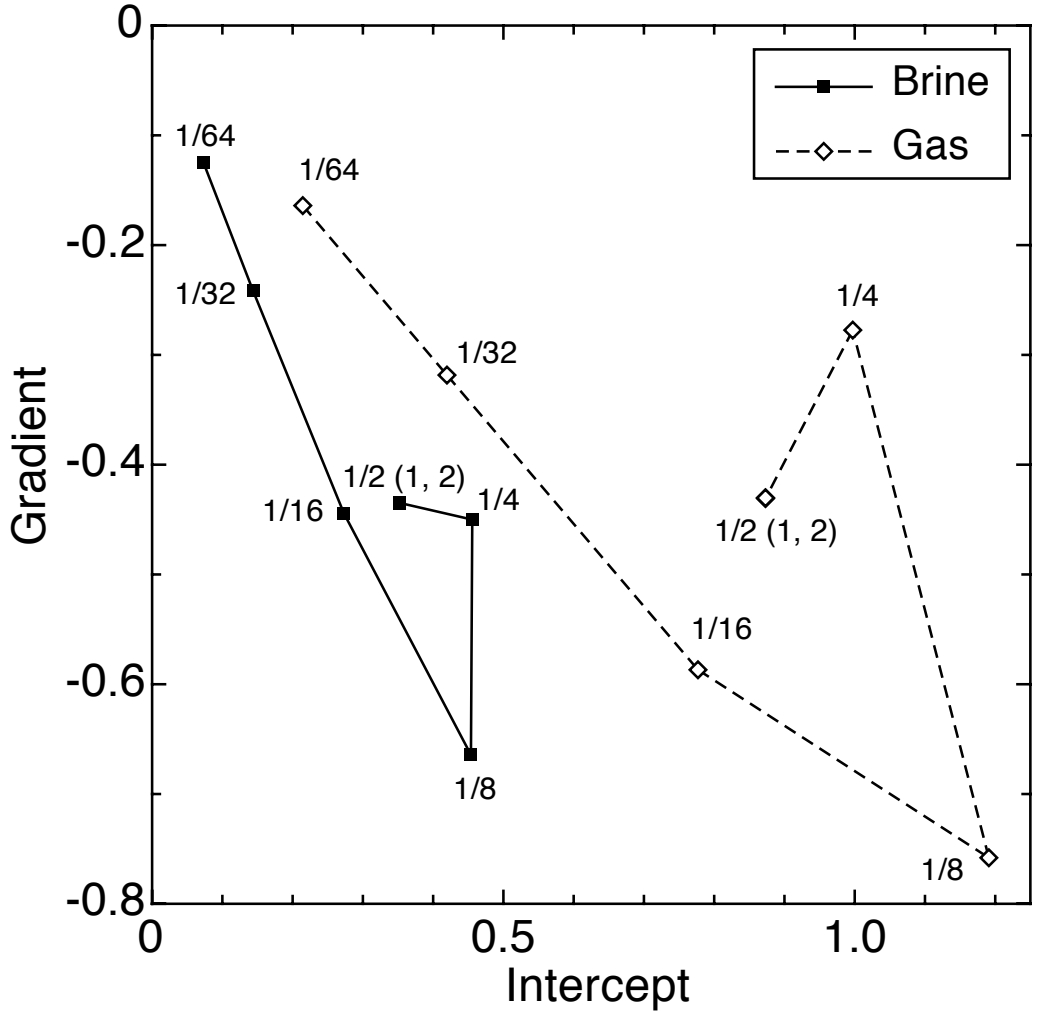

Fig. 4.13. The trajectories of AVO responses for a thin brine or gas sand layer embedded in a half space model while changing the thickness-wavlength ratio (h/λ) from 1/64 to 2. The distance of AVO response between brine and gas models increases with h/λ value. This suggests the thin layer reservoirs may produce more exploration risk because of less differences in AVO responses while gas presents. For h/λ 1/2, 1 and 2, they have very close intercepts and gradients showing AVO responses overlapped.

why exploration risk is higher while applying AVO technique to locate hydrocarbons for turbidite reservoirs in deep water. The intercept shows the amplitude of the normal incident. In the intercept-gradient plot, h/λ at 1/2, 1 and 2 have very similar AVO responses and show the plots overlapped. It suggests that the reflections from top and bottom interfaces of the reservoir are totally separated and it is hard to distinguish the thickness difference while only considering the reflection from the top interface in the intercept-gradient plot.

4.2.3 Fluid Substitution

The Gassmann equation (Gassmann, 1951) has been widely used to predict the variation of elastic properties in rocks for the fluid substitution in the pore space. The saturated bulk modulus κ of a porous rock can be written as

$$\kappa = \kappa^* + \frac{\left(1 - \frac{\kappa^*}{\kappa_s}\right)^2}{\phi\left(\frac{1}{\kappa_f} - \frac{1}{\kappa_s}\right) + \frac{1}{\kappa_s}\left(1 - \frac{\kappa^*}{\kappa_s}\right)}, \tag{4.5}$$

where κ^* is the bulk modulus the porous rock frame, κ_s is the bulk modulus of the mineral matrix, κ_f is the bulk modulus of the pore fluid, and ϕ is porosity.

The shear modulus μ of the rock does not change while the different fluid is saturated. The density ρ of the saturate rock is express as

$$\rho = \rho^* + \phi\rho_f, \tag{4.6}$$

where ρ^* and ρ_f are the densities of the porous rock frame and fluid, respectively. The pore fluid can be gas, and brine, or the mixture of them. The bulk modulus of the fluid κ_f can be computed by Wood's equation (Wood, 1941):

$$\frac{1}{\kappa_f} = \frac{S_w}{\kappa_w} + \frac{S_o}{\kappa_o} + \frac{S_g}{\kappa_g}, \tag{4.7}$$

where κ_w, κ_o, and κ_g are the bulk modulus for water, oil and gas, respectively. S_w, S_o, and S_g are the saturations for water, oil and gas, respectively. The seismic velocities after the fluid substitution can be written as

$$V_p = (\kappa + \frac{4}{3}\mu)^{1/2}, \tag{4.8}$$

Table 4.2. Densities and bulk moduli of the two fluids (Murphy, 1984).

	$\rho\,(g/cm^3)$	$\kappa\,(GPa)$
Grain	2.65	35.0
Water	0.997	2.25
Gas	1.1	0.0008

and

$$V_s = (\frac{\mu}{\rho})^{1/2}, \tag{4.9}$$

Here, a test of computing velocity and density after fluid substitution in a two-fluid system is preformed to verify the implementation of the Gassmann equation. Table 4.2 gives the densities and bulk moduli of the two fluids and grain (quartz).

Figure 4.14 shows P and S wave velocity and density as a function of gas percentile in the two component fluid system in a sand reservoir with a porosity $\phi = 0.224$. The result show a good agreement with the plot in Murphy (1984).

4.3 Examples

4.3.1 Stochastic Turbidite and Binary Models

Figure 4.15a shows the source-receiver geometry and model parameter for generating synthetic seismograms. Figures 4.15b and 4.15c show two STMs with a 30 m thickness in two realizations and Backus averaging results in dashed lines. The STMs is embedded in the half-space. In each model there is a large heterogeneity of layer thicknesses, velocity and density. Figure 4.16 shows a comparison of STM and binary turbidite models and the models after performing fluid substitution. The contrasting properties of sand and shale beds are evident, showing changes in both density and velocity inside each model. Solid lines represent the brine sand models. Dashed lines show values for the model where the brine sands are 80% saturated by gas. Fluid substitution is only performed in sand layers. In the STM, the average velocity of

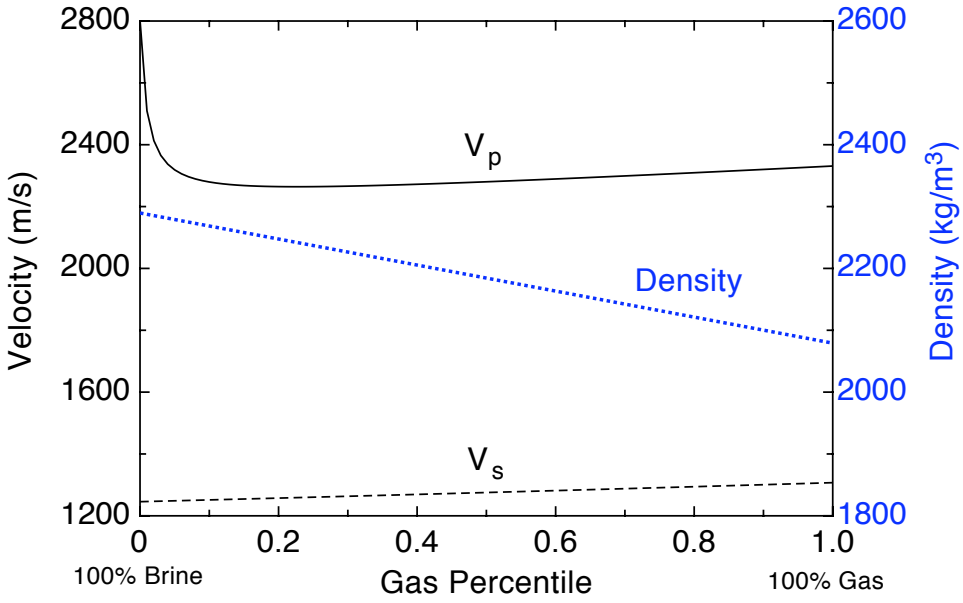

Fig. 4.14. P and S wave velocity and density as a function of gas percentile in the two component fluid system in a sand reservoir.

sand and shale are 2.7 km/s and 3.0 km/s, respectively. These two velocities are for identical sand and shale beds in the binary model.

Figure 4.17 demonstrate qP and qS-wave phase velocity as a function of angle in a Backus-averaged model. qP wave phase velocity in the horizontal direction is about 1.4% faster than in the vertical direction suggests this STM is a weakly anisotropic medium.

4.3.2 Synthetic Seismograms

We applied the ray tracing including the composite reflection coefficient method to generate full waveform synthetic seismograms for P-wave reflections. This helps us interpret the heterogeneity of stochastic models. The first results utilize the left model in Figure 4.15b to compare synthetic seismograms for different source frequencies. Both STM and binary models are considered. The source is located on the free surface, and a Ricker wavelet was applied for 10, 20, and 40 Hz. Eleven receivers spaced at 200 m intervals were located on the surface, and vertical component synthetic seismograms were generated for them (see Figure 4.15a).

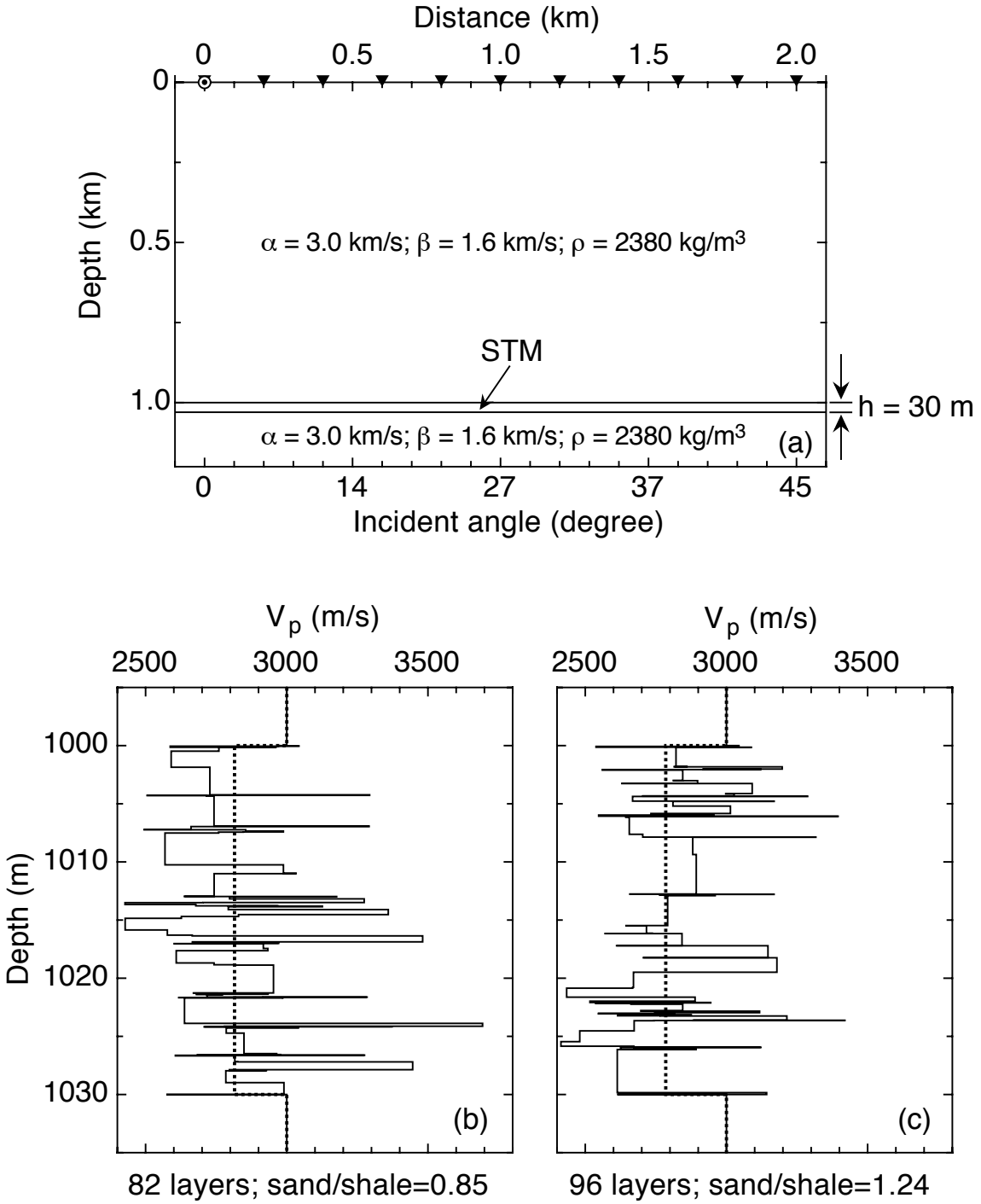

Fig. 4.15. (a) Source-receiver geometry for seismic modeling in stochastic turbidite models. STMs are embedded in a half space. (b) and (c) Examples of two STMs demonstrate a 30 m thick turbidite model with a large heterogeneity of layer thicknesses, velocity and density. Sand and shale beds alternatively appear in the model. Solid line represents the STM. Dashed line represents the P-wave velocity at the vertical direction in the Backus-averaged STM.

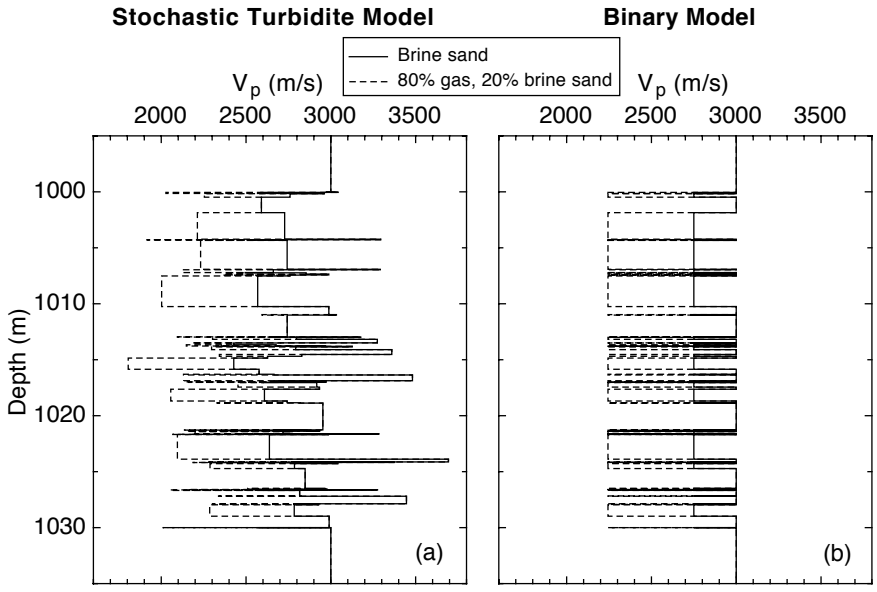

Fig. 4.16. Comparison of STM and binary models and after performing fluid substitution of 80% gas saturation in the sand layers. (a) In the STM, sand and shale beds alternatively appear with a large heterogeneity of layer thicknesses and velocity. (b) In the binary model, the model has the same thickness distribution, but with identical sand and shale properties.

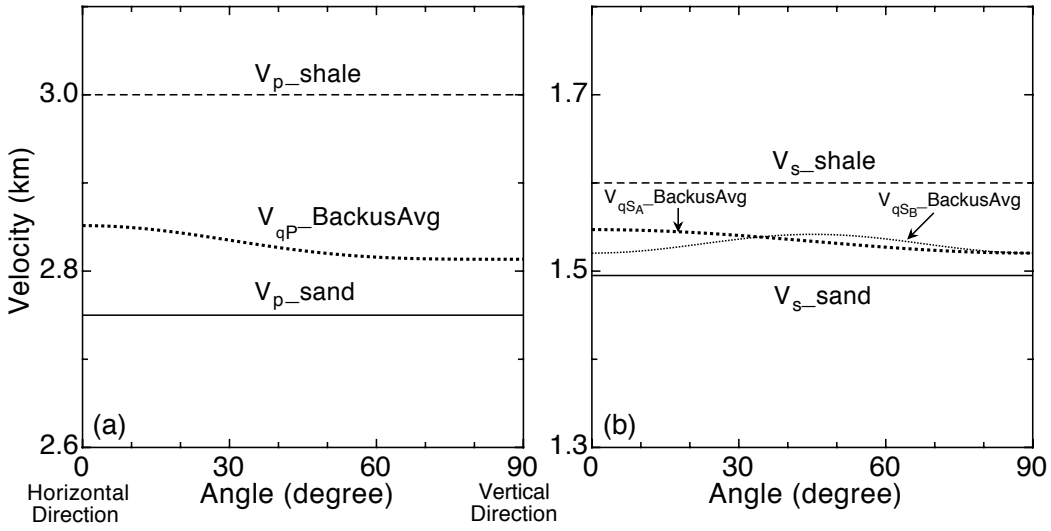

Fig. 4.17. (a) qP-wave phase velocity as a function of angle in a Backus-averaged model (See Figure 4.15b). Phase velocity in the horizontal direction is about 1.4% faster than in the vertical direction. (b) qS-wave phase velocity as a function of angle in a Backus-averaged model for two qS waves.

STM vs. Binary Model

Figure 4.18 shows the P-wave reflections for the three different source central frequencies. At the source frequency of 10 and 20 Hz, the thickness/wavelength ratio is around 1/9 and 2/9, respectively. The wavelength is too long for the seismic reflections to be very sensitive to the details of the structure of the thin turbidite reservoir, and the waveform remains close to that of the input Ricker wavelet. Comparing the wavelets at all three frequencies, the high frequency energy indicates more detail of the interior layer structure because it has more changes in waveform for each of the models. Also, the results after the brine sands are 80% saturated by gas are shown in Figure 4.19. Same gain is applied in both Figures 4.18 and 4.19.

Comparing the wavelets at all three frequencies, the high frequency energy indicates more detail of the interior layer structure because it has more changes in waveform for each of the models. Comparing the amplitudes in STMs and binary models, STMs always have strong amplitudes because of the heterogeneity of velocity and density. Also, because of gas saturation in the sand beds, the models have stronger contrast properties and show the stronger amplitudes in the synthetic seismograms.

STM vs. Backus-averaged STM Model

An important question of the application to the field data is whether it is possible to replace a complex, stratified reservoir by a simple, homogeneous layer using the Backus Averaging. Here, Backus-averaged STMs are used to generate full waveform synthetic seismograms and compared to the original STMs' results.

Figure 4.20 shows the comparison of P-wave reflections between STMs and Backus-averaged models for the three different source central frequencies. All sands in both model are 100% brine-saturated. Figure 4.21 shows after substituting brine by gas in sand beds of STMs and Backus-averaged STMs, we have much stronger reflected energy than the previous brine sand models. Same gain is applied in both figures. Black solid traces represent STM results. Red dashed traces show Backus-averaged STM results. In the lower frequency, the wavelength is too long to be sensitive to the internal fluctuation in velocity and thickness. In the overlapped synthetic seismograms, original and Backus-averaged STMs produce the negligible difference in seismic responses. However, while the source frequency goes higher, the

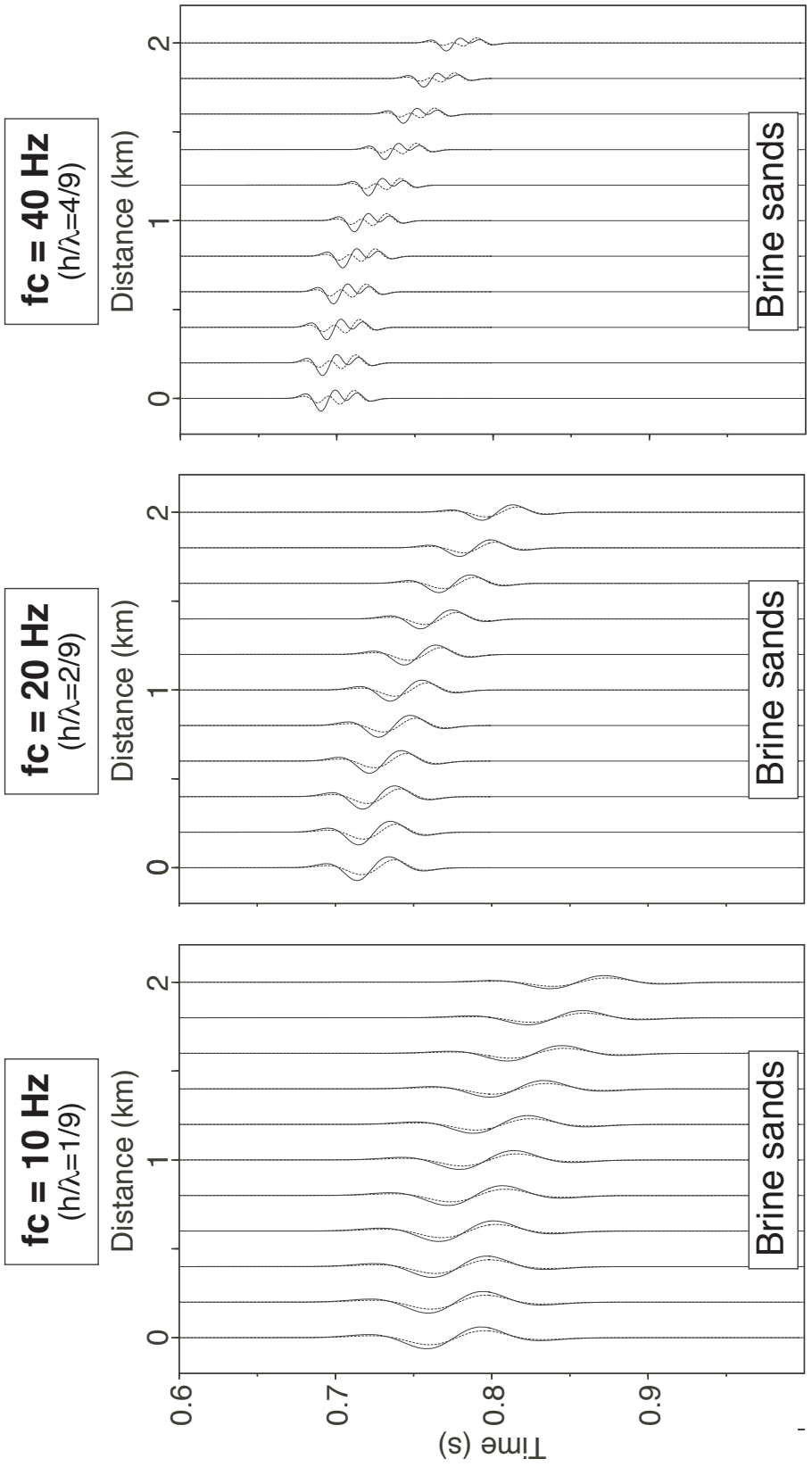

Fig. 4.18. Comparison of P-wave reflections between STMs and binary models for the three different source central frequencies. All sands in both model are 100% brine-saturated. Solid traces represent STM results. Dashed traces show binary model results.

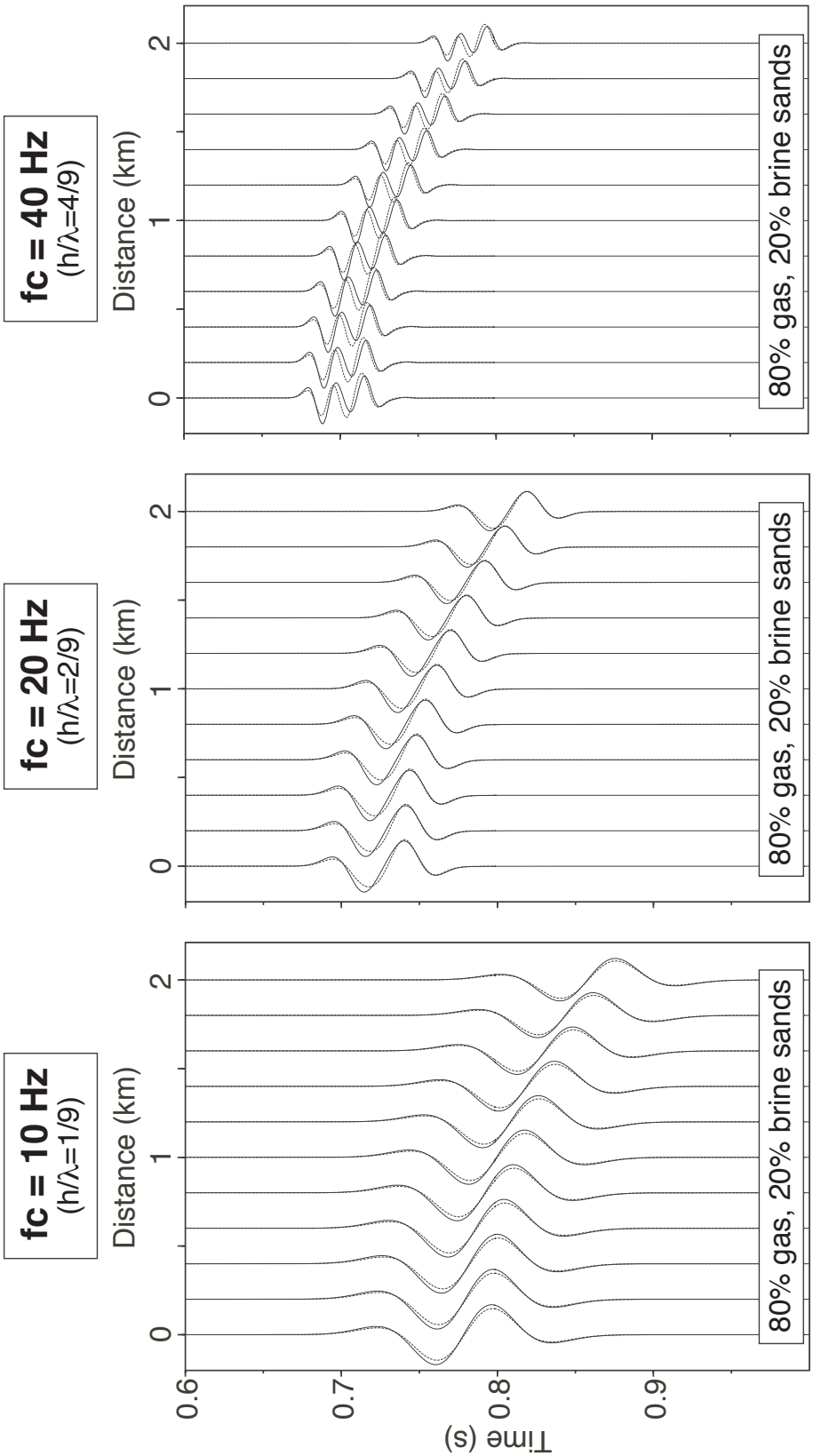

Fig. 4.19. After substituting brine by gas in sand beds of STMs and binary models, we have much stronger reflected energy than the previous brine sand models. Same gain is applied in both Figure 4.18 and 4.19. Solid traces represent STM results. Dashed traces show binary model results.

internal fluctuation is detectable and causes noticeable difference in the synthetic seismograms.

We can assess the variability in seismic signals that might be observed for different turbidite sequences having the same general statistical properties by superposing the near offset traces for each frequency (Figure 4.22). The results show the complexity introduced by changes in the vertical structure of the sand/shale beds. These types of variability might be observed in field settings where different vertical turbidite structures are observed at different positions in the reservoir. More analyses of amplitudes are discussed in the Analyses section.

4.4 Analyses

4.4.1 Statistical Analysis of Maximum Amplitudes

Though synthetic seismograms provide a general illustration of our stochastic models, it is difficult to quantitatively assess the variability from these displays. Therefore, the statistical analysis of seismic attributes may provide a more useful illustration of the results and uncertainty in seismic signals. We measured the maximum amplitude for each trace and computed its mean and standard deviation for each model.

Figure 4.23 shows the mean value of maximum amplitude (symbol) of each refection and its one standard deviation (error bars) for source frequency at 10, 20, and 40 Hz. We have larger means of maximum amplitudes and its standard deviations in STMs than binary models. While increasing source frequency, two models show more differences of their means of maximum amplitudes. At the same time, the standard deviation decreases with increasing offset, showing that the vertical velocity structure has the strongest influence on vertically traveling waves. While gas presents in the sand layers, we have much stronger means of maximum amplitudes and larger standard deviations in each frequency panel. Figure 4.24 shows the results after gas substitution.

4.4.2 AVO Analysis

By taking the maximum amplitudes of the reflection of less than 30° incident angle, removing the geometrical spreading factor, and correcting vector amplitudes, we can measure conventional AVO intercepts and gradients. Figure 4.25 shows AVO analysis

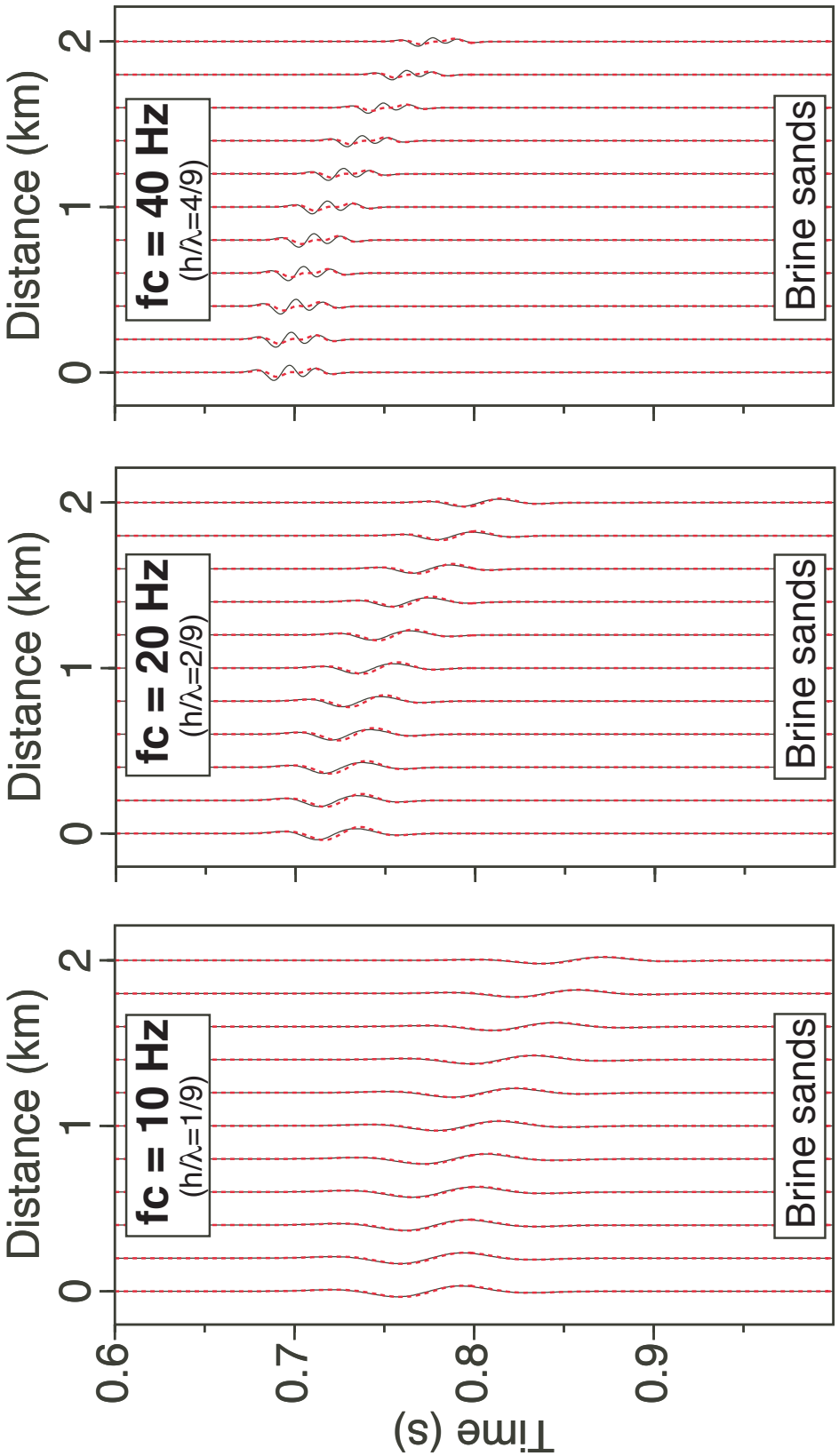

Fig. 4.20. Comparison of P-wave reflections between STMs and Backus-averaged models for the three different source central frequencies. All sands in both model are 100% brine-saturated. Black solid traces represent STM results. Red dashed traces show Backus-averaged STM results. Backus averaging algorithm produces a good equivalent model while the wavelength is relative long to the total thickness of layers.

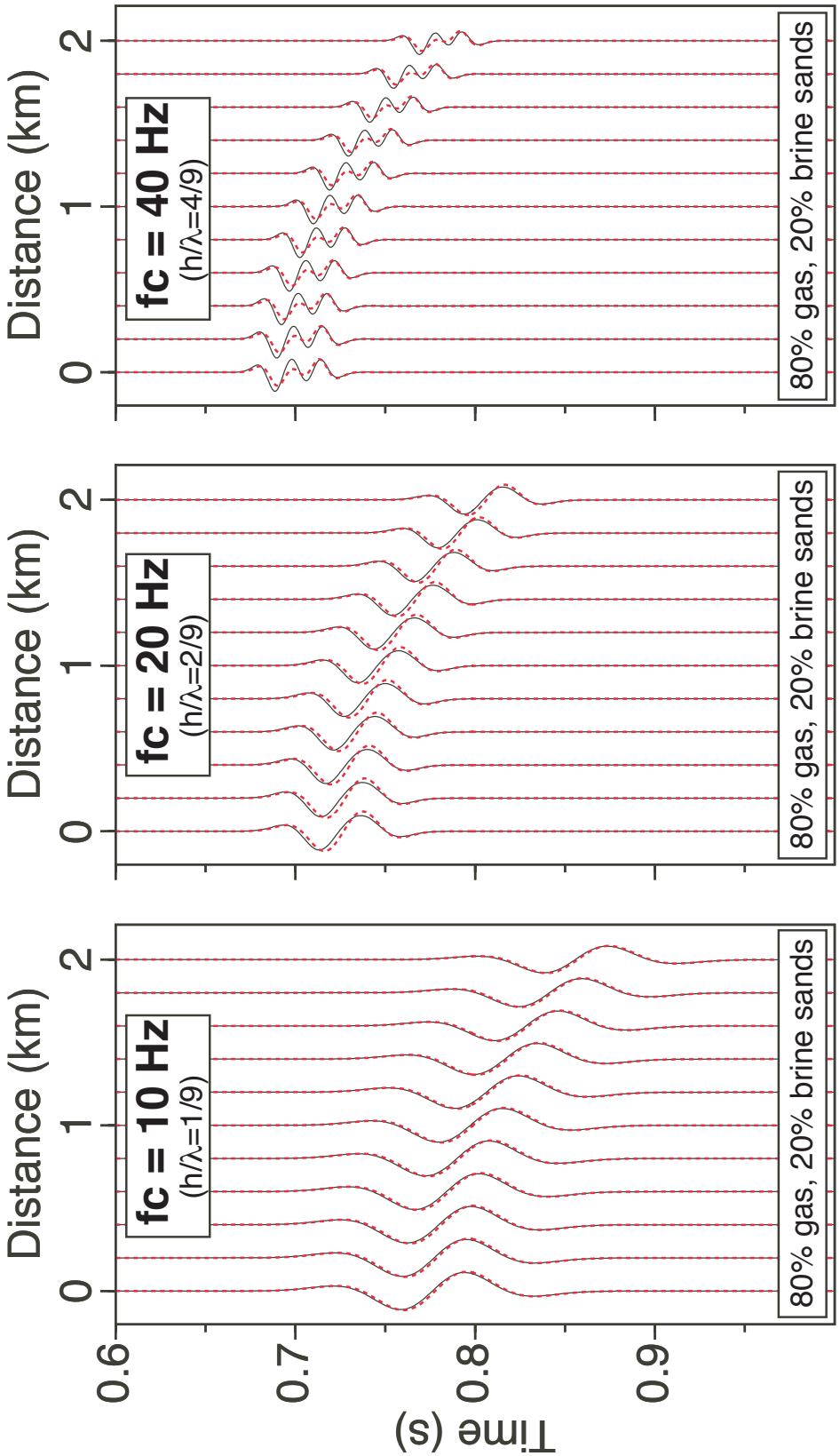

Fig. 4.21. After substituting brine by gas in sand beds of STMs and Backus-averaged STMs, we have much stronger reflected energy than the previous brine sand models. Same gain is applied in both Figure 4.20 and 4.21.

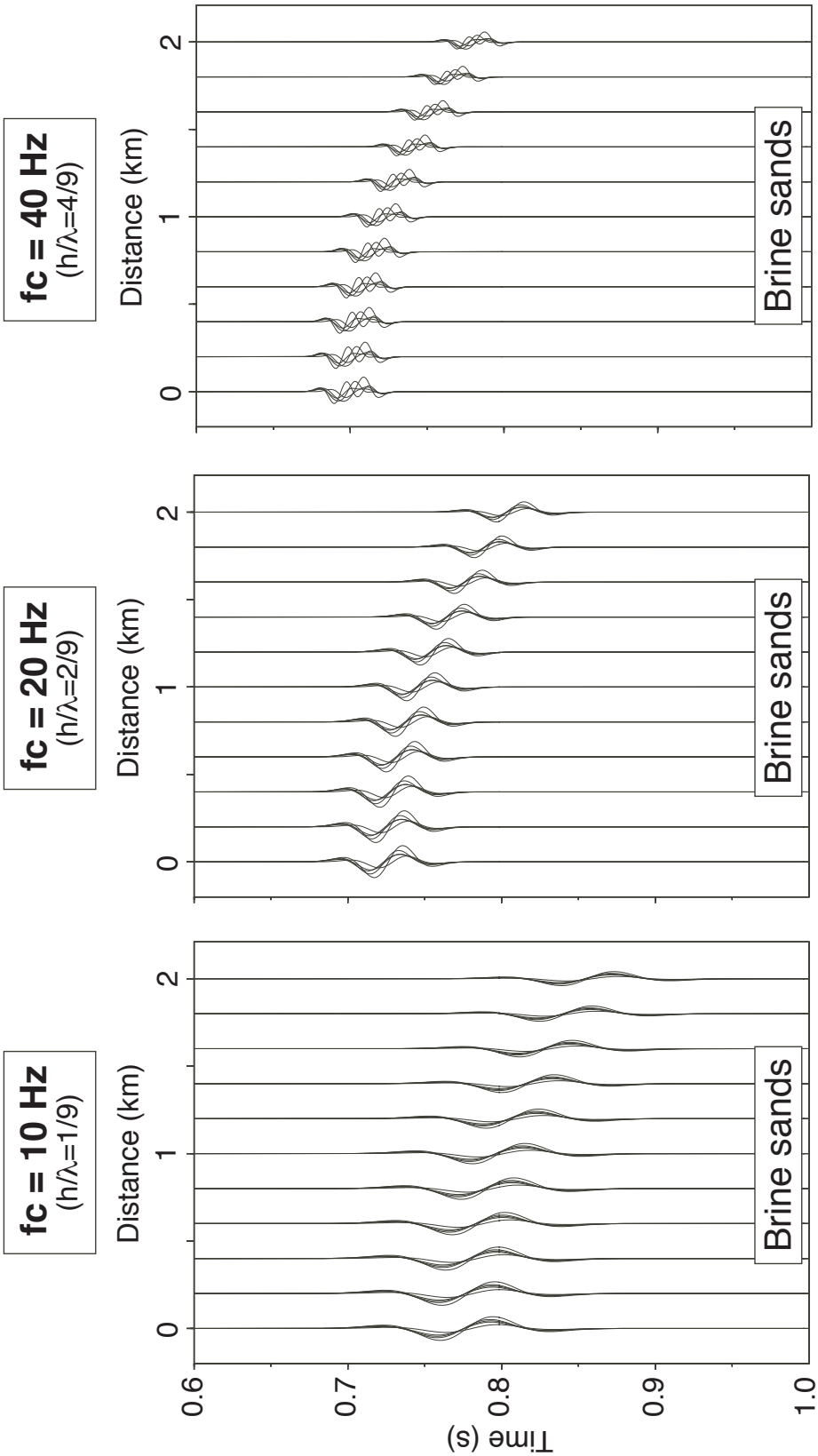

Fig. 4.22. Comparison of synthetic seismograms from 5 realizations in brine sand STMs for three different source central frequencies. The results show the complexity introduced by changes in the vertical structure of the sand/shale beds.

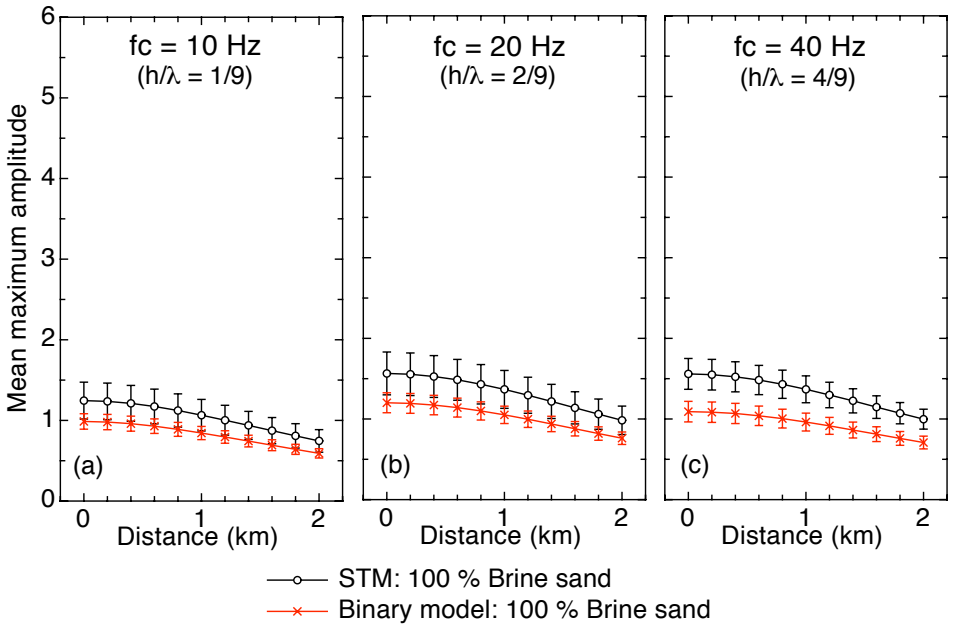

Fig. 4.23. The mean value of maximum amplitude (symbol) of each reflection and its one standard deviation (error bars) for source frequency at 10, 20, and 40 Hz. While increasing source frequency, two models show more differences of their means of maximum amplitudes

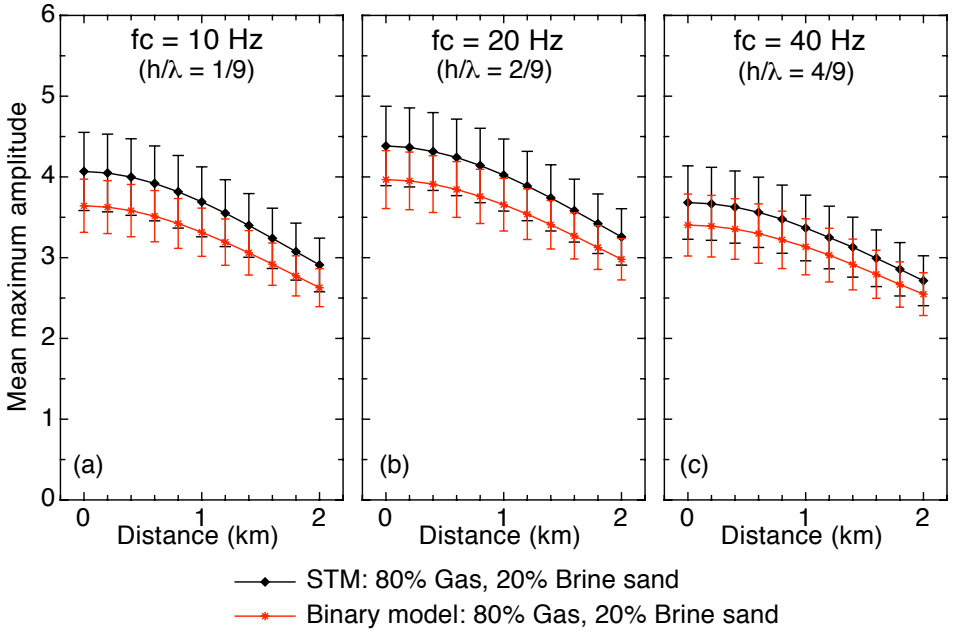

Fig. 4.24. After 80% gas saturating in the sand beds, we have stronger means of maximum amplitudes and larger standard deviations in each frequency panel.

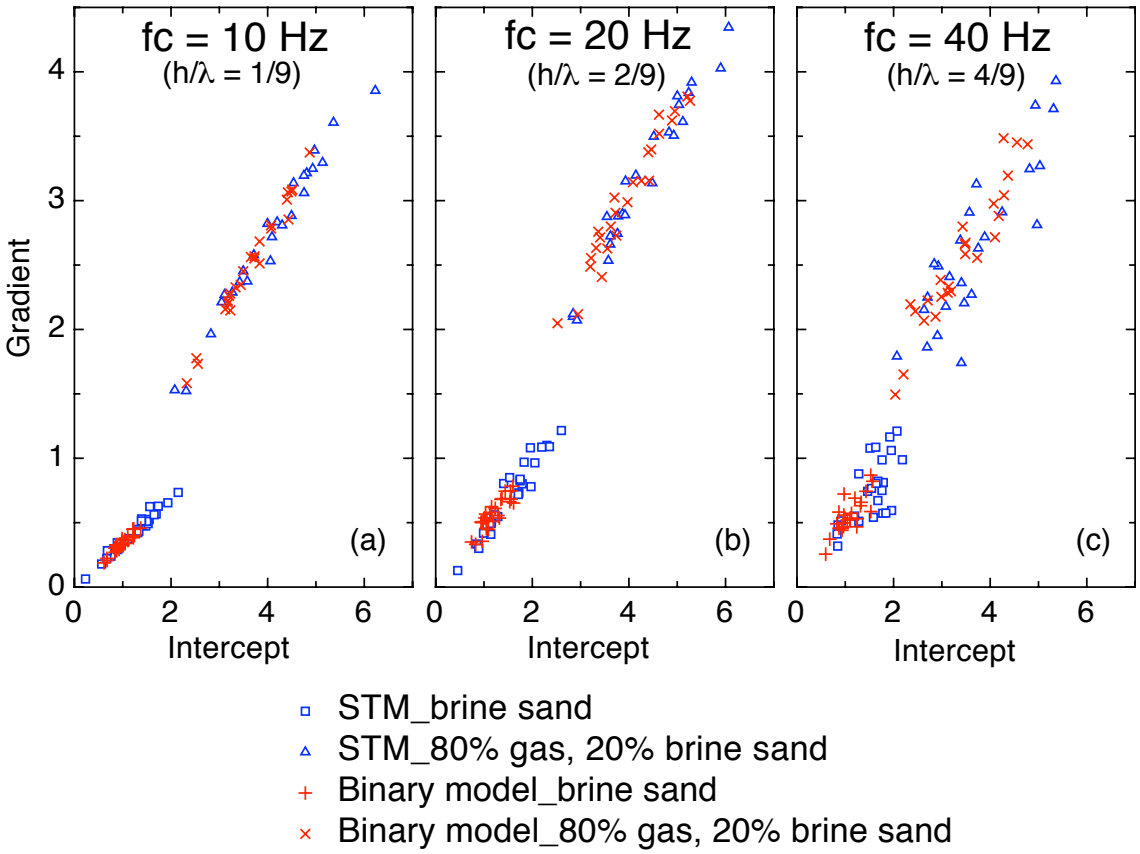

Fig. 4.25. Maximum amplitudes of the reflections less than 30° incident angle are measured for AVO analysis. Binary models have less fluctuation in AVO crossplots than STMs. Also, high source frequency produces more heterogeneity in reflections from the turbidite reservoir models.

for three different source frequencies. In the AVO crossplots, we can distinguish brine sand models from gas sand models easily. However, while the source frequency goes higher (40 Hz case), the widely scattered cloud of AVO responses for brine and gas sands may have been overlapped and cause the false interpretation for AVO responses. There are not much noticeable differences between STMs and binary models in the low frequency. However, binary models always have less fluctuation in AVO responses than the STMs.

4.5 Conclusions

Stochastic modeling incorporating the geological interpretation and well log measurements provides seismic models of typical turbidite sequences. The new model generation scheme produces more realistic models than simple binary mixture approaches.

Synthetic seismograms for models designed to simulate turbidite sequences in the Gulf of Mexico show how much change in seismic data might be associated with vertical heterogeneity. The Backus-averaging algorithm provides a good equivalent model in the the lower frequency and the wavelength is too long to produce the noticeable difference in seismic responses. However, while the source frequency goes higher, the internal fluctuation is detectable and causes noticeable difference in the synthetic seismograms.

Statistical analyses of the maximum amplitudes of the reflections from the simulated turbidite sequences provide clear insights to estimate influence of heterogeneity, showing that scatter increases at near offsets and for higher frequencies. AVO analysis also demonstrates the heterogeneity of the turbidite reservoirs and the presence of gas saturation. Gas-charged sand layers increase the strong contrast of the internal rock properties of the reservoir and produce more scattered AVO responses in both STMs and binary model. However, STMs always have wider distribution of uncertainties of seismic responses than binary models. In the low frequency range, STMs have less difference from the binary models in the synthetic seismograms. As the frequency increases, STMs better show the complexity of turbidite reservoirs. Also, the widely scattered clouds of AVO responses for brine and gas sands predict the possibility of false interpretation in AVO analysis.

CHAPTER V

CONCLUSIONS

Though quasi-shear wave propagation is complicated and is a challenging application in seismic modeling, the WFC still is an attractive modeling approach. We have shown that particle motion vectors are an effective criterion not only for qS wave ray tracing, but also for creating initial wavefront meshes and for guiding wavefront interpolation while propagating wavefronts through an earth model.

Modeling of two qS wave wavefronts through homogeneous, VTI models shows the that line singularities are correctly handled, as well as in the heterogeneous, VTI model. A set of verification for traveltimes and amplitudes demonstrates the accuracy and robustness of WFC algorithms, and multivalued arrivals are correctly mapped. In addition, the ray data obtained by WFC are used to generate synthetic seismograms for these models and compared to the full waveform solutions generated by the discrete wavenumber method. Except for the qSV-wave modeling around triplications, all the comparisons of synthetic seismograms demonstrate negligible differences between these two methods. In the future work, the qS wave synthetic seismograms can be compared with the field data and focus the development of the WFC method in the multi-region models.

Ray tracing including composite reflection coefficients can be a fast and accurate method to generate full waveform synthetic seismograms in the complex, stratified reservoir model. This hybrid method implements fast ray tracing in the overburden and the exact solution of P-wave composite reflection coefficients computed by the propagator matrix method to generate the complete synthetic seismograms for the P-wave reflection. Comparison of P-wave reflection synthetic seismograms for a complex, stratified reservoir model, based on the well logs in Gulf of Mexico, shows a excellent agreement between this hybrid method and discrete wavenumber method. More importantly, the hybrid method demonstrates the capability to generate synthetic seismograms for the tilted, complex stratified reservoir models. In the future work, the hybrid method can include the seismic modeling in the conversion, which also an important information to locate hydrocarbons.

In addition, seismic turbidite models (STMs) generated from a combination of

geological interpretation and well log measurements, are created to simulate direct hydrocarbon indicator associated with turbidite sequences. The hybrid method can be used to generate complete P-wave reflection synthetic seismograms. Accurately estimated amplitudes are applied in AVO analysis. STMs provide important insights to predict the seismic responses for the complexity of turbidite reservoirs. Furthermore, as the source frequency increases, the widely scattered clouds of AVO responses for brine and gas sands predict the possibility of false interpretation in AVO analysis.

REFERENCES

Aki, K., and Richards, P., 2002, Quantitative seismology, 2nd edition: University Science Books.

Alkhalifah, T., and Tsvankin, I., 1995, Velocity analysis for transversely isotropic media: Geophysics, **60**, 1550–1566.

Almoghrabi, H., and Lange, J., 1986, Layers and bright spots: Geophysics, **51**, 699–709.

Avseth, P., and Mukerji, T., 2002, Seismic lithofacies classification from well logs using statistical rock physics: Petrophysics, **43**, 70–81.

Backus, G. E., 1962, Long-wave elastic anisotropy produced by horizontal layering: Journal of Geophysical Research, **67**, 4427–4440.

Bakke, N., and Ursin, B., 1998, Thin-bed AVO effects: Geophysical Prospecting, **46**, 571–587.

Banik, N., 1984, Velocity anisotropy of shales and depth estimation in the North Sea basin: Geophysics, **49**, 1411–1419.

Ben-Menahem, A., Gibson, Jr., R., and Sena, A., 1991, Green's tensor and radiation patterns of point sources in general anisotropic inhomogeneous elastic media: Geophysical Journal International, **107**, 297–308.

Booth, D., and Crampin, S., 1983, The anisotropic reflectivity technique: Theory: Geophysical Journal of the Royal Astronomical Society, **72**, 755–766.

Castagna, J. P., and Smith, S. W., 1994, Comparison of AVO indicators: A modeling study: Geophysics, **59**, 1849–1855.

Castagna, J. P., Swan, H. W., and Foster, D. J., 1998, Framework for AVO gradient and intercept interpretation: Geophysics, **63**, 948–956.

Červený, V., 1972, Seismic rays and ray intensities in inhomogeneous anisotropic media: Geophysical Journal of the Royal Astronomical Society, **29**, 1–13.

——— 1989, Synthetic body wave seismograms for laterally varying media containing thin transition layers: Geophysical Journal International, **99**, 331–349.

——— 2001, Seismic ray theory: Cambridge University Press, Cambridge.

Chapman, C. H., and Shearer, P. M., 1989, Ray tracing in azimuthally anisotropic media – II. Quasi-shear wave coupling: Geophysical Journal of the Royal Astronomical Society, **96**, 65–85.

Coates, R. T., and Chapman, 1990, Quasi-shear wave coupling in weakly anisotropic 3-D media: Geophysical Journal International, **103**, 301–320.

Crampin, S., and Chastin, S., 2003, A review of shear wave splitting in the crack-critical crust: Geophysical Journal International, **155**, 221–240.

Crampin, S., and Yedlin, M., 1981, Shear-wave singularities of wave propagation in anisotropic media: Journal of Geophysics, **49**, 43–46.

Crampin, S., 1985, Evaluation of anisotropy by shear-wave splitting: Geophysics, **50**, 142–152.

Domenico, S. N., 1976, Effect of brine-gas mixture on velocity in an unconsolidated sand reservoir: Geophysics, **41**, 882–894.

Douma, J., and Crampin, S., 1990, The effect of a changing aspect ratio of aligned cracks on shear wave vertical seismic profiles: A theoretical study: Journal of Geophysical Research; B; Solid Earth and Planets, **95**, 11293–11300.

Gajewski, D., and Pšenčik, I., 1987, Computation of high-frequency seismic wavefields in 3-D laterally inhomogeneous anisotropic media: Geophysical Journal of the Royal Astronomical Society, **91**, 383–411.

Gassmann, F., 1951, Über die elastizität poröser medien: Vier. der Natur. Gesellschaft in Zürich, **96**, 1–23.

Gibson, Jr., R. L., Durussel, V., and Lee, K.-J., 2005, Modeling and velocity analysis with a wavefront-construction algorithm for anisotropic media: Geophysics, **70**, T63–T74.

Gibson, Jr., R. L., 1999, Ray tracing by wavefront construction in 3-D, anisotropic media: EOS Trans., Amer. Geophys. Union, **80**, F696.

Gibson, Jr., R. L., 2004, Composite reflection coefficients for stratified reservoir models: SEG Technical Program Expanded Abstracts, **23**, 267–270.

——— 2005, Influence of internal reservoir structure on composite reflection coefficients: SEG Technical Program Expanded Abstracts, **24**, 312–315.

Gilbert, F., and Backus, G. E., 1966, Propagator matrices in elastic wave and vibration problems: Geophysics, **31**, 326–332.

Grech, M. G. K., Lawton, D. C., and Gray, S. H., 2002, A multioffset vertical seismic profiling experiment for anisotropy analysis and depth imaging: Geophysics, **67**, 348–354.

Grechka, V., and Tsvankin, I., 1998, Feasibility of nonhyperbolic moveout inversion in transversely isotropic media: Geophysics, **63**, 957–969.

Grechka, V., Pech, A., Tsvankin, I., and Han, B., 2001, Velocity analysis for tilted transversely isotropic media: A physical modeling example: Geophysics, **66**, 904–910.

Hanyga, A., 1982, Dynamic ray tracing in an anisotropic medium: Tectonophysics, **90**, 243–251.

Haskell, N., 1953, The dispersion of surface waves in multilayered media: Bulletin of the Seismological Society of America, **43**, 17–34.

Hiscott, R. N., Colella, A., Pezard, P., Lovell, A. M., and Malinverno, A., 1992, Sedimentology of deep-water volcaniclastics, Oligocene Izu-Bonin forearc basin, based on formation microscanner images.: Proceedings of the Ocean Drilling Program, Scientific Results, **126**, 75–96.

Hornby, B. E., Howie, J. M., and Ince, D. W., 2003, Anisotropy correction for deviated-well sonic logs: Application to seismic well tie: Geophysics, **68**, 464–471.

Horne, S., MacBeth, C., and Liu, E., 1997, "Unexpected" shear-wave behavior: Geophysics, **62**, 1879–1883.

Isaac, J. H., and Lawton, D. C., 1999, Image mispositioning due to dipping TI media: A physical seismic modeling study: Geophysics, **64**, 1230–1238.

Juhlin, C., and Young, R., 1993, Implications of thin layers for amplitude variation with offset (AVO) studies: Geophysics, **58**, 1200–1204.

Kallweit, R. S., and Wood, L. C., 1982, The limits of resolution of zero-phase wavelets: Geophysics, **47**, 1035–1046.

Kaschwich, T., and Gajewski, D., 2003, Wavefront-oriented ray tracing in 3D anisotropic media: EAGE 65^{th} Conference & Technical Exhibition, P–041.

Kennett, B., and Kerry, N., 1979, Seismic waves in a stratified half space: Geophysical Journal of the Royal Astronomical Society, **57**, 557–583.

Kumar, D., Sen, M. K., and Ferguson, R. J., 2004, Traveltime calculation and prestack depth migration in tilted transversely isotropic media: Geophysics, **69**, 37–44.

Kvam, O., and Landro, M., 2005, Pore-pressure detection sensitivities tested with time-lapse seismic data: Geophysics, **70**, O39–O50.

Lai, H.-L., and Gibson, Jr., R. L., 2005, Stochastic models of turbidite reservoirs for seismic simulations: SEG Technical Program Expanded Abstracts, **24**, 1453–1456.

Lai, H.-L., Gibson, Jr., R. L., and Lee, K.-J., 2004, Quasi-shear wave ray tracing by wavefront construction in 3-D, anisotropic media: SEG Technical Program Expanded Abstracts, **23**, 1909–1912.

Lambaré, G., Lucio, P., and Hanyga, A., 1996, Two-dimensional multivalued traveltime and amplitude maps by uniform sampling of a ray field: Geophysical Journal International, **125**, 584–598.

Landro, M., 2001, Discrimination between pressure and fluid saturation changes from time-lapse seismic data: Geophysics, **66**, 836–844.

Lee, K.-J., and Gibson, Jr., R. L., 2005, Traveltime estimation using a model-based interpolation ray-tracing method for layered models: SEG Technical Program Expanded Abstracts, **24**, 1767–1770.

Leslie, J. M., and Lawton, D. C., 1999, A refraction-seismic field study to determine the anisotropic parameters of shales: Geophysics, **64**, 1247–1252.

Levin, F. K., 1978, The reflection, refraction, and diffraction of waves in media with an elliptical velocity dependence: Geophysics, **43**, 528–537.

——— 1979, Seismic velocities in transversely isotropic media: Geophysics, **44**, 918–936.

——— 1980, Seismic velocities in transversely isotropic media, II: Geophysics, **45**, 3–17.

Liu, Y., and Schmitt, D. R., 2003, Amplitude and AVO responses of a single thin bed: Geophysics, **68**, 1161–1168.

Lucio, P. S., Lambaré, G., and Hanyga, A., 1996, 3D multivalued traveltime amd amplitude maps: Pure and Applied Geophysics, **148**, 449–479.

Meckel, L., Ugueto, G., Lynch, D., Cumming, E., Hewett, B., Bocage, E., Winker, C., and O'Neil, B., 2002, Genetic stratigraphy, stratigraphic architecture, and reservoir stacking patterns of the Upper Miocene-Lower Pliocene Greater Mars-Ursa Intraslope Basin, Mississippi Canyon, Gulf of Mexico: 22nd Annual Gulf Coast Section SEPM Foundation, pages 113–147.

Mispel, J., and Williamson, P., 2001, 3-D wavefront construction for P & SV waves in transversely isotropic media: EAGE 63^{rd} Conference & Technical Exhibition, Paper P094.

Mispel, J., 2001, Transversely isotropic media: 3-D wavefront construction method and pre-stack depth migration: Ph.D. thesis, Imperial College, Univ. of London.

Müller, G., 1985, The reflectivity method: A tutorial: Journal of Geophysics, **58**, 153–174.

Murphy, W., 1984, Acoustic measures of partial gas saturation in tight sandstones: Journal of Geophysical Research, **89**, 11,549–11,559.

Nistala, S., and McMechan, G. A., 2005, 3D modeling of fracture-induced shear-wave splitting in the Southern California basin: Bulletin of the Seismological Society of America, **95**, 1090–1100.

Ostrander, W. J., 1984, Plane-wave reflection coefficients for gas sands at nonnormal angles of incidence: Geophysics, **49**, 1637–1648.

Pirmez, C., Hiscott, R. N., and Kronen, J. D. J., 1997, Sandy turbidite successions at the base of channel-levee systems of the Amazon Fan revealed by FMS logs and cores; unraveling the facies architecture of large submarine fans: Proceedings of the Ocean Drilling Program, Scientific Results, **155**, 7–33.

Ramos, A. C. B., and Castagna, J. P., 2001, Useful approximations for converted-wave AVO: Geophysics, **66**, 1721–1734.

Ramos-Martinez, J., Ortega, A. A., and McMechan, G. A., 2000, 3-D seismic modeling for cracked media: Shear-wave splitting at zero-offset: Geophysics, **65**, 211–221.

Ross, C. P., 2000, Effective AVO crossplot modeling: A tutorial: Geophysics, **65**, 700–711.

Rothman, D. H., Grotzinger, J., and Flemings, P., 1994, Scaling in turbidite deposition: Journal of Sedimentary Research, **64**, 59–67.

Rüger, A., 2004, Aspects of modern raytracing application design: Studia Geophysica et Geodaetica, **48**, 143–165.

Rutherford, S. R., and Williams, R. H., 1989, Amplitude-versus-offset variations in gas sands: Geophysics, **54**, 680–688.

Shearer, P. M., and Chapman, C. H., 1989, Ray tracing in azimuthally anisotropic media – I. Results for models of aligned cracks in the upper crust: Geophysical Journal of the Royal Astronomical Society, **96**, 51–64.

Sheriff, R. E., and Geldart, L. P., 1995, Exploration seismology, 2nd edition: Cambridge University Press, Cambridge.

Shuey, R. T., 1985, A simplification of the Zoeppritz equations: Geophysics, **50**, 609–614.

Simmons, Jr., J. L., and Backus, M. M., 1994, AVO modeling and the locally converted shear wave: Geophysics, **59**, 1237–1248.

Slater, C., Crampin, S., Brodov, L. Y., and Kuznetsov, V. M., 1993, Observations of anisotropic cusps in transversely isotropic clay: Canadian Journal of Exploration Geophysics, **29**, 216–226.

Smith, T. M., and Sondergeld, C. H., 2001, Examination of AVO responses in the eastern deepwater Gulf of Mexico: Geophysics, **66**, 1864–1876.

Stovas, A., Landro, M., and Avseth, P., 2004, Estimation of net-to-gross and fluid saturation in a fine-layered sand-shale sequence — tested on offshore Brazil data: SEG Technical Program Expanded Abstracts, **23**, 228–231.

Stovas, A., Landro, M., and Avseth, P., 2006, AVO attribute inversion for finely layered reservoirs: Geophysics, **71**, C25–C36.

Takahashi, I., Mukerji, T., and Mavko, G., 1999, Effect of thin-layering on seismic reflectivity: Estimation of sand/shale ratio using stochastic simulation and Bayes' inversion: SEG Technical Program Expanded Abstracts, **18**, 1787–1790.

Talling, P. J., 2001, On the frequency distribution of turbidite thickness: Sedimentology, **48**, 1297–1329.

Thomsen, L., and Dellinger, J., 2003, On shear-wave triplication in transversely isotropic media: Journal of Applied Geophysics, **54**, 289–296.

Thomsen, L., 1986, Weak elastic anisotropy: Geophysics, **51**, 1954–1966.

Thomson, W., 1950, Transmission of elastic waves through a stratified solid medium: Journal of Applied Physics, **21**, 89–93.

Vavryčuk, V., 2001, Ray tracing in anisotropic media with singularities: Geophysical Journal International, **145**, 265–276.

——— 2004, Approximate conditions for the off-axis triplication in transversely isotropic media: Studia Geophysica et Geodaetica, **48**, 187–198.

Vestrum, R. W., Lawton, D. C., and Schmid, R., 1999, Imaging structures below dipping TI media: Geophysics, **64**, 1239–1246.

Vinje, V., Iversen, E., and Gjøystdal, H., 1993, Traveltime and amplitude estimation using wavefront construction: Geophysics, **58**, 1157–1166.

Vinje, V., Iversen, E., Åstebøl, K., and Gjøystdal, H., 1996, Estimation of multi-valued arrivals in 3D models using wavefront construction – Part I: Geophysical Prospecting, **44**, 819–842.

Vinje, V., Åstebøl, K., Iversen, E., and Gjøystdal, H., 1999, 3-D ray modeling by wavefront construction in open models: Geophysics, **64**, 1912–1919.

Wandler, A., Evans, B., and Link, C., 2007, AVO as a fluid indicator: A physical modeling study: Geophysics, **72**, C9–C17.

White, J. E., 1982, Computed waveforms in transversely isotropic media: Geophysics, **47**, 771–783.

Widess, M. B., 1973, How thin is a thin bed?: Geophysics, **38**, 1176–1180.

Winterstein, D., 1986, Anisotropy effects in P-wave and SH-wave stacking velocities contain information on lithology: Geophysics, **51**, 661–672.

Wood, A. B., 1941, A textbook of sound: G. Bell and Sons.

Zillmer, M., 2006, A method for determining gas-hydrate or free-gas saturation of porous media from seismic measurements: Geophysics, **71**, N21–N32.

APPENDIX A

FLOWCHARTS OF QUASI-SHEAR WAVE RAY TRACING BY WAVEFRONT CONSTRUCTION

Figure A1 demonstrates the algorithms of qS wave ray tracing by wavefront construction. The extension work of WFC for qS wave modeling is focused on qS wave ray tracing, mesh initialization and mesh interpolation. See the details in Methods section, Chapter II. In order to model two qS waves, for simplicity, WFC algorithm models each wave type wavefront at one time through the earth model.

The WFC starts with setting earth model and ray parameters which include elastic moduli, mesh construction method, takeoff angles of rays, model geometry etc.. Then, we use the particle motion of one qS wave as the criterium to separate two qS wave initial wavefront meshes. See Figure 2.1 of defining two qS wave wavefronts. We model two qS wavefields sequentially. Finally, the ray information at receivers are mapped. Visualization of the wavefront meshes at wavefront times are also available.

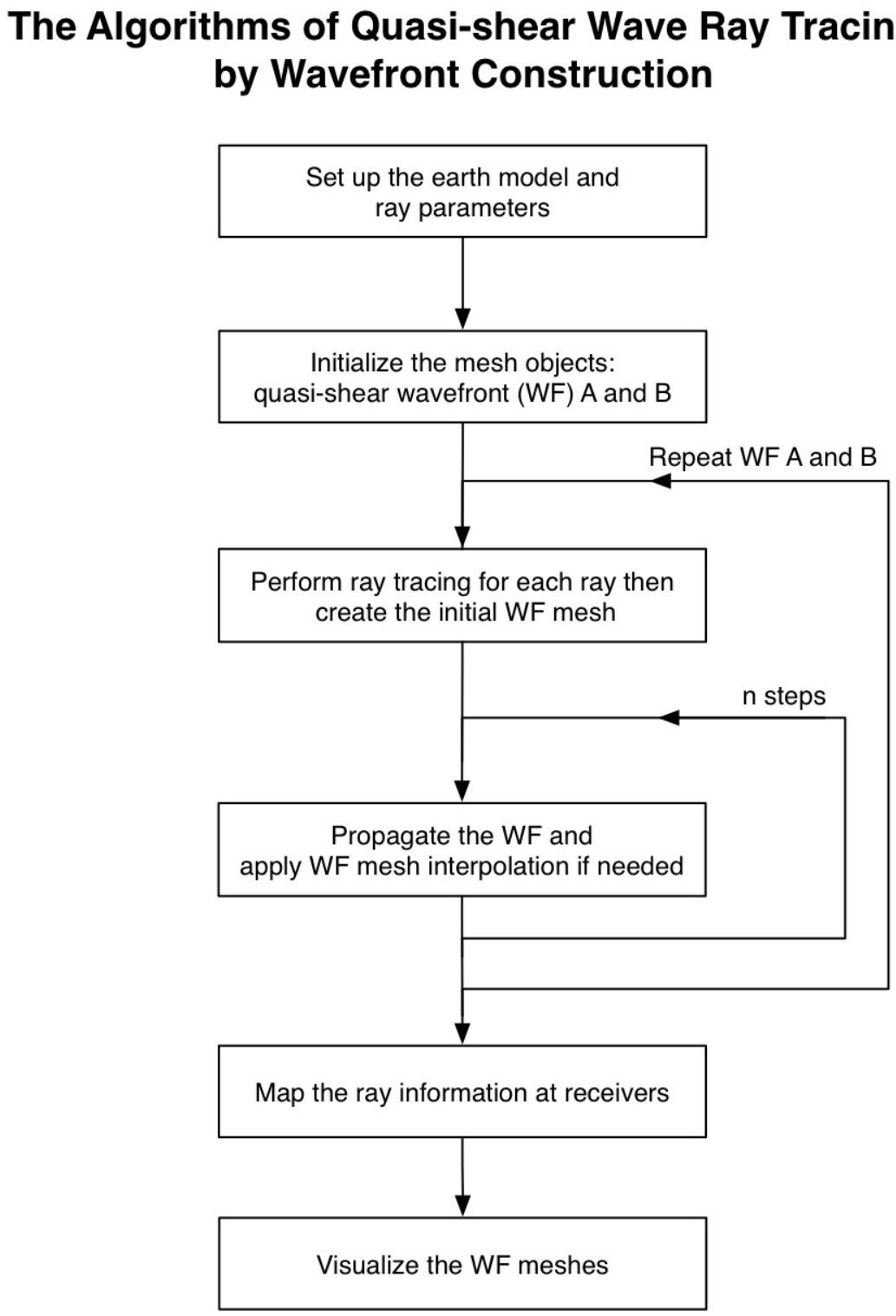

Fig. A1. Flowchart of the algorithms of quasi-shear wave ray tracing by wavefront construction.

APPENDIX B

FLOWCHARTS OF SEPARATING qS_A AND qS_B WAVE WAVEFRONT MESHES

Because physical wavefronts intersect and change order of velocities, the construction of wavefront meshes must instead assign initial ray velocities and geometries using a criterion other than magnitude of phase or group velocity (Figure 2.1). Figure B1 shows the flowchart of determining qS_1 and qS_2 wave types to form a physically meaningful wavefront mesh in the present of the singularity. Because the particle motion vectors will generally change direction relatively slowly on the wavefront, we can use them as criteria to distinguish qS_A and qS_B wavefront meshes. At beginning, we pick $qS1$ wave displacement vector as a reference. While looping over all mesh nodes to separate qS_A and qS_B waves, the inner product of the displacement vectors on the current node and previous (or reference) node have to be smaller than a predefined threshold value. The subsection, Mesh Initialization, in Methods section, Chapter II, explains more details and discussions.

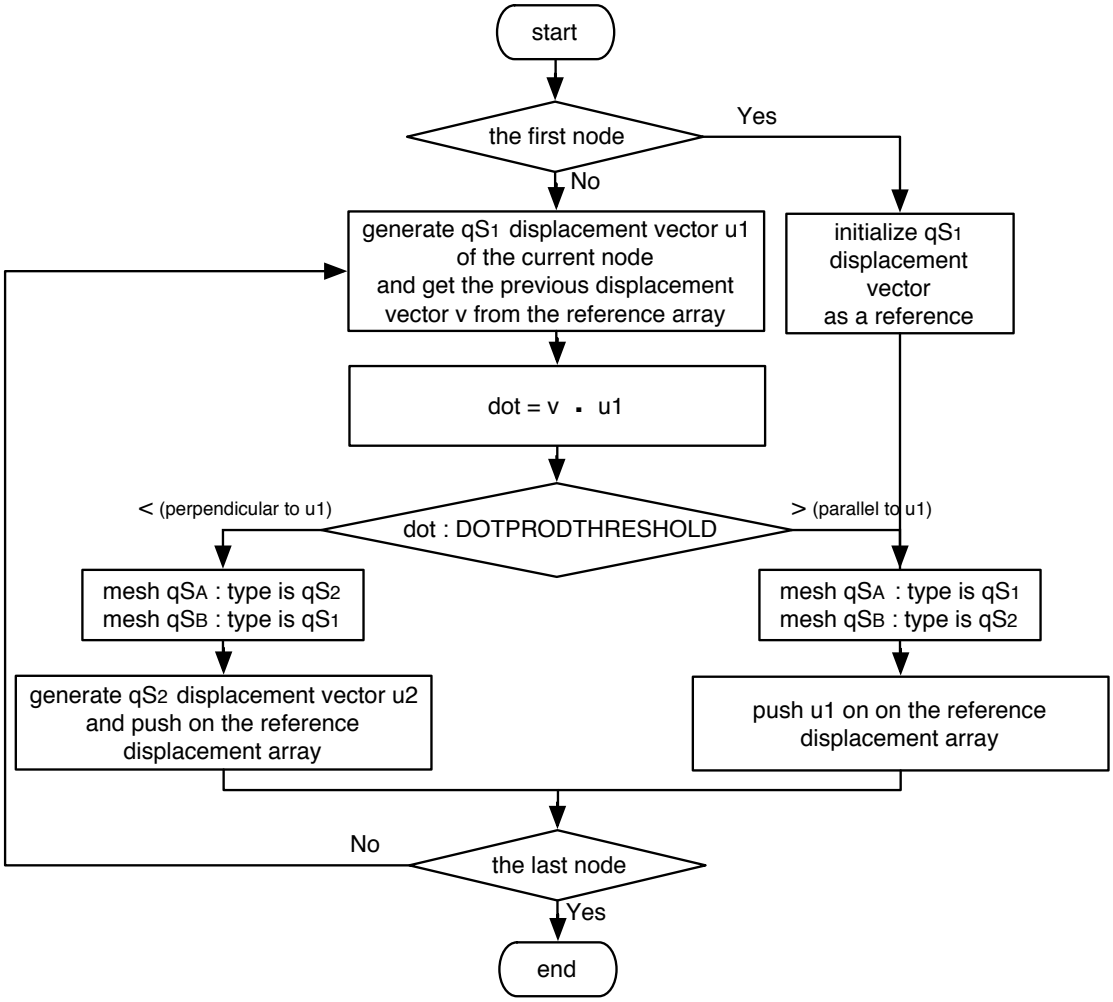

Fig. B1. Flowchart of determining qS_1 and qS_2 wave types to form a physically meaningful wavefront mesh in the present of the singularity.

VITA

Hung-Liang Lai was born in Taichung, Taiwan. He received his B.S. in geology from National Cheng-Kung University, Taiwan, in 1995, and M.S. in geophysics from National Chung-Cheng University, Taiwan, in 1998. After finishing two years of mandatory military service, he came to Texas A&M University for his Ph.D. in geophysics. He started his research under Dr. Richard Gibson in the Fall of 2001. His research interests are wave propagation in anisotropic media, reservoir characterization, and seismic data processing. He received his Ph.D. in May 2007. His permanent address is Dept. of Geology and Geophysics. To Dr. Richard Gibson, 3115 Texas A&M University, College Station, TX 77843. and his email address is geoplai@gmail.com.

This document was typeset in LaTeX by Hung-Liang Lai.